UNIVERSITY OF SOUTHAMPTON

FACULTY OF ENGINEERING, SCIENCE AND MATHEMATICS

School of Chemistry

Effect of ceria and zirconia on nanoparticulate rhodium catalysts

by

Anna Barbara Kroner

Thesis for the degree of Doctor of Philosophy

February 2009

UNIVERSITY OF SOUTHAMPTON

ABSTRACT

FACULTY OF ENGINEERING, SCIENCE AND MATHEMATICS

School of Chemistry

Doctor of Philosophy

EFFECT OF CERIA AND ZIRCONIA ON NANOPARTICULATE RHODIUM CATALYSTS

By Anna Barbara Kroner

Rh metal was implemented as a core component in the so-called three-way automotive exhaust catalyst (TWC) due to its excellent properties such as thermal stability, poison resistance and inert behaviour to react with any support materials. These catalysts are often loaded with small amount of promoter elements such as Ce and Zr that enhance their overall catalytic performances and catalyst lifetime. It is therefore desirable to develop new CeO_x-based catalyst with both high redox activity and high thermal resistance.

Samples of two surface coverages of rhodium on a non-porous high area alumina been synthesised; at 1.6 Rh and 4 wt % Rh loading. Ceria and zirconia have been deposited on the pre-supported Rh catalysts by the controlled surface reaction between the reduced Rh surface and an organometallic precursors: $Zr(acac)_4$ and $Ce(acac)_3$, with different cerium : zirconium ratios: Ce:Zr;1:0, 1:1, 2:1, 0:1. Ceriated Rh catalysts have been also prepared by a different synthesis method, wherein the ceria was deposited on γ-Al_2O_3 and subsequently Rh metal was added. A series of Rh catalysts produced has been characterised *ex situ* by BET surface area measurement, TEM, STEM HAADF, EDX, XPS, and XAFS.

The combination of Diffuse Reflectance Infrared Fourier Transform Spectroscopy (DRIFTS), Mass Spectrometry (MS) and Energy Dispersive X-ray Absorption Fine Structure (EDE) techniques in a synchronous, time-resolved manner has been applied to determine the complementary information about structural and kinetic changes of the chemical system throughout CO exposure and two catalytic processes: CO oxidation and the reduction of NO by CO in the temperature range between 298 K to 573 K.

It has been shown that advanced characterisation techniques, used in the time-resolved, *in situ* manner were needed in order to understand the behaviour of these complex catalytic systems under operating conditions. The effects of the catalysts' composition, temperature and pulsed gas flow on catalyst performance have been effectively mapped by the combined DRIFTS/MS/EDE studies. The synthesis procedure has been found to be crucial to achieve the desired interaction between CeO_x and Rh particles. No enhancement of ceriated Rh catalysts was observed when ceria was deposited directly on γ-Al_2O_3 (method I). The addition of each promoter element by the controlled surface modification procedure (method II) exhibits multiple effects on the catalysts performance. The DRIFTS/XAFS studies have confirmed that CeO_x and ZrO_2 facilitate the protection of Rh particles against extensive oxidation in atmospheres of air, O_2 and CO. Larger Rh core particles of ceriated and zirconiated Rh catalysts have been observed when compared with undoped Rh samples. DRIFTS results indicate that by interaction of CO with Rh particles a significantly larger amount of linear CO species was formed on the ceriated Rh surface than in the non-ceriated Rh catalysts case suggesting the presence of predominant metallic Rh phase for that system. Moreover, only ceria doping was found to improve the catalytic activity of promoted Rh catalysts throughout CO oxidation in the temperature ramp mode under different (O_2/CO) gas composition.

Table of contents

Chapter 3

Chapter 4

Chapter 5

Chapter 7

AUTHOR'S DECLARATION

I, **Anna Barbara Kroner**, declare that the thesis entitled **"Effect of ceria and zirconia on nanoparticulate rhodium catalysts"** and the work presented in the thesis are both my own, and have been generated by me as the result of my own original research. I confirm that:

- this work was done wholly or mainly while in candidature for research degree at this University;
- where any part of this thesis has previously been submitted for a degree or any other qualification at this University or any other institution, this has been clearly stated;
- where I have consulted the published work of others, this is always clearly attributed;
- where I have quoted from the work of others, the source is always given. With the exception of such quotations, this thesis is entirely my own work;
- I have acknowledged all main sources of help;
- where the thesis is based on work done by myself jointly with others, I have made clear exactly what was done by others and what I have contributed myself;
- none of this work has been published before submission.

Signed:

Date: …18.02.2009….

Acknowledgements

First of all my thanks go to my supervisor, Professor John Evans, whose knowledge and patience explaining the more complex aspects of the subject has been instrumental in assisting me complete this research. I am very grateful for having the opportunity to work within this group and carry out this innovative research within two institutes: University of Southampton and the ESRF in Grenoble.

I owe my sincere thanks to Dr. Mark Newton, my supervisor at ESRF for his scientific guidance and interesting discussions, in which he transmitted enthusiasm and inspiration throughout my research.

I express special thanks to Dr. Moniek Tromp for her continuous assistance and knowledgeable discussions during the course of my studies. I am also grateful for her contributions in improving my written English and especially in helping correct this in my thesis.

I would like to thanks to my co-supervisor, Professor Andrea Russell for her encouragement and contributions to my research.

I would like to thank Dr. Andy Dent and Otello Roscioni for their assistance during the beamtimes at ID24. I enjoyed the time we spent undertaking experiments during the hectic and exciting night shifts.

I would like to acknowledge Norman Binsted for his valuable scientific support in the development of the Xmult software.

Special thanks to all my friends and colleagues at University of Southampton: Ewa, Michal, Sergio, Peter, Sarah, Sharmila, Jerome, Bav and Otello for their support during my research and making my time at Southampton so enjoyable. This thanks also extends to the whole of the Polish community at the department: Joanna, Ola, Jozef, Piotr, Magda, Ala, Przemek, Remek, Maciek, Dorota and Angelika for the unforgettable parties. It is so hard not to be a student anymore!

There are a number of people at ESRF who made my time at this institute very pleasant. I would like to thank Sakura and Olivier for their constant assistance, to Florian and Sebastien for their technical support and to my colleagues: Gemma, Guiliana, Angela, Marco, Lello, Matt, Gosia, Marcin, Pilar, Felix, Ivan, Kiran, Tiziana and Fabiola for their friendship during my studies.

I am grateful for having a chance to explore Grenoble for one and half years of my studies and especially for having the opportunity of being surrounded by physicists at ESRF and trying to understand their way of thinking!

I am also indebted to my husband, Karol, for his understanding of my lengthy period of study at university, endless patience, and encouragement.

I wish to thank my best friends, Ania (my own personal psychologist), Monika and Lena for helping me get through the difficult times and for all the emotional support they provided.

Finally, I wish to thank my parents, Janina Kroner and Andrzej Kroner for the support and encouragement they have given me not just during the course of my studies and to my brothers, Mariusz and Arkadiusz for being good friends to me.

Ania

Abbreviations

BET	Brunauer Emmett Teller
DRIFTS	Diffuse Reflectance Infrared Fourier Transform Spectroscopy
EDE	Energy Dispersive EXAFS
EXAFS	Extended X-ray Absorption Fine Structure
FT	Fourier Transform
FWHM	Full width at Half Maximum
HAADF	High-Angle Annular Dark Field
IR	Infra Red
MS	Mass Spectrometry
OSC	Oxygen Storage Capacity
PSD	Particle Size Distribution
SEM	Scanning Electron Microscopy
STEM	Scanning Transmission Electron Microscopy
TEM	Transmission Electron Microscopy
TWC	Three-Way Catalyst
QEXAFS	Quick EXAFS
XAFS	X-ray Absorption Fine Structure
XANES	X-ray Absorption Near Edge Structure
XAS	X-ray Absorption Spectroscopy
XPS	X-ray Photoelectron Spectroscopy
acac	acetylacetonate
fcc	face centred cubic
CN	EXAFS derived coordination number
R/ Å	EXAFS derived distance from the central atom
DW	Debye Waller factor ($2\sigma^2$, where s is the mean square variation both length)

To my Mummy and Daddy

"To understand the heart and mind of a person, look not at what he has already achieved, but at what he aspires to do."

Kahlil Gibran

Chapter 1

Introduction

1.1 Introduction

This chapter gives a general overview of the field of catalysis, highlighting the aspects of the three-way catalyst and its applications, and then concentrates on the characteristics of Rh systems with a review of the relevant literature. The effect of ceria and zirconia doping in the catalytic systems is also discussed. The chapter ends with the objectives and outline of this project.

1.2 The principles of the catalysis

Catalysis plays an essential role in the manufacture from a wide range of products, which would otherwise be unobtainable or prohibitively expensive. Apart of manufacturing processes, successful applications of catalysis are found in the control of pollution and its use in environmental control [1].

Catalysts interact with reactants to provide a reaction pathway with a significantly lower free energy of activation than the corresponding uncatalysed pathway [2]. If alternative routes exist, a catalyst can enhance product selectivity by enhancing just one of the competing reaction sequences, also it can increase reaction rate or enable the reaction at lower temperature. The primary effect of a catalyst on a chemical reaction is to increase its rate coefficient, without being consumed in the process. According to the collision theory, the rate coefficient k is expressed in the Arrhenius equation [3]:

$$k = A * \exp^{\left(-\frac{Ea}{RT}\right)}$$

Where A is the temperature-independent constant called frequency factor, which describes the number of collisions between reactants having the correct orientations. R parameter represents the universal gas constant, equal to 8.314 J $K^{-1}mol^{-1}$. As the reaction rate to activation energy (E_a) and temperature (T) is exponential, small ΔT and ΔE_a causes the large change in the rate of the reaction. In terms of the absolute rate theory, the rate coefficient k can be presented as follow:

$$k = \frac{\kappa T}{h} * \exp^{\left(\frac{\Delta G^{++}}{RT}\right)}$$

Where κ Boltzmann constant, ΔG^{++} is is the Gibbs free energy of activation, h is the Planck's constant.

As indicated in the energy profile diagram (Figure 1.1), the catalyst provides a mechanism involving a different transition state and decrease the free energy of

activation, which is composed of an entropy and enthalpy of activation. The entropy of activation is smaller in the catalysed reaction as the transition state is immobilised on the catalyst surface, which helps in losing the transitional freedom. As a result, the activation energy for a catalysed reaction is smaller than the same uncatalysed reaction. The change of free energy of activation concerns only the differences between initial and final states. The catalyst can increase the rate only of a reaction that is already thermodynamically feasible.

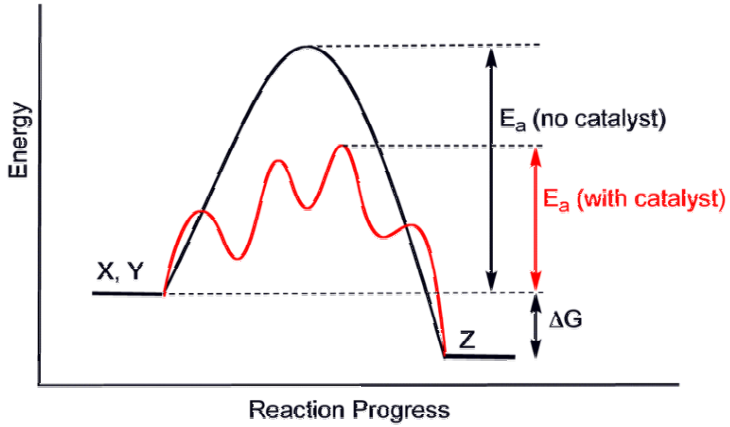

Figure 1.1. Potential energy diagram showing the effect of a catalyst in an exothermic chemical reaction; X, Y – reagents, Z – products, E_a – activation energy, ΔG – free energy

In catalysis, three fields can be distinguished: homogeneous and heterogeneous catalysis and biocatalysis which uses enzymes as catalysts.

Homogeneous catalysts are in the same physical state (gas, liquid, solid) as the reactants and products. The example of this process is hydroformylation, which requires transition metal catalysts such as complexes of cobalt or rhodium [4, 5]. Homogeneous catalysts are more active and selective because their electronic and steric properties can be controlled by changing the ligands around the metal centre. They are mainly used in small batch reaction processes that have demands for pure and selective products, for instance, in the pharmaceutical industry.

Heterogeneous catalysts are in a different physical state to the reactants and products. For a gas-solid system, the catalyst provides a surface for the chemical reaction to take place on. It attracts the reactant molecules on particular centres of its surface where an interface between the catalyst and the reactant molecules exists. Multiple catalytic active sites usually coexist on the surface of the support, therefore the structural characterisation monitored by most of the spectroscopic techniques give insight into the average surface structure. The strength of homogeneous

catalysts is in their generally higher selectivity, whereas the strength of heterogeneous catalysts is their ease of catalysts recovery and products separation [6]. In addition, they are significantly more thermally stable when compared with homogeneous catalysts. Due to this fact, heterogeneous catalysts are extensively used in the petrochemical industry and in large-scale production of base chemicals. The transport of reactants and products from surface to the gas system plays a dominant role in limiting the reaction rate. Understanding these transport phenomena and the dispersion of active sites on support surface are important areas of heterogeneous catalyst research.

Heterogeneous catalysts are extensively used in everyday life for the removal pollutants from automobiles. Figure 1.2 below describes simplified overview of working catalyst. A catalyst is integrated into an exhaust-gas recirculation loop. A relatively small amount of fuel is injected into the recirculation loop upstream of the catalyst allowing the fuel to be converted to exhaust gases by reaction with the steam and air in the exhaust-gas of the stoichiometric fuel-to-air ratio. One of effective catalysts which were extensively studied throughout this project were ceriated Rh catalysts supported on alumina.

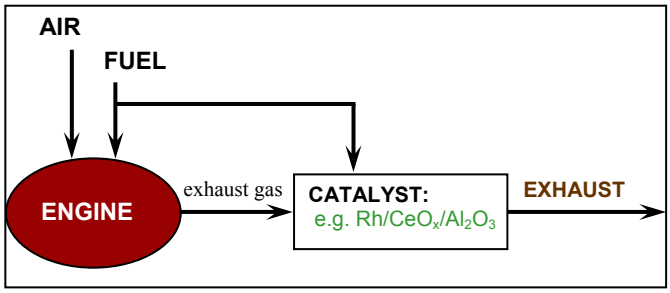

Figure 1.2. A schematic of a working automotive exhaust catalyst system

Automotive exhaust gases formed in gasoline engines contain many environmentally harmful compounds. As a result of incomplete combustion, exhaust gases can include carbon monoxide (CO) and unburnt hydrocarbons (HC). Due to the increased demand for low-emission vehicles, most automobiles are currently supplied with a three-way catalytic converter (TWC) for simultaneous removal of major pollutants CO, NO_x, HC from a gasoline engine's exhaust gases [7].

1.3 Structure of the catalysts

Three-way catalysts (TWC) have a honeycomb-like, monolithic structure, which contains small channels, each about 1 mm in diameter (300 – 600 channels per square inch). The washcoat, which includes the active catalyst material, is impregnated on these channel walls. The thickness of the washcoat layer is ca. 20 – 150 μm and it has a large surface area typically 100 m^2g^{-1} [1]. Thus the diffusional resistance is minimal and gases easily reach the active surface sites, which allows close to 100 % conversion with a high catalytic activity. The main components of the catalyst are precious metals supported on porous oxides such as γ-Al_2O_3, and other base-metal oxides like cerium and zirconium. In addition to these oxides, minor washcoat constituents are included: CaO and MgO as well as the oxides of rare earth elements, such as La_2O_3 [7]. These compounds play a role of promoters or stabilizers in the TWC to increase the catalytic activity or to stabilise the metal dispersion.

The precious metals currently used in three-way catalyst applications are platinum, palladium and rhodium. These metals are well-known catalysts with high activities for controlling the exhaust emissions. Moreover, they are less prone to poisoning compared to metal oxide catalysts, such as CuO. The amount of the active metals in the catalyst is normally ca. 0.5 – 2 wt% of the washcoat. Rhodium has been shown to be an efficient catalyst for NO_x reduction, whereas palladium and platinum metals are used in CO and hydrocarbons oxidation reactions, in particular during cold start. Therefore, commercially-used TWC for gasoline are often a bimetallic combination of the precious metals such as Rh-Pt or Rh-Pd [8].

1.4 Phenomena in the three-way catalyst operation

The performance of a three-way catalyst depends on various factors including the field of catalyst chemistry (preparation, material, and loadings), physical properties (the support, converter design) and the chemical engineering aspects (gas composition, reaction temperatures, dynamic conditions). Three-way catalysts operate under dynamic and fluctuating conditions. The catalytic reactions occur at normal exhaust gas temperatures which, in warmed-up gasoline engines, can vary from 573 K to 673 K during idle, and even up to 1273 – 1373 K, depending on the driving conditions.

Several oxidation and reduction processes take place in the catalytic converter, which is capable of removing simultaneously the major pollutants such as

nitrogen oxides, carbon monoxide, unburnt hydrocarbons, according to the following reactions:

1. Reduction of nitrogen oxides to nitrogen and oxygen

$2NO_X \rightarrow xO_2 + N_2$

2. Oxidation of carbon monoxide to carbon dioxide

$2CO + O_2 \rightarrow 2CO_2$

3. Oxidation of unburnt hydrocarbons (HC) to carbon dioxide and water

$C_XH_Y + nO_2 \rightarrow xCO_2 + y/2H_2O + (n-x-y/2)O_2$

The simultaneous conversion of NO, CO and hydrocarbons in the TWC requires that the air/fuel ratio to be close to the stoichiometric value (air/fuel ratio = 14.6) [9]. The lambda sensor, installed in vehicles to control the air/fuel ratio, has a certain response time leading to oscillations in the gas composition. The air inlet and fuel injection are controlled to provide a stoichiometric ratio between oxygen (air) and fuel. Figure 1.3 highlights the problematic 'balance' a TWC must overcome, which in turn is directly linked to its overall performance as a catalyst. The objective is to keep the air-to-fuel ratio (λ) within the so-called lambda window. In this narrow window, high conversions (>90 – 100 %) of CO, HC and NO_X are achieved simultaneously. When the engine operates under rich conditions the exhaust gas contains more reducing reactants (CO, HC) than oxidising reactants (O_2, NO_X) thus the reduction of NO_X are favoured, whereas the lean conditions favour the catalytic oxidation of CO and hydrocarbons. In order to oxidise CO and HC, the catalytic converter needs also the capability of storing the oxygen from the exhaust gas steam, in case the air fuel ratio goes lean. When insufficient oxygen is available from the exhaust stream the stored oxygen can be released and consumed [10].

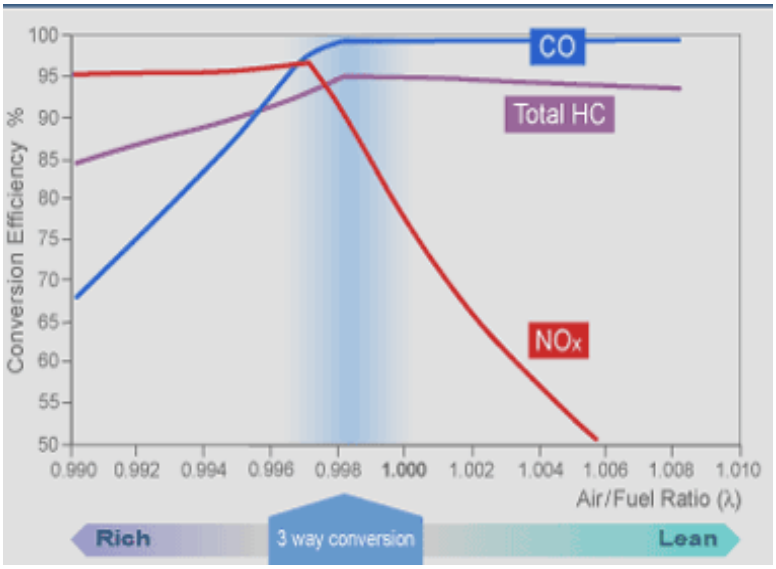

Figure 1.3 Exhaust gas conversions in the three-way catalyst [11]

1.5 Properties of Metal Particles

Most industrial metal catalysts are dispersed as small particles onto high area oxidic support, such as Al_2O_3, SiO_2, TiO_2, and MgO, to allow access of reactants to most of the metal atoms. Due to the very complex structure of supported metal catalysts, a wide range of parameters can be expected to affect catalytic selectivity and activity such as type of metal used, the active size, type and porosity of the support, the induction of promoters to the catalyst composition, and the size and shape of the agglomerated Rh particles. Moreover, some changes in catalytic activity are ascribed to a modification of the electronic properties of the metal particles induced by a metal-support interaction i.e. the hydroxyl groups of alumina support are effective in the particles' degradation and subsequent formation of oxidised metal centres (such as Rh^+) [12-14]. The oxidising effect of γ-Al_2O_3 support on Rh metal may lead to decreased catalytic activity at high temperature. Then the amount of Rh on the catalyst surface is decreased and forms an oxide phase [15].

Due to the specific properties this characteristic brings about, metal particles play a key role in the wide range of the catalytic systems and the main parameters of metal particles which affect the selectivity and activity of the catalyst can be described as follow:

a) Nature of the transition metal

Transition metals are usually defined as elements which possess incompletely filled d orbitals in the ground state. A d-block metal has nine valence shell orbitals (*n*d, (*n*+*1*)s and (*n*+*1*)p) in which accumulate its valence electrons, which are used to

form molecular orbitals in bonding with other groups. Depending upon the nature of the adsorbed molecule these valence orbitals can form both σ and π bonds. The transition metal can form stable compounds in more than one oxidation state and it can readily move between the oxidation states. As a results, during the catalysed reaction the transition metal can be oxidised by one reactant to a higher oxidation state, while is reduced (back to the original form) by reaction with another reactant.

b) Morphology of the metal particles

The size and shape of the metal clusters are of fundamental importance for understanding the catalytic properties of the supported metal catalyst. Yates *et al.* [16] suggested on the basis of TEM measurement on highly dispersed Rh catalysts that rhodium particles are present as raft-like structures with a two-dimensional shape. However van't Blik *et al.* [17] discussed the influence of oxygen on Rh particles and concluded that rhodium particles exist as three-dimensional crystallites with an oxide shell. They have calculated that the average coordination number of the Rh-O shell relatively decreases with increasing particle size in accordance with a three-dimensional structure, while in the case of a two-dimensional raft the coordination number would be independent of the particle size.

c) Nature of the metal – CO bond

CO reacts with most of the transition metals to form metal carbonyl complexes. It has been assumed that in these compounds there are σ and π (by backdonation) bonds between the metal and CO molecule, based on the Blyholder model [18]. The σ bond is obtained by the overlapping of the higher occupied orbital of CO (5σ) and an empty orbital of the metal. The π bond is obtained by the overlapping of an occupied orbital of the transition metal of adapted symmetry with the lower empty orbital of CO (2π). The 5σ and 2π orbitals of CO are localised on the carbon atom, thus the metal – carbon bond can be considered as multiple. The σ and π components give a synergetic effect: by σ donation the metal becomes a better π donor and the CO group becomes a better π acceptor [19]. This feature is effectively visualised in Figure 1.4.

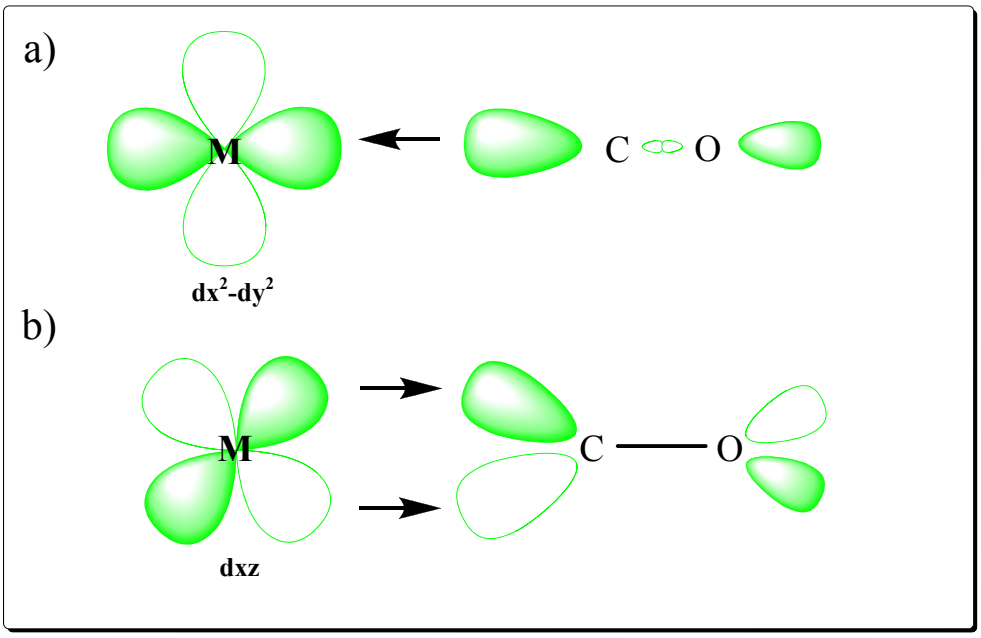

Figure 1.4 Molecular orbital schematic of a CO molecule bonded to a transition metal showing a) the σ-component and b) the π^* component. The arrows indicate the net transfer of electrons.

The π acceptor properties of CO (or π donor of the metal) can be measured by comparison of the ν_{CO} frequencies, because the filling up of the 2π orbital reduces the order of the CO bond thus changing the vibration frequency [20]. Transition metals can therefore combine with a wide range of molecules showing the rich coordination chemistry and thus proves their suitability for catalysis.

d) Interaction between the metal and an adsorbate

The structure of the metal particles can be drastically changed upon adsorption of the adsorbate on their surface; however the structural response of the metal phase is strongly related to its particle size. The disruptive effect of CO adsorption on Rh particles was first suggested by the infrared observations of Yang and Garland [14]. The IR/EXAFS study of well dispersed 0.57 wt% Rh/Al_2O_3 catalysts throughout CO adsorption at 298 K by van't Blik *et. al.* [21] has confirmed that CO molecules significantly disrupt Rh particles, ultimately leading to isolated Rh geminal dicarbonyl species. The oxidative character of CO adsorption was explained by dissociation of CO followed by CO adsorption on the oxidised Rh. However, the EXAFS studies of 1.9 wt% Rh/Al_2O_3 catalysts towards O_2 at room temperature have demonstrated that Rh particles can be oxidised more significantly than after the CO exposure [22, 23]. It has been postulated that the O_2 exposure forms the thin layer of oxide surrounding a metallic core [24]. Nitrogen oxide is

significantly more reactive than CO due to its electron in the antibonding 2p* orbitals, which is empty in gas-phase CO. As a result, NO dissociates on all surfaces of Rh and also on the more corrugated surfaces of platinum [3].The DRIFTS/EDE studies of NO interaction at 373 K alumina supported Rh catalysts have shown that the structural response of Rh particles is strongly related to the Rh loading in the catalytic system [25]. The combined DRIFTS/EDE results for 5 wt% Rh system upon NO exposure has shown the predominant molecular NO adsorption on Rh surface, which significantly limits the extensive oxidation of the Rh nanoparticles, retaining their inherent fcc structure, whereas 2 wt% Rh is completely oxidised under the equivalent conditions. However, above 373 K oxidation of Rh particles dominates for both Rh loadings and there is no net particle size effect.

e) Influence of coverage

The IR results are sensitive to the coverage of metal particles. It has been observed that variation of the coverage of, for example, CO molecules adsorbed on the transition metal shifts the frequency of the species which are associated with metallic rhodium [26]. Such shifts are explained by the following effects [27]:

- Electronic effect – for a given particle, the electron density that the metal can give by backdonation has a finite value. When the number of adsorbed CO molecules increases, each of them has fewer electrons from the metal. Thus, the force constant of the M – C bond decreases as that of the C – O bond increases and as a result, ν_{CO} frequency increases.
- Geometric effect – when the number of adsorbed CO molecules increases, the average CO – CO distances decrease and the dipole – dipole couplings increase and at the same time the blue shift of the ν_{CO} frequency is observed.

However, it needs to be considered that the multiple adsorption sites and switching between them have an influence on the coverage.

f) Alloying Effect

It is well known that some alloys have catalytic properties (activity and selectivity) quite different from those of their components studied alone. Bimetallic catalysts such as Rh-Pt or Rh-Pd often exhibit enhanced properties compared to the single metal catalyst such as improved activity, selectivity and thermal stability. The synergistic effect of platinum and rhodium was demonstrated to be capable of stabilising Rh against the formation of a reduction-resistive oxide phase on alumina

support [15]. In previous work, Oh and Carpenter have been demonstrated the synergistic CO oxidation activity for Pt-Rh alloys [28].

Two effects need to be taken in account:

- Electronic effect – alloying the two metals gives more external electrons as one of the metals is enriched electronically by the second one and the bond strength of adsorbed species will be modified.
- Geometric effect – alloying decreases the number of neighbouring identical atoms (dilution) can increase the selectivity of the catalyst for the particular reaction. Moreover, it affects the types of the adsorption site, surface symmetry (fcc, bcc) and the lattice parameters.

1.6 Rh chemistry – Rh particles supported on γ-Al_2O_3 and CeO_x/Al_2O_3

Rhodium has a different electronic structure to platinum, palladium and nickel; it has nine electrons on the ground state ($4d^8 5s^1$) outside a closed Kr core whereas Pt, Pd, Ni have ten outer electrons. Rhodium salts are easily reducible to the metal, which does not absorb hydrogen and adsorbed hydrogen can be desorbed readily at low temperature [14].

Due to the rich chemistry and thermal stability of Rh compounds they are extensively utilized in many catalytic conversions, for example, in hydrogenation of aromatic components [29], in ring opening and hydrogenolysis of hydrocarbons [30, 31].

However, the main application of Rh metal has been found as an essential constituent of three-way catalysts and as a result Rh catalysts have been investigated since the past decades due to its excellent activity for both CO oxidation [24, 32-36] and NO reduction [35-37]. A wide range of Rh compounds, e.g. single crystals, polycrystalline [38-42] and supported Rh particles [22, 23, 35, 36] have been used to build up the models of reactivity of highly dispersed systems. Studies over single crystals are made with a high degree of control of the surface under study and molecular/kinetic specificity. However, the behaviour of supported Rh catalysts has been revealed to present more complex structures than the Rh single crystal under equivalent conditions. XPS studies of a supported Rh sample performed at 573 K have demonstrated the coexistence of highly oxidised and reduced phases of Rh

particles [43]. These studies have been supported by scanning EXAFS experiment, which have shown that small Rh particles can readily oxidise at room temperature [22, 23]. In contrast, Rh single crystals are extensively oxidised above 500 K and in the extremely lean environment (O_2/CO) > 30 [44]. Kinetic studies by Oh *et al.* [35] have revealed excellent agreement between the specific rates and activation energies (~30 kcal/mol) on Rh single crystals and supported Rh particles throughout CO oxidation. Thus, this reaction has been assumed to be structure insensitive (no significant metal particle size effects on activity) especially at high surface coverage of CO and at low temperature. Moreover, it has been observed that CO oxidation was independent of the metal particle size of supported Rh catalysts but it was sensitive to the nature of support material [36]. By contrast, the reduction of NO by CO [35] has been reported to be structure sensitive, i.e. dependent on changes in the catalyst surface. This was attributed to a large difference in NO dissociation rate between supported and supported Rh models. Furthermore, in the case of supported Rh catalysts the specific rate of the CO-NO reaction increased drastically with increasing Rh particle size; by contrast the nature of the support material had only a small effect on the activity and selectivity of Rh particles [36].

The active catalytic sites may form at the interface between the noble metal (Rh) and the oxide support (CeO_x) and between the metal and partial overlayers of the oxide or suboxide on the metal. The interaction between rhodium and ceria has been extensively studied to fully use the performance of both elements in designing efficient catalysts. However, there are discrepancies in the literature concerning whether Ce aggregates on the Rh surface or interacts with it strongly so as to penetrate inside the bulk Rh. Zhou *et al.* [45] suggested the migration of Rh into ceria and interaction with Ce^{3+}. The extent of the interaction depends on the oxidation state of Ce; Rh retains its metallic state on the surface of a fully oxidised ceria. Imamura *et al.* [46] has also investigated the Ce interaction with Rh throughout the methanol decomposition process and obtained results suggest that Rh penetrates inside CeO_2 and enlarges its lattice parameter. The promotional effect of ceria on Rh catalysts throughout the study of CO – NO reaction by Hecker and Bell [47] was explained by the presence of an oxidised phase of Rh particles. The previous XAS studies of Pt on ceria-based oxide support indicated the formation of the Pt-O-Ce bond, which stabilised the high-oxidation state of Pt and consequently suppressed the sintering of Pt [48]. Furthermore, Zafiris and Gorte [49] found

evidence that the oxygen migration from CeO_2 to Rh plays a key role in enhancing the activity of a Rh/CeO_2 catalyst in CO oxidation. Such an oxygen migration provides the way to regenerate the availability of support oxygen vacancies for NO dissociation forming a catalytic cycle as is indicated in Scheme 1.1.

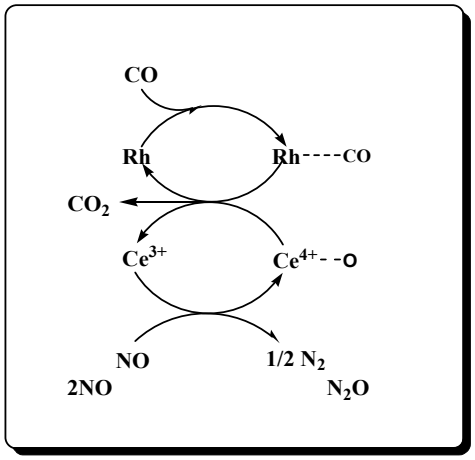

Scheme 1.1 Synergistic promotion effect of Rh – Ce interactions

It has been shown that the rate of the bulk reduction process is related to the structural properties and particularly to the presence of structural defects [50]. Upon repeating the redox cycles, the stress due to the continuous changes of the lattice parameter (larger Ce^{3+} ionic radius compared to that of Ce^{4+}) can easily induce formation of structural defects, promoting oxygen mobility in the framework.

1.7 Ceria as the promoter of the catalyst

Cerium is the second element of the rare earth series with an electronic configuration as $(Xe)6s^25d^14f^1$. In such configuration, the volume of 6s and 5d orbitals are greater than that of the 4f orbital, and, therefore, the three $6s^2$ and $5d^1$ electrons are the only ones participating in chemical bonds. For this reason the valence of the lanthanide elements in their configurations is normally 3+. In the particular case of Ce^{3+}, of which the electronic configuration is $(Xe)4f^1$, the f electron is easily released, acquiring the more stable structure of the tetravalent ion Ce^{4+} [51]. Effectively, cerium dioxide (CeO_2) is its state in nature. Its crystal structure is cubic, of the fluorite type containing four formula units per unit cell [52]. The cerium cations crystallise in a face centred cube and are surrounded by equivalent eight O^{2-} anions. The oxygen anions fill the tetrahedral positions in the metal cage as is shown in Figure 1.5. The lattice parameter of CeO_2 is approximately 0.5411 nm.

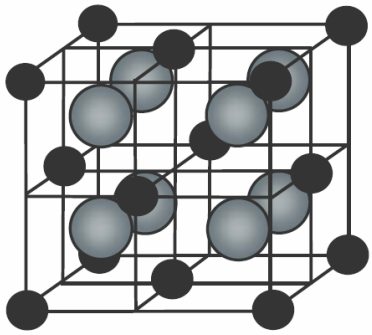

Figure 1.5 Unit cell of CeO_2. Dark atoms are Ce^{4+} and light atoms are O^{2-}

The importance of ceria in catalysis originates from its remarkable oxygen storage capability i.e. its ability to undergo rapid and repeatable redox cycles depending on the conditions in the reactor stream. This feature is strongly related to the facile creation, healing and diffusion of oxygen vacancies, especially at the ceria surfaces [53]. The CeO_2 lattice structure remains intact even after a significant portion of the cerium cations have been reduced from the 4+ to 3+ oxidation state. Ceria may be reduced by increasing temperature or decreasing the oxygen partial pressure. In fact, oxygen deficiencies from ceria lead to the formation of several cerium oxide phases of the type CeO_{2-x} with a range of possible compositions (O =< x <= 0.5) [54-56] and at the same time to occupation of electronic Ce $4f^1$ states with a band gap of ca. 0.6 eV [57]. Thus, CeO_{2-x} becomes conductive to some extent by creating oxygen vacancies in the bulk. Moreover, a chemical reducing agent can be used to facilitate the reduction of ceria at lower temperatures than the thermal O_2 route. During the ceria reduction, gas phase CO interacts with the ceria resulting in carbon dioxide formation; this is similar to the mechanism proposed by Kung on NiO and TiO_2 [58]. Each reaction of a CO molecule with the ceria to form CO_2 removes one oxygen atom from the ceria lattice. The empty lattice site from which the oxygen atom was taken is termed a vacancy. As the lattice oxygen is abstracted as an atom, two electrons remain of the vacancy. A mechanism for abstractive reduction of ceria by CO is shown in Scheme 1.2.

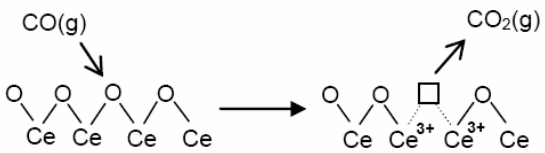

Scheme 1.2 Reduction of CeO_2 by CO

The number of vacancies increases as more oxygen atoms are abstracted. The adsorption of dioxygen on ceria-based oxides has been investigated by FT-IR and Raman spectroscopy to characterise electron defects on the surface [59, 60]. Both superoxide, O_2^-, and peroxide, O_2^{2-}, species were detected on the CeO_x surface which correspond to one- and two-electron defects of CeO_2, respectively. Throughout CeO_2 interaction with H_2 and CO, two-electron defects dominate on the reduced ceria surface for both reductants (CO, H_2). However, the relative concentration of one-electron defects is much higher for the H_2 reduced CeO_x [60]. The surface superoxides are thermally unstable and convert into peroxides as the temperature increases. Moreover, it was postulated that the peroxide species are located on linear and triangular defects of the CeO_2 surface. Oxygen vacancy clusters have been additionally experimentally observed on cerium oxides surfaces using high resolution STM [61] and AFM [62] techniques. The electron localisation detected by STM and the mobility of the surface oxygen atoms observed by AFM determine which defects are formed on a ceria. Thus, complexes of dimers, trimers, lines and larger aggregate vacancies have been observed on ceria surfaces. The structural requirement of the vacancy formed reveals the high propensity of Ce toward reduction upon oxygen deficiency.

Surface oxygen vacancies are proposed to participate in many chemical reactions catalysed by metal oxides. For example, when an adsorbate is oxidised at the surface the oxidant is often a surface lattice oxygen atom, thus creating a surface oxygen vacancy (Mars, van Krevelen mechanism) [63]. Vacancies also bind adsorbates more strongly than normal oxide sites and participate in their dissociation [64, 65]. Control and understanding of the extent and rate of ceria reduction and oxidation, providing the oxygen vacancies, is necessary for many reactions in which ceria exhibits redox behaviour. For example, as a component of water-gas shift (WGS) and hydrocarbons reactions ceria promotes precious-metal catalysts in the elimination of CO and hydrocarbons under reducing conditions [66, 67]. Following the WGS reaction ceria provides an additional pathway for oxidising CO, especially under fuel-rich conditions, and this also produces H_2. The Ce_2O_3 is easily oxidised by H_2O to give H_2 and metal-adsorbed CO can be oxidised by CeO_2. The overall reaction occurs as follows [68]:

1) $CO + * \rightarrow CO_a$

2) $H_2O + Ce_2O_3 \rightarrow 2CeO_2 + H_2$

3) $CO_a + 2CeO_2 \rightarrow CO_2 + Ce_2O_3 + *$

Furthermore, for solid oxide fuel cell electrodes ceria is a mixed ionic and electronic oxidation of the CO or H_2 fuel [69, 70]. However, the most industrially important application of ceria is in automotive emission-control catalysis.

Ceria stabilises the metal dispersion, thus favouring the amount of active surface per weight of the catalyst and base-oxide support e.g. alumina [71]. Moreover, it increases the thermal stability of the three way catalysts [72]. The ageing test of $Ce_{0.75}Zr_{0.25}O_2$ promoted $Rh/Pt/Al_2O_3$ automotive catalysts shows a favourable thermal stability and good TWC performance [73]. Gasoline powered automobile exhausts oscillate between oxidising and reducing conditions, thus the ceria component of TWC stores and releases oxygen as necessary due to the redox couple $2CeO_2 \longleftrightarrow Ce_2O_3 + ½\ O_2$ [74]. The effectiveness of the catalyst redox is quantified by the use of oxygen storage capacity (OSC) measurements. The last point is of relevant technological importance since a high OSC permits an expansion of the operating air/fuel window and thus it increases the overall efficiency of TWC'-s in working conditions. The conversion of CO and HC is increased in reducing conditions as well as the conversion of NO under oxidising conditions. The amount of labile oxygen available under reaction conditions is adjusted by two main factors:

- the surface area of the catalyst – the larger surface area gives larger low-temperature OSC. Thus, under sintering conditions when surface area is lost permanently, there is no oxygen storage available in that system.
- incorporation of a foreign metal cation in the ceria lattice. Though numerous transition metal oxides have been studied [75, 76], zirconia added to ceria has been shown to increase the OSC several times when compared to only ceria promoter content in the system [50, 77, 78].

1.8 Zirconia/Ceria promoters

According to the commercial performance, ceria-zirconia doping is widely used in TWC and exhibits consistent improved OSC properties compared to ceria alone [77-80]. Balducci *et al.* [81] reported that the introduction of Zr into a CeO_2 lattice lowers the energy for Ce^{4+} reduction and leads to more facile diffusion of

oxygen from the bulk to the surface promotes the redox action of the Ce^{4+}/Ce^{3+} couples. Depending on the catalyst preparation, zirconia can form a solid solution in the cubic crystal structure, for CeO_x content above 80 mol% and monoclinic below ca. 10 mol%. In addition to these phases, some metastable tetragonal forms of CeO_x have been reported in the range of CeO_2 content between 20 – 80 mol% [82]. It has been shown that the support with a cubic phase had high homogeneity in which the zirconium and cerium atoms were uniformly distributed in the lattice [83], thus, it was easier to store and release oxygen from this lattice than from that of a tetragonal or a monoclinic phase oxide [84]. Due to the formation of multiple phases of these systems, the processing of the sample, i.e. temperature and extent of reduction and oxidation that have been applied to the mixed oxide precursor, indicate different structural and chemical properties. This phenomenon is employed in catalytic applications as the addition of ZrO_2 increases the thermal stability of CeO_x, which easily sinters above 1073 K, particularly under reducing conditions [85]. The CeO_x/ZrO_2 oxides are more resistant to sintering and loss of surface area at high temperatures compared to ceria. Moreover, the OSC of these materials increases with increasing amounts of dissolved zirconia in the ceria [80]. Indeed, experiments were performed using H_2/H_2O mixtures to control the oxygen content while the equilibrium oxidation state of exposed ceria was monitored using electrochemical methods; results indicated that reduction of ceria-zirconia solid solutions is more thermodynamically favoured than CeO_x reduction under equivalent conditions of temperature and oxygen fugacity [86]. One of the explanations for the increased OSC of the mixed oxide involves a geometric effect, wherein the smaller radius of Zr^{4+} favours the presence of Ce^{3+} ions by eliminating the strain associated with their formation [79, 87]. Figure 1.6 presents the tetragonal distortion of CeO_x/ZrO_2 mixed oxides. This phase leads to the relaxation of the metal – oxygen bonds. The lengthening of the M – O bond moves the oxygen anions closer to the octahedral sites which decrease the energy barrier for the oxygen migration in the bulk, at the same time promoting the ceria reduction [79].

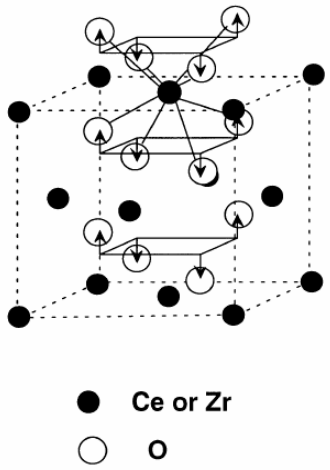

Figure 1.6 Tetragonal distortion of CeO_x/ZrO_2 mixed oxides [79].

However, electronic effects of the role of zirconia addition in the oxygen storage capacity enhancement have also been considered. The electronic structure of ceria and zirconia-ceria compounds have been studied by DFT calculations showing a relaxation pattern which is qualitatively similar for both systems investigated. Thus, the nearest cations move away from the vacancy and oxygen ions move toward it. Nonetheless, for Zr-doped case one O ion, a neighbour of the two reduced Ce^{3+} cations, moves away. The largest effect of the Zr doping can be found in the substantial reduction of the O vacancy formation energy of ca. 0.6 eV [88].

1.9 Aims and outline of the thesis

The goal of the work described in this thesis is the investigation of the structural and catalytic properties of γ-Al_2O_3 supported Rh catalysts promoted by Ce and/or Zr and of the role played by CeO_x as a promoter. This research is focused on a detailed characterisation of wide range of Rh catalysts: Rh/Al_2O_3, $Rh/CeO_x/Al_2O_3$, Rh/ZrO_2, $Rh/CeO_x/ZrO_2/Al_2O_3$ (Ce:Zr;1:1;2:1) with Rh loadings of 1.6 wt% and 4 wt% Rh in the system. Various spectroscopic and microscopic techniques have been used to provide new insights into the particle morphology, the chemical state, the location of ceria and the interaction between Ce, Zr and Rh metals. Special attention has been directed towards the use of three combined techniques XAFS/DRIFTS/MS in an *in situ*, time-resolved manner in order to study directly the behavior of the Rh catalysts throughout CO exposure and two catalytic processes: CO oxidation and the reduction of NO by CO in the temperature range between 298 K and 573 K.

Chapter 3 describes the synthesis and characterisation of ceriated and zirconiated Rh catalysts by BET, TEM, STEM HAADF, EDX, XPS, EXAFS. The choice of the preparation method turned out to be crucial to achieve the desired interaction between ceria and rhodium particles. In **Chapter 4** we have studied the interaction of CO on the supported Rh catalysts, showing the influence of the ceria promoter (placed on the pre-supported Rh particles) on the reducibility of the Rh species. The DRIFTS results demonstrated that ceria is in the close vicinity of the Rh metal particles inducing changes in the CO IR adsorption properties; in good correlation EXAFS analysis indicated the presence of larger Rh particles of the ceriated Rh catalysts. In **Chapter 5** we have studied the CO oxidation over supported Rh catalysts using the array of XAFS/DRIFTS/MS techniques. Additionally, the reactivity's of ceriated and non-ceriated Rh catalysts have been compared under different feedstock gas composition using the microreactor set up. The performance of Rh catalysts turned out to be enhanced by Ce doping showing better catalytic activity which is attributed to strong interaction between ceria and rhodium. **Chapter 6** focuses on the studies of Rh catalysts throughout the second catalytic process: the reduction of NO by CO using the same approach of techniques in the *in situ*, time-resolved manner. The combination of the XAFS/DRIFTS/MS proved to be an excellent approach to elucidate the chemical structure of small Rh particles in the different catalysts and to follow their interaction with particular gases under varied conditions.

1.10 References

1. Twigg, M.V., Catal. Today, 2006. **117**: p. 407-418.
2. Spessard, G.O., Miessler, G. L., *Organometallic Chemistry*. 1997, New York: Prenctice Hall.
3. van Santen R. A., N., J. W., *Chemical kinetics and catalysis*. Fundamental and applied catalysis. 1995, New York: Plenum Press.
4. Abou Rida, M., Smith, A., K., J. Mol. Catal. A, 2003. **202**: p. 87-95.
5. Chen, W., Xu, Y., Liao, S., J. Mol. Catal. A, 1998. **129**: p. 153-158.
6. Gates, B.C., *Catalytic Chemistry*. 1992, Canada: John Wiley & Sons.
7. Heck, R.M., Farrauto, R. J., App. Catal. A, 2001. **221**: p. 443-457.
8. Gandhi, H.S., Graham, G. W., McCabe, R. W., J. Catal., 2003. **216**: p. 433-442.
9. Shelef, M., McCabe, R. W., Catal. Today, 2000. **62**: p. 35-50.
10. Rogemond, E., Frety, R. Perrichon, V., Primet, M., Salasc, S., Chevrier, M., Gauthier, C., Mathis, F., J. Catal., 1997. **169**: p. 120-131.
11. http://ect.jmcatalysts.com/technologies-3way.htm.
12. Smith, A.K., Hugues, F., Thedier, A., Basset, J. M., Ugo, R., Zanderighi, G. M., Bilhou, J. L., Graydon, W. F., Inorg. Chem., 1979. **18**: p. 3104-3112.
13. Worley, S.D., Rice, C. A., Mattson, G. A., Curtis, C. W., Guin, J. A., Tarrer, A. R., J. Chem. Phys., 1982. **86**: p. 2714-2717.
14. Yang, A.C., Garland, C. W., J. Phys. Chem., 1957. **61**: p. 1504-1512.
15. Polvinen, R., Vippola, M., Valden, M., Lepisto, T., Suopanki, A., Harkonen, M., J. Catal., 2004. **226**: p. 372-381.
16. Yates, D.C., Murrell, L. L., Prestridge, E. B., J. Catal., 1979. **57**: p. 41-61.
17. Van't Blik, H.F.J., Van Zon, J. B. A. D., Huizinga, T., Vis, J. C., Koningsberger, D. C., Prins, R., J. Chem. Phys., 1983. **87**: p. 2264-2267.
18. Blyholder, G., J. Phys. Chem., 1964. **68**: p. 2772-2777.
19. Cotton, F.A., Wilkinson, G., *Advanced Inorganic Chemistry*. 1962, New York: Interscience.
20. Twigg, M.V., Spencer, M. S., *Fundamental and applied catalysis*. 1994, New York: Plenum Press.
21. Van't Blik, H.F.J., Van Zon, J. B. A. D., Huizinga, T., Vis, J. C., Koningsberger, D. C., Prins, R., J. Am. Chem. Soc., 1985. **107**: p. 3139-3147.

22. Martens, J.H.A., Prins, R., Zandbergen, H., Koningsberger, D. C., J. Phys. Chem., 1988. **92**: p. 1903-1916.
23. Martens, J.H.A., Prins, R., Koningsberger, D. C., J. Phys. Chem., 1989. **93**: p. 3179-3185.
24. Newton, M.A., Dent, J. A., Diaz-Moreno, S., Fiddy, S. G., Jyoti, B., J., Evans, J., Chem. Eur. J., 2006. **12**: p. 1975-1985.
25. Newton, M.A., Dent, A. J., Fiddy, S. G., Jyoti, B., Evans, J., J. Mater. Sci., 2007. **42**: p. 3288-3298.
26. Rice, C.A., Worley, S. D., Curtis, C W., Guin, J. A., Tarrer, A. R., J. Chem. Phys., 1981. **74**: p. 6487-6497.
27. Imelik, B., Vedrine, C., *Catalyst characterisation*. Physical techniques for solid materials. 1994, New York: Plenum Press.
28. Oh, S.H., Carpenter, J. E., J. Catal., 1988. **98**: p. 543-555.
29. Benseradj, F., Sadi, F., Chater, M., App. Catal. A, 2002. **228**: p. 135-144.
30. Fuchs, M., Jenewein, B., Penner, S., Hayek, K., Rupprechter, G., Wang, D., Schlogl, R., Calvino, J. J., Bernal. S., App. Catal. A, 2005. **294**: p. 279-289.
31. Hayek, K., Goller, H., Penner, S., Rupprechter, G., Zimmermann, C., Catal. Lett., 2004. **92**: p. 1-9.
32. Cavers, M., Davidson, J. M., Harkness, I. R., Rees, L. V. C., McDougall, G. S., J. Catal., 1999. **188**: p. 426-430.
33. Ioannides, T., Efstathiou, A. M., Zhang, Z. L., Verykios, X. E., J. Catal., 1995. **156**: p. 265-272.
34. Newton, M.A., Dent, A. J., Diaz-Moreno, S., Fiddy, S. G., Evans, J., Angew. Chem. Intl. Ed., 2002. **41**: p. 2587-2589.
35. Oh, S.H., Fisher, G. B., Carpenter, J. E., Goodman, D. W., J. Catal., 1986. **100**: p. 360-376.
36. Oh, S.H., Eickel, C. C., J. Catal., 1991. **128**: p. 526-536.
37. Granger, P., Dujardin, C., Paul, J. -F., Leclercq, G., J. Mol. Catal. A, 2005. **228**: p. 241-253.
38. Brown, L.S., Sibener, S. J., J. Chem. Phys., 1988. **89**: p. 1163-1169.
39. Gustafson, J., Mikkelsen, A., Borg, M., Lundgren, E., Kohler, L., Kresse, G., Schmid, M., Varga, P., Yuhara, J., Torrelles, X., Quiros, C., Andersen, J. N., Phys. Rev. Lett., 2004. **92**: p. 126102,1-4.

40. Gustafson, J., Mikkelsen, A., Borg, M., Andersen, J. N., Lundgren, E., Klein, C., Hofer, W., Schmid, M., Varga, P., Kohler, L., Kresse, G., Kasper, N., Stierle, A., Dosch, H., Phys. Rev. Lett., 2005. **71**: p. 115442,1-9.
41. Hopstaken, M.J.P., Niemantsverdriet, J. W., J. Chem. Phys., 2000. **113**: p. 5457-5465.
42. Gustafson. J., W., R., Mikkelsen, A., Torrelles, X., Balmes, O., Bovet, N., Andersen, J. N., Baddeley, C. J., Lundgren, E., Phys. Rev. B., 2008. **78**: p. 045423-1-6.
43. Oh, S.H., Carpenter, J. E., J. Catal., 1983. **80**: p. 472-482.
44. Kellogg, G.L., J. Catal., 1985. **92**: p. 167-177.
45. Zhou, T., Nakashima, M., White, J. M., J. Phys. Chem., 1988. **92**: p. 812-819.
46. Imamura, S., Yamashita, T., Hamada, R., Saito, Y., Nakao, Y., Tsuda, N., Kaito, C., J. Mol. Catal. A, 1998. **129**: p. 249-256.
47. Hecker, W.C., Bell, A. T., J. Catal., 1983. **84**: p. 200-215.
48. Nagai, Y., Dohmae, K., Shinjo, H., Hirabayashi, T., Takagi, N., Minami, T., Matsumoto, S., R&D Review of Toyota CRDL, 2006. **41**: p. 32-39.
49. Zafiris, G.S., Gorte, J., J. Catal., 1993. **143**: p. 86-91.
50. Fornasiero, P., Di Monte, R., Ranga Rao, G., Kaspar, J., Meriani, S., Trovarelli, A., Graziani, M., J. Catal., 1995. **151**: p. 168-177.
51. Duran, F., Gonzalez, M., Moure, C., Pasucual, C., J. Mater. Sci., 1990. **25**: p. 5001-5006.
52. Trovarelli, A., Comm. Inorg. Chem., 1999. **20**: p. 263-284.
53. Ganduglia-Pivorano, M.V., Hofmann, A., Sauer, J., Surf. Sci. Rep., 2007. **62**: p. 219-270.
54. Kummerle, E.A., Heger, G., J. Solid. State Chem., 1999. **147**: p. 485-490.
55. Ricken, M., Nolting, J., Riess, T., J. Solid. State Chem., 1984. **54**: p. 89-95.
56. Zhang, J., Kang, Z. C., Eyring, L., J. Alloys. Comp., 1993. **192**: p. 57-65.
57. Pfau, A., Schierbaum, K. D., Surf. Sci., 1994. **321**: p. 71-80.
58. Kung, H.H., *Transition Metal Oxides: Surface Chemistry and Catalysis*. 1989, New York: Elsevier.
59. Li, C., Domen, K., Maruya, K., Onishi, T., J. Am. Chem. Soc., 1989. **111**: p. 7683-7687.

60. Pushkarev, V.V., Kovalchuk, V. I., d'Itri, J. L., J. Phys. Chem. B, 2004. **108**: p. 5341-5348.
61. Esch, F., Fabris, S., Zhou, L., Montini, T., Africh, C., Fornasiero, P., Comelli, G., Rosei, R., Science, 2005. **309**: p. 752-755.
62. Fukui, K., Namai, Y., Iwasawa, Y., App. Surf. Sci., 2002. **188**: p. 252-256.
63. Descorme, C., Taha, R., Mouaddib-Moral, N., Duprez, D., App. Catal. A, 2002. **223**: p. 287-299.
64. Henderson, M.A., Epling, W. S., Perkins, C. L., Peden, C. H. F., Diebold, U., J. Phys. Chem. B, 1999. **103**: p. 5328-5337.
65. Lu, G., Linsebigler, A., Yates, J. T., J. Phys. Chem., 1995. **99**: p. 7626-7632.
66. Hilaire, S., Wang, X., Luo, T., Gorte, R., Wagner, J., App. Catal. A, 2004. **258**: p. 271-276.
67. Oran, U., Uner, D., App. Catal. B, 2004. **54**: p. 183-191.
68. Bunluesin, T., Gorte, R. J., Graham, G. W., App. Catal. B, 1998. **15**: p. 107-114.
69. Martinez-Amesti, A., Larranaga, A., Rodriguez-Martinez, L. M., Aguayo, A. T., Pizarro, J. L., No, M. L., Laresgoiti, A., Arriortua, M. I., J. Power. Sources, 2008. **185**: p. 401-410.
70. Xie, K., Yan, R., Jiang, Y., Liu, X., Meng, G., J. Memb. Sci., 2008. **325**: p. 6-10.
71. Martinez-Arias, A., Soria, J., Conesa, J. C., J. Catal., 1998. **168**: p. 364-374.
72. Holmgren, A., Andersson, B., Duprez, D., App. Catal. B, 1999. **22**: p. 215-230.
73. Wu, X., Xu, L., Weng, D., App. Surf. Sci., 2004. **221**: p. 375-383.
74. Hu, Y., Jin, H., Liu, J., Hao, D., Chem. Engineer. J., 2000. **78**: p. 147-152.
75. Pijolat, M., Prin, M., Soustelle, M., Touret, O., Nortier, P., J. Chem. Soc. Faraday Trans., 1995. **91**: p. 3941-3948.
76. Zhang, Y., Andersson, S., Muhammod, M., App. Catal. B, 1995. **6**: p. 325-337.
77. Kaspar, J., Fornasiero, P., Graziani, M., Catal. Today, 1999. **50**: p. 285-298.
78. Ozawa, M., Kimura, M., Isogai, A., J. Alloys. Comp., 1993. **193**: p. 73-75.
79. Fornasiero, P., Balducci, G., Di Monte, R., Kaspar, J., Sergo, V., Gubitosa, G., Ferrero, A., Graziani, M., J. Catal., 1996. **164**: p. 173-183.
80. Sugiura, M., Catal. Surv. Asia, 2003. **7**: p. 77-87.

81. Balducci, G., Kaspar, J., Fornasiero, P., Graziani, M., Islam, M. S., Gale, J. D., J. Phys. Chem., 1997. **101**: p. 1750-1753.
82. Di Monte, R., Kaspar, J., J. Mater. Chem., 2005. **15**: p. 633-648.
83. Wang, J.A., Lopez, T., Bokhimi, X., Novaro, O., J. Mol. Catal. A, 2005. **239**: p. 249-256.
84. Sugiura, M., Ozawa, M., Suda, A., Suzuki, T., Kanazawa, T., Bull. Chem. Soc. Jpn, 2005. **78**: p. 752-767.
85. Perrichon, V., App. Catal. A, 1995. **129**: p. 69-79.
86. Kim, T., Vohs, J. M., Gorte, R. J., Ind. Eng. Chem. Res., 2006. **45**: p. 5561-5565.
87. Mamontov, E., Egami, T., Brezny, R., Koranne, M., Tyagi, S., J. Phys. Chem. B, 2000. **104**: p. 11110-11116.
88. Yang, Z., Woo, T. K., Hermansson, K., J. Chem. Phys., 2006. **124**: p. 224704-224711.

Chapter 2

Experimental techniques

2.1 General introduction

The catalysts investigated in this project have the form of amorphous powders and cannot be prepared as single crystals that would allow exact determination of surface structure. Due to this fact the best available characterisation of most catalysts are based on the measurement of the composition, structure, bonding between adsorbed molecules and the surface, and the oxidation state of surface atoms. The whole range of desired information can be provided only by using the several experimental techniques. Several of these methods involve the detection of electrons which are emitted or scattered from the surface. They are based on the similar principles. In particular, all derive their surface sensitivity due to the fact that electrons in this energy range have a high probability of inelastic scattering. Generally, all of these techniques use the fundamental physics of electron-matter interactions in various ways to yield their particular information. For instance, XPS and XAFS share core hole generation as the initial excitation event.

Rhodium catalysts synthesized in this project firstly have been characterized using Brunauer Emmett Teller measurements (BET), transmission electron microscopy (TEM), energy dispersive analysis of X-rays (EDX), X-ray photoelectron spectroscopy (XPS) and X-ray absorption fine structure (XAFS). BET provides information about the surface area and pore size analysis of the material, TEM examines the nanostructure of the particles and EDX measurements give quantitative elemental composition of the samples. In turn, the XPS is applied to establish the oxidation state of the elements parallel with the estimation of relative concentrations of Rh, Ce, Zr, Cl in the systems. XAFS technique was used to probe the local structure of the catalysts.

The structure, reactivity and functionality of the supported rhodium catalysts have been investigated in the operating conditions by the combination of three techniques: mass spectrometry (MS), diffuse reflectance infrared Fourier transform spectroscopy (DRIFTS) and one of the family of X-ray absorption fine structure (XAFS) spectroscopies - energy dispersive EXAFS (EDE) in a synchronous and time-resolved manner. These techniques are complimentary, and have assisted in understanding the structure and chemistry of the Rh catalysts. EDE is a technique, which probes the local structure around absorbing metal centre. DRIFTS includes the information about the type and bonding of absorbed molecules to the metal. MS shows the gas evolution during the reaction or decomposition of surface species.

This chapter provides a background regarding the theoretical and practical aspects of the experimental techniques used in this project. This includes the capability of the technique, its strengths and limitations relative to alternative applications.

2.2 BET surface area measurement

Isothermal nitrogen adsorption analysis is the most common technique for analysing the surface area of the sample. In addition, this method gives information about the porosity and pore size analysis, which is very important for nanoporous materials. The method of evaluating these values involves studying the adsorption and desorption of an inert gas such as nitrogen onto the surface of the solid at liquid temperature and relative pressures (P/P_0) ranging from 0.05 – 1, highlighting P_0 as a vapour pressure above a layer of nitrogen that is more than one molecule thick, essentially thought of as a pure bulk liquid.

All the surface areas presented in this work were calculated using the technique developed by Brunauer, Emmett and Teller (BET) in 1938 [1]. The BET isotherm (Eq. 2.1) is applied to the adsorption data as follows:

$$\frac{V}{V_m} = \frac{cz}{(1-z)\{1-(1-c)z\}} \qquad \text{Eq. 2.1}$$

Where z is the relative pressure (P/P_0), V is the volume of gas adsorbed, V_m is the volume of gas adsorbed corresponding to monolayer coverage and c is a constant. When this coefficient is large (c>>1), the isotherm simplifies to the Equation 2.2:

$$\frac{V}{V_m} = \frac{1}{1-z} \qquad \text{Eq. 2.2}$$

From this the calculated volume can be related to the number of moles of gas adsorbed, and hence the surface area in m^2. A value of m^2g^{-1} can be found if the mass of the material is known. The BET surface area measurements were collected on Micrometrics GEMINI III 2375 surface Area Analyzer.

2.3 Transmission Electron Microscopy

In electron microscopy, a narrow beam of high energy electrons is directed at a specimen. Images are formed either by electrons passing through a thin sample via transmission electron microscopy (TEM), or by secondary emissions from the surface of a thick sample, using so called scanning electron microscopy (SEM). Materials for TEM must be specially prepared to thicknesses which allow electrons

to transmit through the sample, much like light is transmitted through materials in conventional optical microscopy. Because the wavelength of electrons is much smaller than that of light, the optimal resolution attainable for TEM images is many orders of magnitude better than that from a light microscope. Thus, TEM can reveal the details of internal structure – in some cases as small as individual atoms. The technique was used to obtain visual information on the nanostructure of supported metal catalysts produced throughout the research, approximate the shape and size of the particles including the particle size distribution.

The TEM analysis has been obtained using the electron microscope Tecnai F20 at the Johnson Matthey Technology Centre by one of their technicians, operating at 200 keV, with a point resolution of < 2 Å. It was also equipped with a high-angle annular dark field (HAADF) detector for scanning transmission electron microscopy (STEM) and an energy dispersive X-ray (EDX) detector. This instrumentation is capable of detecting even very small metal particles (< 1 nm) by Z contrast and of analysing selected points by EDX spectroscopy. Additionally, some TEM images were obtained using a JEM-3010 analytical transmission electron microscope at University of Southampton. The electron gun is capable of accelerating the electrons through a selected potential difference in the range 100-300 keV, yielding the resolution of 2.1 Å and a magnification $1.5x10^6$. The appropriate electron energy depends upon the nature of the specimen and the information required. For some applications, particularly if the specimen is relatively thick or very high resolution is required; it is an advantage to use much higher electron energies.

Focusing and magnification is achieved using a series of electromagnetic lenses. The electron beam is focused onto the specimen by the condenser lenses and magnification of the transmitted image is achieved using objective and projector lenses. Finally, the image is formed on a fluorescent screen. The primary electrons that pass through the specimen can be transmitted without being detected, elastically or inelastically scattered. Scattering of the primary electrons of the beam by the specimen gives rise to the contrast in the image in brightfield mode. The image appears darker when the inelastic scattering increases which occurs when the mean atomic number and thickness of the sample increases. The darkfield image can be produced by selecting a diffracted beam, and moving the detector off the axis of the incoming electrons. The specimen must be very thin (<100nm) [2].

2.4 Energy Dispersive Analysis of X-rays (EDX)

Energy Dispersive X-ray analysis (EDX) is a technique used to identify the elemental composition of the specimen or the interesting area of the sample. The EDX analysis system works as an integrated feature of SEM. Its capabilities are due to the principle that each element of the periodic table has a unique electronic structure and thus, a unique X-ray emission spectrum.

The detector used in EDX was a lithium drifted silicon detector operated at liquid nitrogen temperatures. When X-ray photons strike the detector, photoelectrons are generated within the body of the Si and as the photoelectrons travel through the Si, they generate electron-hole pairs which are attracted to opposite ends of the detector with the aid of a strong electric field. The size of the current pulse thus generated depends on the number of electron-hole pairs created, which in turn depends on the energy of the incoming X-ray photon. Thus, an X-ray spectrum can be acquired giving information on the elemental composition of the material under examination [2]. EDX data was taken for the catalyst samples using a JEOL JSM-6500F SEM machine integrated with an Oxford instruments 300 for EDX data acquisition. The Rh L edge was analyzed for each sample as the upper limit of the EDX machine was ca. 20 keV. The resolution of the microscope is between 100-200 eV, thus the detector have the capacity to resolve the difference in Rh L and Cl K edges. In a typical experiment, ten scans sampling of the sample were performed with EDX; the average weight and atomic percentages are reported in chapter 3. An example of SEM image of the area under investigation and corresponding EDX spectrum is given in Figure 2.1 showing the resolution of the equipment used.

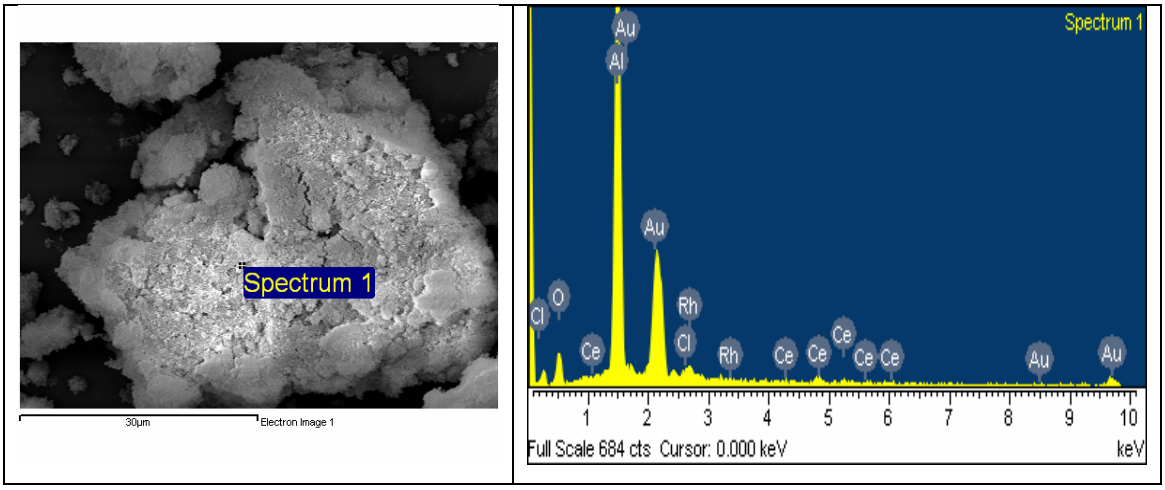

Figure 2.1 EDX data collection showing: a) SEM image and b) corresponding EDX spectrum of 4 wt% $Rh/CeO_x/Al_2O_3$ sample.

2.5 X-ray Photoelectron Spectroscopy

The principle in X-ray photoelectron spectroscopy experiments is to study the properties of electrons photo emitted from a sample by monoenergetic photons. It is a quantitative spectroscopic technique which utilises core level shift to derive chemical and electronic state information on the elemental components of the sample penetration depth ~ 10-100 Å. When a photon of energy hν penetrates the surface of a solid and is absorbed by an electron with a binding energy E_B below the vacuum level, the electron emerges from its initial state to an excited state. If the photon is sufficiently energetic, the final state lies above the vacuum level and the photoelectron can escape from the solid with a kinetic energy. The following equation shows the Einstein relationship (Eq. 2.3) which is known as the photoelectric effect [3].

$$E_K = h\nu - E_B - \phi \quad \text{Eq. 2.3}$$

Where hν is the energy of the incident photon, E_B is the binding energy of the ejected electron, defined as the energy of the core level of the emitted electron relative to the Fermi level. E_B of electrons directly reflects the effective charge felt by the initial core level electron and is therefore indicative of the chemical state of the unexcited atom; E_K is its kinetic energy and ϕ is the work function of the sample, i.e. the energy difference between the Fermi level (E_F) and the vacuum level [4]. The energy required to remove the electron depends only on the energy of the level it originally occupied relative to that of an unbound electron. The energy of the photoelectrons is directly related to the atomic and molecular environment from which they originated and the number of photoelectrons emitted is related to the concentration of the emitting atoms in the sample [5]. The photoemission process is shown in Figure 2.2.

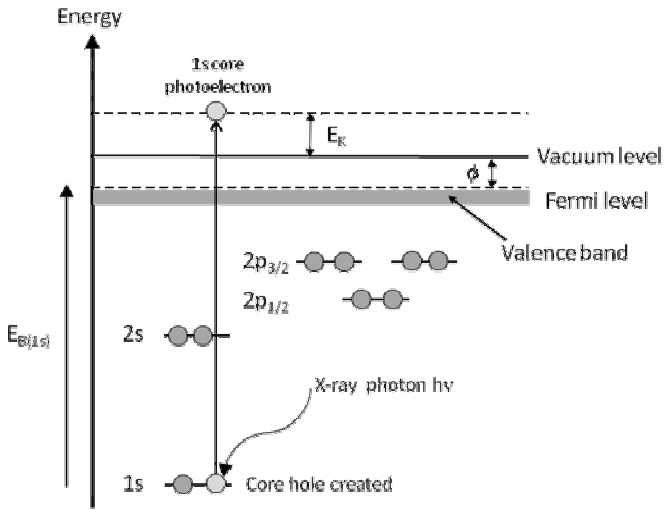

Figure 2.2. X-ray photoemission of a 1s core level electron

Since hν and ϕ are known (composite of both analyser and sample values), and E_K is measured by the energy analyser it is possible to calculate E_B for every peak in the spectrum. As E_B for each emitted electron is specific to its original elemental orbital, analysing the position and height of the peaks in the spectrum provides qualitative and quantitative information respectively on all the elements present in the surface. The additional information on exact peak positions may then be capable of indicating the chemical state of the elements. The surface atomic concentrations were determined from photoelectron peaks areas using the atomic sensitivity factors reported by Scofield [6]. The fixed full width at half maximum (FWHM) and the fixed positions of the components were similar to those collected on our reference samples.

However, in reality the processes of photoionisation and photoemission are very rapid. The result is that the final state may be one in which an electron is an excited bound state of the atom, or in which another electron is ejected into the continuum of unbound states above the vacuum level. Such processes leave less energy for the emitted photoelectron and this gives rise to lower kinetic energy satellites, these are usually referred to as shake-up features (when excitation is to a bound state) and shake-off (when excitation is to the continuum).

If an electron is removed from a d-orbital the interaction of the electron spin angular momentum (quantum number s) with the orbital angular momentum (quantum number l) generates two possible states for the ion, depending on whether the angular momenta added or subtracted. The overall quantum number j can be 5/2 or 3/2 and the difference in energy between these states is related to the spin-orbit

coupling constant for the atom. Similar effects operate for p-orbital, but not for s-orbital, which have no orbital angular momentum.

Conventional X-ray sources are created by bombarding a solid target with energetic electrons. The emission from this target consists of characteristic line emissions associated with the filling of core holes created by the incident electron, superimposed on a continuum background up to the incident electron energy.

The XPS experiment reported here were carried out in the Scienta ESCA300 Spectrometer at NCESS in the Daresbury Laboratory. The instrument employs a high power rotating anode and monochromatised AlK_α ($h\nu$=1486.7 eV) X-ray source with energy resolution ~ 0.35 eV. The apparatus consists of three chambers: the ultra-high vacuum (UHV) chamber, preparation chamber and an introduction fast loading chamber. The sample is rack-and-pinion transfer mechanism easily transferred from one vessel to the other with little disturbance to the UHV chamber base pressure. The sample, in powder form, is mounted on a stainless steel holder with double-sided adhesive carbon tape.

2.6 X-ray Absorption Spectroscopy (XAS)

X-ray absorption spectroscopy (XAS) is a probe of the local structure around selected atom species in solids, liquids and molecular gases. For atoms in a condensed system, the observed x-ray absorption spectrum is not a smooth function of energy but oscillates for several hundreds eV above the absorption edge. The details of these oscillations, called EXAFS (extended x-ray absorption fine structure), depend strongly on the local atomic environment of the absorbing atom, with a few nearest neighbouring atoms accounting for essentially all the observed variations in the absorption.

In a typical XAS experiment, performed in the transmission geometry, the intensity $I(\omega)$ of transmitted x-rays through a sample thickness x is measured as a function of energy. The loss of x-ray intensity is given by the exponential Lambert-Beer attenuation law (Eq. 2.4):

$$I(\omega) = I_0(\omega)e^{-\mu(\omega)x} \qquad \text{Eq. 2.4}$$

where $\mu(\omega)$ is the linear absorption coefficient. As well as depending on the energy of the incident beam, μ also depends on the composition of the irradiated sample. The absorption coefficient $\mu(\omega)$ is approximated well by a sum of the absorption

coefficients of individual atoms, proportional to the x-ray absorption cross section $\sigma(\omega)$.

The X-ray absorption spectrum is traditionally divided into two regimes: x-ray absorption near edge structure (XANES) and extended x-ray absorption fine structure (EXAFS), as Figure 2.3 indicates. Though the two regions overlap and have the same physical origin, this distinction is convenient for the interpretation:

- XANES region: (within about 50-100 eV above the absorption edge) the photoelectron is strongly scattered by the atoms surrounding the photo-absorber and the amplitude. XANES probes the chemical state and electronic structure, and is a direct probe of the density of states. However, as the inelastic mean free path curves of the electrons at these energies (<50 eV) are relatively short, this situation greatly complicated by the potential for complex multiple scattering events. The shape of the XAS spectra in this region is strongly sensitive to the formal oxidation state and coordination chemistry of the absorbing atom. However, it includes also transitions to bound states.
- EXAFS region: (from about 80 eV above the edge) the photoelectron has sufficient energy for treating the multiple scattering in terms of distinct two-, three-… n-body contributions. Nevertheless, the two-body contributions are generally the dominant terms.

In the x-ray region (below approximately 50 keV), the cross section for the interaction of radiation with matter is dominated by photoelectric excitation processes which manifest themselves as sharp rises in the absorption, usually termed edges (i. e. K, L_1, L_2 and L_3), when the incident photon has an energy equal to the binding energy of a core-level electron (i. e. 1s, 2s, $2p_{1/2}$ and $2p_{3/2}$). Clear oscillations of the absorption coefficient are observed in a wide energy region above the edge (of about 1000 eV). The absence of such modulations in low density systems and gases points to a strict relationship between EXAFS oscillations and the presence of neighbouring atoms.

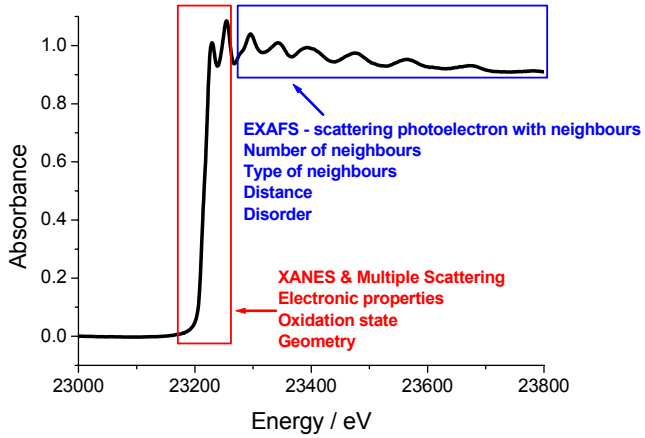

Figure 2.3. XAFS Rh K edge of 4 wt% Rh/Al_2O_3 under 5 % H_2/He showing the XANES and EXAFS region

EXAFS and its local nature are best understood in terms of wave-behaviour of the photoelectron created in the absorption process. If the incident radiation is of sufficient energy, this absorption effect causes the subsequent ejection of a core electron as shown in Figure 2.4. This in turn results in an outgoing photoelectron wave from the absorbing atoms. Modulation of this wave occurs by backscattering from the surrounding atoms. EXAFS is therefore the phenomenon of oscillations in the absorption coefficient as both the outgoing and backscattered waves interfere constructively or destructively on the variation of the X-ray beam wavelength. The energies of the absorption edges correspond to the core-level energy which are characteristic for each element.

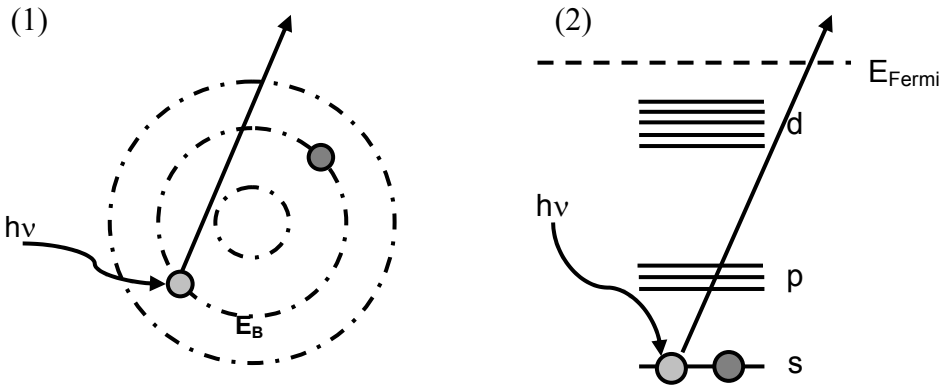

Figure 2.4. The photoelectric effect in terms of excitation of the orbital (1) or different energy levels (2) [7].

The interference between the outgoing and back-scattered photoelectron waves results in the oscillatory behaviour of the absorption observed above the

absorption edge. The absorption coefficient above the absorption edge is defined in Equation 2.5:

$$\mu_{tot} = \mu_0(1+\chi) \qquad \text{Eq. 2.5}$$

where μ_0 is the background absorption of a single atom as a result of elastic and inelastic scattering. χ refers to the EXAFS oscillations which can be extracted from the experimental data using Equation 2.6, where the oscillatory behaviour is given as a function of the photoelectron wave number, k.

$$\chi(k) = \frac{\mu_{tot}(k) - \mu_0(k)}{\mu_0(k)} \qquad \text{Eq. 2.6}$$

In the following we report the simple analytic form of the EXAFS signal $\chi(k)$. It assumes both the approximation of spherical waves for the wavefunction associated to the outgoing and backscattered photo-electrons and the single scattering approximation (meaning that it considers only two-body contributions). The final analytic form for Equation 2.6 is expressed below
(Eq. 2.7):

$$\chi(k) = \sum_j \frac{N_j f_j(k) e^{-2Rj/\lambda(k)} e^{-2k^2\sigma_j^2}}{kR_j^{\,2}} \sin\left[2kR_j + \delta_j(k)\right] \qquad \text{Eq. 2.7}$$

Where the sum over *j* involves all the coordination shells around the photo-absorber atom. The backscattering amplitude $f_j(k)$ is proportional to *Nj* i.e. the number of surrounding atoms in the *j*th shell and it is inversely proportional to $kR_j^{\,2}$ (R_j is the distance between the photoabsorber site and the atoms in the *j* shell). The term $e^{-2Rj/\lambda(k)}$ is used to account for the inelastic losses in the scattering process with λ(k) being the electron mean free path. The term $\delta_j(k)$ describes the phase-shift due to photoelectron diffusion from the photoabsorber site and from the neighbouring atoms. The Debye-Waller factor $e^{-2k^2\sigma_j^2}$ describes the structural and thermal disorder of the sample. The EXAFS equation shows the close relationship between the DW factor and the effective coordination number obtained which is expressed as follows $N \approx \frac{I}{e^{(-\sigma^2)}}$. Therefore, the occupation number (*N*) is a sensitive function of

the DW factor and a small variation of this parameter results in a relatively large change in the value of coordination number to fit the measured intensity (*I*). The static disorder is due to the variance of the distance between the absorbing and scattering atoms. When the atoms are close to the central atom, the photoelectron waves become synchronise. This correlation becomes weaker for shells at larger distances from the central atom and consequently the DW factor is larger. Additionally, the distance of an atom from the absorbing species is not constant due to thermal motion effects and contributes to the dynamic disorder. The relative thermal motion between absorber and backscatter will be most consistent with each other when the central atom and the neighbouring shells are closer together. Due to the influence of the thermal motion of atoms on Debye-Waller factors, cooling the sample down to low temperatures will lead to an increase in the oscillations, increasing the signal to noise ratio and producing enhanced fits for more distant shells. However, at higher temperature an increased DW factor is observed, which has a dampening effect on the EXAFS amplitude as the oscillations are broadened.

The plane wave approximation described above was used to explain the parameters involved; however, the analysis was done via a spherical wave methodology.

2.6.1 Data Acquisition

X-ray absorption spectroscopy results give the absorption of a high energy X-ray by an atom in a sample. This absorption occurs at a defined energy corresponding to the binding energy of the electron in the material. Therefore, XAFS is usually applied at synchrotron radiation facilities that provide intense and continuously tuneable X-rays. The radiation is produced by the acceleration of electrons in an ultra high vacuum at speeds close to that of light. The photons are projected at a tangent to the storage ring and the electron trajectory is maintained by arrays of magnets that constrain and bend the path of the electrons into a circular shape. When the electrons travel at a fixed energy around circular path, synchrotron radiation is emitted and is released to the experimental hutch at a tangent. The beamlines can originate at bending magnet or insertion devices such as wigglers and undulators, which increase the overall energy distribution of the radiation and reduce its divergence. The beamline include X-ray optical devices which control the bandwidth, photon flux, beam dimensions, focus and collimation of the rays. This

radiation can cover a wide range of energies from far infrared to hard X-rays [8]. X-ray absorption experiments performed in the framework of this thesis mainly have been carried out at the European Synchrotron Radiation Facility (ESRF) in Grenoble and at the station 9.3 at the Synchrotron Radiation Source (SRS) in Daresbury, UK.

2.6.1.1 Scanning EXAFS

In standard scanning mode, EXAFS spectra are acquired by scanning the photon energy in a step wise method. X-ray absorption measurements have been performed in transmission geometry at the BM29 beamline and at the station 9.3. The synchrotron produces white radiation with the full range of x-ray wavelengths. The particular energy is selected by a monochromator, comprised of, a pair of parallel silicon single crystals, by making use of the Bragg diffraction relationship (Eq. 2.8).

$$n\lambda = n\frac{hc}{E} = 2d\sin\Theta \quad \text{Eq. 2.8}$$

The variation in absorption of the X-rays as the energy of the incident photons is increased is measured by a series of ion chambers where the absorption of the sample is obtained in absorbance form $\ln(I_0 / I_t)$. The ion chambers are positioned before and after the sample (Figure 2.5). The first measures I_0 to give the incoming intensity and is filled with the mixture of noble gases to absorb approximately 20% of the incident flux while a second measures the transmitted intensity: I_t and is filled with a gas mix to absorb 80%. A third detector I_r is used to calibrate the energy against a metal foil. This is important as the energy calibration may not be exact and small edge shifts can contain valuable information. A high constant voltage is applied across the ionisation chambers so that the ions are attracted to the negative side and the electrons to the positive and as a result a current flows directly proportional to the number of photons entering.

BM29 is the general purpose X-ray absorption spectroscopy beamline [9] of the ESRF, built tangentially to a bending magnet of this 3rd generation synchrotron radiation source.

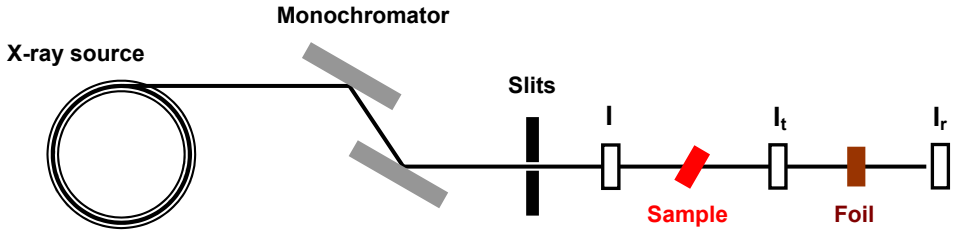

Figure 2.5. Schematic of XAS experiment operating in transmission mode.

The beamline optics includes a double flat crystal monochromator and a pair of harmonic rejection mirrors. The lower of these two mirrors can be additionally used to focus the beam down to 20-30 μm.

Four different Si crystal pairs can be installed, depending upon the requirements for energy and photons flux. For the experiments related to this work, Si(311) crystals having operational energy between 5 and 50 keV, have been used. The energy resolution when using Si(311) monochromator is $\Delta E/E=4 \times 10^{-5}$ at 15 keV. This is well below the natural broadening of the spectra given by the core hole widths (~2×10^{-4}).

Beam intensities are measured using sealed ionization chambers filled with optimal He/Ar or He/Kr mixtures at a total pressure of 2 bars and operated at a field of between 300-800 V cm^{-1}. The gas noble species, gas pressure and applied voltage control the detector efficiency.

2.6.1.2 Energy Dispersive EXAFS

In situ investigations of catalysts under realistic reaction conditions are necessary since the structure of catalysts may be very different from that found *ex situ*. Therefore, over the past decades, great efforts have been devoted to develop methods to characterise catalysts under operating conditions [10, 11]. Energy dispersive extended X-ray absorption fine structure spectroscopy (EDE) has been used on selected samples to gain insight into the oxidation state and particle size during initiation and termination of the catalytic processes. The main advantage of dispersive experiments is very fast data acquisition (less than 1s), as during data acquisition no optical elements are required to move, and the energetic bandwidth required to obtain EXAFS may be applied to a sample instantaneously, rather than requiring a stepwise approach to obtaining data over the required energy range. As such the EDE experiment should be both intrinsically stable and be limited only by the time sequence to accumulate sufficient statistics for EXAFS to be obtained.

Therefore, the principal issues to the quality of EDE data is the sample homogeneity and stability and size of the beam.

ID24 is the ESRF XAS beamline with parallel detection of the whole spectrum made possible by energy dispersive highly focusing x-ray optics.

The beamline satisfies the main requirements

- position stability of focal spot in whole energy range;
- high flux; for measurements in transmission geometry the x-ray beam traverses the sample bed. Using the energy dispersive EXAFS, the total flux is spread over the whole bandwidth and at the Rh K edge energy is between 1.5 – 2 keV;
- small focal spot; plays a key role for high pressure experiments.

However, analysing the heterogeneous catalysts, massive improvements in data quality can be achieved by increasing the vertical size of the dispersive beam [12]. This is due to the fact that heterogeneous catalysts are often comprises of very small quantities of the element of interest for structural study, and supported upon a dispersant that comprises other heavy elements like Ce and Zr that may scatter X-rays.

The geometrical arrangement of the energy dispersive optics is given in Figure 2.6. A quasi-parallel and polychromatic beam, supplied by an undulator source, is energy-dispersed and focused by an elliptically curved crystal. Because the incident X-rays strike the crystal at slightly different angles along its length, the bent crystal acts as a polychromator diffracting a different energy at each point. This energy-dispersed beam converges to a focus at the sample position. The beam, transmitted through the sample position, then diverges towards a position sensitive detector. The position of the beam, incident on the detector, can be directly correlated to energy. By measuring the spatial X-ray intensity distribution in the presence (I_t) and absence (I_0) of the sample, a transmission geometry X-ray absorption spectrum can consequently be obtained.

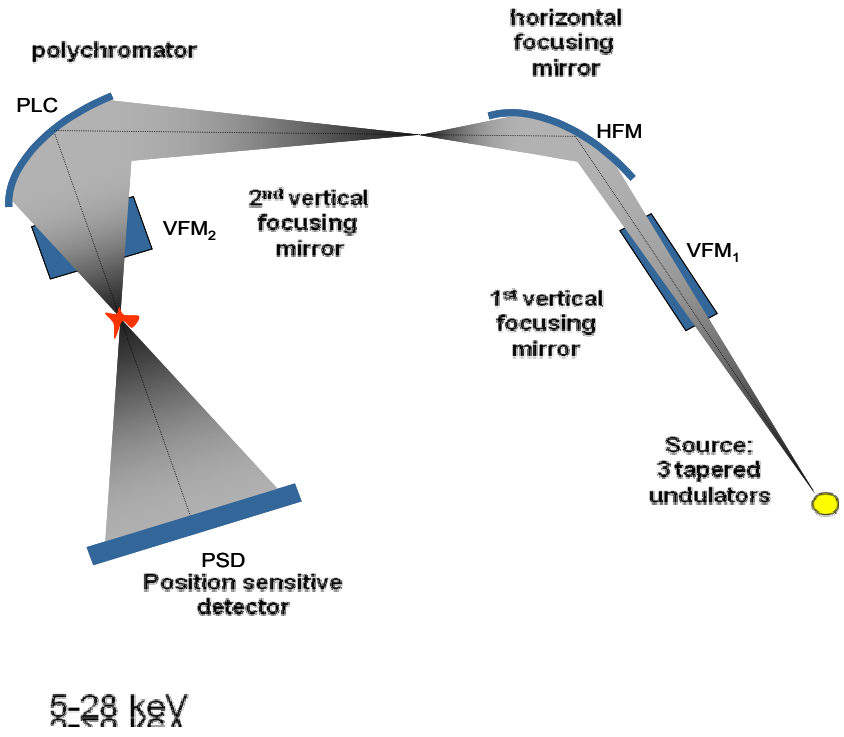

Figure 2.6. Present optical layout of beamline ID24. The polychromator is coupled to two undulators through a Kirkpatrick-Baez optical system.

The two Kirkpatrick-Baez mirrors [13] reflect the beam at a fixed grazing angle of 3 mrad and ensure efficient harmonic rejection in the whole energy range of operation, between 5 and 27 keV. The first mirror, placed at 30m from the source, is in a quasi 1:1 configuration and vertically focuses the beam on the detector through a pneumatic bender mechanism. For experiments requiring a small focal spot a third mirror to refocus the beam in the vertical direction at the sample position is added to the optical configuration. The horizontal divergence necessary to obtain the requested energy bandwidth (ΔE) after diffraction from the polychromator is produced by the second mirror. A strongly focusing mirror, placed at 32.5 m from the source, creates a horizontally-demagnified image of the source that becomes the effective source for the polychromatic crystal. The polychromator consists of a curved Si crystal in a Bragg [14] or Laue [15] geometry. Si (111) and Si (311) crystals are used to match the energy resolution/energy bandwidth requirements for the specific applications.

The ΔE necessary for acquiring all data points in parallel is directly proportional to the footprint of the beam on the polychromator crystal and to the cotangent of the

Bragg angle [16]. The latter factor severely limits ΔE at low energies. Typical values for ΔE/E range are from 5% to 15% at low and high energies respectively.

Using air as a reference measurement represents the simplest and most often used approach to normalization in dispersive measurements. However, in our study, the reference of the particular oxide such as Al_2O_3, CeO_x/Al_2O_3, $CeO_x/ZrO_2/Al_2O_3$ and ZrO_2/Al_2O_3 has been utilised for collecting EDE data of Rh catalysts. It has been previously reported that the use of such a reference improves the absolute S/N achieved under the same conditions as well as an improvement in the normalization (in terms of the background and diminution of glitches) [12].

2.6.2 EXAFS data analysis

EXAFS analysis involves fitting data to the EXAFS equation to obtain a structural model. However, before this stage is reached a number of steps have to be carried out. The first of these involves initialising and calibrating the data and the second is to normalise and background subtract the data to extract χ(k).

2.6.2.1 Energy Calibration

Dispersive EXAFS (EDE) measurements were carried out at Rh K edge using a Si (311) polychromator mounted in a Bragg configuration. The EDE calibration is carried out using XOP programme [17] by comparing an EDE foil spectrum to an EXAFS foil spectrum and correcting the offset of the edge jump and multiplying the pixel number by a factor to obtain the energies. From the calibrated EDE foil the offset and multiplication factor parameters are used to calibrate of the EDE spectra collected.

2.6.2.2 Background subtraction

The background subtraction is carried out using the computer program Xmult, the new version of PAXAS written by Norman Binsted and developed at the University of Southampton [18, 19].

The first step of this process is to determine E_0 and subtract the pre-edge background from the data. The removal of the background involves the subtraction of a second or third order polynomial from the absorption spectrum. The polynomial is defined by three points: L1 and U1 are pre-defined at the beginning and end of the pre-edge region, whilst the third point, P1, is chosen at the end of the post-edge region. P1 is

usually weighted and its Y-coordinate can be adjusted to achieve approximately horizontal background subtracted absorption.

The post edge background is subtracted by fitting a high order, inverse or two linked polynomials of order 6, 7 or 8, which are defined by three points, U2, L2 and P2 as it is indicated in Figure 2.7. The polynomial order is chosen to minimise unwanted features observed below distances of 1 Å in the Fourier transform spectrum. Only shells which contain the structural information are therefore selected and back transformed. The EXAFS intensity is normalised versus the edge jump and plotted against the photoelectron wavevector, k.

The Xmult software allows for the reading and refinement together of multiple scans acquired for the same experiment with the array of 1400 spectra.

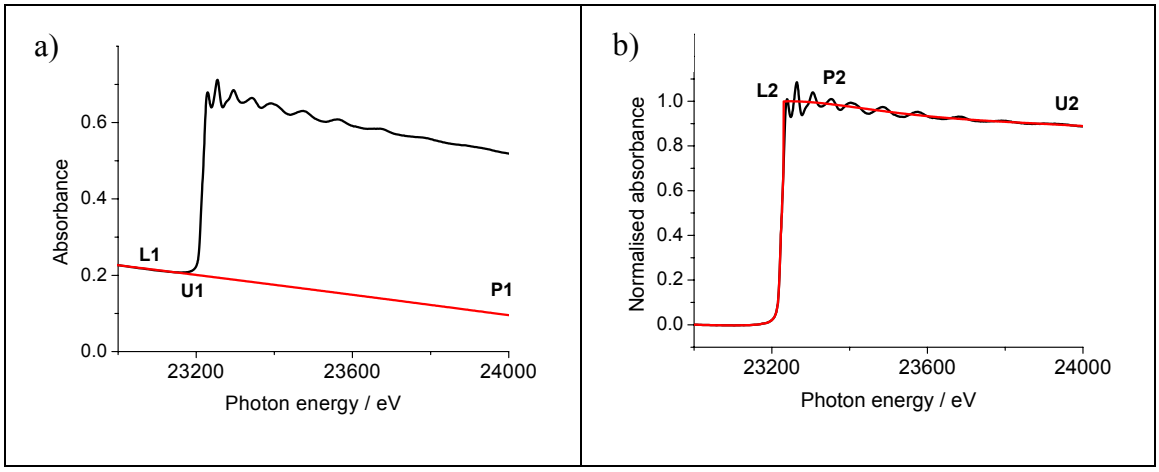

Figure 2.7. Background removal in Xmult for Rh K-edge a) pre-edge, b) post-edge

2.6.2.3 Refinement of the parameters

The curve fitting programme EXCURVE version 98 employs curved wave theory [20] and Rehr-Albers theory [21-23] to model the oscillations in the EXAFS and to determine structural parameters. The phaseshifts corresponding to the photoelectron wave associated with the central atom and potential surrounding atoms are calculated by ab initio methods, using Hedin-Lundqvist potentials and a muffin tin approximation [24]. During the refinement each element is treated as part of a 3D lattice, for which the other atom type has to be defined as the nearest neighbour. With the excited atom, the core hole is assumed to have decayed and the outer electrons are treated as fully relaxed. The EXAFS data is fitted in k-space where the coordination number (N), distance to the nearest neighbour (r), the Debye Waller term ($2\sigma^2$) and the shift in Fermi energy (E_f) are all parameters which can be refined.

This is carried out using a least-squares minimisation of the fit index. The goodness of fit is determined in the Equation 2.9:

$$R_{exafs} = \sum_i^N \frac{1}{\sigma_i}\left(\left|\chi_i^{\exp}(k) - \chi_i^{th}(k)\right|\right) * 100\% \qquad \text{Eq. 2.9}$$

Where N is the number of data points, σ_i the standard deviation for each data point, *i*, and $\chi_i^{\exp}(k)$ and $\chi_i^{th}(k)$ the experimental and theoretical EXAFS, respectively. The R factor should not exceed ~ 30% for standard compounds. However, for supported systems containing a low percentage of the absorbing atom, and displaying a lower signal to noise ratio, the R-factor is expected to exceed this value significantly, with values up to 45% observed in this study. The number of parameters, *n*, that can be justifiably fit can be estimated from the Nyqvist theorem (Eq. 2.10):

$$n = \frac{2\Delta k \Delta r}{\pi} + 1 \qquad \text{Eq. 2.10}$$

Where Δk and Δr are the ranges in k- and r-space over which the data are analysed. However, this mathematical theorem does not take into account intrinsic nature of real and particularly dispersive data. As such it states only what might be statistically justified assuming perfect data.

As the coordination numbers are highly correlated to the Debye Waller factors, they should not be refined together. As such a methodology to establish the appropriate DW factors for a given system and temperature is needed. Due to the fact that the static and dynamic components of the DW factors and their variation with temperature are not the same in the nanoparticulate system as in the bulk foil, the use of a foil is not necessary the most effective method to determine the DW factors.

In our studies, analysing the nanoparticulate Rh catalysts under varied conditions, mainly the first two shells have been considered: the first shell Rh-Rh and the second one Rh-O. The DW factor constant for the first shell Rh-Rh has been established by B. Jyoti [25]. The linear correlation between DW for the first Rh-Rh shell and R factor provides the correct DW factors to be utilised at different temperatures, as is displayed in Figure 2.8.

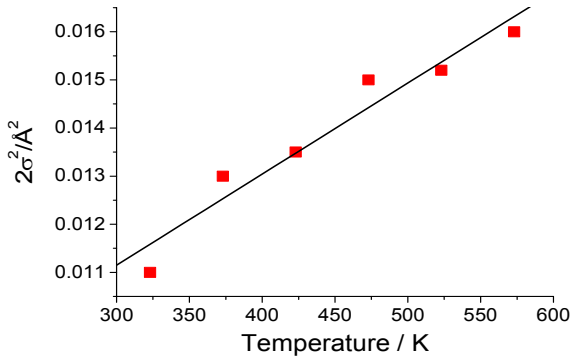

Figure 2.8. DW factor of the first Rh-Rh shell versus temperature dependence as determined for a 5wt% RhCl sample.

In order to determine the DW factor for the second shell Rh-O the same methodology has been followed as for the first shell. The last ten spectra of 5 wt% Rh catalyst under flowing 5% O_2/He were averaged and analysed at given temperature. The resulting spectra were refined for the second shell metal-oxygen over a constant spectral width (Δk=3-11 Å) holding the DW factor constant for the first shell Rh-Rh. At each temperature a range of DW factors (0.002-0.04) of the second shell Rh-O was analysed and the R factor determined. The minimum in the subsequent plot of R factor versus DW parameter should yield the correct DW factor for the given temperature. This method can be visualised in Figure 2.9 which shows the DW factors obtained via the minima of the subsequent R factor at a given temperature. The plot highlights the errors involved in determining DW factor, as the curves minima are very broad, the determination of the correct DW parameter is difficult. In addition the accuracy of this factor utilised in analysis have an error of +/- 10% involved.

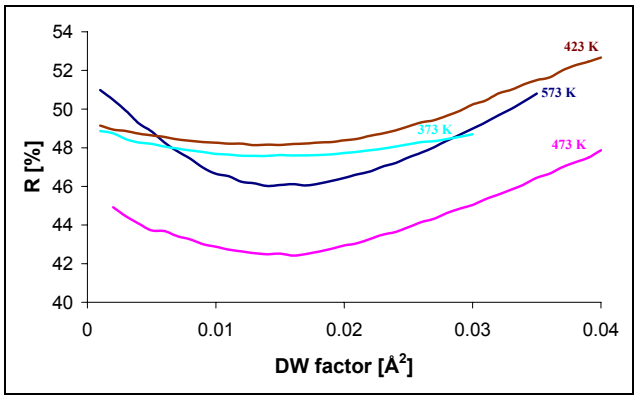

Figure 2.9. Plot of R factor ($2\sigma^2$/ Å^2) highlighting the method used for correct DW factor determination.

Figure 2.10 shows the extrapolation of the corrected DW factors of the Rh-O shell in a function of temperature.

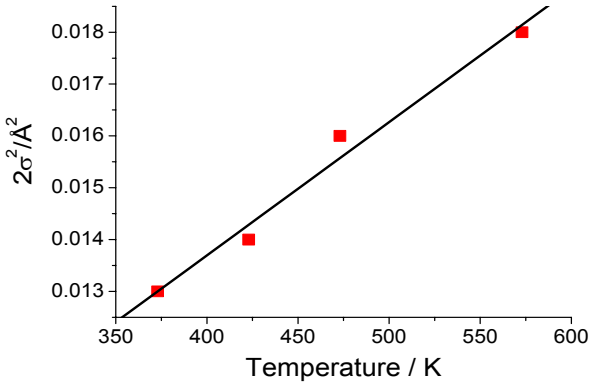

Figure 2.10. Plot of the temperature dependence of the Debye-Waller factor for the Rh-O shell determined for 5 wt% $RhCl/Al_2O_3/CeO_x$ – I method

The data produced from the EXCURV98 software is shown as χ data and its corresponding Fourier transform. The radial distribution function (real part of the Fourier Transform) provides a convenient way of presenting the EXAFS data where the peak positions give the coordination shell radii, peak heights corresponds to coordination numbers, and peak width give an idea of disorder.

2.7 Diffuse Reflectance Infrared Fourier Transform Spectroscopy

Many analytical developments have been carried out for *in situ* analysis in order to obtain a detailed description of the structural changes in catalysts under reactive atmospheres. Infrared spectroscopy is a technique that is widely used to characterise the acidity of supports and adsorption of the molecules. This technique is limited to the analysis of samples transparent to IR radiation and formed into the shape of a self-supported pellet.

DRIFTS is a powerful technique for non-transparent materials for *in situ* measurements under varying environmental and reaction conditions. This kind of spectroscopy offers a number of advantages including:

- minimal or no sample preparation;
- ability to study most non-reflective materials, including highly opaque or weakly absorbing materials;
- ability to investigate irregular surfaces or coating, such as polymer coating;

- ability to analyse very large, intractable samples.

The Kubelka-Munk equation is applied in diffuse reflectance spectroscopy [26, 27]. A sample, of thickness d, is subjected to an incident flux I_0 in direction x and reflects flux J_0, along the same axis but in the opposite direction (Figure 2.11). The fraction of light transmitted is proportional to the absorption coefficient k and the fraction of light diffused is proportional to the diffusion factor s.

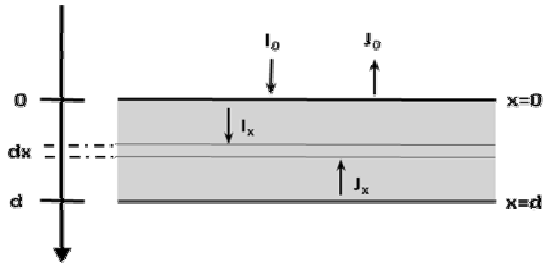

Figure 2.11. Path of particles which absorb and diffuse light.

The Kubelka-Munk function f(R_∞) gives the relationship between absorption (*k*) and scattering coefficient (*s*) and the diffuse reflection (R_∞) versus the wavenumber (Eq. 2.11).

$$f(R_\infty) = \frac{k}{s} = \frac{(1-R_\infty)^2}{2R_\infty} \quad \text{Eq. 2.11}$$

The DRIFTS cell consists of 4 flat, 2 aspherical reflectors and an alignment mirror (Figure 2.12). The infrared beam is aligned by these mirrors on the surface of the sample placed in a sample holder. The aspherics are off-axis ellipsoids which focus and collect infrared energy with 6x concentration of the beam. The collection angle on the detector is a full 2π steridians, collecting 50% of the available diffuse energy.

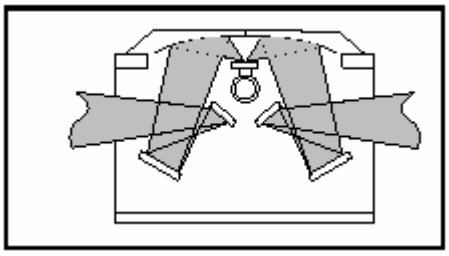

Figure 2.12. Optical layout of the collector.

The DRIFTS cell can be used during *in situ* experiments at high temperatures. The sample holder, a ceramic crucible containing a heating resistor and a thermocouple, is placed inside a dome. To decrease the heat of the chamber, the dome is surrounded

by coils transporting a stream of nitrogen gas. Additionally, the inlet and outlet are provided to send the gases into dome and through the sample. Figure 2.13 shows the path of the gases inside the dome. The flow of the gases and surface reactions are controlled at the desired temperatures. This *in situ* cell allows us to:

- study samples at the reactive conditions by flowing of different gaseous mixtures;
- record the sample spectra at elevated temperatures:
- directly measure the sample temperatures by a thermocouple in direct contact with the powder.

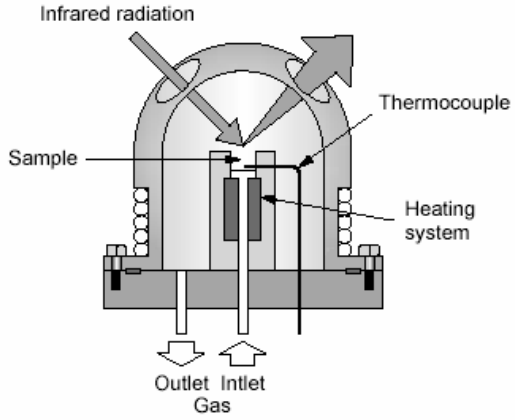

Figure 2.13. Scheme of dome interior [28].

When the infrared beam is focused on the sample surface it penetrates a particle then scatters or "diffuses". Depending on the angle at which it emerges from the particles through the sample material. The diffuse light is partially absorbed by particles of the sample, and thus contains information on the absorption characteristics of the sample.

Figure 2.14 shows that IR beam may be directly reflected by the sample surface, giving refraction, which is a function of the refractive index and absorbability of the sample. The radiation can also undergo multiple reflections at the surface of the particles.

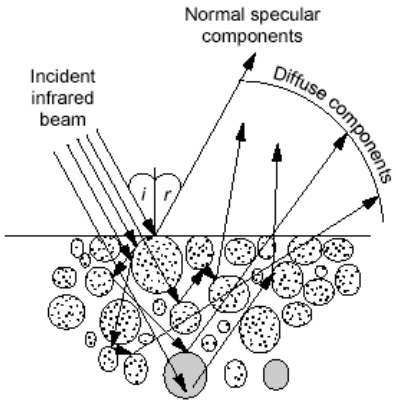

Figure 2.14. Collection of the infrared beam from the powder [28].

The target of diffuse reflectance spectroscopy is thus to maximize the diffused component, which contains information on the absorption characteristics of the sample, and to minimize the specular component, which causes distortions in the absorption line shapes. When the specular component of a diffuse reflectance measurement is large, the bands in the resulting spectrum tend to broaden and the relationship between intensity and sample concentration becomes nonlinear. In addition, the specular component depends on the particle size of the sample. Materials with a higher particle size are particularly reflective and can produce bands that are completely inverted.

2.8 Mass spectrometry

A mass spectrometer is an instrument in which ions are produced from a sample, separated according to their mass-to-charge ratios and then recorded, in terms of intensity (number of ions). The gas molecules are converted into charged particles, typically positive ions, fragments by electron bombardment generated from a hot wire filament. Ions are extracted into the mass filter, e.g. quadrupole, which differentiates the ions produced and selects species for detection. Ions are differentiated by their characteristic mass: charge ratio using the controlled RF/DC field of the quadrupole. The filtered ions strike the detector assembly and ion current produced is measured by sensitive amplifier. The majority of ions have single positive charges, and so appear close to integral mass values, but it is quite normal to observe small numbers of doubly or triply charged ions. In this project mass spectrometry with a Pfeiffer Quadstar 422 system is used as a simple tool for gas

analysis. It gives fast sample response times combined with accurate, repeatable results. The basic system includes:

- quadrupole mass spectrometer, comprising 200 amu mass range capability and Dual Faraday/Electron Multiplier detectors ;
- an Ultra-High Vacuum (UHV) housing;
- inlet system (the capillary directly connected with the cell);
- bypass/inlet evacuation pump;
- pressure gauges;
- heaters;

Within this project the mass spectrometer with the given appropriate calibration is the only easily and reliably quantitative tool for *in situ* experiments. Taking into account the mass of the sample, the gas flow rates and relative sensitivity factors it is possible to quantify gas uptake and production in terms of the amount of Rh in the system. This is very important for studying effects in catalytic reactivity and selectivity. The calculation of the gas uptake is done as follows:

- the evolution of the gas, i.e. CO over the particular support and the catalyst is baseline corrected by the ratio of CO/He signals;
- the baseline of the blank and experimental data is subtracted as the Figure 2.15 indicates and the subtracted area is integrated;

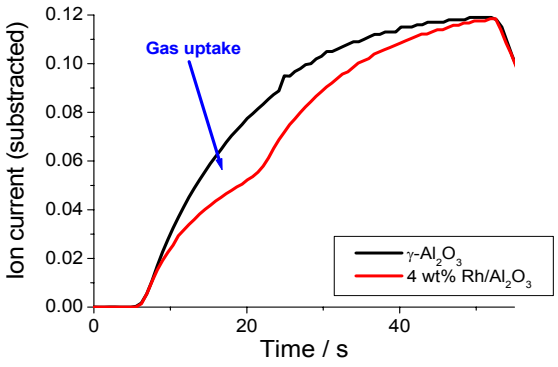

Figure 2.15. CO/He baseline subtraction between the blank and experimental data

- number of Rh atoms in the sample bed and number of gas molecules for 1 s of gas exposure is calculated.

2.9 Experimental set up of XAFS/DRIFTS/MS techniques

Spectroscopic experiments provide direct structural information about the metal in the relevant conditions. The reaction environments may be altered very rapidly by pulsing the reagents, changing the temperature or pressure jumps. Therefore, spectra should be acquired quick enough to establish the structures under varied conditions to probe the kinetics of the structure changes and identify any intermediate species. The two XAFS methods to achieve this are QEXAFS (Quick EXAFS), in which the crystal monochromator is rotated by the small angle rapidly to provide a rapid scan time (acquisition time of seconds) [29] or energy dispersive EXAFS (EDE), described in the section 2.6.1.1. Time-resolved XAFS can be combined simultaneously with other complementary techniques to provide powerful analytical strategies for investigating the relationship between chemical structure and reactivity. The most widely used combination is of X-ray diffraction with scanning (Quick) EXAFS in the study of solid and powdered systems [30, 31]. The first method provides information involved with the overall structural integrity and phase identification, and from the second one gives information in relation to the local atomic environment of the absorbing atom. These techniques have been used synchronously in the *in situ* structural study of heterogeneous catalysts. Other combinations of techniques that are combined with the EXAFS are UV-visible and Raman spectroscopy [29, 32, 33], Raman [34], XRD with Raman spectroscopy [35], and Raman/UV-visible/SAXS/WAXS developed by Beale *et al*. [36].

2.9.1 EDE/DRIFTS/MS studies

During this project *in situ* characterisation of heterogeneous catalyst has been carried out by the combined spectroscopies EDE/DRIFTS/MS (ID24, ESRF). Figure 2.16 is a schematic overview of the equipment used. The infrared beam is focused on the surface of the particulate sample through two flat and one aspherical reflector. After penetrating the surface of the sample, the diffuse light is collected by the MCT detector. Evaluation of the gases is performed by a mass spectrometer, connected directly to the cell by the capillary. The valves, mass flow controller and switching driver valves are necessary to use in order to flow gases and control their flux.

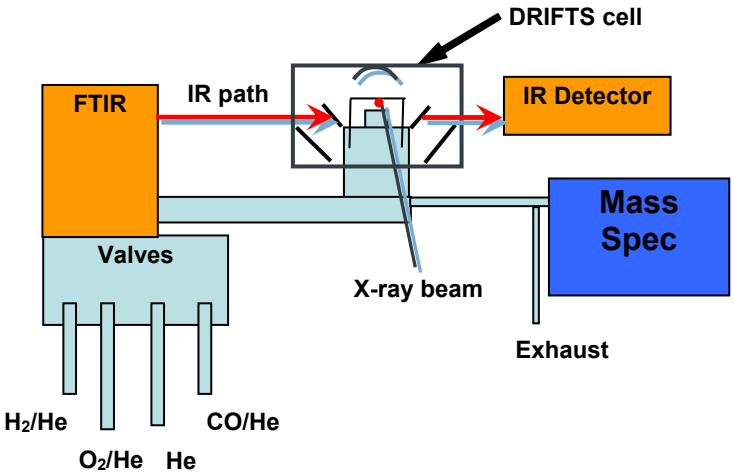

Figure 2.16. Schematic of the combined EDE/DRIFTS/MS apparatus.

In this project a Bruker IFS 66/S spectrometer was used, which is a flexible FT-IR spectrometer, with a spectral range from far-IR to the near-UV. The set up contains the following modules:

- optical bench (interferometer, optics, detector, sample chamber);
- electronics unit (source power supplier, laser power supplier);
- source cooling system (thermostatically controlled closed loop water circular for sources);
- purge flow meter (valves and indicators in a separate mount which monitor and regulate gas flow to the purge system).

The interferometer is controlled using a HeNe laser which emits 633 nm (red) light. The cell is mounted on the external optical part of spectrometer with a high sensitivity MCT detector, which is presented in Figure 2.17.

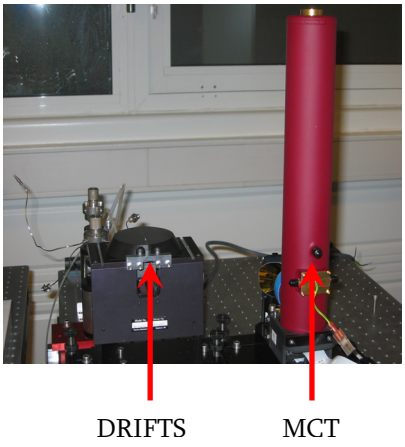

Figure 2.17. DRIFTS setting up at ESRF

The designed DRIFTS cell is compatible with the XAFS experiment. Figure 2.18 shows the cross-section of the DRIFTS cell. The x-ray path is directed through a small catalytic cell, perpendicular to the IR beam direction. Sample cup is made from boron nitride to permit transmission of the X-rays through the sample.

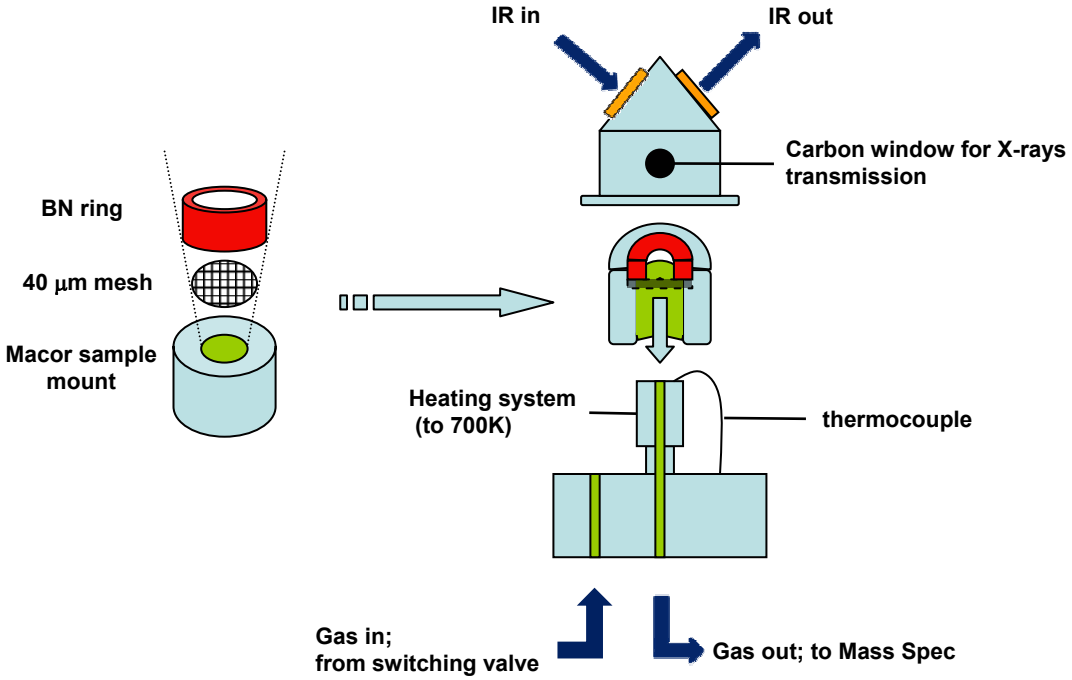

Figure 2.18. The cross-section of the XAFS/DRIFTS cell.

This cell arrangement allows the switching of gas feeds the cell under mass flow control (in this case the total flow of the gases is 25 ml min^{-1}), heating of the sample to 600 K and water cooling the chamber.

Figure 2.19 presents the set up of the DRIFTS/EDE/MS combination at ID24. The cell is mounted on the optical bench beside the DRIFTS spectrometer with a high sensitivity MCT detector for the IR. The mass spectrometer is directly connected to the cell a capillary. The Fast Readout Low Noise (FReLoN) was used as the X-ray detector [37].

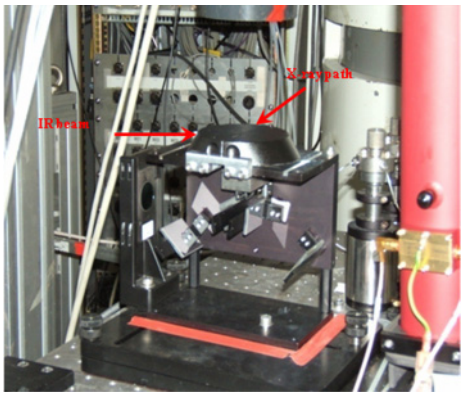

Figure 2.19. Set up of the experiment with the use of DRIFTS/EDE/MS techniques.

The FreLoN camera is low noise CCD camera which combines high readout speed, accuracy and improved duty cycle in a single image. The fast data acquisition and read-out allow the XAS characterisation of fast changing systems, down to millisecond time-scales. The basic FreLoN platform is made of a camera head and a data acquisition board, both linked by a serial line fibre optic cable and a power supply unit [37, 38]. Due to the careful design of the electronics and Pletier cooling of the CCD chip down to 255 K, both readout noise and dark noise level can be kept low. At the same time a maximum readout speed of 20 Mpixel/s through four outputs provides the possibility of high frame rate imaging (4.2 frames/s).

Synchronous EDE/IR/MS experiments were carried out at the Rh K edge ID24 at the ESRF using a Si[311] polychromator mounted in the Bragg configuration. The EDE experiments were made synchronously with DRIFTS, yielding the same sampling rates for each spectroscopy of ca. 100 ms whilst a quadrupole mass spectrometer continuously measured the composition of the gas phase.

During the typical experiment, all samples have been pre-treated beforehand according to the same procedure: reduction at 573 K under 5 % H_2/He, oxidation at 573 K under 5 % O_2/He and re-reduction at 573 K. The oxidation reaction is necessary before using in the catalytic process, because it cleans the catalyst from the impurities. This reaction is carried out until the formation of H_2O and oxidation of carbonaceous deposits disappears from the system, which is detected from the MS. After full pre-treatment in H_2 the system is cooled down to the working temperature and purged by He.

2.9.2 MS microreactor based studies

The microreactor apparatus used parallel with the mass spectrometer in this study allows the *in situ* characterisation of the catalyst's reactivity. However, this microreactor was specifically designed for the study of *in situ* reactions by Energy Dispersive EXAFS [39, 40]. Therefore, the sample and the reference materials are held in a configuration that allows the transmission of X-rays. This is achieved with the use of a quartz tube as a sample holder with holes in the heater block to allow X-rays to pass through. The schematic drawing of the microreactor is given in Figure 2.20.

The catalyst charge (~25 mg) was loaded into the centre of a 200 mm long quartz tube with an internal diameter of 3 mm. The powdered sample is held in place with two plugs of glass wool to give a catalyst bed length of 4-6 mm. The ends of the quartz tubes were glued with a push-on fitting. One end was attached to the outlet from the valves and through the other a thermocouple type K was simultaneously introduced to the centre of the catalyst bed. Another end of the quartz tube was directly connected to the mass spectrometer with Pfeiffer Quadstar 422 system via the capillary. The valve arrangement allowed up to two different gases to be used at the same time.

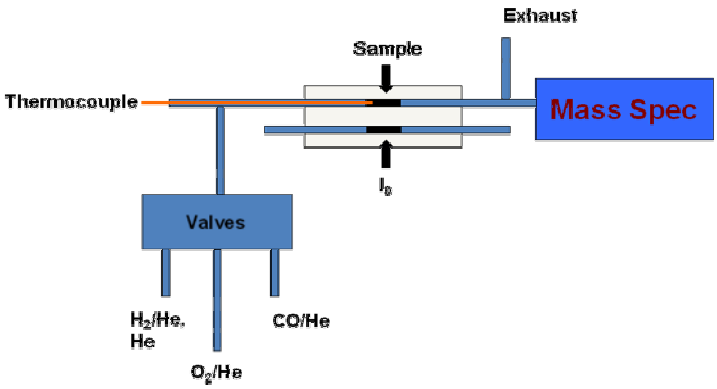

Figure 2.20. A schematic diagram of the microreactor system.

Figure 2.21 shows a detailed view of the sample stage. The heating system for this microreactor consists of twelve cartridge heaters inserted into a two-piece brass block. The two pieces of that block screwed together have a groove cut in each half to accommodate the quartz tube. A ceramic insulating hood is then placed over the block to reduce temperature variations on heating, and allow higher temperatures to be achieved. An Eurotherm 902 series temperature controller used in this study

controls the power output to the cartridge heaters with the desired heating rate. This set up allows the sample to be heated to ca. 673 K.

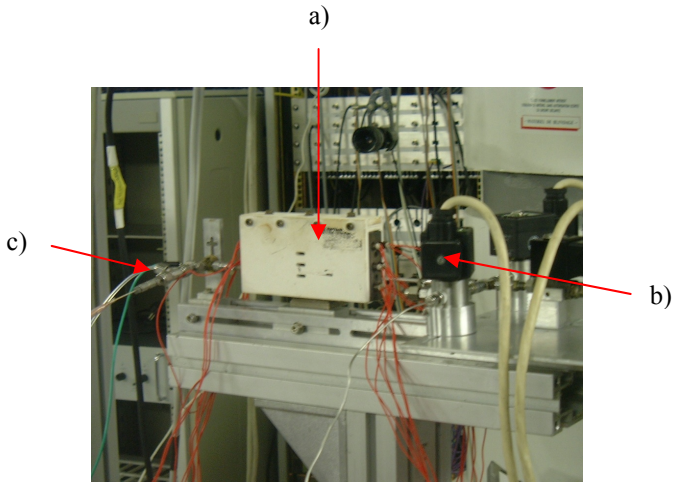

Figure 2.21 Sample stage of microreactor; a) brass heating block housing the quartz tubing, b) gas switching valve c) thermocouple.

2.10 References

1. Brunauer, S., Emmett, P. H., Teller, E., J. Am. Chem., 1938. **60**: p. 309-319.
2. Goodhew, P.J., J. Humphreys, and R. Beanland, *Electron Microscopy and Analysis*. 3rd ed. 2001, London: Taylor & Francis.
3. Einstein, A., Ann. Phys., 1905. **17**: p. 132-148.
4. Woodruff, D.P., Delchar, T. A. , *Modern Techniques of Surface Science*. 1986, Cambridge: Cambridge University Press.
5. Seah, M.P., Briggs, D., *Practical Surface Analysis by Auger and X-ray Photoelectron Spectroscopy*, ed. J. Wiley. 1990, New York.
6. Scofield, J.H., J. Electron. Spectrosc. Relat. Phenom., 1976. **8**: p. 129-137.
7. Newville, M., *Fundamentals of XAFS*. 2004, Consortium for Advanced Radiation Sources: Chicago. p. 1-41.
8. Koch, E.E., *Handbook on Synchrotron Radiation*, ed. NorthHolland. 1983, Amsterdam.
9. Filiponi, A., Borowski, M., Bowron, D. T., Ansell, S., Di Cicco, A., De Panfilis, S., J. P. Itie Rev. Sci. Instr. , 2000. **71**: p. 2422-2432.
10. Couves, J.W., Thomas, J. M., Catlow, C. R. A., Greaves, G. N., Baker, G., Dent, A. J., J. Phys. Chem., 1990. **265**: p. 6517-6519.
11. Newton, M.A., Dent, A. J., Evans, J., Chem. Soc. Rev., 2002. **31**: p. 83-95.
12. Newton, M.A., J. Synchrotron Rad., 2007. **14**: p. 372-381.
13. Kirkpatrick, P., Baez, A. V., J. Opt. Soc. Am., 1948. **38**: p. 766-777.
14. Pellicer-Porres, J., San Miguel, A., Fontaine, A., J. Synchrotron Rad. , 1998. **5**: p. 1250-1257.
15. San Miguel, A., Borrel, M. H. L., Marot, G., Reiner, M., J. Synchrotron Rad., 1998. **5**: p. 1396-1397.
16. Phizackerley, R.P., Rek, Z. U., Stephenson, G. B., Conradson, S. D., Hodgson, K. O., Matsuchita, T., Oyanagi, H., J. Appl. Cryst., 1983. **16**: p. 220-232.
17. Sanchez del Rio, M., *Xop/Xplot User's Guide*. 2001, Grenoble.
18. Binsted, N., *PAXAS, Program for the Analysis of X-ray Absorption Spectra*. 1992, University of Southampton.
19. Binsted, N., *X-Mult*, in *University of Southampton*. 2006: Southampton.
20. Gurman, S.J., J. Phys. C., 1988. **21**: p. 3699-3717.
21. Rehr, J.J., Albers, R. C., Phys. Rev. B., 1990. **41**(12): p. 8139-8149.

22. Rehr, J.J., Albers, R. C., Zabinsky, S. I., Phys. Rev. Lett., 1992. **69**(23): p. 3397-3400.
23. Rehr, J.J., Albers, R. C., Rev. Mod. Phys., 2000. **72**(3): p. 621-654.
24. Gurman, S.J., J. Phys. C., 1983. **16**: p. 2987-3000.
25. Jyoti, B., *PhD Thesis*, in *Chemistry*. 2006, University of Southampton: Southampton.
26. Kubelka, P., Munk, F. Z., Tech. Phys., 1931. **12**: p. 593-595.
27. Kubelka, P., J. Opt. Soc. Am., 1948. **38**: p. 448-450.
28. Armaroli, T., Becue, T., Gautier, S., Oil Gas Sci. Technol., 2004. **59**(2): p. 215-237.
29. Briois, V., Lutzenkirchen-Hecht, D., Villain, F., Fonda, E., Belin, S., Griesebock, B., Frahm, R., J. Phys. Chem. A, 2005. **109**: p. 320-329.
30. Grunwaldt, J.D., Clausen, B. S., Top. Catal. , 2002. **18**: p. 37-43.
31. Clausen, B.S., Grabek, L., Steffensen, G., Hansen, P. L., Topsoe, H., Catal. Lett., 1993.
32. Tromp, M., *Development of Time-Resolved XAFS Spectroscopy Techniques, Applications in Homogeneous Catalysis*. 2005, Utrecht.
33. Tinnemans, S.J., Mesu, J. G., Kervinen, K., Visser, T., Nijhuis, T. A., Beale, A. M., Keller, D. E., van der Eerden, Ad M. J., Weckhuysen, B. M., Catal. Today, 2006. **113**: p. 3-15.
34. Beale, A.M., van der Eerden, Ad. M. J., Kervinen, K., Newton, M. A., Weckhuysen, B. M., Chem. Commun. , 2005: p. 3015-3017.
35. Boccaleri, E., Carniato, F., Croce, G., Viterbo, D., van Beek, W., Emerich, H., Milanesio, M., J. Appl. Cryst., 2007. **40**: p. 684-693.
36. Beale, A.M., van der Eerden, Ad. M. J., Jacques, S. D. M., Leynaud, O., O'Brien, M. G., Meneau, F., Nikitenko, S., Bras, W., Weckhuysen, B. M., J. Am. Chem. Soc., 2006. **128**: p. 12386-12387.
37. Labiche, J.C., Guilera, G., Hohms, A., Mathon, O., Newton, M. A., Pascarelli, S., Vaughan, G., , *The Fast Readout Low Noise camera as a versatile X-ray detector for time-resolved studies of dymanic problems in material science, chemistry and catalysis*. 2006, Grenoble.
38. Bravin, A., Fiedler, S.,, Coan, P., Labiche, J.-C., Ponchut, C., Peterzol, A., Thomlinson, W., Nucl. Instrum. Methods Phys. Res., Sect. A, 2003. **510**: p. 35-40.

39. Fiddy, S.G., Newton, M. A., Dent, A. J., Salvini, G., Corker, J. M., Turin, S., Campbell, T., Evans, J., Chem. Commun., 1999: p. 851-853.

40. Newton, M.A., Dent, J. A., Diaz-Moreno, S., Fiddy, S. G., Jyoti, B., J., Evans, J., Chem. Eur. J., 2006. **12**: p. 1975-1985.

Chapter 3

Synthesis and structural investigation of the Rh catalysts

3.1 Introduction

The requirements for high selectivity and activity, which current three-way catalysts have to fulfill, are amongst the most crucial demands for a successful commercial application. Therefore, the understanding of structure-property correlations is an important issue in the design and preparation of a catalytic system. Thus, it is essential to study the application of different commercial catalysts consisting of Pd, Pt, Rh and different promoters such as Ce and Zr, in order to understand the relevant physical and chemical mechanisms of catalysis using a particular three-way catalyst.

Before testing the catalytic activity of the catalysts, it is important to have a clear understanding of their structure and composition. The catalysts investigated, derived from the deposition of inorganic Rh precursors onto amorphous inorganic solids, are usually very difficult to study due to their predominantly amorphous or poorly crystalline nature. Therefore, several characterisation techniques have been utilized in order to investigate their structural and electronic properties and the interactions between the different elements present. The structural characterisation of the supported Rh catalysts is commonly performed by a wide range of techniques: nitrogen physisorption [1, 2], transmission electron microscopy (TEM) [3, 4], energy dispersive X-ray analysis (EDX) [5], X-ray photoelectron spectroscopy (XPS) [6], X-ray absorption near edge structure (XANES) [7, 8] and extended X-ray absorption fine structure spectroscopy (EXAFS) [7].

In spite of the vast information already available on the supported metal system, there is always a growing interest in finding new supports and adopting new techniques to disperse the metal more efficiently which could improve the catalytic activity and selectivity. Therefore, the design and development of specific supported metal catalysts is a challenging task.

In this study, a series of novel Rh nanoparticulate systems, of variable Rh and Ce, Zr loadings and supported on γ-alumina have been synthesised. These have then been characterised using a diverse range of complimentary *ex situ* methods as have been described in the previous chapter.

3.2 Sample preparation

It is often difficult to synthesise the bimetallic catalyst systems such as $Rh/CeO_x/Al_2O_3$ with an optimum surface composition using conventional catalyst

preparation methods such as impregnation, precipitation or electrochemical deposition. One method which allows the deposition of the secondary metal onto the surface sites of the primary metal in a controlled manner is the use of surface organometallic chemistry (SOMC) in which an organometallic precursor of the secondary metal is reacted with the reduced surface of the first [9-11].

In this work, two synthesis methods have been applied in order to prepare the Rh catalysts promoted by ceria and/or zirconia. In the first method, the ceria/zirconia is deposited on the alumina support and subsequently Rh metal is added; however, the second one follows the method called controlled surface modification, where ceria and zirconia are placed on the previously deposited Rh particles on the support. Initially, the ceria-alumina supports have been produced using various precursors, such as cerium (IV) ammonium nitrate ($(NH_4)_2Ce(NO_3)_6$), cerium (III) nitrate ($Ce(NO_3)_3 \cdot 6H_2O$) and cerium (III) 2,4-pentanedionate ($Ce(acac)_3$). However, EDX analysis has shown that only the ceria particles derived from $Ce(acac)_3$ are deposited regularly on the alumina. Therefore, the whole series of the ceriated Rh catalysts has been prepared using $Ce(acac)_3$ only.

3.2.1 Catalyst preparation – method I

a. $CeO_x/\gamma\text{-}Al_2O_3$ – first step

To produce 5 wt% $Ce/\gamma\text{-}Al_2O_3$, 0.509 g of cerium (III) 2,4-pentanedionate, $Ce(acac)_3$ supplied from Alfa Aesar, was dissolved in toluene and 1.805 g of $\gamma\text{-}Al_2O_3$ (Degussa aluminium oxide C, S_{BET}=88 m^2/g) was added to this solution. The sample was dried overnight in air before being calcined under 5 % O_2/He for 6 h at 773 K. A yellow powder was obtained.

b. 4 wt% Rh + $CeO_x/\gamma\text{-}Al_2O_3$ – second step

The aqueous solution of $RhCl_3 \cdot 3H_2O$ from Aldrich (0.200 g in 8 ml of water) was added to a suspension of CeO_x/Al_2O_3 support (1.92 g) and stirred. The sample was dried overnight before being calcined under 5 % O_2/He for 6 h at 673 K. The sample was subsequently reduced under 5 % H_2/He during 5 h at 573 K.

3.2.2 Catalyst preparation – method II

a. $Rh/\gamma\text{-}Al_2O_3$ – first step

Supported Rh catalysts (2 g), with loadings of 1.6 and 4 wt% Rh, were synthesised via incipient wet impregnation of alumina (1.97 and 1.92 g) under

constant stirring, with aqueous solutions of $RhCl_3 \cdot 3H_2O$ supplied from Aldrich, with the adequate amounts of Rh precursor for particular loading: 0.084 g and 0.210 g, respectively. Samples were dried overnight in air. Subsequently the samples were calcined for 6 h at 673 K in 5 % O_2/He and reduced for 5 h under flowing 5 % H_2/He at 573 K.

b. $Rh/\gamma\text{-}Al_2O_3 + CeO_x$ – second step

The produced catalyst, 1 g of $Rh/\gamma\text{-}Al_2O_3$, was re-reduced under flowing 5 % H_2/He for 3 h at 573 K. To prepare 5 wt% Ce of Rh catalysts, the solution of $Ce(acac)_3$ (0.164 g of $Ce(acac)_3$ in 100ml of toluene) was placed in the three-way tap dropper, purged by N_2 for 15 min and added drop wise to the reduced catalyst. Subsequently, the reagents were mixed under flowing 5 % H_2/He at 353 K for 8 h. Then the sample was filtered and dried in air overnight. The final colour of filtrate was colourless, which means the reaction has succeeded and is completed. The sample was again reduced under 5% H_2/He at 573 K for 3 h. All preparations were performed under N_2 atmosphere.

In order to produce Rh catalysts doped by Zr, 0.281 g of $Zr(acac)_4$ was dissolved in 100 ml of toluene. Catalysts promoted by ceria and zirconia of two different mixture ratios (Ce:Zr;1:1;2:1) have been produced by simultaneous dissolving the appropriate amount of $Ce(acac)_3$ and $Zr(acac)_4$ in toluene. It needs to be mentioned that the two different mixture ratios of Zr to Ce: indexed as 1:1 and 2:1 throughout the whole thesis derives only from the theoretical assumption. The apparatus used for the preparation of catalysts detailed in this study is shown below in Figure 3.1.

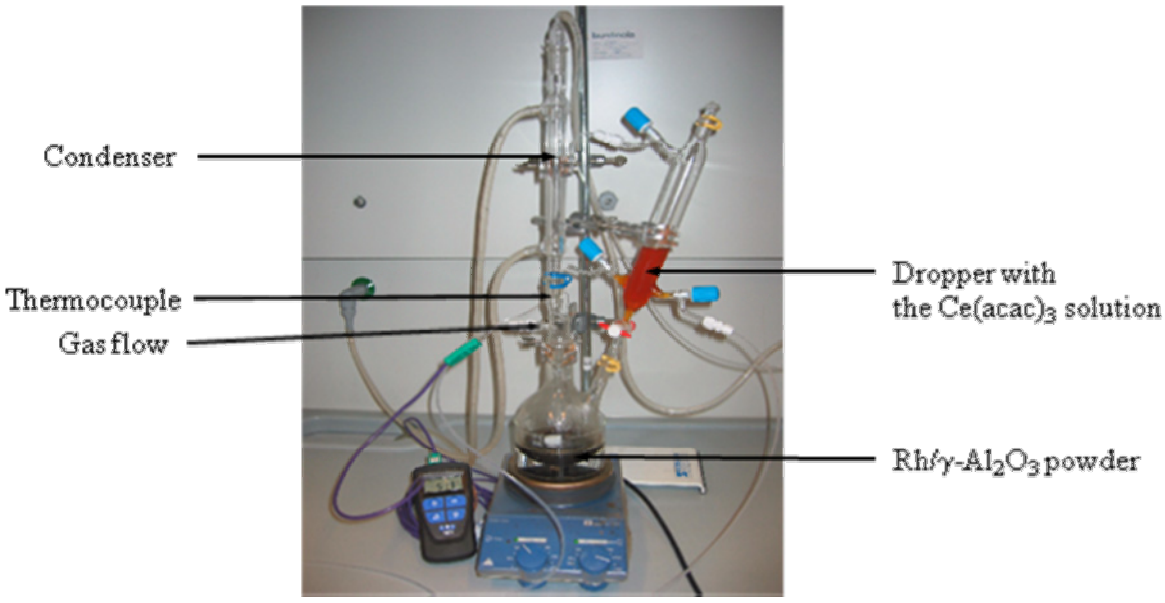

Figure 3.1. Set up of the controlled surface modification reaction.

The reactor used was specifically designed for the preparation of catalysts via the controlled surface modification route [12, 13]. The apparatus consists of several glassware connections with the PTFE tubing. A removable dropper is used for the addition of dissolved organometallic compounds. Additionally, air sensitive materials, prepared in the glove box, can be transferred to the reactor via this dropper without being exposed to air. The three-way tap dropper also allows purging any dissolved oxygen before addition of the precursor to the pre-reduced surface. The same orientation of gas flow to purge the contents of the dropper is used to transfer the precursor.

The following samples has been synthesised and investigated in this study:

- 4 wt% Rh/γ-Al_2O_3
- 4 wt% Rh/5 wt% Ce/γ-Al_2O_3 (method I)
- 4 wt% Rh/5 wt% Ce/γ-Al_2O_3 (method II)
- 4 wt% Rh/5 wt% (Ce/Zr)/γ-Al_2O_3 (Ce:Zr;1:1) (method II)
- 4 wt% Rh/5 wt% (Ce/Zr)/γ-Al_2O_3 (Ce:Zr;2:1) (method II)
- 4 wt% Rh/5 wt% Zr/γ-Al_2O_3 (method II)

1.6 wt% Rh supported catalysts have been produced according to the same procedure.

3.3 Results

3.3.1 BET surface area measurement

Nitrogen adsorption/desorption experiments were carried out to characterise the surface area and porosity of the synthesised materials. The BET surface area of the supports and catalysts are calculated and summarized in Table 3.1.

Sample	BET surface area [m^2/g]
γ-Al_2O_3	88
5 wt% Ce/γ-Al_2O_3	81
5 wt% Ce/Zr/γ-Al_2O_3	89
4 wt% Rh/Al_2O_3	95
4 wt% Rh/CeO_x/Al_2O_3 (method I)	70
4 wt% Rh/CeO_x/Al_2O_3 (method II)	89
1.6 wt% Rh/Al_2O_3	91
1.6 wt% Rh/CeO_x/Al_2O_3 (method I)	68
1.6 wt% Rh/CeO_x/Al_2O_3 (method II)	82

Table 3.1. BET surface area results for the sample investigated.

The BET surface area measured for γ-alumina and ceria and/or zirconia doped γ-Al_2O_3 were close to value of 90 m^2g^{-1} as it was reported in the previous studies [14]. The surface area for all rhodium on γ-Al_2O_3 supported catalysts was also found to be approximately 90 +/- 5 m^2g^{-1}, which is in good agreement with the literature results (96 m^2g^{-1} for 0.5 wt% Rh/γ-Al_2O_3) given by McCabe *et al.* [14] The addition of rhodium did not change the value of the BET surface area relative to the pure alumina or ceria-alumina, meaning that the addition of Rh is not associated with significant textural changes of γ-alumina. The BET surface area of the ceriated Rh catalysts shows that Rh/CeO_x/Al_2O_3 (I) for both Rh loading results in a lower total surface area (20 %) than Rh/CeO_x/Al_2O_3 (II) as well as undoped Rh on alumina case. The drop of BET surface area for these samples can be due to some γ-Al_2O_3 particle

sintering induced by the 773 K calcinations that is used in method I. The BET surface area of the whole range of Rh catalysts promoted by ceria-zirconia and zirconia was found to be approximately 90 m^2g^{-1}. The BET measurement provides also the adsorption isotherms, which are constructed by plotting the amount adsorbed V against the relative pressure (P/P_0). Figure 3.2 presents N_2 adsorption/desorption for 1.6 wt% $Rh/\gamma\text{-}Al_2O_3$, indicating that there is no mesoporosity present in the sample. The microporous alumina does not exhibit pore filling until high relative pressure, therefore a hysteresis loop is not observed for this type of materials. The same trend is observed for a whole range of alumina supported Rh catalysts. The surface area comes from external surface area of the very fine particles and any microporosity present.

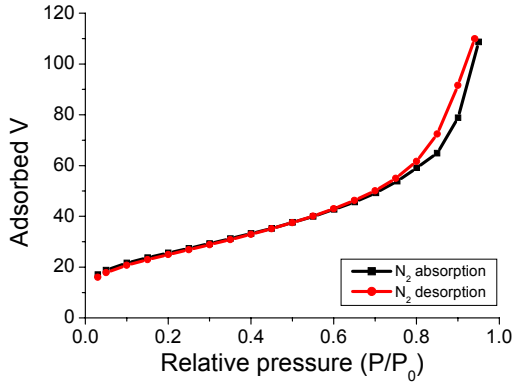

Figure 3.2. N_2 adsorption/desorption isotherm for 1.6 wt% Rh/Al_2O_3

3.3.2 Energy Dispersive X-ray analysis (EDX)

EDX measurement was used to quantify the elemental composition of the supported Rh catalysts. The sample, in powdered form, is mounted on a stainless steel holder with double-sided adhesive carbon tape. The specimen was cooled prior the analysis to avoid accumulation of charge. The experimental values are displayed in Table 3.2, along with the theoretically calculated amounts, assuming no loss of material occurs during sample synthesis. A slightly higher rhodium versus a lower amount of chlorine is observed. The discrepancies with theoretical values could be due to the fact that a considerable amount of chlorine is removed from the sample in the calcinations/reduction process. Moreover, the amount of oxygen is difficult to determine, because of the low sensitivity of EDX for low Z elements (below Na) due to the low binding energy of the electrons and low energy of the consequent fluorescence emission. Thus, during the quantification analysis, the software is set-

up as such that it includes the present elements in the form of oxides only. Firstly the amount of rhodium, cerium, zirconium and aluminium is established and then the quantity of oxygen is taken from the stoichiometry for the particular oxides as such Rh_2O_3, CeO_2, and ZrO_2. EDX results are an average of ten area scans. In order to check the accuracy of this measurement and methodology described above the reference compounds such as γ-Al_2O_3, $Ce(acac)_3$, $Zr(acac)_4$, Rh_2O_3 have been measured and the expected elemental compositions have been obtained. The analysed EDX elemental compositions are compared to XPS results, where the elemental composition was obtained by the curve fitting of core-level spectra corrected with theoretical sensitivity factors based on Scofield's photoionisation cross-sections [15]. In general, the EDX and XPS results are in good agreement with the theoretical values. This suggests that ceria and zirconia have been deposited on the Rh catalysts. In the case where the experimental value is greater or lower than the theoretical value this can be explained by the accuracy of the balance used and the error in the measurement.

Sample	Atom	Wt% exp **EDX**	Wt% theory	At% exp **EDX**	At% exp **XPS**	At% theory
1.6 wt% Rh/Al_2O_3	Rh	2.0 (4)	1.6	0.4	0.5	0.3
	Cl	1.1 (2)	1.6	0.6	0.8	0.9
	Al	50.9 (4)	51.2	39.3	40.2	39.5
	O	46.2 (4)	45.5	59.6	58.5	59.2
4 wt% Rh/Al_2O_3	Rh	4.3 (5)	4	0.9	1	0.8
	Cl	0.5 (2)	4	0.5	0.8	2.4
	Al	49.6 (4)	48.7	38.8	40.2	38.7
	O	45.3 (4)	43.3	59.6	58	58
1.6 wt% $Rh/CeO_x/Al_2O_3$ (I)	Rh	2.0 (5)	1.6	0.4	0.5	0.3
	Cl	1.2 (2)	1.6	0.8	0.9	1
	Al	46.0 (5)	45.9	37.8	37.8	37.8
	Ce	8.6 (5)	8	1.4	1.5	1.3
	O	42.5 (5)	42.8	59.5	59.2	59.5

Table 3.2. Elemental composition for the series of Rh samples as indicated.

Sample	Atom	Wt% exp EDX	Wt% theory	At% exp EDX	At% exp XPS	At% theory
4 wt% $Rh/CeO_x/Al_2O_3$(I)	Rh	5.1 (5)	4	1.1	1.2	0.9
	Cl	1.6 (2)	4	1	1.7	2.6
	Al	44.1 (5)	43.4	37.2	36.9	36.9
	Ce	7.4 (5)	8.1	1.2	1.3	1.3
	O	41.7 (5)	40.6	59.7	58.8	58.3
1.6 wt% $Rh/CeO_x/Al_2O_3$ (II)	Rh	2.0 (5)	1.6	0.9	0.5	0.4
	Cl	0.8 (2)	1.6	0.5	0.4	0.9
	Al	47.5 (5)	48.6	38.4	41	39.3
	Ce	6.1 (5)	5	1	1	0.8
	O	43.7 (6)	43.2	59.7	57.1	58.6
4 wt% $Rh/CeO_x/Al_2O_3$(II)	Rh	4.1 (5)	4	0.9	1	0.9
	Cl	0.9 (2)	4	0.6	0.3	2.5
	Al	46.5 (5)	46.1	38.1	40.9	38.4
	Ce	5.2 (5)	5	0.8	1.1	0.8
	O	43.1 (5)	40.9	59.6	56.7	57.4
1.6 wt% $Rh/CeO_x/ZrO_2/Al_2O_3$ (Ce:Zr;1:1)	Rh	1.8 (4)	1.6	0.4	0.5	0.3
	Cl	0.6 (3)	1.6	0.4	0.3	1
	Al	48.9(8)	48.6	39.9	41.3	39.1
	Ce	2.5 (6)	2.5	0.6	0.7	0.4
	Zr	1.9 (8)	2.5	0.5	1	0.6
	O	44.3 (8)	43.2	58.2	56.2	55.5
4 wt% $Rh/CeO_x/ZrO_2/Al_2O_3$ (Ce:Zr;1:1)	Rh	4.3 (5)	4	0.9	1.1	0.8
	Cl	0.8 (2)	4	0.5	0.5	2.3
	Al	47.1 (5)	46.1	38.2	39.5	35.5
	Ce	2.2 (3)	2.5	0.3	0.7	0.4
	Zr	2.0 (4)	2.5	0.5	1	0.6
	O	43.6 (5)	40.9	59.6	57.6	53.1
1.6 wt% $Rh/CeO_x/ZrO_2/Al_2O_3$ (Ce:Zr;2:1)	Rh	1.6 (4)	1.6	0.4	0.4	0.3
	Cl	0.5 (2)	1.6	0.3	0.4	1
	Al	48.8 (7)	48.6	38.8	40.4	39.1
	Ce	3.4 (3)	3.3	0.7	0.7	0.5
	Zr	1.6 (4)	1.7	0.6	0.6	0.4
	O	44.1 (6)	43.2	59.2	57.5	58.6

Table 3.2... (Continued) Elemental composition for the series of Rh samples as indicated.

Sample	Atom	Wt% exp EDX	Wt% theory	At% exp EDX	At% exp XPS	At% theory
4 wt% $Rh/CeO_x/ZrO_2/Al_2O_3$ (Ce:Zr;2:1)	Rh	4.0 (5)	4	0.9	1	0.9
	Cl	0.7 (2)	4	0.4	0.5	2.5
	Al	46.2 (6)	46.1	37.7	39.2	38.3
	Ce	3.3 (4)	3.3	0.5	0.8	0.5
	Zr	1.2 (3)	1.7	0.3	0.7	0.4
	O	43.7 (6)	40.9	60.2	57.8	57.3
1.6 wt% $Rh/ZrO_2/Al_2O_3$	Rh	2.2 (5)	1.6	0.5	0.4	0.3
	Cl	0.6 (2)	1.6	0.4	0.6	1
	Al	48.1 (8)	48.6	38.1	39.9	39.1
	Zr	3.6 (6)	5	0.8	1.3	1.2
	O	45.0 (7)	43.2	60.2	57.8	58.5
4 wt% $Rh/ZrO_2/Al_2O_3$	Rh	3.4 (5)	4	0.7	1	0.9
	Cl	0.9 (2)	4	0.6	0.5	2.5
	Al	46.9 (6)	46.1	37.8	39.4	38.2
	Zr	4.6 (7)	5	1.1	1.9	1.2
	O	44.2 (5)	40.9	59.8	57.2	57.2

Table 3.2... (Continued) Elemental composition for the series of Rh samples as indicated.

3.3.3 TEM analysis

Transmission electron microscopy (TEM) was not only used to determine the rhodium particle size, but also to get some insights in the homogeneity in size and shape distributions of the Rh phase within the catalysts. To prepare the specimens, hexane suspensions of the powder were treated in an ultrasonic bath and then placed drop wise onto a holey carbon film supported by a copper grip. Then, the solvent was allowed to evaporate in air. Many areas and grains were investigated in order to obtain representative conclusions. Figure 3.2 gives the TEM image of the dispersion state of the mounted Rh nanoparticles for 4 wt% Rh sample supported on alumina. It can be seen that the supported rhodium catalyst consist of conglomerations of round platelets of alumina, which support rounded, well-dispersed Rh nanoparticles. The areas indicated show the Rh particles present on the γ-Al_2O_3 support display approximately the spherical morphology. Additionally, the EDX analyses for the whole range of rhodium compounds investigated in this project have confirmed the presence of aluminium, and shows that the nanoparticles are indeed, rhodium.

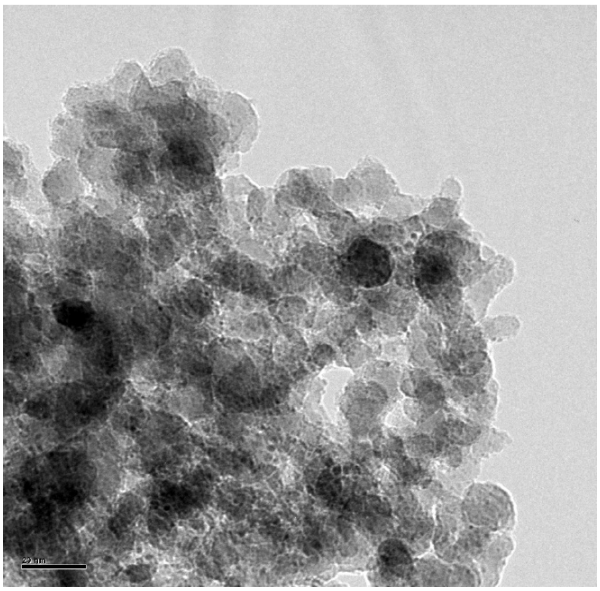

Figure 3.2. TEM image of 4 wt% Rh/γ-Al_2O_3. Scale bar: 2 nm.

Only particles from the size of 0.4 nm and larger are detected in the TEM measurement which is due to limitations in instrumental resolution. Assuming spherical particles with an fcc structure are present, TEM will only detect the metal particles consisting of a minimum of 13 atoms in the reduced state. Moreover, it is known that rhodium particles in such systems under ambient condition are oxides rather than metallic and therefore this mean particle size refers to fraction of oxidic Rh and metallic Rh particles [16]. A collation of the particle size distributions derived from the TEM images is included in Figure 3.3 and Figure 3.4 with the relevant statistics given in Table 3.3. To obtain these distributions the diameters of ca. 200 particles per sample were measured. The 1.6 wt% Rh samples displayed relative narrow particle size distributions with rhodium particles ranging from approximately 0.7 to 3 nm. As can be seen the distributions for the 1.6 wt% Rh/Al_2O_3 and 1.6 wt% Rh/CeO_x/Al_2O_3 (I) are almost similar. However, the particle size distributions for the catalysts with γ-alumina modified by CeO_x (method II) differ from the distributions of the first two catalysts. In this case the mean Rh particles size has slightly increased to value of 2.1 nm, which corresponds to the previous studies of these types of Rh catalysts. A broader particle size distribution of ca. 0.7 – 4 nm is seen for the 4 wt% Rh supported systems (Figure 3.4). Again, a clear increase in average particle size is observed for the ceriated catalyst derived from method II, whereas the other two sample display similar average Rh metal particle sizes.

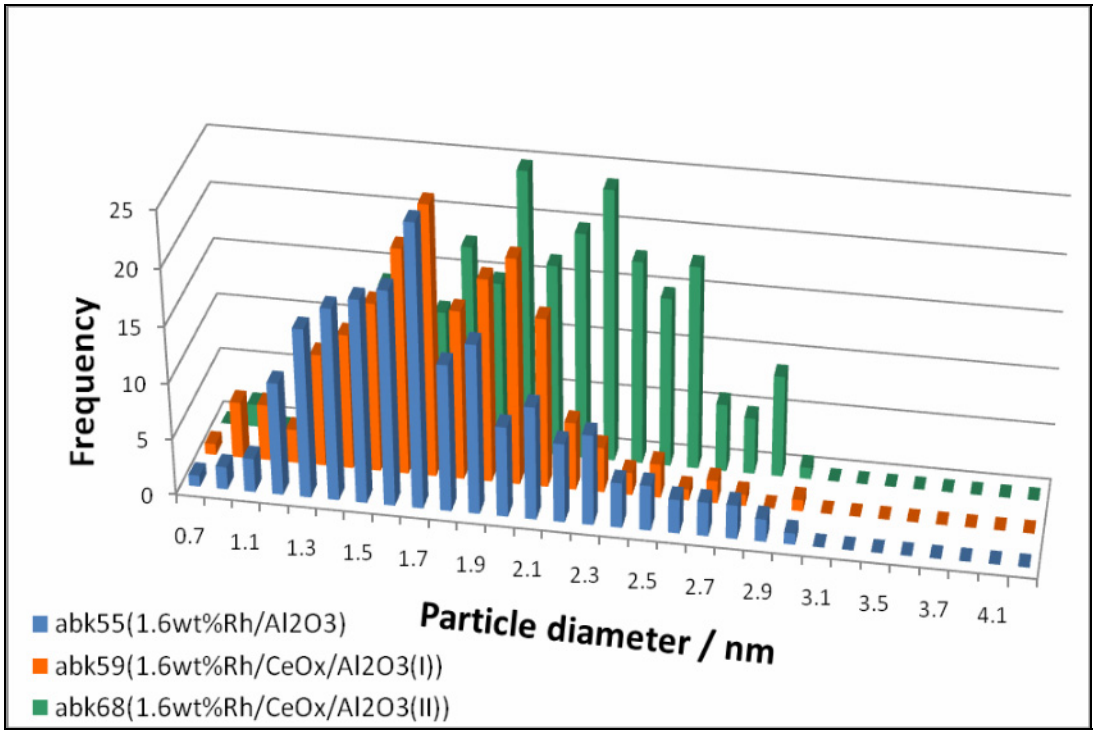

Figure 3.3. Particle size distributions derived from TEM for 1.6 wt% Rh catalysts

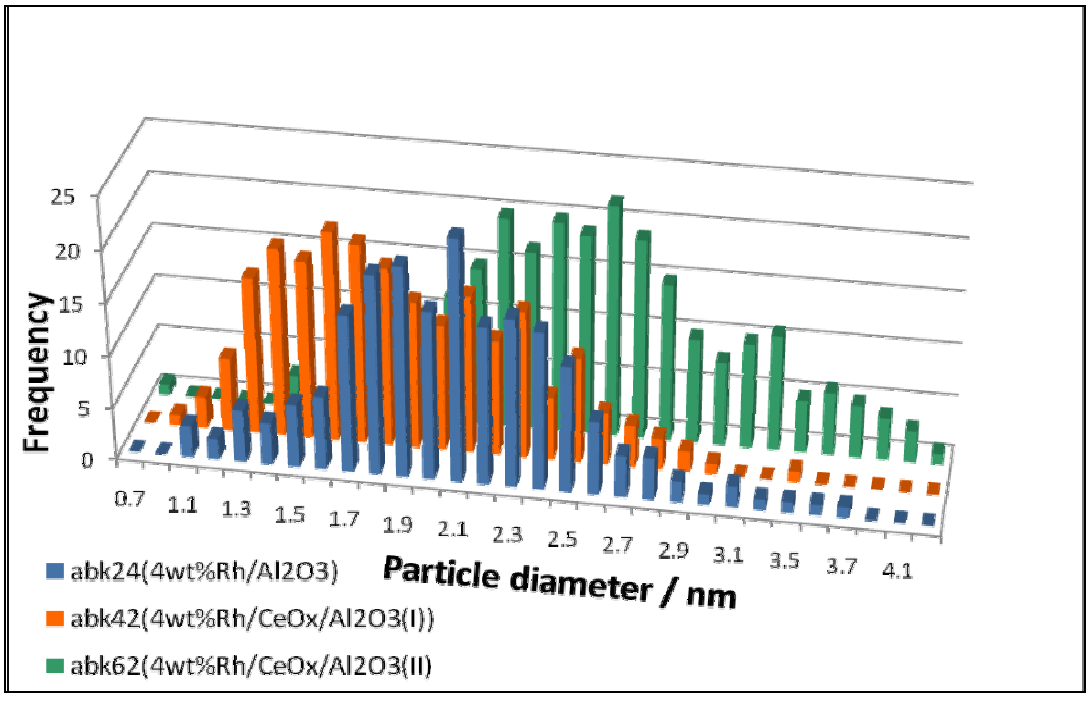

Figure 3.4. Particle size distributions derived from TEM for 4 wt% Rh catalysts

Rh catalysts promoted with zirconia, or ceria and zirconia all have very similar particle size distributions between ca. 1.5 – 3 nm (Figure 3.5, Table 3.3), comparable to the non-promoted versions. The majority of particles are around 2 nm. Comparing with the 1.6 wt% Rh only loaded samples, a broader particle size distribution can be seen as for ceriated catalysts. It appears that ceria and/or zirconia doping of 4 wt%

Rh catalysts does not affect the averaged Rh particle size. In general, the metal particles for each Rh catalyst were observed to have a very uniform and narrow size distribution. However, the dependent of Rh particle size on the Rh loading was not observed as expected according to th previous studies by B. Jyoti [8]. This phenomenon can indicate the strong interaction between Rh particles and the support.

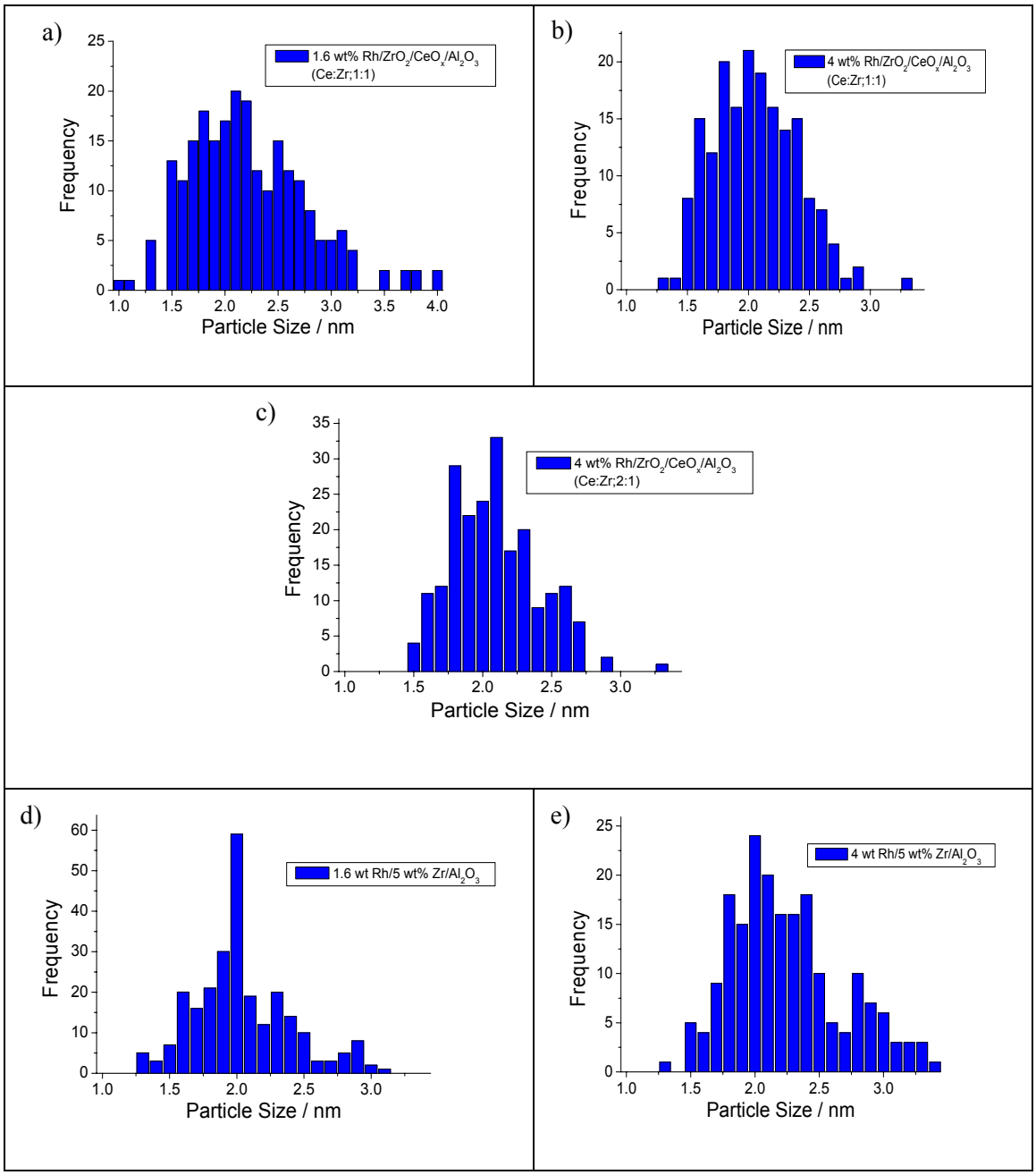

Figure 3.5. Particle size distributions of 1.6 and 4 wt% Rh catalysts doped by ceria and zirconia, or zirconia only.

Sample	Points	Average Particle Size
1.6 wt% Rh/Al_2O_3	189	1.7 (4)
1.6 wt% $Rh/CeO_x/Al_2O_3$(I)	183	1.8 (4)
1.6 wt% $Rh/CeO_x/Al_2O_3$(II)	212	2.1 (4)
4 wt% Rh/Al_2O_3	201	2.1 (4)
4 wt% $Rh/CeO_x/Al_2O_3$(I)	199	1.9 (4)
4 wt% $Rh/CeO_x/Al_2O_3$(II)	226	2.6 (5)
1.6 wt% $Rh/CeO_x/ZrO_2/Al_2O_3$ (Ce:Zr;1:1)	231	2.2 (5)
4 wt% $Rh/CeO_x/ZrO_2/Al_2O_3$ (Ce:Zr;1:1)	201	2.1 (3)
4 wt% $Rh/CeO_x/ZrO_2/Al_2O_3$ (Ce:Zr;2:1)	181	2.0 (3)
1.6 wt% $Rh/ZrO_2/Al_2O_3$	234	2.1 (4)
4 wt% $Rh/ZrO_2/Al_2O_3$	198	2.2 (4)

Table 3.3. Rhodium particle size distributions for the series of Rh samples as determined with TEM

In this report the STEM HAADF technique uses also the EDX function to study the distribution of elements across the material. The STEM EDX HAADF line profile for 1.6 wt% $Rh/CeO_x/Al_2O_3$ (method I), presented in Figure 3.6, primarily shows that the Rh and Ce are found in the area investigated. The data needs to be treated with a certain amount of caution as the intensity of Rh is of a similar level as the background counts. The STEM EDX HAADF line profile shows that the Rh and Ce distributions do follow each other well only across the small range of the area investigated. Mostly it can be observed that the Ce particles are placed on the γ-alumina support separately. This can be explained by the low Rh loading which is not sufficient for the amount of ceria used.

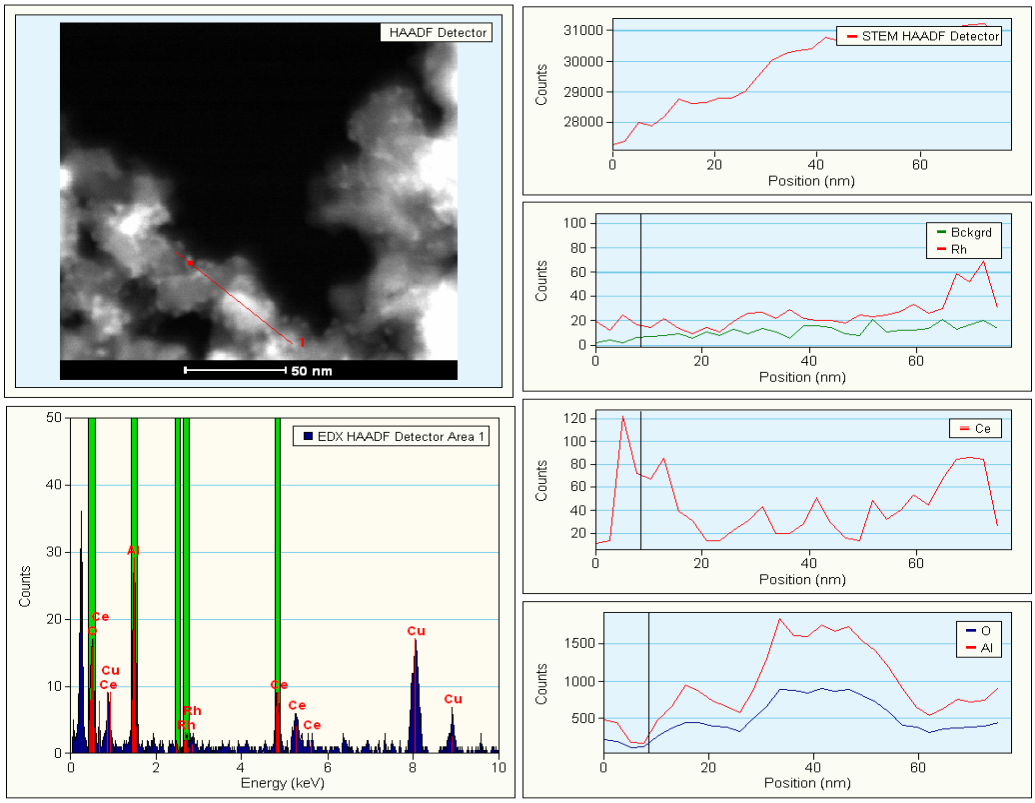

Figure 3.6. STEM EDX HAADF line profile analysis for 1.6 wt% $Rh/CeO_x/Al_2O_3$ (method I). The upper left box shows the STEM HAADF image of the area under investigation. The HAADF EDX response for the red line labelled 1 is shown below the STEM image. The HAADF EDX response across the red line are shown on the right hand side and in descending order show total counts, counts from Rh, Ce and the last plot indicate O and Al trend.

Figure 3.7 presents the STEM EDX HAADF line profile analysis for the ceria-promoted catalysts using method II: 1.6 wt% $Rh/CeO_x/Al_2O_3$. The line profile analysis, giving the number of Rh and Ce counts, indicates that the Rh and Ce distributions are related: the Ce appears together with the Rh. It can also be seen that there are small fragments of Ce on the support just outside the Rh particles which is likely due to the larger Ce loading compared to the Rh. This result shows that the surface modification procedure (method II) seems to work, wherein Ce is deposited on the pre-reduced Rh supported catalysts, directing the Ce metal onto Rh particles.

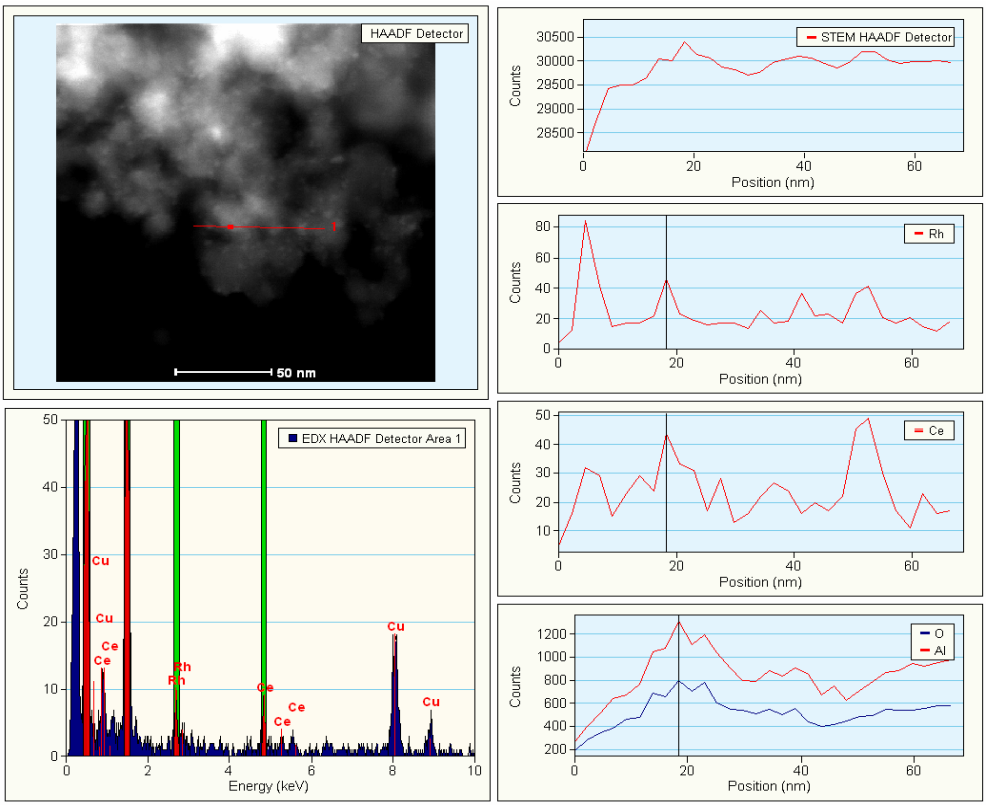

Figure 3.7. STEM EDX HAADF line profile analysis for 1.6 wt% $Rh/CeO_x/Al_2O_3$ (method II). The upper left box shows the STEM HAADF image of the area under investigation. The HAADF EDX response for the red line labelled 1 is shown below the STEM image. The HAADF EDX response across the red line are shown on the right hand side and in descending order show total counts, counts from Rh, Ce and the last plot indicate O and Al trend.

Figure 3.8 presents STEM EDX HAADF line profile analysis for a ceria-promoted catalyst with higher Rh metal loading: 4 wt% $Rh/CeO_x/Al_2O_3$ (method I). The STEM EDX line profiles show that the Rh and Ce distributions do not follow each other across the particle completely: There are Ce peaks that appear together with Rh, but there are also separate Rh peaks. This fact suggests that Rh is placed on the Ce particles as well as small Rh nanoparticles, and either larger Rh nanoparticles, or conglomerations of Rh nanoparticles are found on the alumina. This Rh distribution is due to the synthesis method I, wherein firstly CeO_x is deposited on γ-alumina and then Rh is placed on the ceria-alumina support.

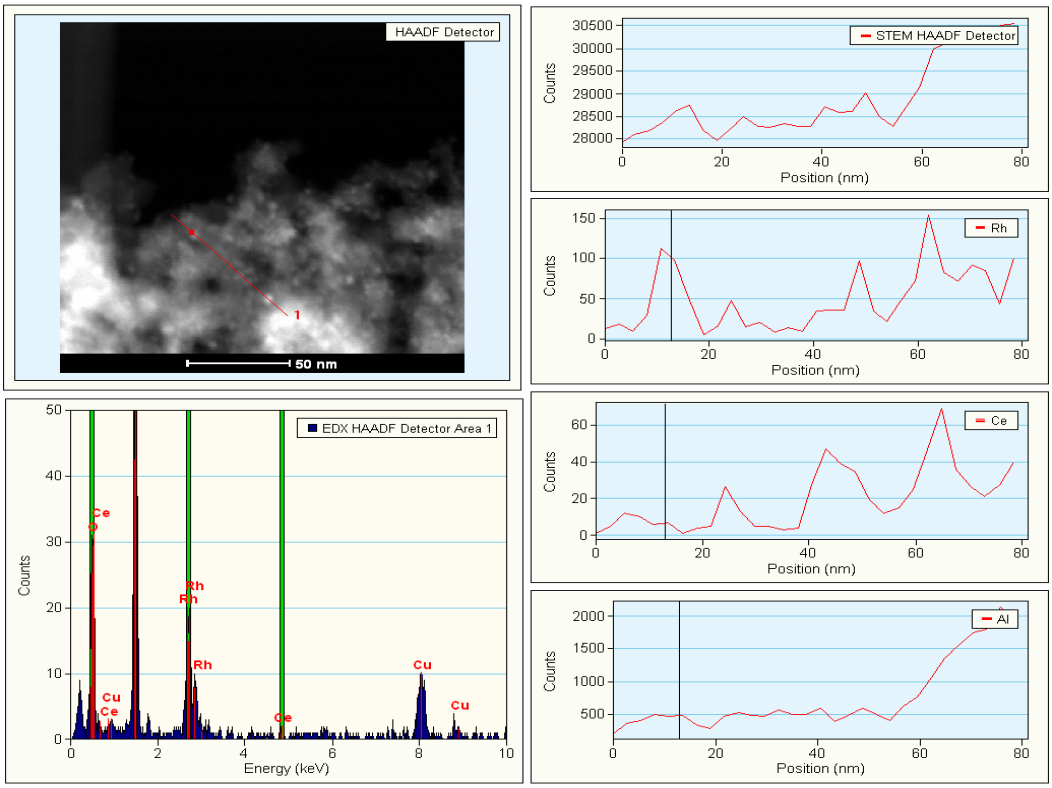

Figure 3.8. STEM EDX HAADF line profile analysis for 4wt% $Rh/CeO_x/Al_2O_3$ (method I). The upper left box shows the STEM HAADF image of the area under investigation. The HAADF EDX response for the red line labelled 1 is shown below the TEM image. The HAADF EDX response across the red line are shown on the right hand side and in descending order show total counts, counts from Rh, Ce and Al.

Figure 3.9 presents STEM EDX HAADF line profile analysis for a ceria-promoted catalyst i.e. 4 wt% $Rh/CeO_x/Al_2O_3$ (method II). The line profiles show that the Rh and Ce distributions follow each other quite well across the material: There are Ce peaks appear together as Rh, however there are also isolated Rh peaks. This fact suggests that during the surface modification method, large amount of Rh particles are active to let the deposition of Ce particles towards them. The evidence of Rh in isolation may be as a result of small Rh particles not being as active towards the controlled surface modification procedure, or due to small clusters of Rh breaking off the main Rh particle during the CeO_x deposition.

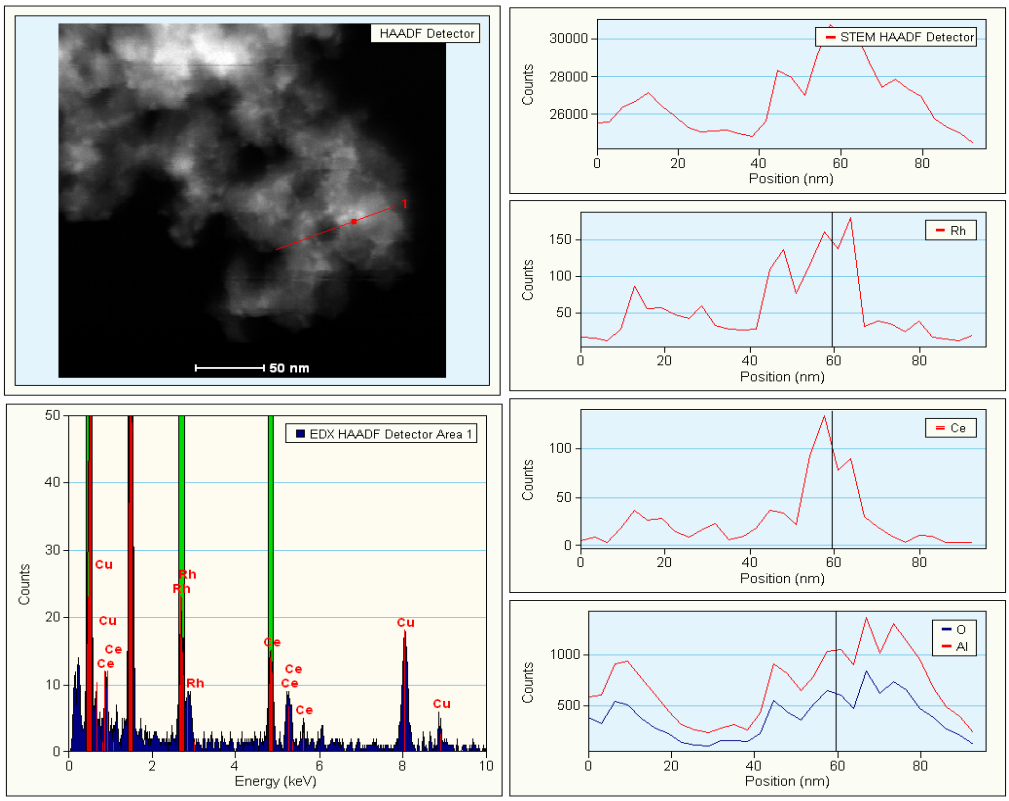

Figure 3.9. STEM EDX HAADF line profile analysis for 4 wt% $Rh/CeO_x/Al_2O_3$ (method II). The upper left box shows the STEM HAADF image of the area under investigation. The HAADF EDX response for the red line labelled 1 is shown below the STEM image. The HAADF EDX response across the red line are shown on the right hand side and in descending order show total counts, counts from Rh, Ce and the last plot indicate O and Al trend.

The TEM study provides an overview of the Rh particle size and the STEM EDX HAADF gives insights on the elemental distribution across the material. However, the limitations of this methodology and technology prevent an identification of the particular Rh and Ce phases present in the system. Therefore, the Rh catalysts have been further investigated using XPS and XAFS techniques.

3.3.4 X-ray Photoelectron Spectroscopy

The electronic properties of the alumina supported rhodium particles as well as the promoters such as ceria and zirconia were further studied by XPS. The sample, in powder form, is mounted on a stainless steel holder with double-sided adhesive carbon tape.

The effect of metal loading and ceria/zirconia doping were studied for the series of 1.6 and 4 wt% Rh samples. These 2 samples were subsequently promoted with CeO_x and ZrO_2 via two methods as described above. The characteristic photoemission from the Ce(3d), Zr(3d), Rh(3d), O(1s), Cl(2p), Al(2p) core levels were recorded for

each sample. For consistency, all binding energies reported, are calibrated to the C(1s) transition at 284.6 eV [17].

3.3.4.1 Rh 3d core-level spectra

Figure 3.10 and Figure 3.11 show the Rh $3d_{5/2}$ and $3d_{3/2}$ XPS spectra bands for a Rh foil, a Rh_2O_3 reference and representative spectra for a series of fresh 1.6 and 4 wt% Rh catalysts, respectively. The positions of the two broad bands clearly show that in the fresh Rh catalysts, the Rh particles exist as the mixture of Rh on the different oxidation states. For Rh/Al_2O_3 catalysts, two broad photoemission peaks were observed; indicating that various oxides existed in the system. In the case of CeO_x-promoted Rh catalysts, the position of the Rh 3d peaks differ remarkably depending on the synthesis method. Rh particles in the $Rh/CeO_x/Al_2O_3$ (method I) for both Rh loadings seem to be more oxidised with the shift of 3d peaks towards the bigger value of binding energy. However, the Rh particles derived from the method II are less oxidised. When compared to rhodium on alumina, Rh particles derived from the sample doped by ceria and zirconia (method II) appear to be less oxidised with the shift of Rh 3d peaks towards the lower value of binding energy. There is no visible difference in the peak positions between the loadings of Rh metal in the catalytic system. The ceria and zirconia presence essentially could insulate the Rh component against any rapid oxidation under ambient conditions.

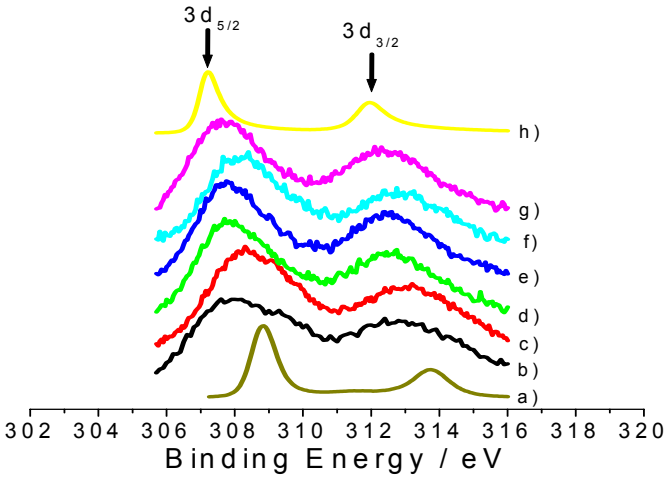

Figure 3.10. XPS spectra of the fresh catalysts: a) Rh_2O_3, b) 1.6 wt% Rh/Al_2O_3, c) 1.6 wt% $Rh/CeO_x/Al_2O_3$ (I), d) 1.6 wt% $Rh/CeO_x/Al_2O_3$ (II), e) 1.6 wt% $Rh/CeO_x/ZrO_2/Al_2O_3$ (Ce:Zr;1:1), f) 1.6 wt% $Rh/CeO_x/ZrO_2/Al_2O_3$ (Ce:Zr;2:1), g) 1.6 wt% $Rh/ZrO_2/Al_2O_3$,h) Rh foil

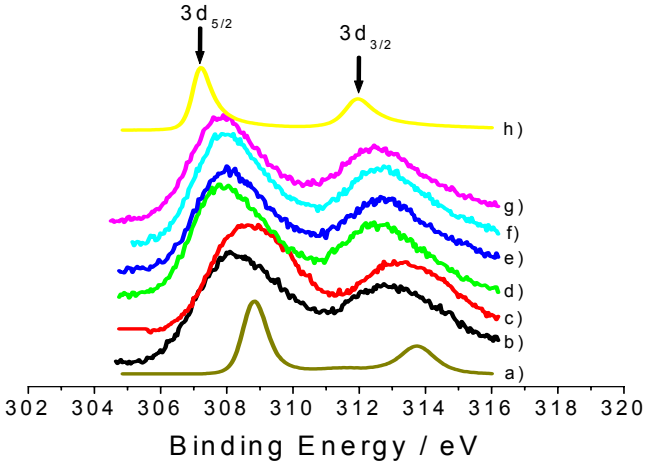

Figure 3.11. XPS spectra of the fresh catalysts: a) Rh_2O_3, b) 4 wt% Rh/Al_2O_3, c) 4 wt% $Rh/CeO_x/Al_2O_3$ (I), d) 4 wt% $Rh/CeO_x/Al_2O_3$ (II), e) 4 wt% $Rh/CeO_x/ZrO_2/Al_2O_3$ (Ce:Zr;1:1), f) 4 wt% $Rh/CeO_x/ZrO_2/Al_2O_3$ (Ce:Zr;2:1), g) 4 wt% $Rh/ZrO_2/Al_2O_3$, h) Rh foil

The reported BE values of the Rh catalysts and reference rhodium compounds with Rh in different level of Rh oxidation are given for comparison in Table 3.4 [18-20]. For pure rhodium metal foil the Rh $3d_{5/2}$ and Rh $3d_{3/2}$ peaks occur at 307.3 and 312.1 eV, respectively, which is attributed to Rh^0. The doublet at 308.9 and 313.7 eV is attributed to rhodium particles in Rh^{3+} oxidation state.

All Rh 3d spectra could be fitted using two sets of doublets corresponding to the metallic and oxidic Rh^{3+} chemical environments, with $3d_{5/2}$ components centred around 307.5 and 308.9eV binding energy, respectively (Figure 3.12). The energy differences of the $3d_{3/2}$ and $3d_{5/2}$ peaks were kept constant at the cited value of 4.5 eV. The FWHMs were 2.2 +/- 0.3 eV for the metallic component and 3.2 eV for Rh^{3+} [21]. After the curve fitting procedure the fraction of Rh^{3+} for each rhodium catalyst has been calculated using the area ratio of the peaks derived from Rh^{3+} to the total area of the Rh 3d spectrum (Table 3.4).

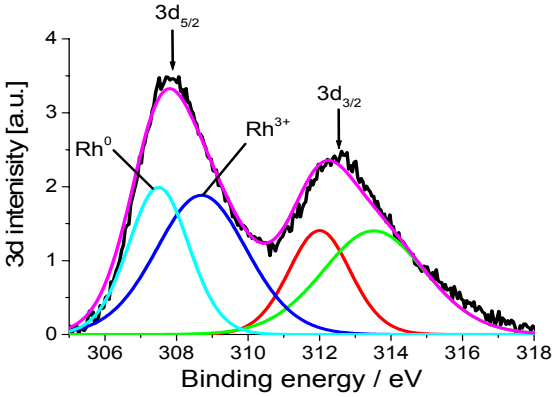

Figure 3.12. Fitted Rh 3d XPS spectra of 4 wt% Rh catalyst

The calculated parameters indicate that Rh particles of 1.6 wt% Rh/Al_2O_3 and 4 wt% Rh/Al_2O_3 are mostly oxidised in the air. However, a higher loading of Rh gives larger particles, which keeps a slightly more reduced form in the system. Therefore, larger Rh particles provide better protection from the extensive oxidation. Furthermore, the Rh particles of $Rh/CeO_x/Al_2O_3$ (I) catalysts for both loadings are also extensively oxidised in the air (~90% of oxidation).

On the other hand, there is a significantly larger amount of the Rh metallic part in the ceriated Rh catalysts produced by method II. This phenomenon is attributed to the synthesis method; pre-reduced Rh particles supported on alumina are active for the Ce deposition via the surface modification method. Moreover, this synthesis procedure of method II does not involve calcinations after second high temperature reduction step as in method I.

The introduction of zirconia to the ceriated Rh catalysts does not cause any further reduction of Rh particles. However, the Rh particles in the zirconiated Rh samples are the least oxidised among all Rh systems investigated for both Rh loadings. Generally, the additives of ceria and zirconia strongly protect the rhodium particles from oxidation, as a large part of metallic fraction is still present in these systems. However, a large proportion of Rh^{3+} (ca. 80 %) was detected for 1.6 wt% $Rh/CeO_x/ZrO_2/Al_2O_3$ (Ce:Zr;2:1) system.

The XPS parameters have been compared with the XANES analysis which also provides information regarding the electronic properties and oxidation state of the metal under investigation. Figure 3.13 shows the normalised XANES spectra obtained at the Rh K edge for the Rh catalysts along with reference materials. The

data were acquired under an atmosphere of air. The energy of 23246 eV has been chosen in order to study the XANES changes for each Rh catalyst. The XANES intensity of the Rh foil at this energy, representative for Rh^0, has been set to 0. The maximum XANES variation as can be obtained with this approach is 1, for the fully oxidised Rh_2O_3. As a result, the variation of XANES gives information about the degree of oxidation of the Rh for a particular Rh sample.

When compared to XPS results a similar trend is observed, 1.6 wt% and 4 wt% Rh/Al_2O_3 catalysts contain mostly oxidised Rh particles.

The ceria doping introduced by method I does not have any influence on the oxidation state of Rh particles, keeping almost the same level of Rh oxidation, when compared to rhodium on alumina. On the other hand, the XANES changes for Ce-doped Rh catalysts (method II) indicate that Rh particles become less oxidised.

The XANES variations of Zr and Ce-promoted catalysts show the similar trend, demonstrating generally less oxidised Rh particles apart from single Rh system, indicated above, whose Rh oxidation level is relatively high (1.6 wt% $Rh/CeO_x/ZrO_2/Al_2O_3$ (Ce:Zr;2:1)).

Additionally, the XAFS edge jump of these samples are positioned at a lower energy, suggesting a lower Rh oxidation state when compared to Rh/Al_2O_3 catalysts and it is assumed that this is a result of association with Ce and Zr.

Table 3.4 presents the percent of Rh^{3+} of the total rhodium existed in the system, derived from the XPS and XANES calculations. As it can be observed, the results from both techniques fit well to each other, indicating the same level of Rh oxidation for the systems with lower Rh loading. However, for a series of 4 wt% Rh catalysts, XANES results show lower values of Rh^{3+} fraction when compared with the XPS data. This can be due to the additional multiple scattering of RhRh shells in this feature which complicates this procedure.

This quantification of the XANES variation to obtain the overall oxidation states of the Rh particles cannot be carried out. This is due to the fact that the chosen XANES feature is not only dependent on the electronic properties of the Rh, but also on the particle size and geometry.

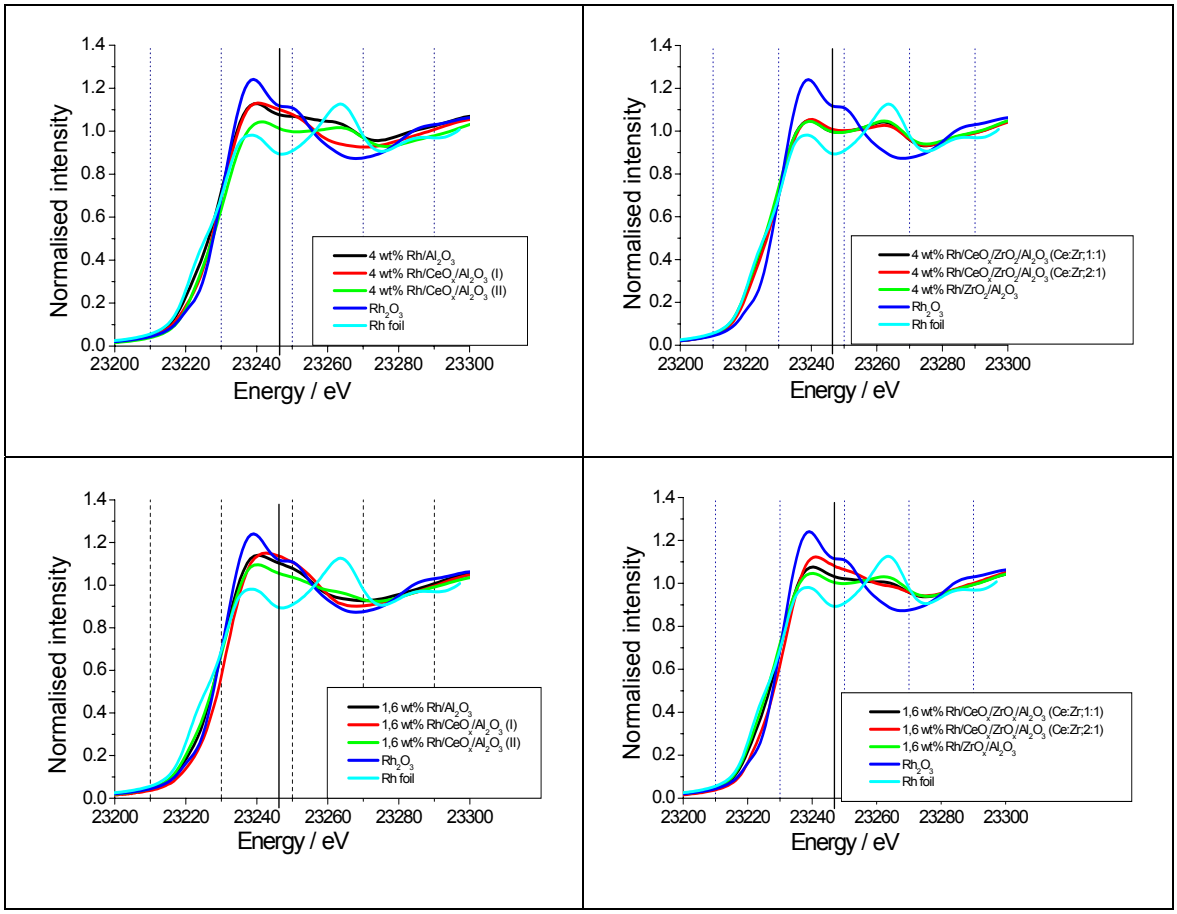

Figure 3.13. Rh K edge XANES spectra of Rh catalysts acquired in an atmosphere of air; Rh_2O_3 and Rh foil are included for comparison.

Sample	Rh^0	Rh^{3+}	Rh^{3+}/Rh^{tot} (XPS)	Rh^{3+} (XANES)
1.6 wt% Rh/Al_2O_3	307.3	308.7	0.83	0.92
1.6 wt% $Rh/CeO_x/Al_2O_3$ (I)	307.5	308.7	0.91	0.96
1.6 wt% $Rh/CeO_x/Al_2O_3$ (II)	307.5	308.7	0.65	0.73
1.6 wt% $Rh/CeO_x/ZrO_2/Al_2O_3$ (Ce:Zr;1:1)	307.5	308.7	0.58	0.62
1.6 wt% $Rh/CeO_x/ZrO_2/Al_2O_3$ (Ce:Zr;2:1)	307.5	308.7	0.78	0.85
1.6 wt% $Rh/ZrO_2/Al_2O_3$	307.4	308.7	0.51	0.49
4 wt% Rh/Al_2O_3	307.5	308.7	0.78	0.82
4 wt% $Rh/CeO_x/Al_2O_3$ (I)	307.5	308.7	0.87	0.95
4 wt% $Rh/CeO_x/Al_2O_3$ (II)	307.5	308.8	0.56	0.54
4 wt% $Rh/CeO_x/ZrO_2/Al_2O_3$ (Ce:Zr;1:1)	307.5	308.7	0.56	0.46
4 wt% $Rh/CeO_x/ZrO_2/Al_2O_3$ (Ce:Zr;2:1)	307.5	308.7	0.62	0.52
4 wt% $Rh/ZrO_2/Al_2O_3$	307.5	309.1	0.48	0.46
Rh foil	307.3	-	0	0
Rh_2O_3	-	308.9	1	1

Table 3.4. XPS and XANES oxidation state fitting parameters for all Rh systems; the fraction of Rh^{3+} of the total of rhodium is also included in the table.

3.3.4.2 Ce 3d core-level spectra

The Ce 3d XPS core-level spectra exhibit three-lobed envelope (around 879-890 eV, 895-910 eV and approximately 917 eV) such as those depicted in Figures 3.14a and 3.14b for the series of 1.6 wt% and 4 wt% rhodium catalysts, respectively. The complex shape of the spectra of cerium in cerium oxide suggests that the Ce 3d spectra arise from Ce with mixed oxidation state +3 and +4 [22, 23]. The peak at a binding energy of 917 eV can be attributed to the initial state of the tetravalent Ce (called "f0" configuration) only and it is thus possible to differentiate between the two oxidation states. Comparing the intensity of the peak at ~ 917 eV for both series of Rh catalysts, it can be seen that for the ceria and zirconia-promoted samples versus the ceria-only doped ones, this peak is very small indicating that the proportion of Ce^{4+} to that of Ce^{3+} is low. As has been already published, the incorporation of ZrO_2 into the CeO_2 lattice strongly promotes the reducibility of the

mixed oxide and the oxygen mobility in the bulk [24, 25]. In order to quantify the two possible oxidations states of Ce ions it is necessary to curve fit the Ce $3d_{5/2}$ and the Ce $3d_{3/2}$ spin-orbit doublet spectrum for each rhodium catalyst.

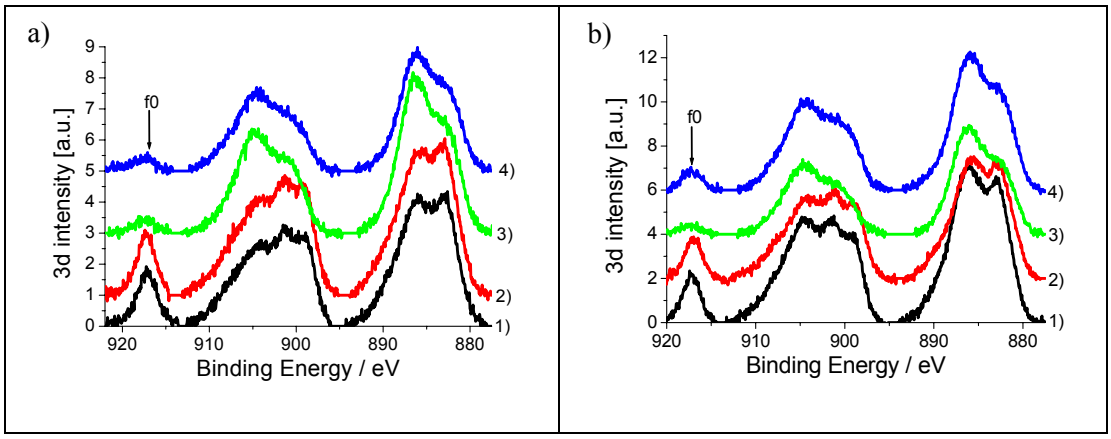

Figure 3.14. Ce 3d photoemission core level spectra for; a) 1.6 wt% Rh catalysts b) 4 wt% Rh catalysts: 1) $Rh/CeO_x/Al_2O_3$ (I), 2) $Rh/CeO_x/Al_2O_3$ (II), 3) $Rh/CeO_x/ZrO_2/Al_2O_3$ (Ce:Zr;1:1), 4) $Rh/CeO_x/ZrO_2/Al_2O_3$ (Ce:Zr;2:1)

XPS spectra of oxides CeO_2 and Ce_2O_3 can be individually resolved into up to six and four features grouped as *v* and *u* lines to depict the electronic transitions in Ce^{4+} and Ce^{3+}, respectively. Figure 3.15 presents curve fitting of Ce 3d XPS spectra of Rh catalysts with the individual peak contributions. For valence +4 cerium, the v_0 and v_2 components represent the intense peaks, and v_1 a satellite, in the Ce $3d_{5/2}$ spin-orbit split doublet. Correspondingly, v_0' and v_2' components characterise the Ce $3d_{3/2}$ doublet intense peaks, and v_1' the associated weak satellite. For the valence state +3, the main components, u_0 and associated shake-down peak, u_1, characterise the Ce $3d_{5/2}$ contribution. Subsequently, Ce $3d_{3/2}$ doublet is indicated by main peak, u_0', and associated shake-down peak, u_1'. The deconvolution of Ce 3d spectrum has been done for each Rh catalyst and the peak positions, FWHMs and relative contributions are derived from fitting the reference spectra: CeO_2 for Ce^{4+} and $Ce(acac)_3$ for Ce^{3+}. The binding energy positions of the fitted contributing to Ce $3d_{5/2}$ and Ce $3d_{3/2}$ are presented in Table 3.5. The values obtained are in good agreement with the ones reported in the literature [22, 23].

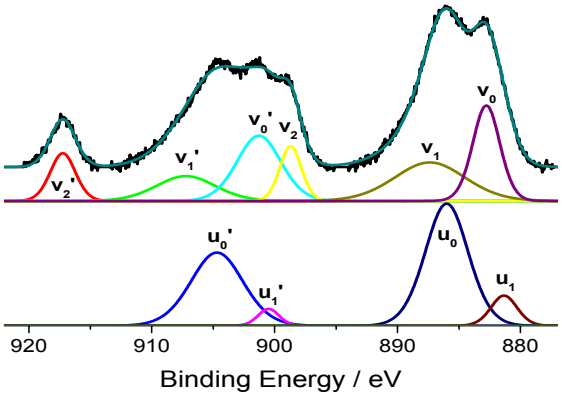

Figure 3.15. Fitted Ce 3d XPS spectra of a representative Rh catalyst with the individual peak contributions corresponding to Ce^{3+} (*u* lines) and Ce^{4+} (*v* lines).

Sample	v_0	v_1	v_2	v_0'	v_1'	v_2'	u_0	u_1	u_0'	u_1'
1.6 wt% Rh/ CeO_x/Al_2O_3 (I)	882.2	887.9	898.5	901.0	907.0	916.6	885.8	880.9	903.7	899.8
1.6 wt% Rh/ CeO_x/Al_2O_3(II)	882.2	887.6	898.6	901.0	907.3	916.5	885.6	880.6	903.8	899.9
1.6 wt% Rh/ $CeO_x/ZrO_2/Al_2O_3$ (Ce:Zr 1:1)	882.2	887.5	898.8	901.3	906.9	916.8	886.0	880.8	904.1	899.8
1.6 wt% Rh/ $CeO_x/ZrO_2/Al_2O_3$ (Ce:Zr 2:1)	882.4	887.4	898.5	901.4	907.4	916.9	886.0	881.0	904.0	899.9
4 wt% Rh/ CeO_x/Al_2O_3 (I)	882.2	887.5	898.7	901.3	907.2	916.6	886.0	880.7	904.1	900.0
4 wt% Rh/ CeO_x/Al_2O_3 (II)	882.1	887.4	898.5	901.1	907.0	916.5	885.7	881.0	904.0	899.9
4 wt% Rh/ $CeO_x/ZrO_2/Al_2O_3$ (Ce:Zr 1:1)	882.0	887.9	898.8	901.0	906.9	916.9	886.0	880.7	904.0	899.8
4 wt% Rh/ $CeO_x/ZrO_2/Al_2O_3$ (Ce:Zr 2:1)	882.2	887.6	898.9	901.0	906.9	916.7	886.0	880.7	903.7	899.8
Ce_2O_3	-	-	-	-	-	-	885.6	880.9	904.0	899.7
CeO_2	882.3	887.7	898.6	901.3	907.1	917.0	-	-	-	-
Ce_2O_3/CeO_2 [22]	882.4	888.8	898.3	901.0	906.8	916.5	885.5	880.8	903.5	898.9
$CeO_2/Na_2O/SiO_2$ [23]	882.2	888.6	898.0	900.7	907.2	916.5	884.4	880.6	903.5	899.3

Table 3.5. Energy positions of the spectral components in Ce $3d_{5/2}$ and Ce $3d_{3/2}$ observed in rhodium catalysts. The error of the measurement is 0.2 eV. Data taken from literature are given for comparison.

The relative amount of Ce^{3+} in the ceria supports and catalysts can be calculated using the area ratio of the sum of the various peaks derived from Ce^{3+} to the total area of the Ce 3d spectrum. The percentages of the particular Ce oxidation

state in the samples estimated from the XPS data are shown in Table 3.6. It can be observed that the ceria-alumina support contains mainly Ce^{4+} (~ 70 %). Insertion of Zr into the CeO_2 lattice decreases the amount of Ce^{4+} (~ 40%), irrespective of the amount of Zr inserted.

Rhodium catalysts promoted by ceria form mostly equivalent amounts of both ceria oxidation states: Ce^{3+} and Ce^{4+}. Deposition of 1.6 wt% and 4 wt% Rh onto a ceria-alumina support (method I) seems to oxidise the cerium in a similar way to sample prepared via method II (ceria on Rh-Al_2O_3). Additional zirconia doping promotes the reducibility of ceria and the dominant form in the system becomes Ce^{3+} irrespective of how much Zr is added. It can be seen that there is no variation between different Rh loadings.

	Sample	Ce^{3+} (%)	Ce^{4+} (%)
Supports	5 wt% CeO_x/Al_2O_3	27	73
	5 wt% (Ce/Zr)/Al_2O_3 (Ce:Zr; 1:1)	58	42
	5 wt% (Ce/Zr)/Al_2O_3 (Ce:Zr; 2:1)	60	40
Catalysts	1.6 wt% Rh/CeO_x/Al_2O_3 (I)	47	53
	1.6 wt% Rh/CeO_x/Al_2O_3(II)	42	58
	1.6 wt%Rh/$CeO_x/ZrO_2/Al_2O_3$ (Ce:Zr 1:1)	65	35
	1.6 wt% Rh/$CeO_x/ZrO_2/Al_2O_3$ (Ce:Zr 2:1)	64	36
	4 wt% Rh/CeO_x/Al_2O_3 (I)	47	53
	4 wt% Rh/CeO_x/Al_2O_3 (II)	47	53
	4 wt% Rh/$CeO_x/ZrO_2/Al_2O_3$ (Ce:Zr 1:1)	71	29
	4 wt% Rh/$CeO_x/ZrO_2/Al_2O_3$ (Ce:Zr 2:1)	59	41

Table 3.6. Percent area of the individual contributions of Ce^{3+} and Ce^{4+} in the total Ce 3d region

3.3.4.3 Zr 3d core-level spectra

The Zr $3d_{5/2}$ spectra for the all Rh catalysts promoted by zirconia exhibit a spin-orbit doublet of 3d core level which split into $3d_{5/2}$ and $3d_{3/2}$ (Figure 3.16A, B). The Zr $3d_{5/2}$ peak is found to be centred at the binding energy range of 182.0-182.4 eV which corresponds to the literature value of 182.2 eV for ZrO_2 [26]. Moreover, the results obtained are in good agreement with pure $Zr(acac)_4$, taken as a reference for Zr^{4+}. An extensive broadening of Zr 3d spectra for zirconiated samples has been observed which might be due to strong interaction between zirconia and ceria, and/or with the rhodium particles. It may also be the result of static disorder in the poor crystallinity of the Zr components. The binding energies obtained for $Zr(acac)_4$,

zirconia supports and zirconiated Rh catalysts are presented in Table 3.7. The Ce and Rh presences do not change any electronic properties of Zr, which exists on the same oxidation state, +4, in all range of samples.

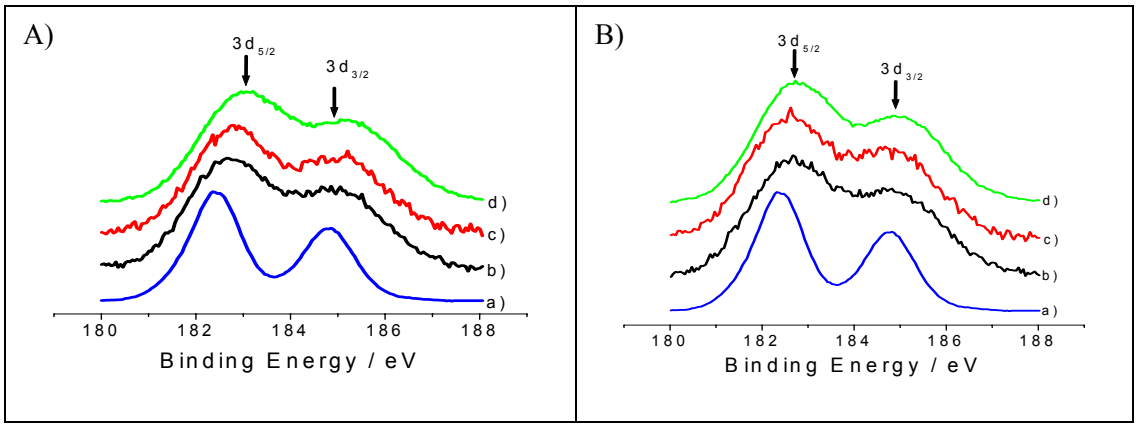

Figure 3.16. Zr 3d photoemission core level spectra for A) 1.6 wt% Rh catalysts B) 4 wt% Rh catalysts: a) ZrO_2, b) $Rh/CeO_x/ZrO_2/Al_2O_3$ (Ce:Zr;1:1), c) $Rh/CeO_x/ZrO_2/Al_2O_3$ (Ce:Zr;2:1), d) $Rh/ZrO_2/Al_2O_3$

Sample	Zr ($3d_{5/2}$) [eV]	Zr ($3d_{3/2}$) [eV]
$Zr(acac)_4$	182.2	184.6
5 wt% Zr/Al_2O_3	182.1	184.5
5 wt% $(Ce/Zr)/Al_2O_3$ (Ce:Zr; 1:1)	182.4	184.8
5 wt% $(Ce/Zr)/Al_2O_3$ (Ce:Zr; 2:1)	182.4	184.8
1.6 wt% $Rh/CeO_x/ZrO_2/Al_2O_3$ (Ce:Zr;1:1)	182.1	184.5
1.6 wt% $Rh/CeO_x/ZrO_2/Al_2O_3$ (Ce:Zr;2:1)	182.1	184.5
1.6 wt% $Rh/ZrO_2/Al_2O_3$	182.3	184.7
4 wt% $Rh/CeO_x/ZrO_2/Al_2O_3$ (Ce:Zr;1:1)	182.0	184.4
4 wt% $Rh/CeO_x/ZrO_2/Al_2O_3$ (Ce:Zr;2:1)	182.1	184.5
4 wt% $Rh/ZrO_2/Al_2O_3$	182.1	184.5

Table 3.7. Energy positions of the spectral components in Zr $3d_{5/2}$ and Zr $3d_{3/2}$ observed in rhodium catalysts

3.3.4.4 Cl 2p core-level spectra

Figures 3.17A and 3.17B exhibit the Cl 2p photoemission spectra for all the Rh catalysts along with the Cl 2p spectrum of $RhCl_3 \cdot 3H_2O$ as a reference. XPS

spectrum of the Cl 2p for $RhCl_3 \cdot 3H_2O$ exhibits two peaks derived from $2p_{3/2}$ and $2p_{1/2}$ core level regions centred at 198.9 and 200.6 eV. However, XPS spectra of the Cl 2p core level for all Rh catalysts show only one broad signal with no spin-orbit coupling observed. The Cl 2p peak is found to be centred at the binding energy range of 199.1 – 199.7 eV which correlates well with literature values for Cl ligands in the terminal bonding configuration [27]. This distortion can be attributed to the different particle distribution. Among all Rh samples studied, relatively the largest Cl content is observed for both ceriated Rh catalysts (method I), which can be due to the preparation method (induction of $RhCl_3 \cdot 3H_2O$ in the last step of the reaction).

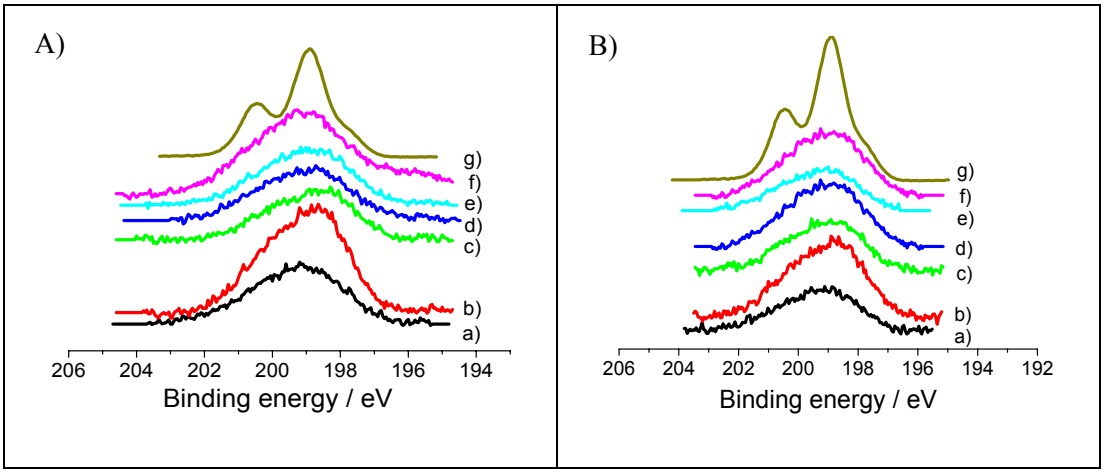

Figure 3.17 Cl 2p photoemission core level spectra for A) 1.6 wt% Rh catalysts B) 4 wt% Rh catalysts: a) Rh/Al_2O_3, b) $Rh/CeO_x/Al_2O_3$ (I), c) $Rh/CeO_x/Al_2O_3$ (II), d) $Rh/CeO_x/ZrO_2/Al_2O_3$ (Ce:Zr;1:1), e) $Rh/CeO_x/ZrO_2/Al_2O_3$ (Ce:Zr;1:1), f) $Rh/ZrO_2/Al_2O_3$, g) $RhCl_3 \cdot 3H_2O$.

Valuable information on the interaction between Rh metal and Ce,- and Zr promotors was obtained by XPS study. The XPS and XANES analysis of the Rh oxidation state reveal that Rh is mostly oxidised for Rh/Al_2O_3 and $Rh/CeO_x/Al_2O_3$ (I) catalysts, while Rh supported on Ce (method II), Zr or Ce-Zr mixed oxides remains in more reduced form. Moreover, the rhodium oxidation state is slightly dependent on the overall Rh loading; as the total Rh coverage increases the degree of oxidation falls, which is attributed to the Rh protection from oxidation by larger particles. It has been found that the Zr doping in Rh catalysts, being always in the system on +4 oxidation state, greatly enhanced the reducibility of CeO_x. This phenomenon can be attributed to the structural perturbation of CeO_2 lattice by the Zr incorporation, which enhances the oxygen mobility forcing the reaction: $CeO_2 \rightarrow CeO_{2-x} + 1/2O_{2\ (g)}$.

3.3.5 Scanning EXAFS measurement

EXAFS analyses of rhodium catalysts were carried out to characterise the local structure around the Rh atoms and to assess the effect of ceria and zirconia doping on the structural properties of the rhodium particles. Generally, Rh particles supported on alumina are easily oxidised after exposure to air [28-30]. Therefore, the Rh-Rh coordination numbers determined with EXAFS was additionally utilized to estimate the amount of metallic form in the system and the Rh-O occupations were used to assess the amount of Rh oxidised. XAFS data were collected at the Rh K edge on BM29 at ESRF and at station 9.3 of the SRS in Daresbury. A Si crystal (111) monochromator was used on BM29 and a Si crystal (220) at station 9.3. EXAFS were acquired in transmission mode. All samples in the form of powder were placed in the sample holder and have been measured at room temperature in air.

3.3.5.1 1.6 wt% Rh catalysts

Figure 3.18 shows k^3 weighted EXAFS spectra for 1.6 wt% Rh/Al_2O_3 along with the corresponding Fourier transforms. The experimental data can be well fitted using five shells, though the three most significant are the first Rh-O and Rh-Rh shell and a Rh-Cl contribution. As such, and consistent with the results of the EDX and XPS, the calcination/reduction procedure does not result in complete removal of Cl from this system and ca. 1 Cl per 2 Rh atoms was retained. Moreover, and again in agreement with both the XPS and XANES analyses, these fits shown that the 1.6 wt% Rh/Al_2O_3 sample after these procedures and subsequent RT exposure to air was essentially oxidised. The obtained results were expected and consistent with the previous EXAFS studies on similar systems [32, 33], in a form that retains a relatively short Rh-Rh (2.65 Å) interaction.

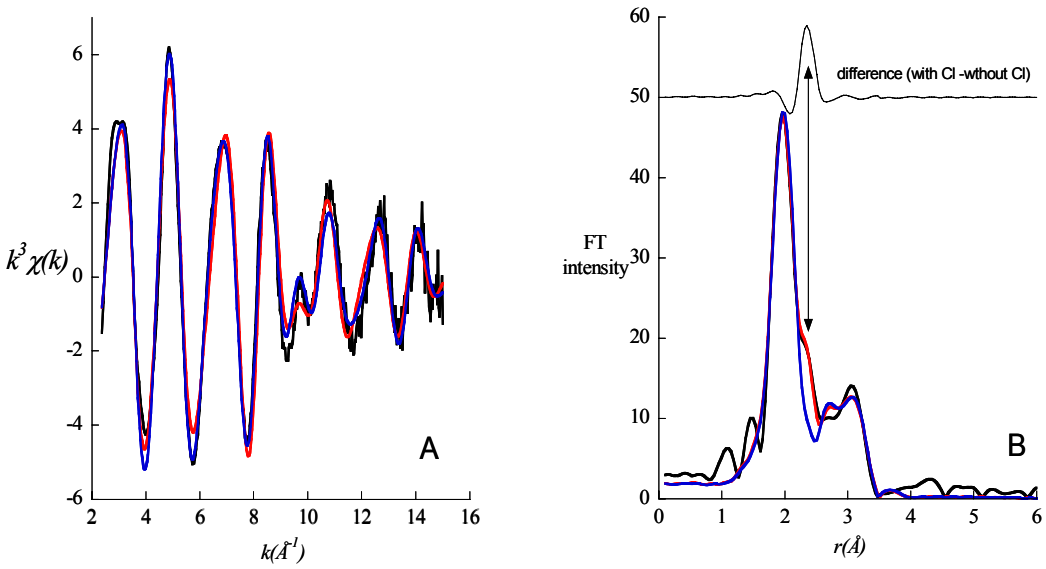

Figure 3.18. The rhodium K edge k^3-weighted EXAFS (A) and Fourier transform (B) for 1.6 wt% Rh/Al_2O_3. The experimental data is given by the black line. Two theoretical fits are shown: one with a Rh-Cl contribution (red) and one with no Rh-Cl component (blue). In panel (B) the difference between the FT's from each of these model is shown.

Rhodium oxide is known to exist in two stoichiometric forms (RhO_2 and Rh_2O_3).

RhO_2 has a tetragonal rutile structure, (Figure 3.19) [34]. In this structure each rhodium ion has six oxygen neighbours with the Rh-O distance of 1.96 Å.

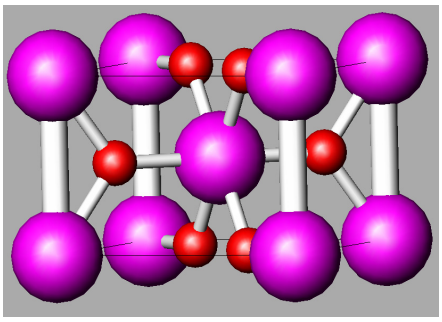

Figure 3.19. The unit of RhO_2.

Further, recent UHV surface science studies regarding the oxidation of low index Rh single crystals, Lundgren an co-workers [35, 36] have shown that the oxidation of the planar Rh surfaces results in a hexagonal, RhO_2 like trilayer surface region which is shown in Figure 3.20. The formation of this phase appears independent of the low index plane studies ((111), (100), 110)) and the formation of this structure self limits the level of oxidation obtainable under the conditions applied. The proposed model includes the metallic Rh core and the Rh oxidic shells,

where the oxygen atoms in the interface layer are located in top and bridge sites of the Rh surface.

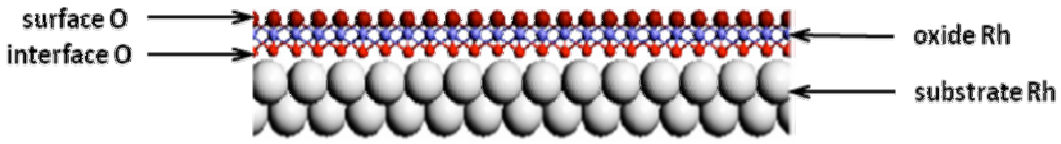

Figure 3.20. The model of a hexagonal RhO_2 surface oxide trilayer [36].

Rh_2O_3 has been found in the forms of three polymorphs (Figure 3.21):

- Rh_2O_3 I – a hexagonal form having the corundum structure with a=5.47 Å and a=55.70^o was identified first by Lunde [37]. Each rhodium ion has six oxygen neighbours, three at 2.03 Å and three at 2.07 Å. Within an oxygen octahedron the distance between oxygen ions in the same layer is either 2.62 Å or 3.14 Å.
- Rh_2O_3 II – an orthorhombic form with a=5.17 Å, b=5.38 Å, c=7.24 Å was found by Shannon [38]. This structure is related to that of corundum in that it contains pairs of RhO_6 octahedra which share faces. However, each octahedron shares only two edges with other octahedra. The average Rh-O distance is 2.04 Å and the Rh-Rh distance is 2.80 Å.
- Rh_2O_3 II – an orthorhombic form with lattice constants a=5.15 Å, b=5.44 Å, c=14.69 Å was first described by Wold *et al.* [39]. In this structure each rhodium ion is surrounded by six oxygen ions, forming a distorted octahedron. The Rh-O distances vary from 1.8 to 2.3 Å. Each oxygen ion is surrounded by four rhodium ions.

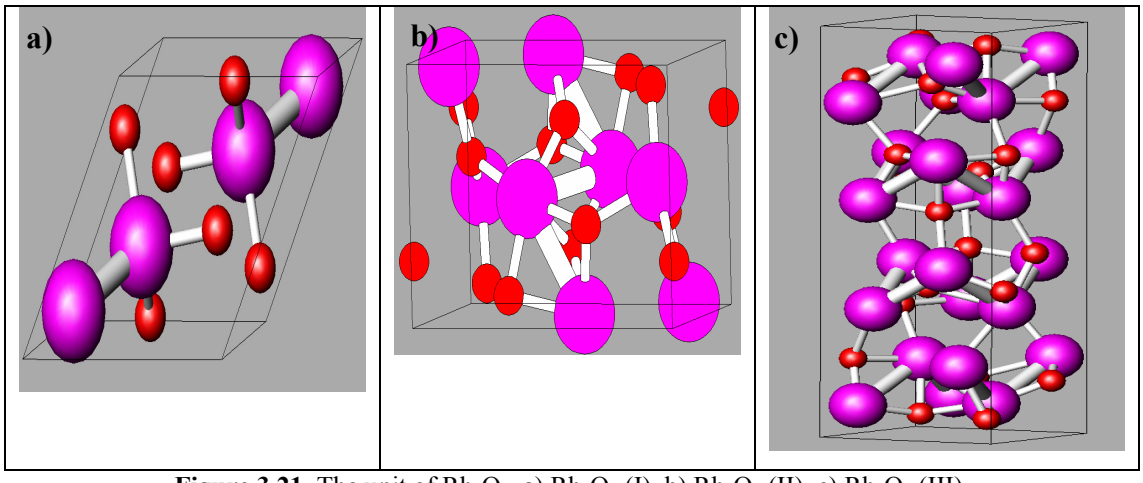

Figure 3.21. The unit of Rh_2O_3. a) Rh_2O_3 (I), b) Rh_2O_3 (II), c) Rh_2O_3 (III).

Figure 3.22 shows the Fourier transform for the 1.6 wt% Rh/Al_2O_3 along with those for a number of forms of known Rh oxide: RhO_2 [34], the hex-RhO_2 trilayer structure due to Lundgren *et. al* [36], Rh_2O_3 (I: hex, Lunde [37]), Rh_2O_3 (II: ortho, Shannon [38]), Rh_2O_3 (III: ortho, Wold [39]). Clearly, none of the "bulk" or extended forms of these various Rh oxides matches that obtained from the oxidised 1.6 wt% Rh/Al_2O_3 sample in an exact manner. The first shell Rh-O feature matches best that obtained from the known hexagonal and/or RhO_2 phase. However, the first two Rh-Rh shells match best with the known orthorhombic shell progressions, particularly the low temperature, low pressure phase identified by Wold *et al.* [39].

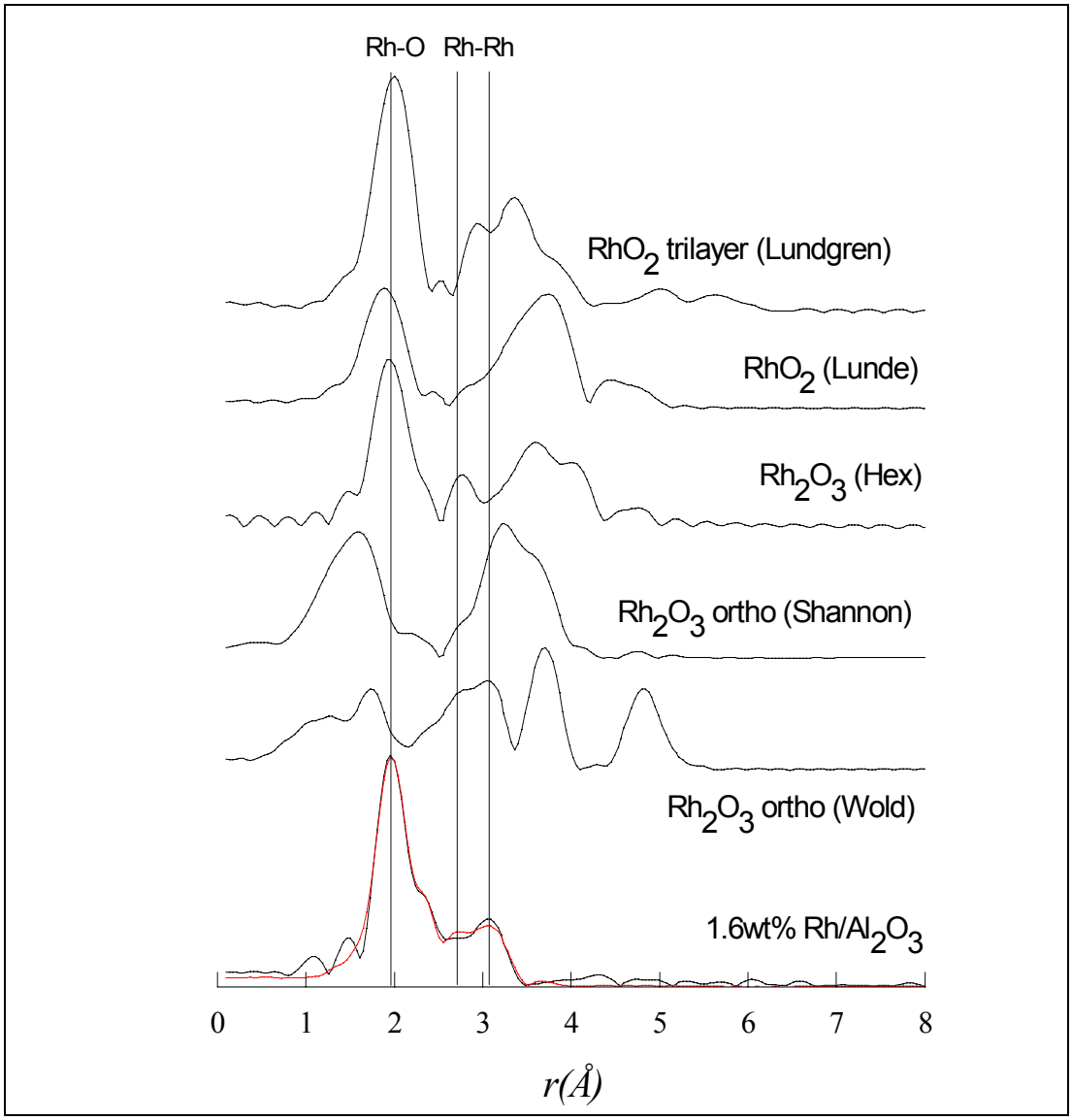

Figure 3.22. Fourier transform for 1.6 wt% Rh/Al_2O_3 together with the fit derived from analysis in EXCURV98 (Figure 3.18). FT spectra (for presentation purposes scaled down by a factor of 2.5) from five possible Rh oxides – as indicated – are shown sequentially above. The solid vertical lines highlight the correspondence between the experimental data and the known "bulk" oxides for first shell Rh-O, and first and second shell Rh-Rh contributions.

As such, in the case of highly dispersed Rh/Al_2O_3 and particularly in the case where it is evident that a substantial level of Cl is present, the detailed structure of the nano-oxide phase resulting from the catalysts preparation is not easily resolved in terms of known Rh oxide structures. On the basis of the implied level of Cl retention, and the best match between the Rh-Rh shells, it was speculated that this nanostructure has an approximate Rh_2O_2Cl stochiometry and possible orthorhombic type structure.

The 1.6 wt% Rh/Al_2O_3 case may be contrasted, within the samples studied, with the EXAFS result derived from the 1.6 wt% $Rh/ZrO_2/Al_2O_3$ case shown in Figure 3.23. Clearly, when synthesised on a support containing 5 wt% Zr on γ-alumina, the resulting Rh EXAFS is dominated by metallic Rh-Rh interactions that extend to shells beyond the first. This is indicative of a much more reduced Rh state and the presence of sizeable Rh nanoparticles in this case. Qualitatively this is again consistent with the XPS and the XANES analysis, both of which indicate that in this case ca. 50 % of the Rh is metallic (set against ca. 14 % in the 1.6 wt% Rh/Al_2O_3 case). The obtained results shown nicely the considerable effect the nature of the support can have on the size and phase of the Rh supported upon it under a given set of conditions.

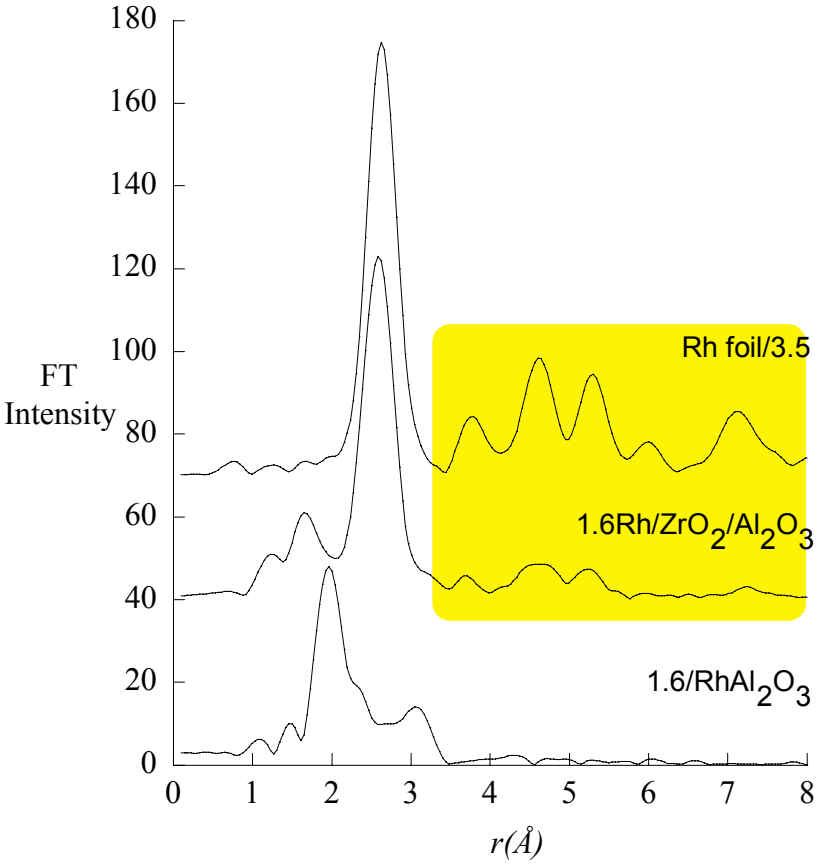

Figure 3.23. Fourier transforms of Rh K edge EXAFS derived from 1.6 wt% Rh/Al_2O_3 and 1.6 wt% $Rh/ZrO_2/Al_2O_3$ samples as indicated. The FT derived from a Rh foil (scaled by a factor of 3.5 for the presentation reason) is also shown. The coloured are highlights the radial position of higher Rh-Rh shells within the FT.

Figure 3.24 and Table 3.8 summarises the results of the EXAFS analyses made for the range of 1.6 wt% Rh systems supported on alumina doped with ceria and/or zirconia using EXCURV98 [31]. These data show that the addition of promoter materials such as Ce and Zr can have a profound effect on the state of the Rh component that exists in the catalyst after the various synthesis used. Only in the case of Rh deposition to a Ce modified Al_2O_3 support made via method I that the state of the Rh post synthesis can be seen to be very similar to that obtained in the absence of the Ce modifier. The Rh is essentially oxidised and a highly significant Rh-Cl shell is observed in both of these cases. However, even here there seem to be subtle differences between the Ce free and Ce modified Rh phases. In the latter sample case, a Rh-Rh interaction – expected from the orthorhombic phase of Rh_2O_3 – at 2.65 Å appears to be completely absent from FT, whereas it does appear in the 1.6 wt% Rh/Al_2O_3 case. All of the other samples made in this study – using method II and adding Ce and Zr, or even just Zr – show considerably different EXAFS. All

of these now show clear Rh-Rh interactions at ca. 2.67 Å that could be due to metallic Rh-Rh bonding. More definitively, the FT's show clear evidence, to varying degrees, of higher shell structure (via a vis Figure 3.23) that shows a bondlength progression e.g., 3.77, 4.65 and 5.25 Å indicating the presence of the Rh metal nanoparticles in these systems.

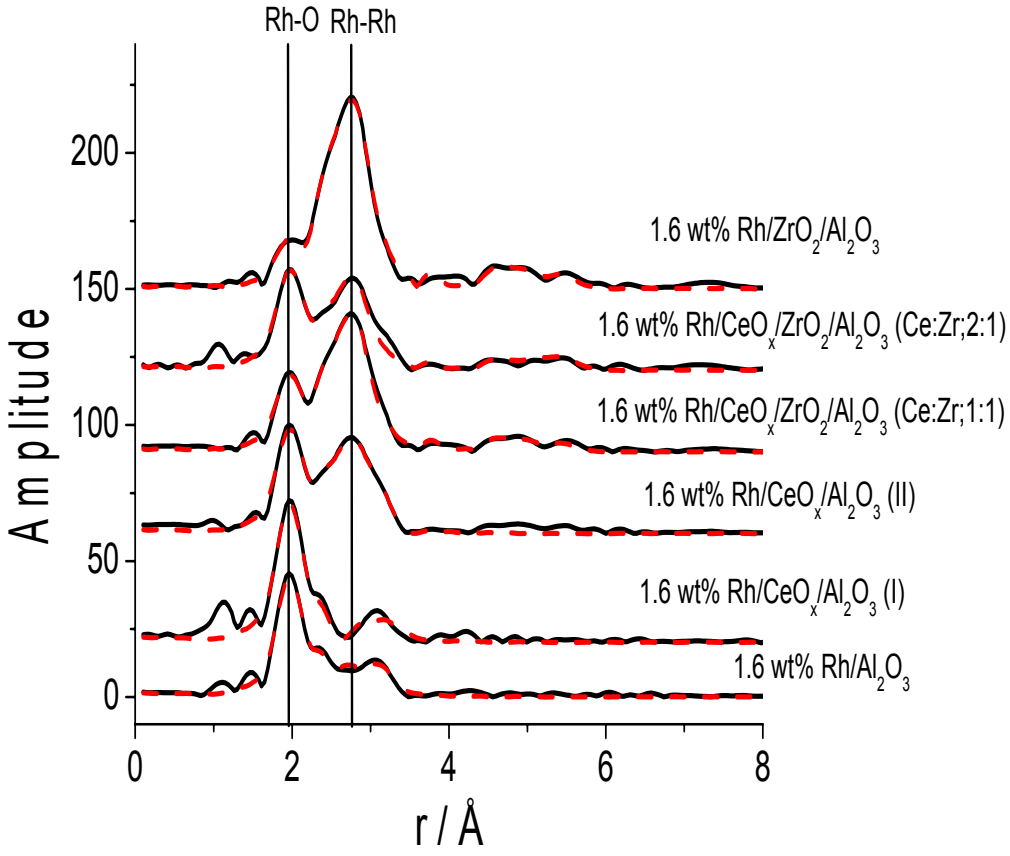

Figure 3.24. Fourier transforms of Rh K edge EXAFS derived from the range of 1.6 wt% Rh catalysts synthesised in this study after the calcinations and reduction procedures outlined in Chapter 3, at RT exposure to air. Fits to the data, derived from analysis in EXCURV are shown in red.

Sample	Scatterer	CN	R / Å	DW / $2\sigma^2$	R / %	EF / eV
1.6 wt%	O	3.6 (2)	2.02 (1)	0.01	41	0.6
Rh/Al_2O_3	Rh	0.9 (1)	2.65 (1)	0.014	31	
	Cl	0.5 (1)	2.31 (1)	0.007	28	
	Rh	0.7 (1)	3.05 (1)	0.012	22	
1.6 wt% Rh	O	4.2 (2)	2.03 (3)	0.01	41	0.4
Ce/Al_2O_3 (I)	Rh	0.9 (2)	3.03 (1)	0.014	38	
	Cl	0.5 (1)	2.33 (1)	0.007	32	
1.6 wt% Rh	O	3.0 (2)	2.02 (3)	0.01	68	1
Ce/Al_2O_3 (II)	Rh	2.5 (1)	2..67 (2)	0.014	27	
	Cl	0.2 (1)	2.28 (2)	0.007	25	
	Rh	0.7 (1)	3.06 (1)	0.012	21	
1.6 wt% Rh	O	2.2 (1)	2.02 (1)	0.01	84	2
$CeO_x/ZrO_x/Al_2O_3$	Rh	3.7 (1)	2.67 (1)	0.014	20	
(Ce:Zr;1:1)	Cl	0.2 (1)	2.30 (1)	0.007	18	
	Rh	0.4 (1)	3.77 (1)	0.012	17	
	Rh	1.5 (2)	4.66 (1)	0.012	15	
	Rh	1.5 (4)	5.21 (1)	0.012	14	
1.6 wt% Rh	O	2.9 (2)	2.02 (1)	0.01	70	0.8
$CeO_x/ZrO_x/Al_2O_3$	Rh	2.5 (1)	2.67 (1)	0.014	31	
(Ce:Zr;2:1)	Cl	0.2 (1)	2.28 (3)	0.007	30	
	Rh	0.3 (1)	3.75 (3)	0.012	29	
	Rh	1.1 (5)	4.63 (2)	0.012	28	
	Rh	2.2 (4)	5.29 (2)	0.012	27	
1.6 wt% Rh	O	1.4 (1)	2.02 (1)	0.01	94	0.3
ZrO_2/Al_2O_3	Rh	5.2 (1)	2.67 (1)	0.014	22	
	Cl	0.3 (1)	2.33 (1)	0.007	19	
	Rh	0.5 (2)	3.77 (1)	0.012	18	
	Rh	2.3 (3)	4.65 (1)	0.012	15	
	Rh	2.4 (4)	5.27 (1)	0.012	13	

Table 3.8. Structural and statistical data derived from the analysis of Rh K edge EXAFS derived from a range of 1.6 wt% Rh samples (Figure 3.24) after calcination, reduction, and after subsequent exposure to air at RT. Data range used was 2.5-15 k. R factor are given for the stepwise addition of shells such that their significance may be more easily assessed.

The persistence, along these shells of significant Rh-O bonding in all these cases, would indicate that the Rh particles are comprised of metallic core surrounded by thin oxide layers. These observations are consistent with both the XANES and the XPS result reported above. They also have implications for the interpretation of the

TEM PSD's for all of these systems as to compare each of these cases correctly. As the TEM obtained does not have the resolution to actually determine the phase of the Rh present in each case, the measured PSD is a convolution of the relative amounts of oxide and metal in each system. As these phases have significantly different volumes, and accurate assessment of the real atomicity of the Rh particles formed in each of these cases requires that this be taken into account – as has been recognised and carried out previously [16]. Nonetheless, a pattern of Rh behaviour can be defined and would indicate that the addition of CeZr, or simply Ce via method II, effectively reduces the susceptibility of the Rh phase produced to oxidation. One might hypothesise that method II yields in this effect largely as a result of forming the promoter oxides after Rh nanoparticles have themselves been synthesised on the Al_2O_3 support. As such this method may result in the partial covering of the reduced Rh nanoparticles by the promoter oxide phase, and as a result reduced susceptibility to subsequent oxidation.

3.3.5.2 4 wt% Rh catalysts

Figure 3.25 and Table 3.9 summarises the results of the EXAFS analyses made for the series of 4 wt% Rh catalysts supported on γ-Al_2O_3 and doped with ceria and/or zirconia. Generally, the experimental data of each Rh system fits Fourier transform well to the model, which contains the three most significant shells: the first Rh – O shell (r = 2.02 Å), Rh – Cl shell (r ~ 2.35 Å) and Rh – Rh shell (r = 2.68 Å). The presence of the further Rh – Rh shells can be also detected for undoped Rh/Al_2O_3 and all Ce and/or Zr promoted Rh catalysts (method II) indicating the predominant of metallic Rh-Rh interactions. The RhCl contribution is the most evident for Rh/Al_2O_3 and Rh/CeO_x/Al_2O_3 (method I) as was the case of 1.6 wt% Rh catalysts.

Clearly, it can be observed that the preparation method of promoted Rh catalysts has a substantial effect of the existing phase of the Rh particles supported on γ-Al_2O_3. The presented example on ceriated Rh catalysts shows a good comparison, within the Rh particles are predominantly oxidised for Rh/CeO_x/Al_2O_3 (method I), wherein Rh was deposited to ceria modified Al_2O_3 support. However, much more metallic Rh state was reported for ceriated Rh catalysts (method II), in which the Ce deposition was placed on the pre-supported Rh particles on Al_2O_3. Moreover, the Rh systems doped by zirconia and ceria/zirconia, prepared by method

II, highlight the largest RhRh contributions among all the Rh samples being under investigation indicating the presence of the major contribution of the reduced Rh component and sizeable Rh nanoparticles in these cases. Due to the complexity of supported Rh particles on alumina as such the presence of the metallic Rh core and the oxidic Rh component (Rh oxides and oxidised Rh layer) the accurate structure of the investigated Rh systems cannot be distinguished based on these results. Nevertheless, it can be said that the interaction between metal particles and the reductive oxides of the Rh catalysts derived from method II provides some protection to the rhodium oxidation.

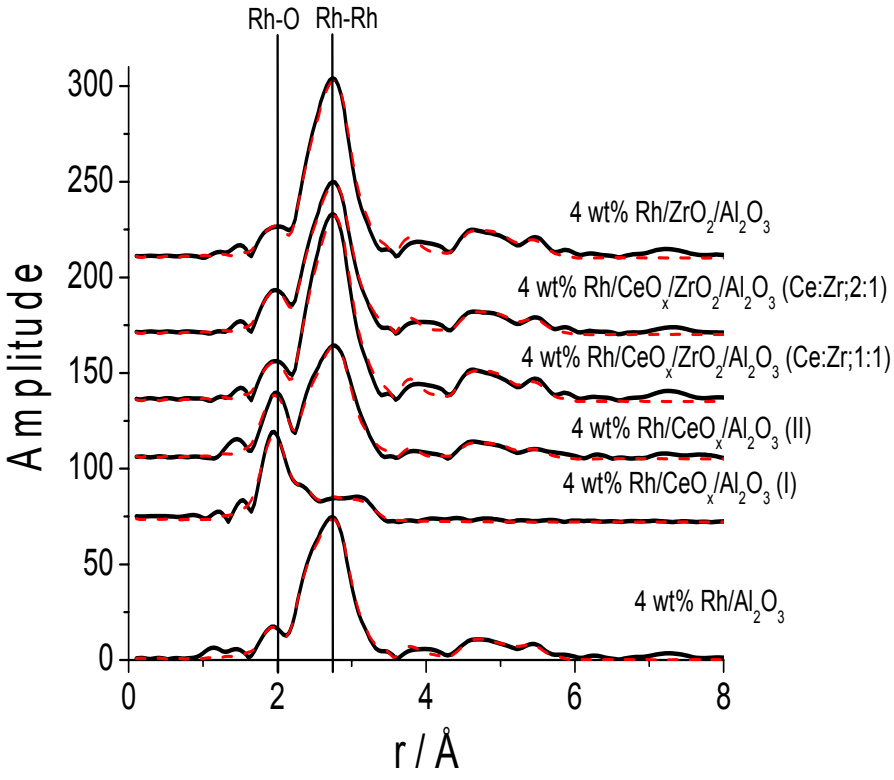

Figure 3.25. Fourier transforms of Rh K edge EXAFS derived from the series of 4 wt% Rh catalysts synthesised in this study after the calcinations and reduction procedures, exposure to air at RT. Fits to the data, derived from analysis in EXCURV are shown in red.

Sample	Scatterer	CN	R / Å	DW / $2\sigma^2$	R / %	EF / eV
4 wt% Rh/Al_2O_3	O	1.4 (1)	2.02 (1)	0.01	94	1.5
	Rh	5.4 (2)	2.68 (2)	0.014	27	
	Cl	0.8 (1)	2.34 (1)	0.012	21	
	Rh	0.9 (2)	3.78 (1)	0.012	19	
	Rh	0.4 (1)	4.66 (2)	0.012	16	
	Rh	3.2 (4)	5.28 (2)	0.012	12	
4 wt% Rh	O	3.6 (2)	2.02 (1)	0.01	44	1.4
Ce/Al_2O_3 (I)	Rh	1 (1)	2.66 (2)	0.014	33	
	Cl	0.7 (1)	2.33 (1)	0.009	27	
	Rh	0.7 (1)	3.06 (2)	0.012	21	
4 wt% Rh	O	2.6 (2)	2.02 (1)	0.01	83	1.2
Ce/Al_2O_3 (II)	Rh	4.4 (3)	2.68 (1)	0.014	26	
	Cl	0.1 (1)	2.34 (2)	0.009	26	
	Rh	0.1 (1)	3.79 (3)	0.012	25	
	Rh	0.6 (2)	4.67 (3)	0.012	22	
	Rh	2.4 (2)	5.28 (2)	0.012	20	
4 wt% Rh	O	1.6 (1)	2.02 (1)	0.01	96	1.5
$CeO_x/ZrO_x/Al_2O_3$	Rh	7.2 (2)	2.68 (2)	0.014	25	
(Ce:Zr;1:1)	Cl	0.4 (1)	2.38 (2)	0.009	24	
	Rh	1.4 (1)	3.78 (3)	0.012	24	
	Rh	4.6 (3)	4.66 (1)	0.012	19	
	Rh	4.5 (4)	5.28 (2)	0.012	15	
4 wt% Rh	O	1.8 (2)	2.02 (2)	0.01	94	0.9
$CeO_x/ZrO_x/Al_2O_3$	Rh	5.9 (2)	2.68 (1)	0.014	23	
(Ce:Zr;2:1)	Cl	0.2 (1)	2.37 (2)	0.009	22	
	Rh	1 (2)	3.78 (2)	0.012	21	
	Rh	3.4 (3)	4.67 (3)	0.012	16	
	Rh	3.6 (3)	5.28 (3)	0.012	13	
4 wt% Rh	O	1.3 (1)	2.02 (1)	0.01	97	1.6
ZrO_x/Al_2O_3	Rh	6.9 (2)	2.68 (2)	0.014	25	
	Cl	0.4 (1)	2.38 (2)	0.009	23	
	Rh	1.2 (1)	3.78 (3)	0.012	22	
	Rh	4.1 (2)	4.66 (3)	0.012	18	
	Rh	4.4 (2)	5.27 (2)	0.012	14	

Table 3.19. Structural and statistical data derived from the analysis of Rh K edge EXAFS derived from a series of 4 wt% Rh samples (Figure 3.25) after calcination, reduction, and after subsequent exposure to air at RT. Data range used was 2.5-16 k. R factor are given for the stepwise addition of shells such that their significance may be more easily assessed.

The EXAFS analysis confirms that supported Rh particles, after exposure to air at room temperature, contains the mixture of the Rh oxide, the oxidic Rh surface as well as the metallic Rh form. However, the Ce and Zr doping provides the Rh catalysts with significant part of metallic core. The obtained parameters are in good agreement with TEM and XPS results. Larger Rh particles of ceriated and zirconiated Rh catalysts contains extensive fraction of metallic form.

3.4 Discussion

The TEM results indicate particle sizes with a distribution of 0.7 to 4 nm for the whole range of the investigated samples. As it is established from the XPS, the particle size determined is attributed to the metallic and oxidic fraction of the Rh particles. The XANES analysis of the Rh K-edge data for the fresh samples resulted in similar level of Rh oxidation as determined by the Rh XPS analysis, confirming the validity of the two techniques.

Rh XPS, XANES, EXAFS results on the fresh samples indicate that the supported rhodium particles of Rh/Al_2O_3 and $Rh/CeO_x/Al_2O_3$ (I) are oxidic rather than metallic. Furthermore, Rh particles, deriving from ceriated Rh catalyst (method I), are even more oxidised (~90% of oxidation) than the particles of undoped rhodium on alumina (~80% of oxidation). The addition of the promoters such as ceria and zirconia introduced to the system by method II (Ce, Zr deposition on pre-supported Rh on Al_2O_3) protects Rh particles against extensive oxidation, forming an equivalent proportion of metallic and oxidic form of Rh particles. In general, the whole series of FT simulations done for the particular Rh oxides and the Rh surface oxide has shown that the oxidised Rh nanoparticles supported on alumina represents a complex structure and it is very difficult to solve the exact structure based on one model only.

The oxidation state fitting parameters taken from Rh XPS and XANES analysis show that the samples with larger Rh loading do not visibly form larger Rh metallic fraction, as it would be expected [41]. However, this could be explained by the TEM results, that indicate only slightly broader particle size distribution for 4 wt% Rh systems (0.7-4 nm), when compared to 1.6 wt% Rh samples (0.7-3 nm). On the other hand, the detailed EXAFS analysis indicates larger Rh-Rh occupation of the first and further RhRh shells in the case of 4 wt% Rh catalysts when compared to

1.6 wt% Rh sample. Nonetheless, the larger Rh-Rh coordination can indicate bigger particle size as well as may give information over the particle shape.

Moreover, TEM only detects particles with a minimum diameter of 5 Å, whereas EXAFS determined an average of all particle sizes (including atomic Rh). Assuming spherical particles are formed on the γ-Al_2O_3 support; TEM will only detect particles in the regime of ca. 13 atoms or greater i.e. with an EXAFS coordination number of 5 and higher. Nonetheless, the studied Rh catalysts exhibit a larger average PSD than the resolution limit to exert an attenuated influence on the results.

By the EXAFS analysis, the Rh particles are simulated well using spherical fcc structure, indicating this to be a good approximation for the particle shape present in these systems.

EDX and XPS results show that Cl is retained in the Rh systems after the initial calcination and reduction processes in the fresh Rh samples. Moreover, the detailed EXAFS analysis clearly show strong contribution of Rh – Cl shell for Rh catalysts, however, the presence of Rh – Cl bond is the most evident for Rh/Al_2O_3 and $Rh/CeO_x/Al_2O_3$ (method I).

Since the investigated Rh system is very complex, considering that Rh particles under ambient conditions are easily oxidised forming various oxides or oxidising the Rh surface as well as keeping some Rh fraction metallic, it is unattainable to establish the structure of the investigated systems. Moreover, the caution needs to be applying when analysis EXAFS data as this is an averaging technique where similar materials can possess different structures but still give rise to the same average local structure.

3.5 Conclusion

This chapter was dedicated to the investigation of the structural parameters of Rh catalysts supported on alumina, ceria-alumina, ceria-zirconia-alumina and zirconia-alumina highlighting the effect of the reducing additives on the Rh particles. A wide range of the rhodium catalysts have been successfully prepared and analysed by BET, TEM, EDX, XPS and XAFS. The quantitative EDX and XPS analysis of the elements in the catalytic system is consistent with the theoretical parameters suggesting that the Ce and Zr additives are deposited on Rh particles. The TEM results indicate particle size with a distribution of 1.5 to 3 nm for the whole series of Rh samples.

Rh EXAFS, XANES, XPS results on the fresh samples suggest that the supported rhodium particles on alumina are easily oxidised, however the Zr- and Ce-doping prevent such facile oxidation of Rh particles. On the other hand, the method of preparation plays a crucial role in the efficiency of the oxides additives. The ceria promoted Rh catalysts produced by method II shows a lower degree of rhodium oxidation which may be due to strong Rh – Ce interaction. The extended time of reduction over Rh catalysts within method II which might provide larger, metallic Rh fraction cannot be excluded. Due to the fact that method II provided the Rh catalysts with more desired properties for our application, the whole series of Rh catalysts doped by Ce and/or Zr has been synthesised following only method II. Additionally EDX profile analysis confirms that Rh and Ce sites are in close proximity to each other, which explains the present of Rh-Ce redox couple.

As it has been already investigated, Ce^{3+} as oxygen storage plays a crucial role in enhancing the catalytic activity in reducing conditions [42]. Therefore, the reducing Zr effect on Ce and Rh particles suggests the promising results for the catalytic activity experiments which will be described in the following chapters.

Nonetheless, since Rh particles undergo facile oxidation even after brief exposure to air at room temperature, the caution needs to be applied when comparing the results of different *ex situ* and *in situ* characterisation techniques.

3.6 References

1. Coung, P.H., Marin, S., Ledoux, M. J., Appl. Catal., B, 1994. **4**: p. 45-63.
2. Rogemond, E., Frety, R. Perrichon, V., Primet, M., Salasc, S., Chevrier, M., Gauthier, C., Mathis, F., J. Catal., 1997. **169**: p. 120-131.
3. Alini, S., Bottino, A., Capannelli, G., Comite, A., Paganelli, S., Appl. Catal., A, 2005. **292**: p. 105-112.
4. Jansen, W.P.A., Harmsen, J. M. A., Denier v. d. Gon, A. W., Hoebink, J. H. B. J., Schouten, J. C., Brongersma, H. H., J. Catal., 2001. **204**: p. 420-427.
5. Men, Y., Gnaser, H., Zapf, R., Hessel, V., Ziegler, C., Kolb, G., Appl. Catal., A, 2004. **277**: p. 83-90.
6. Suhonen, S., Valden, M., Hietikko, M., Laitinen, R., Savimaki, A., Harkonen, M., Appl. Catal., A, 2001. **218**: p. 151-160.
7. Hosokawa, S., Taniguchi, M., Utani, K., Kanai, H, Imamura, S., Appl. Catal., A, 2005. **289**: p. 115-120.
8. Jyoti, B., *PhD Thesis*, in *Chemistry*. 2006, University of Southampton: Southampton.
9. Agnelli, M., Louessard, P., El Mansour, A., Candy, J. P., Bournonville, J. P., Basset, J. M., Catal. Today, 1989. **6**: p. 63-72.
10. Humblot, F., Didillon, D., Lepeltier, F., Candy, J. P., Corker, J., Clause, O., Bayard, F., Basset, J. M., J. Am. Chem. Soc., 1998. **120**: p. 137-146.
11. Tomishige, K., Asakura, K., Iwasawa, Y., J. Catal., 1994. **149**: p. 70-80.
12. Crabb, E.M., Marshall, R., Thompsett, D., J. Electron. Soc., 2000. **147**: p. 4440-4447.
13. Crabb, E.M., Ravikumar, M. K., Thompsett, D., Hurford, M., Rose, A., Russell, A. E., Phys. Chem. Chem. Phys., 2004. **6**: p. 1792-1798.
14. McCabe, R.W., Usmen, R. K., Ober, K., Gandhi, H. S., J. Catal., 1995. **151**: p. 385-393.
15. Scofield, J.H., J. Electron. Spectrosc. Relat. Phenom., 1976. **8**: p. 129-137.
16. Newton, M.A., Dent, J. A., Diaz-Moreno, S., Fiddy, S. G., Jyoti, B., J., Evans, J., Chem. Eur. J., 2006. **12**: p. 1975-1985.
17. Polvinen, R., Vippola, M., Valden, M., Lepisto, T., Suopanki, A., Harkonen, M., Surf. Interface Anal., 2004. **36**: p. 741-744.
18. Kondarides, D.I., Verykios, X. E. , J. Catal. , 1998. **174**: p. 52-64.

19. Suhonen, S., Polvinen, R., Valden, M., Kallinen, K., Harkonen, M., App. Surf. Sci., 2002. **200**: p. 48-54.
20. Wang, R., Xu, H., Li, X., Ge, Q., Li, W., Appl. Catal., A, 2006. **305**: p. 204-210.
21. Talo, A., Lahtinen, J., Hautojarvi, P. , Appl. Catal., B, 1995. **5**: p. 221-231.
22. Larachi, F., Pierre, J., Adnot, A., Bernis, A., Appl. Surf. Sci., 2002. **195**: p. 236-250.
23. Mekki, A., J. Electron. Spectrosc. Relat. Phenom., 2005. **142**: p. 75-81.
24. Wu, X., Xu, L., Weng, D., App. Surf. Sci., 2004. **221**: p. 375-383.
25. Yang, Z., Woo, T. K., Hermansson, K., J. Chem. Phys., 2006. **124**: p. 224704-224711.
26. Moulder, J.F., Strickle, W. F., Sobol, P. E., Bomben, K. D., *Handbook of X-ray Photoelectron Spectroscopy*. 1992, Minnesota: Perkin-Elmer.
27. Nefedov, V.I., J. Electron. Spectrosc. Relat. Phenom., 1977. **12**: p. 459-467.
28. Wang, Y., Song, Z., Ma, D., Luo, H. Y., Liang, D. B., Bao, X. H., J. Mol. Catal., 1999. **149**: p. 51-61.
29. Zhou, S., Zhao, H., Ma, D., Miao, S., Cheng, M., Bao, X., Z. Phys. Chem., 2005. **219**: p. 949-961.
30. Koningsberger, D.C., van Zon, J. B. A. D., van't Blik, H. F. J., Visser, G. J., Prins, R., Mansour, A. N., Sayers, D. E., Short, D. R., Katzer, J. R., J. Phys. Chem., 1985. **89**: p. 4075-4081.
31. Binsted, N., *EXCURV(9.301)*, in *CCLRC Daresbury Laboratory Computer program*. 1998.
32. Martens, J.H.A., Prins, R., Zandbergen, H., Koningsberger, D. C., J. Phys. Chem., 1988. **92**: p. 1903-1916.
33. Martens, J.H.A., Prins, R., Koningsberger, D. C., J. Phys. Chem., 1989. **93**: p. 3179-3185.
34. Shannon, R.D., Solid State Comm., 1968. **6**: p. 139-143.
35. Gustafson, J., Mikkelsen, A., Borg, M., Lundgren, E., Kohler, L., Kresse, G., Schmid, M., Varga, P., Yuhara, J., Torrelles, X., Quiros, C., Andersen, J. N., Phys. Rev. Lett., 2004. **92**: p. 126102,1-4.
36. Gustafson, J., Mikkelsen, A., Borg, M., Andersen, J. N., Lundgren, E., Klein, C., Hofer, W., Schmid, M., Varga, P., Kohler, L., Kresse, G., Kasper, N., Stierle, A., Dosch, H., Phys. Rev. Lett., 2005. **71**: p. 115442,1-9.

37. Lunde, G., Z. Anorg. Allg. Chem., 1927. **163**: p. 345-350.
38. Shannon, R.D., Prewitt, T., J. Solid. State Chem., 1970. **2**: p. 134-136.
39. Wold, A., Arnott, R. J., Croft, W. J., Inorg. Chem., 1963. **2**: p. 972-974.
40. Coey, J.M.D., Acta Crystall. B., 1970. **26**: p. 1876-1877.
41. Jentys, A., Phys. Chem. Chem. Phys., 1999. **1**: p. 4059-4065.
42. Fornasiero, P., Di Monte, R., Ranga Rao, G., Kaspar, J., Meriani, S., Trovarelli, A., Graziani, M., J. Catal., 1995. **151**: p. 168-177.

Chapter 4

4. The structure-function response of Rh systems to CO

4.1 Introduction

The interaction of CO with Rh-containing catalysts has been intensively studied in the last decades [1-7]. This interest stems largely from the use of Rh in three way automotive exhaust catalysts (TWC). Rh is included in the formulation of such catalysts due to its superior ability to catalyse the reduction of NO in reducing atmospheres where CO is present along with other reductants such as hydrocarbons. However, in a more fundamental and wide ranging sense, Rh can display wide ranging carbonyl and nitrosyl co-ordination chemistry [4, 8]. Indeed, this aspect of the behaviour of Rh is also exploited practically in solution and vapour phase carbonylation chemistry [9].

As such, how this "organometallic" aspect of the Rh behaviour might transfer and complete with "extended metal surface" type behaviour within, for instance, the TWC paradigm, is an intriguing and largely unanswered question.

Further to the metal components of modern TWC's, a complex mixture of precious-metal particles (Rh, Pt, Pd), various oxide materials are included in the catalysts formulation. Amongst these, cerium oxide has emerged as a highly important promoter material [10, 11]. The addition of ceria (CeO_2) to the (Al_2O_3 based) supports greatly enhances catalysts performance, in part due to its ability to store and release oxygen. Moreover, recently, ceria has been re-placed by ceria-zirconia mixed oxide, which has even better oxygen storage properties as well as improved thermal stability [12-14].

In the infrared region of the electromagnetic spectrum, the stretching mode of CO, a molecule that has an intrinsically large dipole moment, has a high extinction coefficient. As such, whether free in the gas phase or adsorbed on a surface, it is a molecule that is easy to detect using infra red spectroscopy. Furthermore, when CO is chemisorbed on metal (such as Rh) particle or surface it is a sensitive probe of the character of supported Rh catalysts. As established in the pioneering work of Yang and Garland [7], the three typical forms of CO chemisorbed on Rh are (a) the geminal dicarbonyl species (represented by the symmetrical and anti symmetrical IR modes), (b) the linearly bonded form, and (c) the bridged form as indicated in Figure 4.1.

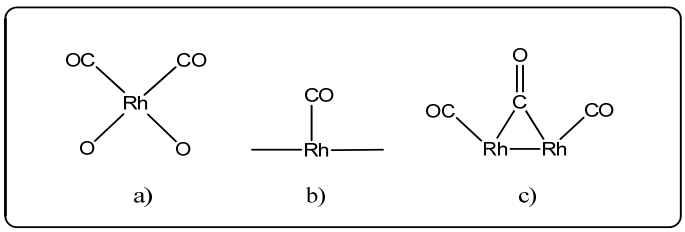

Figure 4.1 Structure of CO species formed on the Rh surface: (a) geminal dicarbonyl species, (b) linear and (c) bridged forms.

It has also been demonstrated that, under certain conditions, a number of other minor species are formed, i. e. upon oxidation the new band appeared at 2127 cm^{-1} which was assigned to the RhO(CO) species [15, 16] .

With regard to the much studied $Rh(CO)_2$ species, it has been suggested that an irregular and well-dispersed Rh particle would favour its formation, while more regular and bulk-like Rh would favour the linear and bridged CO forms [17]. For instance, according to Hyde *et al*. [18] dicarbonyl species are formed on monoatomically, as isolated surface organometallic species, or at edge sites in rafts. Infra red spectroscopy on it own, however, is not able to decide definitively, whether one or other of these cases (or indeed both) is the correct answer. Linear and bridged species are suggested to be formed on metallic Rh sites in larger crystallites (Rh^0_x) [17, 19] and the veracity of this notion has been demonstrated by numerous IR studies performed on both powder catalysts and extended, low index, Rh surfaces.

The role that the geminal dicarbonyl species might play in a number of catalytic processes occurring over supported Rh catalysts is at best partially understood. Whilst, within CO oxidation using O_2 over supported Rh systems, a number of infrared studies have shown that it appears to be a spectator to the catalytic events themselves, however, it contains an atom of the supposedly active element within it. As such, one might hypothesise that this species should have an indirect role to play in determining the overall course of the oxidation of CO by O_2: if all of the Rh is tied up as "spectating" $Rh(CO)_2$ species, then there will not be any Rh left to provide the catalytic events that make them spectators in the first place. Indeed, this notion appears to be borne out by *in situ* dispersive EXAFS measurements that correlate increasing light off temperatures with increasing levels of $Rh(CO)_2$ formation in 5 wt% Rh/Al_2O_3 catalysts under progressively CO rich CO/O_2 feedstock [20].

More fundamentally, there are numerous questions that surround how this species might be formed and how we might parameterise its formation. A number of studies have investigated the inhibition of its formation by removing hydroxyl groups via thermal and chemical dehydroxylation methods [21-23]. However, set against these, for example, this is time resolved study of the formation of this species using dispersive EXAFS [5]. This study resulted in a model of the formation $Rh(CO)_2$ species (as an isolated surface organometallic species) from small Rh clusters that does not need to invoke the participation of any surface OH group. Moreover, studies on model Rh/TiO_2 (110) catalysts, wherein the surface OH concentration should be very small, have also shown that $Rh(CO)_2$ formation from metallic Rh clusters is also possible [24].

Other parameters that have shown to have a considerable bearing on the extent to which this species may be formed from Rh nanopartciles are (1) the average size of the Rh particles and (2) the presence or not, of Cl in the catalysts. Joyner and Johnston [25] provided convincing evidence that Cl promotes the formation of the $Rh(CO)_2$ species when compared to the cases wherein Cl in not present but the average Rh particle size in the catalysts was very similar. Typically, however, it is also clear that this species can be formed within the systems that do not contain Cl [26].

The work of Konigsberger [27], and more latterly, Iwasawa [5], has shown that for CO alone adsorbing onto "Cl free" catalysts, large scale $Rh(CO)_2$ formation is restricted to cases where the average particle size of Rh does not exceed, ca. 10 – 15 atoms. However, in the study of CO oxidation over supported Rh catalysts on alumina [20], it is quite clear that large scale $Rh(CO)_2$ formation can be detected even though the average particle size of the initially reduced Rh catalyst is significantly greater (on average ca. 35 – 50 atoms) [28].

A second valuable technique in studying supported metal catalysis is EXAFS. Where vibrational spectroscopies provide information on the adsorbate, EXAFS provides information on the catalysts itself, i.e. the metal particle size, morphology and overall structural changes during reaction [29, 30]. For example, an EXAFS study of Rh/Al_2O_3 by van't Blik *et al.* provided direct confirmation that adsorption of CO significantly perturbs the Rh-Rh coordination number of the supported Rh clusters, leading to the formation of atomically dispersed Rh^I sites [31].

In order to better establish relationships between the nature of "metal surface" centres, and their catalytic activity, techniques that allow a study of the catalysts structure and reactivity are required, preferably in an *in situ* manner i.e. while the catalytic reactions are taking place. The dynamic structural changes of metal sites in supported nanoparticle catalysts such as the formation and disintegration of the active structure induced by reaction gases and the bonding rearrangement have been monitored simultaneously by the combined techniques of energy dispersive extended X-ray absorption fine structure (EDE), diffuse reflectance infrared Fourier transform spectroscopy (DRIFTS) and mass spectrometry (MS).

This chapter will focus on the role of ceria, ceria-zirconia on the Rh catalysts structure and performance upon CO exposure at different temperatures.

4.2 Experimental section

4.2.1 EDE/DRIFTS/MS experiment

The CO interaction with Rh catalysts has been studied in the DRIFTS cell using the combined EDE/DRIFTS/MS apparatus at ID24 at ESRF in Grenoble, France. The detailed description of these techniques is given in chapter 2. The catalyst has been pre-treated *in situ* before reaction by heating up to 573 K under the flow of 5 % H_2/He, then oxidised by 5 % O_2/He until the H_2O and carbonaceous deposition disappeared from the system, and subsequently was switched back to 5 % H_2/He [20]. After full pre-treatment, the system was cooled down in H_2 to the working temperature and purged by He. The sample was exposed to 5 % CO/He (25 ml/min) for 60 s and next the flowing gas was switched to He for 60 s. All experiments last 120 seconds and the EDE/DRIFTS/MS data were collected simultaneously. EXAFS detection was done via the FReLoN CCD camera with a total acquisition time with 10 spectra of ca. 10 ms. The DRIFTS measurement was performed simultaneously, with the same sampling rates for each spectroscopy whilst a mass spectrometer continuously measured the composition of the gas phase.

4.2.2 XAFS/MS experiment

Due to the lower quality of the EDE data, the detailed EXAFS analysis of Rh structural perturbation during CO interaction was also studied with scanning XAFS at BM29. The sample pre-treatment was done by the same procedure as described

above. The catalytic system was cooled down to 323 K in the flow of He and subsequently exposed to 5 % CO/He until the XAFS spectrum was recorded with the acquisition time of 1 spectrum of ca. 30 minutes. The catalyst was then heated up to 423 K and 573 K under continuous CO flow.

The spectra were collected at 323 K under He, after cleaning, and then while purging with 5 % CO/He at 323 K, 423 K and 573 K.

4.3 Results

4.3.1 Rh/γ-Al_2O_3 catalysts

4.3.1.1 4 wt % Rh systems

Figures 4.2a and 4.2b show the averaged DRIFTS spectra (4 spectra averaged at 59 s of CO exposure) indicating the full range of IR active species present on the Rh surface of 4 wt% Rh/Al_2O_3 during CO exposure at different temperatures. In the range of 323 – 423 K (Figure 4.1a), all spectra display two sharp peaks which can be assigned to the geminal dicarbonyl species (Rh^+-$(CO)_2$), representing a symmetric and an asymmetric C-O stretch (ν~2101 cm^{-1} and 2028 cm^{-1} respectively) [7]. The formation of geminal dicarbonyl species is certainly indicative of a structural change of Rh particles (oxidative disruption). These bands overlap with the vibration of the linear species (Rh-CO) at 2070 cm^{-1} (323 K), 2063 cm^{-1} (373 K) and 2059 cm^{-1} (423 K) [17]. The bridged CO species (Rh_n-(CO), $n \geq 2$) gives a broad peak (ν~1883-1895 cm^{-1}) [16]. The geminal dicarbonyl species remains unchanged, with no significant shift in wavenumber although a relative increase in the amount of the species formed with increasing temperatures is observed. A red shift is observed for the linear CO species at higher temperatures, from ν~2070 cm^{-1} at 323 K to ν~2059 cm^{-1} at 423 K, and to ν~2047 cm^{-1} at 573K. The broad peak due to bridged CO species does not permit accurate analysis of this region, although the data suggests an overall red shift in the peak position, from ν~1895 cm^{-1} at 323 K to ν~1883 cm^{-1} at 423 K, and to ν~1855 cm^{-1} at 573 K. The red shift of the linear and bridged CO frequencies at higher temperature was expected, and this phenomenon is due to the decrease of the CO coverage as a result of stronger backbonding to CO from Rh and weaker CO bond.

At higher temperatures (473 K – 573 K), the amount of the geminal dicarbonyl species absorbed is less significant and mostly linear and bridged CO

species adsorb on the Rh surface. Furthermore, no absorption of geminal dicarbonyl species on the Rh^+ surface was observed at 573 K in contrast to the CO exposure at lower temperatures (≤ 473 K). This result could suggest that at 573 K the Rh particles are fully reduced, agglomerating to large particles, which inhibits the Rh^+-$(CO)_2$ formation as it is the case at lower temperature. It could also simply suggest that the geminal dicarbonyl species, though they may form, are not stable at 573 K within the lifetime of the measurement, and as such they are not observed. A small red shift of the symmetric dicarbonyl species from 2101 cm^{-1} at 323 K to 2097 cm^{-1} at 473 K has been observed which may be due to the increase of the electrodynamic coupling between the dynamic moment of the adsorbed complex and the alumina substrate [32].

Both spectra present one sharp peak in the range 2057-2047 cm^{-1}, which is assigned to linear CO species on Rh (Rh-CO). The bridged CO species again gives a broad signal around 1875-1855 cm^{-1}. The linear and bridged CO bands present are typical of sites on metallic rhodium.

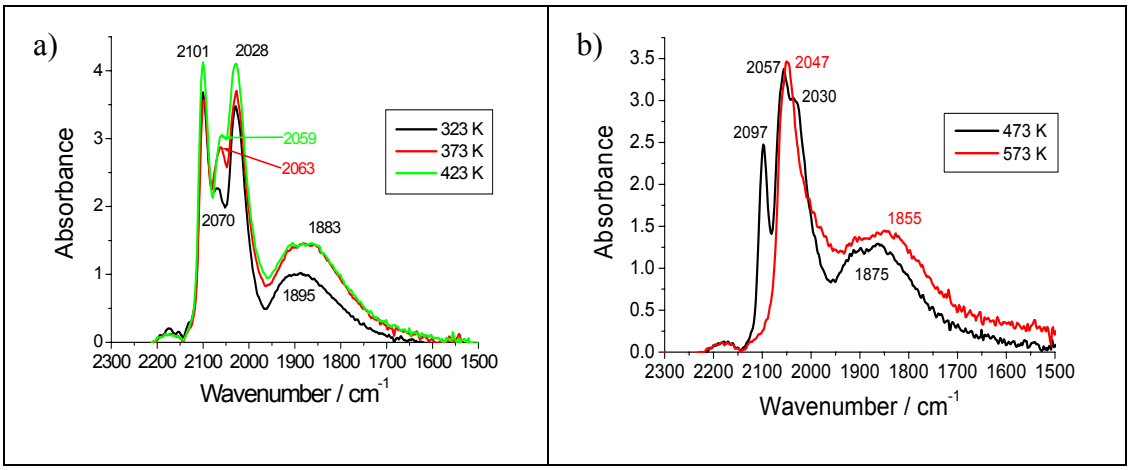

Figure 4.2. DRIFTS spectra of 4 wt% Rh/Al_2O_3 after CO exposure at various temperatures: a) 323 K, 373 K, 423 K, b) 473 K, 573 K

Figures 4.3a and 4.3b show two representative profiles of the evolution of the three main surface species within first 5 s of the CO exposure to 4 wt% Rh/Al_2O_3 system, highlighting both the quantity and quality of the DRIFTS spectra that are obtained from a typical experiment. At 323 K, first CO species adsorb linearly on the Rh surface, and then the geminal dicarbonyl and bridged species are formed. However, at 573 K, the CO species mainly adsorb linearly on the Rh surface. The sequence of formation of different CO adsorbates on the Rh surface is in accordance with previous studies [5]. Moreover, a small blue shift of the linear CO species is

observed at 573 K as a function of CO exposure. The results obtained suggest that the CO coverage increases as the number of electrons that a Rh particle can donate is finite and therefore the CO bond can become stronger with the continuous CO flow.

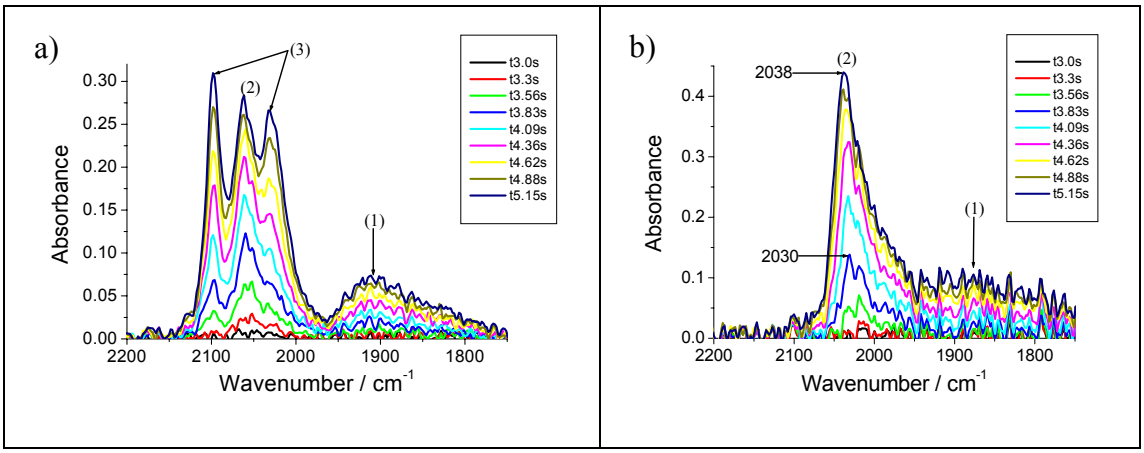

Figure 4.3. DRIFTS spectra of 4 wt% Rh/Al_2O_3 as a function of time after exposure to CO at a) 323 K and b) 573 K showing the evolution of bridged species (1), linear (2), geminal dicarbonyl species (3)

Figure 4.4 suggests that the evolution of geminal dicarbonyl Rh species is, within error, independent of the temperature used. The carbonyl entities are seen to evolve and stabilize by ca. 20 seconds. The figure also highlights the relative increase in the amount of the geminal species present on the Rh surface from 323 K to 423 K indicating the more extensive oxidative disruption of the Rh overlayer to produce isolated $Rh(CO)_2$ species at higher temperature. Furthermore, no desorption of geminal dicarbonyl species is present during the He flow. However, at 473 K the amount of the geminal dicarbonyl species formed is smaller and this CO species desorbs from the Rh surface during the He exposure. After 40 s exposure to He, the $Rh(CO)_2$ entities are completely removed from the surface. However, the IR analysis indicates that the other CO species such as linear and bridged species are not desorbed from the Rh surface throughout the whole He exposure. These results indicate that the geminal dicarbonyl species are not stable at higher temperature (> 423 K) and decompose from the Rh surface immediately.

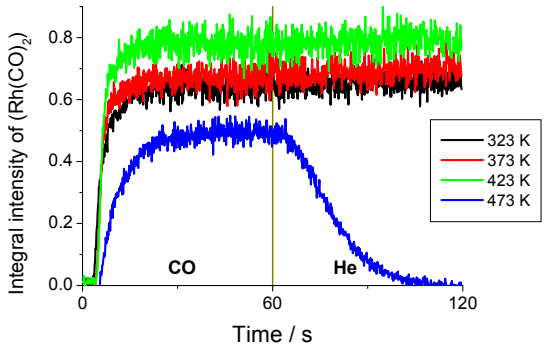

Figure 4.4 The evolution of the integral intensity of symmetric stretch of the carbonyl group in $Rh^{I}(CO)_2$ at different temperatures. After 60 s of CO exposure, the gas was switched back to He for 60 s.

The DRIFTS data demonstrate that various surface processes occur in the system as a function of temperature and CO/He flow, which suggests that some structural changes of the Rh metal particles should occur for the 4 wt% Rh catalysts, which can be verified by the synchronously obtained EXAFS data.

Figure 4.5 shows k^3 weighted EDE spectra for 4 wt% Rh/Al_2O_3 before and after 5 % CO/He exposure at 323 K, along with the corresponding Fourier transforms. The structural and statistical information derived from the analyses is given in Table 4.1. For each of the spectral analyses, ten experimental spectra have been averaged, taken at the beginning and over the final second of CO exposure. The figures show that, within the timescales of this experiment, EXAFS reveals structural changes to have occurred to the catalyst upon exposure to a flow of 5 % CO/He at 323 K. The coordination number of the RhRh shell decreases from ca. 7.2 under He to ca. 5.4 after 59 seconds of CO exposure. The Rh-Rh bond length changes throughout this CO exposure from 2.64 to ca. 2.68 Å. It should be noted that the initial step of the Rh particles is under He, after the pre-treatment procedure (5 % H_2/He -5 % O_2/He – 5 % H_2/He), described in details in section 4.2 of this chapter.

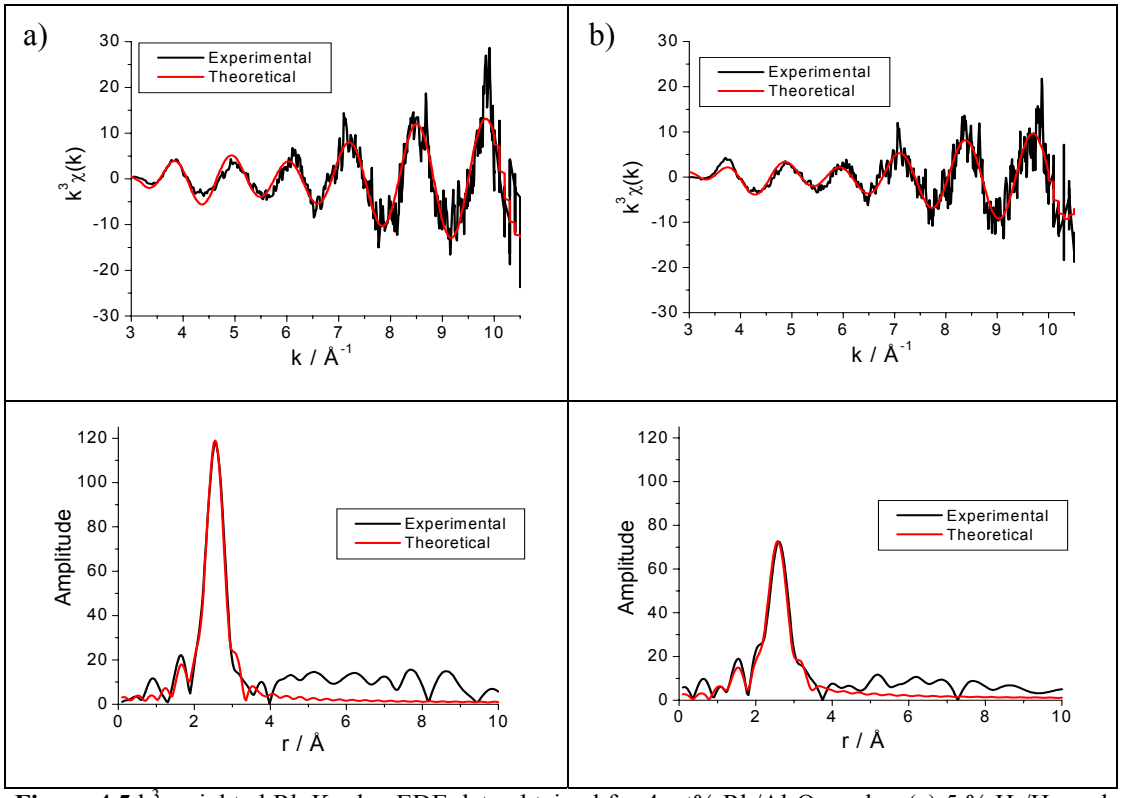

Figure 4.5 k^3 weighted Rh K edge EDE data obtained for 4 wt% Rh/Al_2O_3 under; (a) 5 % H_2/He and (b) 5 % CO/He (average of ten spectra taken at 59 s) at 323 K. The corresponding Fourier transforms are given underneath each spectrum.

Conditions	Scatterer	CN	r / Å	E_F	$2\sigma^2/Å^2$	R (%)
He at 323 K	Rh	7.2 (4)	2.64 (1)	-2.7	0.0115	52
5 % CO/He at 323 K	Rh	5.4 (3)	2.68 (1)	-2.5	0.0115	53

Table 4.1 Structural and statistical data for 4 wt% Rh/Al_2O_3 derived from the analyses of spectra given in Figure 4.5. Data range used was 3-10.5 k.

Similar results are observed for the catalysts at increased temperatures up to 423 K (Figure 4.6). After switching gas from He to CO, a reduction in the RhRh first shell coordination number of ca. 2 at 373 K or ca. 3.1 at 423 K is observed, as well as an increase in the Rh-Rh bond length from 2.64 to 2.69 Å. However, it can be observed that the initial Rh particle size does not increase with temperature as expected, it rather decreases. This may be attributed to the non-ideal method of the Debye-Waller factor determination and/or the presence of Cl in the system which is known to aid in the re-dispersion of the metal particles supported on γ-Al_2O_3. The structural changes of 4 wt% Rh/Al_2O_3 catalysts are in good agreement with DRIFTS results highlighting the larger oxidative disruption of Rh particles with increasing temperature up to 423 K. In the range of temperatures 473 – 573 K there is no significant change in the EXAFS after 60 seconds of CO exposure; the N_1^{Rh} value

decreases from ca. 7 under He to ca. 6, which is not significant at the 10 % error level of this data. A summary of the results obtained at these temperatures is given in Table 4.2.

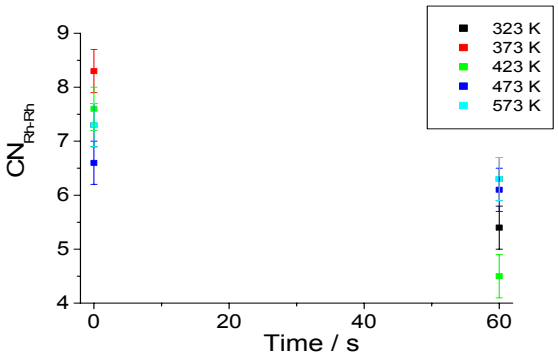

Figure 4.6 Variation of RhRh coordination number of 4 wt% Rh/Al_2O_3 before and after CO exposure as a function of temperature

Conditions	Scatterer	CN	r / Å	E_F	$2\sigma^2/Å^2$	R (%)
He at 373 K	Rh	8.3 (5)	2.65 (1)	1.7	0.012	47
5 % CO/He at 373 K	Rh	6.3 (4)	2.68 (1)	1.3	0.012	53
He at 423 K	Rh	7.6 (4)	2.64 (1)	-4.9	0.0135	54
5 % CO/He at 423 K	Rh	4.5 (4)	2.69 (1)	-6.7	0.0135	59
He at 473 K	Rh	6.6 (5)	2.64 (1)	4.6	0.015	58
5 % CO/He at 473 K	Rh	6.1 (5)	2.67 (1)	3.1	0.015	52
He at 573 K	Rh	7.3 (6)	2.64 (1)	3.4	0.0175	56
5 % CO/He at 573 K	Rh	6.3 (6)	2.66 (1)	2.9	0.0175	56

Table 4.2 Structural and statistical data derived from EXAFS analyses of 4 wt% Rh/Al_2O_3 at temperatures and conditions indicated. Data range used was 3-10.5 k.

The EXAFS analyses only reveal the presence of Rh-Rh contributions for the 4 wt% Rh systems after CO exposure. The DRIFTS data however clearly show a range of CO species adsorbed on the Rh surface. Therefore, the CO interaction with nanoparticulate rhodium catalysts has been additionally investigated by scanning XAFS at BM29 in order to obtain more accurate structural parameters and verify the presence of other neighbours around the Rh metal.

Figure 4.7 shows k^3 weighted EXAFS spectra for 4 wt% Rh/Al_2O_3 before and after exposure to CO at 323 K, 423 K and 573 K, along with the corresponding Fourier transforms. The structural parameters obtained for the first shell RhRh contribution are given in Table 4.3. The DW factor constant for the first shell Rh-Rh

shell is established by B. Jyoti [33]. The DW parameters for the further RhRh shells are refined according to the lowest R value throughout EXAFS analyses. The Rh-Rh bond length of 2.67 Å with the Rh-Rh CN of ca. 6.8 is in good agreement with those determined by the EDE data (CN_{Rh-Rh} ~ 7.2) under He at 323 K reported above (Table 4.1). However, the long acquisition time of the EXAFS spectrum (~30 minutes) improves signal to noise ratio data which allows detecting the further distances of Rh-Rh as follow: 3.77, 4.64, 5.24 Å with the coordination numbers of 1.7, 4.7, and 3.6, respectively. The suggested model corresponds to the fcc metallic structure [28]. The figure shows that, after 30 minutes of CO exposure at 323 K, EXAFS only detects minor structural changes. The value for the first RhRh coordination number decreases from ca. 6.8 under 5 % H_2/He to ca. 5.3 after 30 minutes of CO exposure. The Rh-Rh bond length increases from 2.67 Å to 2.69 Å. This expansion can be explained by the fact that average Rh particle seems to "expand" under CO dragging electron density out of Rh particle and therefore weakening Rh-Rh bonding. However the CO interaction is not sufficient to collapse Rh particles completely into $Rh(CO)_2$. The similar effect of partial Rh disruption was seen upon NO adsorption at 373 K [34]. Increasing the temperature up to 423 K does not cause any significant structural changes observed by EXAFS. However at 573 K, stronger disruption of the Rh particles is seen, by a decrease in CN_{Rh-Rh} and Rh-Rh bond length decreases. But even after long CO exposure at increased temperature, the Rh particles of 4 wt% Rh/Al_2O_3 still contains further RhRh shells that are typical of the 2nd, 3rd and 4th shells of a fcc metallic structure. The EXAFS and FT spectra at different temperatures cannot be directly compared since the DW factor increases relatively with the temperature, which is due to larger disorder of the investigated system. It appears that the Rh-Rh bond lengths of the first and higher shells are temperature dependant, decreasing the Rh-Rh distances at higher temperature.

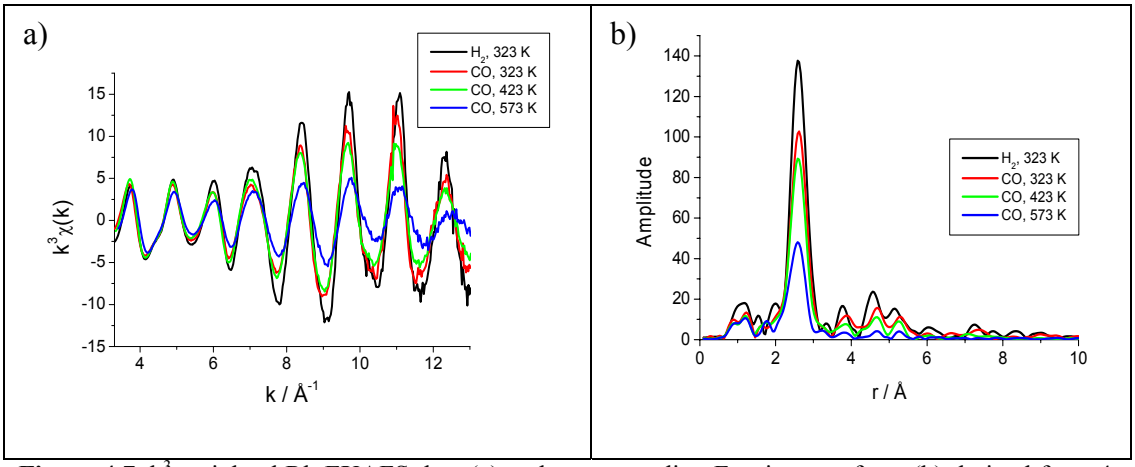

Figure 4.7. k^3 weighted Rh EXAFS data (a) and corresponding Fourier transform (b) derived from 4 wt% Rh/Al_2O_3 under 5 % H_2/He at 323 K (black line), 5 % CO/He at 323 K (red), 5 % CO/He at 423 K (green), 5 % CO/He at 573 K (blue).

Conditions	Scatterer	CN	r (Å)	$2\sigma^2$/Å^2	E_F (eV)	R (%)
5 % H_2/He at 323 K	Rh	6.8 (2)	2.674 (4)	0.011 (1)	0.3	30
	Rh	1.7 (2)	3.773 (3)	0.011 (1)		
	Rh	4.7 (1)	4.645 (4)	0.011 (2)		
	Rh	3.6 (2)	5.242 (5)	0.012 (2)		
5 % CO/He at 323 K	Rh	5.3 (2)	2.689 (5)	0.012 (1)	1.5	24
	Rh	1.4 (1)	3.819 (4)	0.012 (1)		
	Rh	3.4 (2)	4.676 (3)	0.012 (2)		
	Rh	3.5 (2)	5.293 (4)	0.012 (1)		
5 % CO/He at 423 K	Rh	5.7 (3)	2.684 (5)	0.014 (2)	2.5	21
	Rh	1.4 (2)	3.786 (3)	0.016 (2)		
	Rh	3.0 (3)	4.666 (4)	0.014 (1)		
	Rh	3.5 (2)	5.274 (3)	0.015 (2)		
5 % CO/He at 573 K	Rh	4.7 (3)	2.667 (5)	0.018 (2)	3.9	36
	Rh	0.8 (2)	3.739 (4)	0.018 (2)		
	Rh	1.2 (3)	4.652 (3)	0.017 (3)		
	Rh	1.9 (2)	5.265 (3)	0.017 (3)		

Table 4.3. Structural and statistical data derived from EXAFS analyses of 4 wt% Rh/Al_2O_3 at temperatures and conditions indicated. Data range used was 3.3-13 k.

The EXAFS data acquired throughout the CO exposure at 323 K do not display any significant corrosion taking place. The majority of Rh atoms remain in relatively big particles on the surface. The extensive particle disruption is not observed even at 573 K. On the other hand, the drop of the RhRh CN of ca. 2 at 573 K indicates ~30 % isolated Rh sites within the Rh particles and major fraction of Rh particles remains large.

4.3.1.2 1.6 wt% Rh systems

Figure 4.8 shows the whole range of IR active species present on the Rh surface of 1.6 wt% Rh/Al_2O_3 after 59 s of CO exposure as a function of temperature. The same three carbonyl species formed on the catalyst surface are observed as in the case of the 4 wt% Rh sample. At 323 K and 423 K mainly rhodium geminal dicarbonyl species (Rh^+-$(CO)_2$) are detected at 2100 and 2027 cm^{-1}. The linear CO species have been assigned at 2070 cm^{-1} and the bridged bonded CO species give broad signal in the range of 1860-1850 cm^{-1}. As it was already seen for the 4 wt% Rh catalysts, at 573 K, CO absorption only takes place as linear and bridged species. There are red shifts of the linear CO entities from 2070 cm^{-1} at 323 K to 2045 cm^{-1} at 573 K, as well as the bridged CO species from 1857 cm^{-1} at 323 K to 1832 cm^{-1} at 573 K.

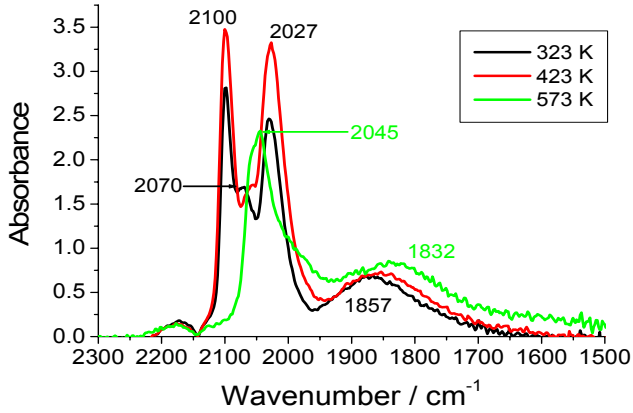

Figure 4.8 DRIFTS spectra of 1.6 wt% Rh/Al_2O_3 after CO exposure at three different temperatures: 323 K, 423 K, and 573 K.

Moreover, the synchronously obtained EDE data indicate that significant structural changes have occurred for the 1.6 wt% Rh/Al_2O_3 upon exposure to a flow of 5 % CO/He at 323 K as presented in the k^3 weighted EDE spectra along with the corresponding Fourier transforms (Figure 4.9). The reduced system has an average Rh-Rh coordination number of ca. 5 under 5 % H_2/He prior to the start of the experiment (Table 4.4). After 59 seconds of being exposed to the flow of 5 % CO/He the EXAFS shows a reduction of the RhRh CN to 3.6 and the presence of an additional RhO shell with the coordination number of ca. 1. The bond length of Rh-Rh and Rh-O are around 2.63 and 2 Å, respectively. However, caution needs to be applied when analysing and interpreting the EDE data of low Rh loading due to the narrow k range and poor quality of data.

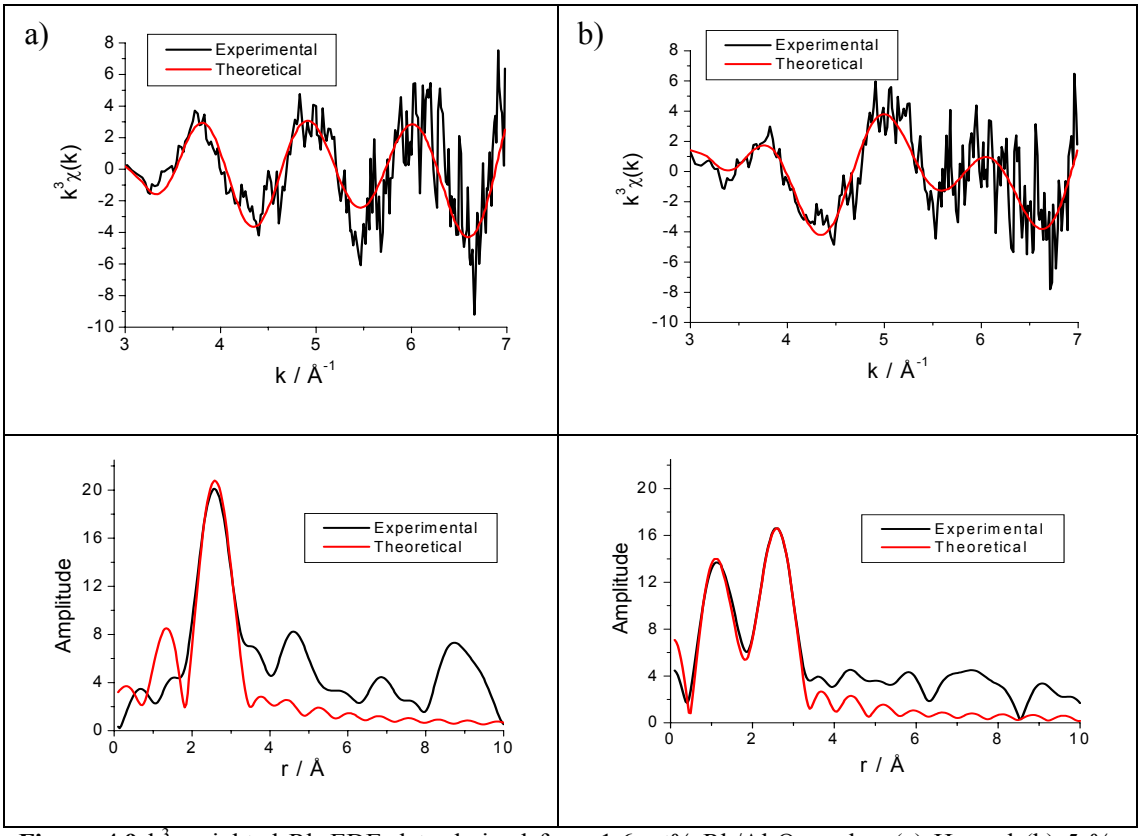

Figure 4.9 k^3 weighted Rh EDE data derived from 1.6 wt% Rh/Al_2O_3 under; (a) He and (b) 5 % CO/He (average of ten spectra taken at 59 s) at 323 K. The corresponding Fourier transforms are given underneath each spectrum.

Conditions	Scatterer	CN	r / Å	E_F	k (Å^{-1})	$2\sigma^2$/Å^2	R (%)
He at 323 K	Rh	5.1 (5)	2.63 (1)	-2.3	3-7	0.0115	60
5 % CO/He at 323 K	Rh	3.6 (6)	2.63 (1)	-3.5	3-7	0.0115	55
	O	1.3 (3)	1.99 (3)			0.012	

Table 4.4 Structural and statistical data derived of 1.6 wt% Rh/Al_2O_3 from the analysis of spectra given in Figure 4.9. Data range used was 3-7 k.

Figure 4.10 shows the variation of RhRh coordination number of 1.6 wt% Rh on alumina before and after CO exposure at the temperatures indicated. Analogous structural behaviour of 1.6 wt% Rh/Al_2O_3 catalyst throughout CO exposure can be reported as for larger Rh loading. Below 573 K, the drop of the RhRh CN of ca. 1.4 is observed after 60 s of CO exposure indicating the particle disruption. However, at 573 K no significant structural change has been observed (Figure 4.10).

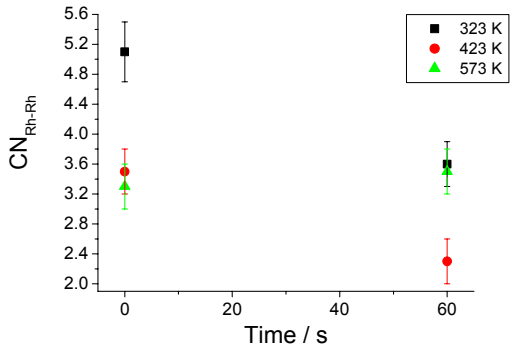

Figure 4.10 Variation of RhRh coordination number of 1.6 wt% Rh/Al_2O_3 before and after CO exposure as a function of temperature

4.3.2 $Rh/CeO_x/\gamma\text{-}Al_2O_3$

4.3.2.1 4 wt% Rh systems

The effect of ceria on the catalytic performance of rhodium catalysts has been studied considering two samples derived from the two different preparation methods as described in chapter 3, section 3.2. In the first method, the ceria is deposited on the alumina support and subsequently Rh metal; the second follows the method called controlled surface modification, where ceria is placed on the pre-supported Rh metal.

Figures 4.12a and 4.12b show the DRIFTS spectra of 4 wt% $Rh/CeO_x/Al_2O_3$ (method I) after 59 s of 5 % CO/He exposure at the temperature indicated. As was already observed for 4 wt% Rh/Al_2O_3, at lower temperatures (323-423 K) two sharp peaks are present at 2102 and 2031 cm^{-1} assigned to rhodium geminal dicarbonyl species (Rh^{+}-$(CO)_2$). A sharp band of linear bonded CO species (Rh-CO) is observed at 2073 and 2059 cm^{-1} for 323 and 423 K, respectively. The broad signal around 1875 cm^{-1} is attributed to the bridging carbonyl species. However, in the temperature range of 473-573 K, relatively significant amounts of the linear and bridged species adsorb on the metallic rhodium particles. As it is the case with Rh on alumina, a red shift was observed for linear species from 2073 to 2053 cm^{-1} and bridged from 1875 to 1866 cm^{-1} when increasing the temperature. It can be noted that the only apparent difference between 4 wt% Rh/Al_2O_3 and 4 wt% $Rh/CeO_x/Al_2O_3$ (method I) is the presence of the additional peak around ~1720 cm^{-1} at 323 K, red shifted to 1670 cm^{-1} with increasing temperature. Based on comparisons to the IR spectra of known metal carbonyl compounds [35, 36], the peak centred at 1720 cm^{-1} at 323 K can be ascribed to a Rh adsorbed CO species in which the C atom of the molecule is bound

to Rh and the O atom interacts with the cerium cation of the support CO. This chemisorbed CO species between Rh and Ce^{3+} cation is presented in Figure 4.11.

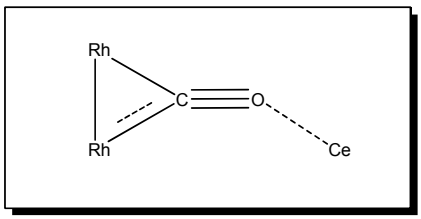

Figure 4.11. The bridged CO species between Rh and Ce atoms.

In an FTIR study of the CO interaction with $Rh/CeO_2/SiO_2$ Kiennenmann *et al.* has observed this characteristic peak of CO at 1725 cm^{-1} [37]. Furthermore, in the study of CO and NO interaction with $Rh/Pt/CeO_2/Al_2O_3$ catalysts by TPD, Loof *et al.* proved that reduced ceria as a support has strong influences on both CO and NO bonding and desorption on Pt and Rh [38].

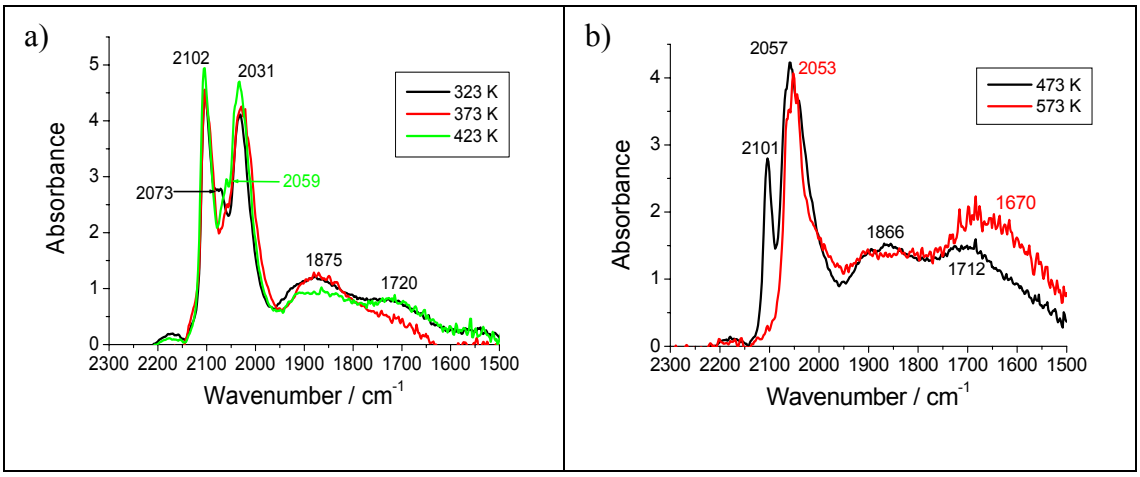

Figure 4.12 DRIFTS spectra of 4 wt% $Rh/CeO_x/Al_2O_3$ (method I) after CO exposure at varied temperatures: a) 323 K, 373 K, 423K, b) 473 K, 573 K

Figures 4.13a and 4.13b show the DRIFTS spectra of 4 wt% $Rh/CeO_x/Al_2O_3$ (method II) after 59s of 5 % CO/He exposure at the temperature indicated. In the temperature range of 323-473 K the spectra show mainly a sharp peak appearing around 2073 cm^{-1} assigned to the linear CO species which intensity is relatively higher than the residual CO peaks present when compared with other Rh catalysts. The bridged CO species give a broad signal around 1889 cm^{-1}. There are two shoulders associated with the rhodium geminal dicarbonyl species at 2098 and 2030 cm^{-1}. The broad signal around 1725 cm^{-1} is characteristic for bridged CO species between Rh and Ce atoms that is red shifted to 1685 cm^{-1} at 573 K.

Increasing the temperature to 573 K a red shift for the linear species from 2073 to 2056 cm^{-1} can be observed as well as a blue shift for the bridged species from 1889 to 1900 cm^{-1}. Others have associated such shifts with an increase of the Rh particle size to which the bridged CO species is bound [3]. Furthermore, no (Rh^{+}-$(CO)_2$) species are reported as is the case for all Rh catalysts at 573 K.

The results presented indicate that the synthesis methods have an effect on the 'Rh-CO' intermediate formed during CO exposure. Method I wherein rhodium is supported on ceria-alumina does not seem to change the structure of the Rh catalyst showing a similar structural behaviour with and without ceria. At lower temperatures significant adsorption of (Rh^{+}-$(CO)_2$) species indicate a strong Rh bonding with O from the alumina support. However, in the case where ceria is deposited on pre-supported Rh sample (method II) the apparent difference in the structural behaviour is observed as the formation of the geminal dicarbonyl species is much less relative to the Rh/Al_2O_3 or ceriated Rh catalysts (method I). The close vicinity of ceria and Rh particles keeps Rh particles metallic that can be proved by the adsorption of linear and bridged CO species mostly on the Rh surface. Furthermore, the partial Ce coverage could also prevent the oxidative disruption even if the metal particle size remains the same.

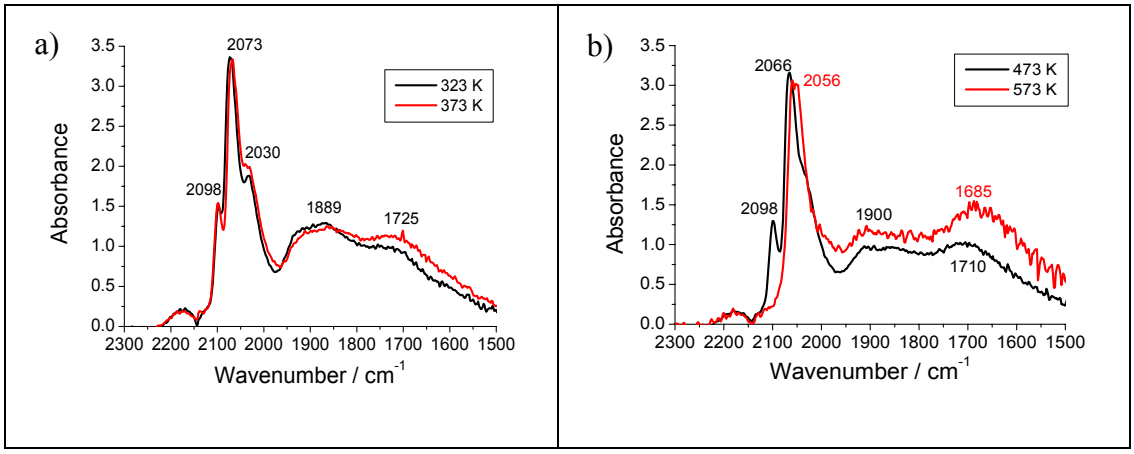

Figure 4.13 DRIFTS spectra of 4 wt% $Rh/CeO_x/Al_2O_3$ (method II) after CO exposure at various temperatures: a) 323 K, 373 K, b) 473 K, 573 K

Figures 4.14a and 4.14b show the variation of RhRh coordination number of the two types of ceriated Rh catalysts before and after CO exposure at the temperatures indicated. Similar structural behaviour of the non-ceriated Rh samples and the Rh catalysts doped by ceria (methods I and II) throughout CO exposure can be observed by the EDE analyses. In the case of 4 wt% $Rh/CeO_x/Al_2O_3$ (I), the Rh-Rh coordination number under He is ~ 5.4 at 323 K and 4.7 at 423 K which

corresponds to ~ 16 and 10 Rh atoms averaged in the particle. Rh particles of 4 wt% $Rh/CeO_x/Al_2O_3$ (II) under reducing conditions (<473 K) are clearly larger than non-ceriated and ceriated Rh catalysts (method I) (CN_{Rh-Rh}~8.0 at 323 K, 7.2 at 423 K). Assuming a constant (spherical) morphology and fcc structure [28], an average particle contains 68 atoms at 323 K and 37 atoms at 423 K. There are small changes in the Rh-Rh coordination number (CN_{Rh-Rh}) with the gas switching from He to CO. For both systems, at the start of the experiment the rhodium particles are bigger and during CO exposure the CN_{Rh-Rh} drops with ca. 2. A similar trend is observed in the TEM analysis done over fresh Rh catalysts. The larger particle size distribution is observed for the Rh catalysts supported on ceria-alumina (method II) when compared with 4 wt% $Rh/CeO_x/Al_2O_3$ (method I). However, the particle size determined by TEM corresponds to the metallic and oxidic fraction of the Rh particles.

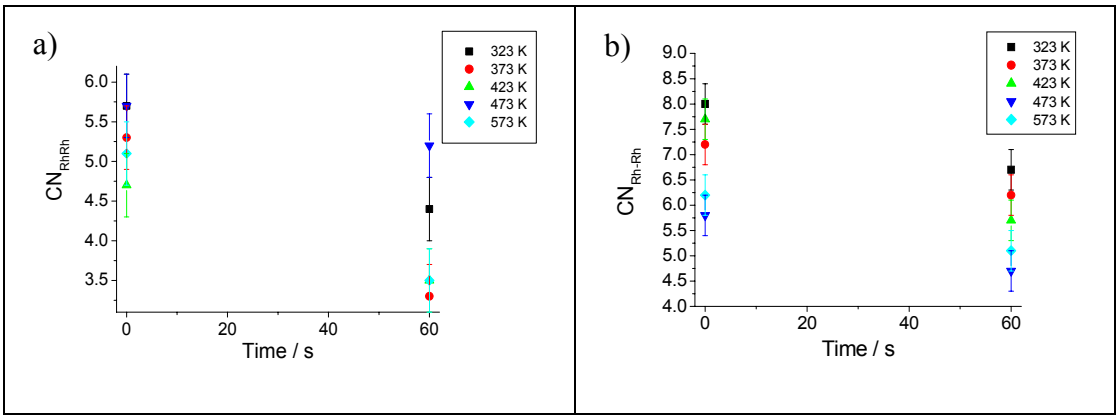

Figure 4.14 Variation of RhRh coordination number of 4 wt% $Rh/CeO_x/Al_2O_3$: a) method I, b) method II before and after CO exposure as a function of temperature.

The structural changes for the Rh particles after CO exposure at various temperatures have been additionally monitored with conventional EXAFS study. The RhRh bond lengths and coordination numbers of 4 wt% Rh/Al_2O_3 and 4 wt% $Rh/CeO_x/Al_2O_3$ (method I, II) under the conditions indicated were plotted in Figure 15a and 15b. Generally, a comparable trend of structural changes after CO exposure has been obtained for each Rh catalyst. Under H_2 (A), a similar Rh-Rh distance of ca. 2.67 Å for each Rh system can be observed. The Rh-Rh coordination number determined by scanning EXAFS is in good agreement with the EDE results obtained at identical conditions, e.g. in the case of 4 wt% $Rh/CeO_x/Al_2O_3$ (I), CN_{EXAFS} ~ 5.6 and CN_{EDE} ~ 5.7. After CO exposure at 323 K (B), the RhRh coordination number decreased, accompanied by elongation of the Rh-Rh bond lengths. The Rh-Rh bond

lengths of ceriated Rh catalysts were almost constant, with an increasing RhRh CN at the elevated temperature of 423 K (C). Further increasing the temperature to 573 K (D) decreases the Rh-Rh distance of all samples. The RhRh coordination number, however, increases for ceriated Rh catalysts and decreases for the non-ceriated Rh catalyst. The Rh particle size of 4 wt% Rh/Al_2O_3 is smaller for the highest temperature of CO exposure. CO is a reductant and at the same time it appears to be acting as a redispersant over undoped Rh catalyst. A smaller variation of Rh-Rh CN throughout the whole experiment is observed for 4 wt% Rh/Al_2O_3 than for the ceriated Rh catalysts.

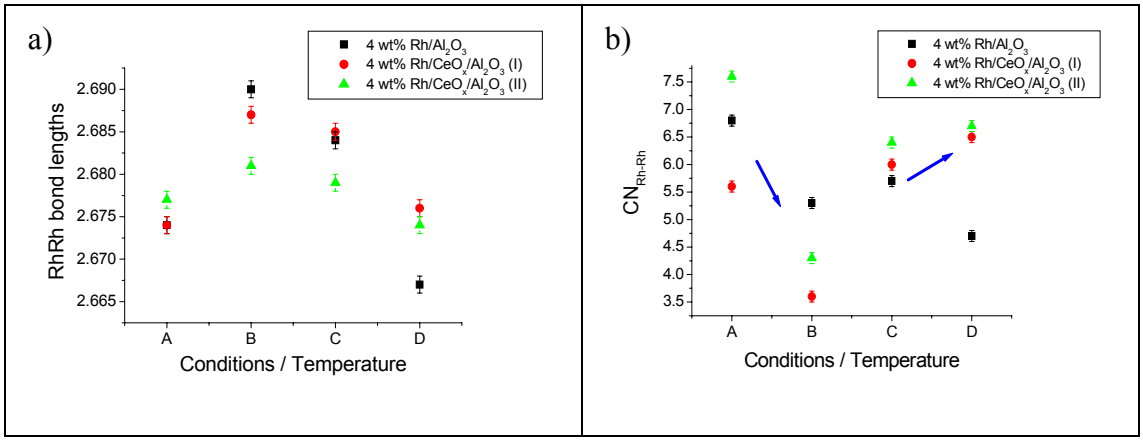

Figure 4.15 Variation of RhRh bond lengths (a) and RhRh coordination number (b) of 4 w% Rh/Al_2O_3 and 4 wt% $Rh/CeO_x/Al_2O_3$ (method I and II) under different conditions; A – 5 % H_2/He, 323 K, B – 5 % CO/He, 323 K, C – 5 % CO/He, 423 K, D – 5 % CO/He, 573 K.

Figure 4.16 presents the CO uptake per single Rh atom calculated from the MS data. The temperature dependent CO uptake (no. of CO molecules per 1 Rh atom) supports the EXAFS/DRIFTS analyses (Figure 4.16). Generally, a decrease of CO uptake with temperature is observed, especially up to 573 K, which suggests the agglomeration of Rh particles or no significant disruption of Rh particles upon CO exposure. In the temperature range of 323 – 423 K, approximately two CO molecules per Rh were adsorbed for the Rh/Al_2O_3, which corresponds to the fact that significant amount of geminal dicarbonyl species are detected by IR. On the other hand, the EXAFS study indicates the presence of large Rh particles even after long CO exposure. At higher temperature, the CO uptake diminished as it can be attributed to the presence of linear and bridged species mostly on the Rh surface. Similar levels of CO uptake have been observed for 4 wt% $Rh/CeO_x/Al_2O_3$ (I). However, a significantly lower amount of CO uptake has been monitored for the ceriated Rh catalyst prepared by method II, over the entire temperature range

investigated. This is in good agreement with IR data, in which mostly the adsorption of linear CO species was observed. This study has shown that an increased CO uptake most likely corresponds to the occurrence of geminal dicarbonyl species.

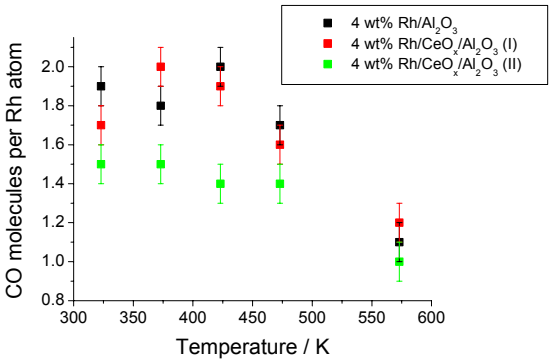

Figure 4.16. CO coverage for 4 wt% Rh systems in the function of temperature

4.3.2.2 1.6 wt% Rh systems

The effect of ceria has been additionally studied over rhodium catalysts with lower Rh loadings. Figures 4.17a and 4.17b present the same types of CO species adsorbed on both Rh catalysts derived from method I and II, respectively. A red shift in linear species as a function of temperature is reported as for all investigated Rh samples; from ~ 2073 cm^{-1} at 323 K to ~ 2053 cm^{-1} at 573 K for ceriated Rh catalyst (I) and from ~ 2072 cm^{-1} at 323 K to 2047 cm^{-1} for $Rh/CeO_x/Al_2O_3$ (II). Moreover, at 323 and 423 K, a relatively larger amount of linear species is adsorbed on the Rh surface of ceriated rhodium catalysts produced by method II than by method I. The same trend of CO species formation has been detected for 1.6 wt% rhodium catalysts as for larger Rh loadings. Again, the peak around 1710 cm^{-1} detected at 323 K is assigned to bridged CO species bonded with Rh and Ce atoms. Following method II, wherein Ce is deposited on the pre-reduced Rh supported catalysts; the ceria partially isolated Rh particles from oxidation.

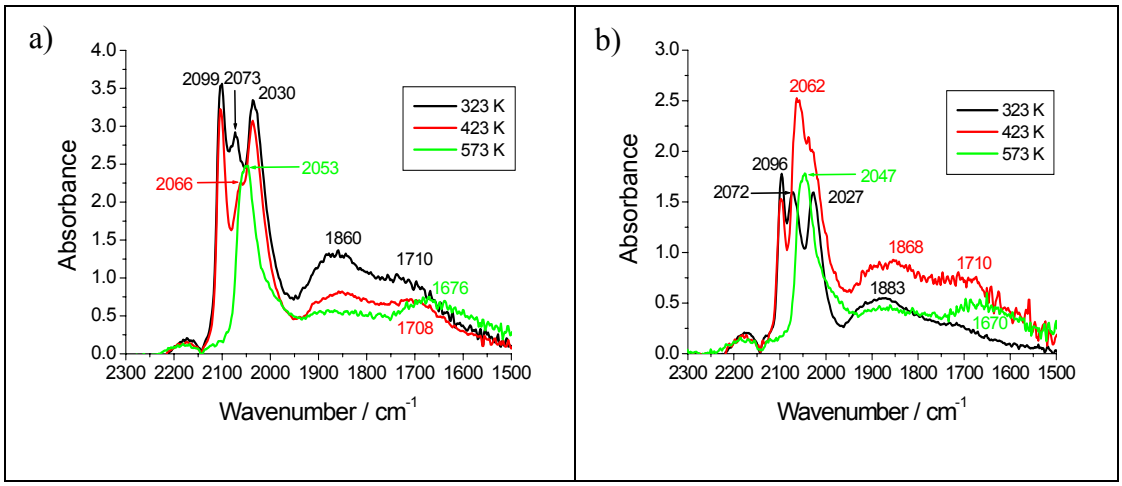

Figure 4.17 DRIFTS spectra of 1.6 wt% $Rh/CeO_x/Al_2O_3$ a) method I; b) method II after CO exposure at varied temperatures: 323 K, 423K, 573 K

Simultaneously EDE data have been collected. Figures 4.18a and 4.18b, showing the variation of RhRh CN upon 5 % CO/He exposure, indicate larger Rh particles in the ceriated Rh catalysts produced by method II (e.g. ~ 23 Rh atoms under He at 323 K) when compared to method I (~ 8 Rh atoms). Therefore, a slight drop of RhRh occupation was observed for ceriated Rh catalyst (I) after CO exposure at 323 K – 423 K. At 573 K, even an increase of RhRh occupation number was reported. In the view of ceriated Rh catalysts (II) more significant drop of RhRh occupation was detected upon CO exposure over all temperature employed.

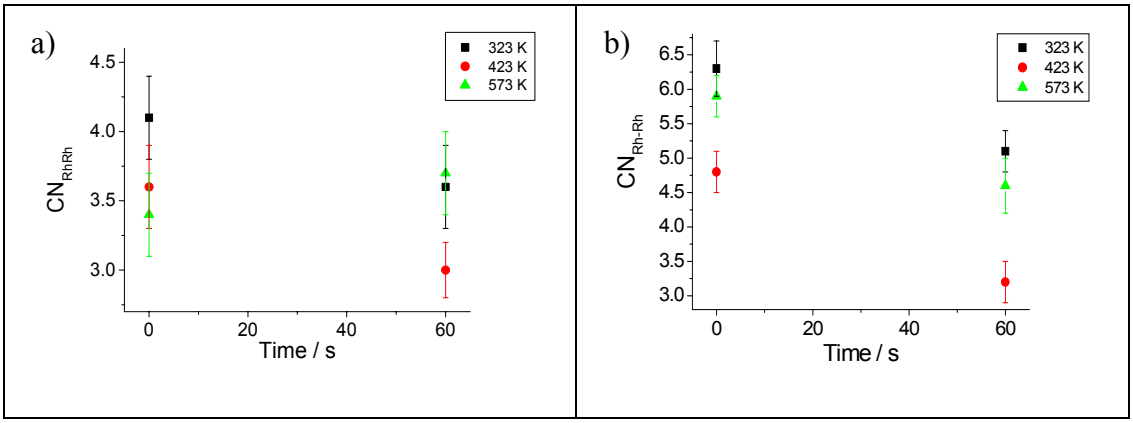

Figure 4.18 Variation of RhRh coordination number of 1.6 wt% $Rh/CeO_x/Al_2O_3$: a) method I, b) method II before and after CO exposure as a function of temperature.

Figures 4.19a and 4.19b show respectively the variation of RhRh bond lengths and RhRh coordination numbers of 1.6 wt% Rh/Al_2O_3 and 1.6 wt% $Rh/CeO_x/Al_2O_3$ (I, II) catalysts. The behaviour of the 1.6 wt% Rh system is analogous to the larger Rh loaded samples (4 wt% Rh). After CO exposure at 323 K, the Rh-Rh distance of each Rh sample expands and the RhRh CN decreases which is due to the disruption of Rh particles by CO molecules. Further increase of the

temperature to 573 K increased the RhRh CN and decreased the Rh-Rh bond lengths of all the samples studied which can be attributed to the Rh agglomeration. Moreover, the 1.6 wt% $Rh/CeO_x/Al_2O_3$ (II) consists of the largest averaged Rh particles; a size is comparable with the Rh particles of the 4 wt% Rh/Al_2O_3 under 5 % H_2/He at 323 K.

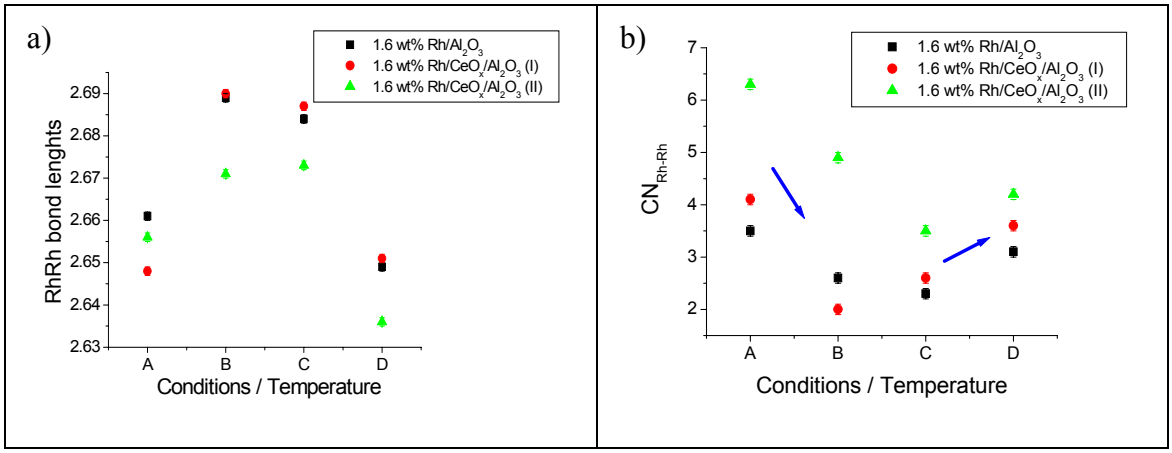

Figure 4.19 Variation of RhRh bond lengths (a) and RhRh coordination number (b) of 1.6 w% Rh/Al_2O_3 and 1.6 wt% $Rh/CeO_x/Al_2O_3$ (method I, II) under different conditions; A – 5 % H_2/He, 323 K, B – 5 % CO/He, 323 K, C – 5 % CO/He, 423 K, D – 5 % CO/He, 573 K.

Figure 4.20 highlights the uptake of CO molecules per Rh atom. Analogous capacity of CO uptake to Rh particles has been observed for 1.6 wt% Rh system when compared to larger loading: in the case of Rh/Al_2O_3 and $Rh/CeO_x/Al_2O_3$ (I), the CO coverage correspond to ca. 2 CO molecules per 1 Rh atom at 323 – 423 K, however, a significant drop of CO uptake occurs at 573 K. The similar trend of CO uptake when increasing temperature has been monitored for 1.6 wt% $Rh/CeO_x/Al_2O_3$ (II), nonetheless significantly smaller CO uptake has been detected at 423 K, which correlates to the presence of mainly linear CO species, as viewed by IR data.

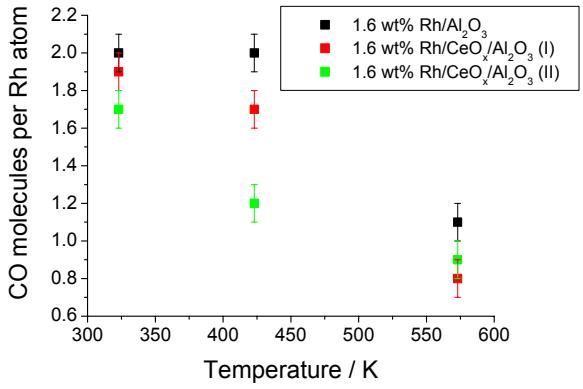

Figure 4.20. CO coverage for 1.6 wt% Rh systems in the function of temperature

4.3.3 $Rh/CeO_x/ZrO_2/\gamma\text{-}Al_2O_3$

The effect of zirconia and ceria/zirconia on the structural behaviour of rhodium catalysts has been studied, in view of three samples with different Ce:Zr ratio as 0:1, 1:1, and 2:1.

4.3.3.1 4 wt% Rh systems

The DRIFTS spectra of the series of catalysts indicated were plotted in Figure 4.21 displaying the same three carbonyl containing species (Rh-CO, $Rh(CO)_2$ and bridged) formed on the Rh surface of zirconia and ceria-zirconia doped catalysts as in the 4 wt% Rh/Al_2O_3 case. A red shift in the frequency of the linear CO species is observed from ~ 2067 cm^{-1} at 323 K to ca. 2052 cm^{-1} at 423 K and ~ 2039 cm^{-1} at 573 K for $Rh/ZrO_2/Al_2O_3$. There is no peak around 1700 cm^{-1} in the zirconiated only sample as observed for the ceriated samples. The red shift in the wavenumber of the linear CO species is also observed for Ce/Zr promoted Rh catalysts; however the position of this peak appears at higher frequency with increasing Ce loading. The blue shift for the linear CO species as a function of ceria concentration can be explained by the increased Ce interaction with Rh atoms that remove the electron density of the back bonding to the CO and weaken the CO bond [39]. It can be observed that the relative amount of linear species increased with the larger Ce doping in the Rh system at the entire temperature range studied.

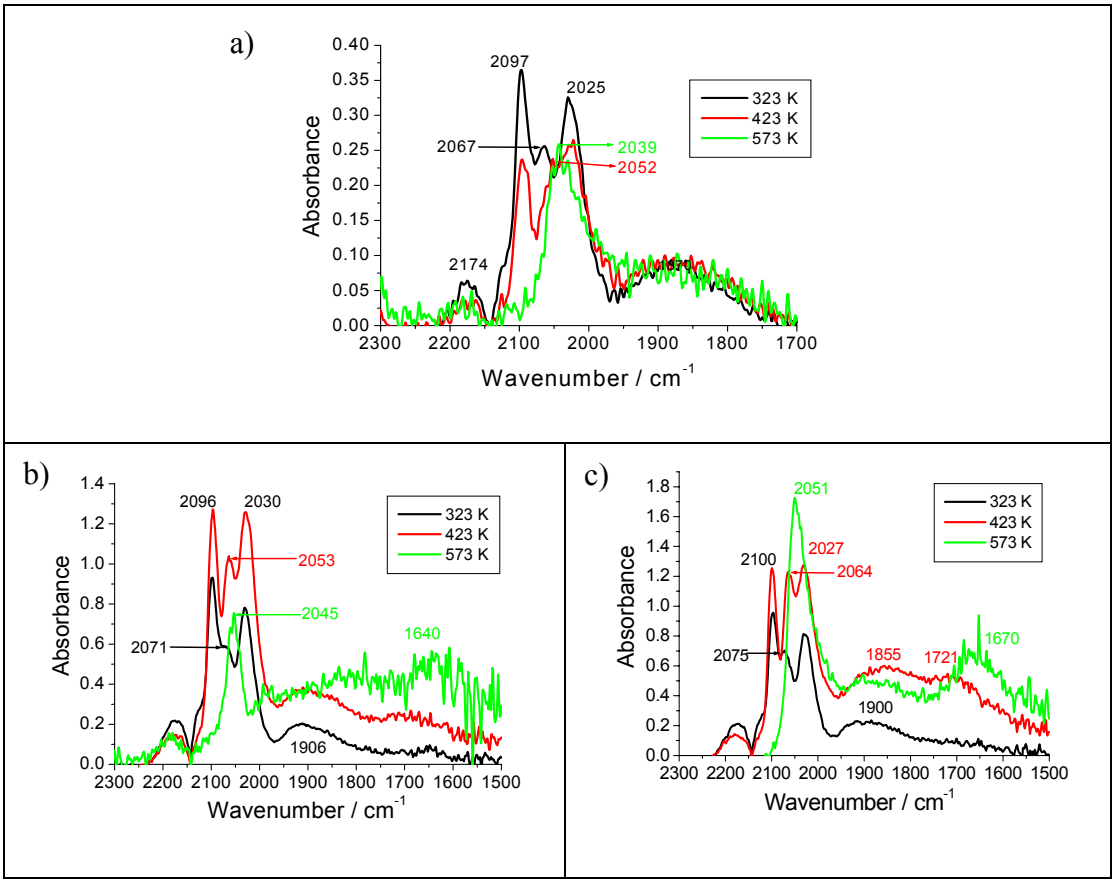

Figure 4.21 DRIFTS spectra of 4 wt% $Rh/ZrO_2/Al_2O_3$ (a), 4 wt% $Rh/CeO_x/ZrO_2/Al_2O_3$ (Ce:Zr;1:1); (b) (Ce:Zr;2:1) (c) after CO exposure at varies temperature: 323 K, 423K, 573 K

The EDE data, obtained simultaneously with the DRIFTS data presented above, display the structural changes for the Rh particles after 60 s of 5 % CO/He exposure (Figure 4.22). For $Rh/ZrO_2/Al_2O_3$ at 323 K, the RhRh coordination number seems to be constant, at elevated temperatures of 423 – 573 K, however a decrease in RhRh CN of ~ 1 can be observed, which might be insignificant considering the extensive error level. It can be observed that Zr-promoted Rh catalysts have the largest RhRh CN indicating the large size of Rh particles. Similar level of the variation of the CN_{RhRh} is detected for both ceria and zirconia doped Rh catalysts. The ceria-zirconia doping does not generate any different as well as significant structural changes over the temperatures indicated.

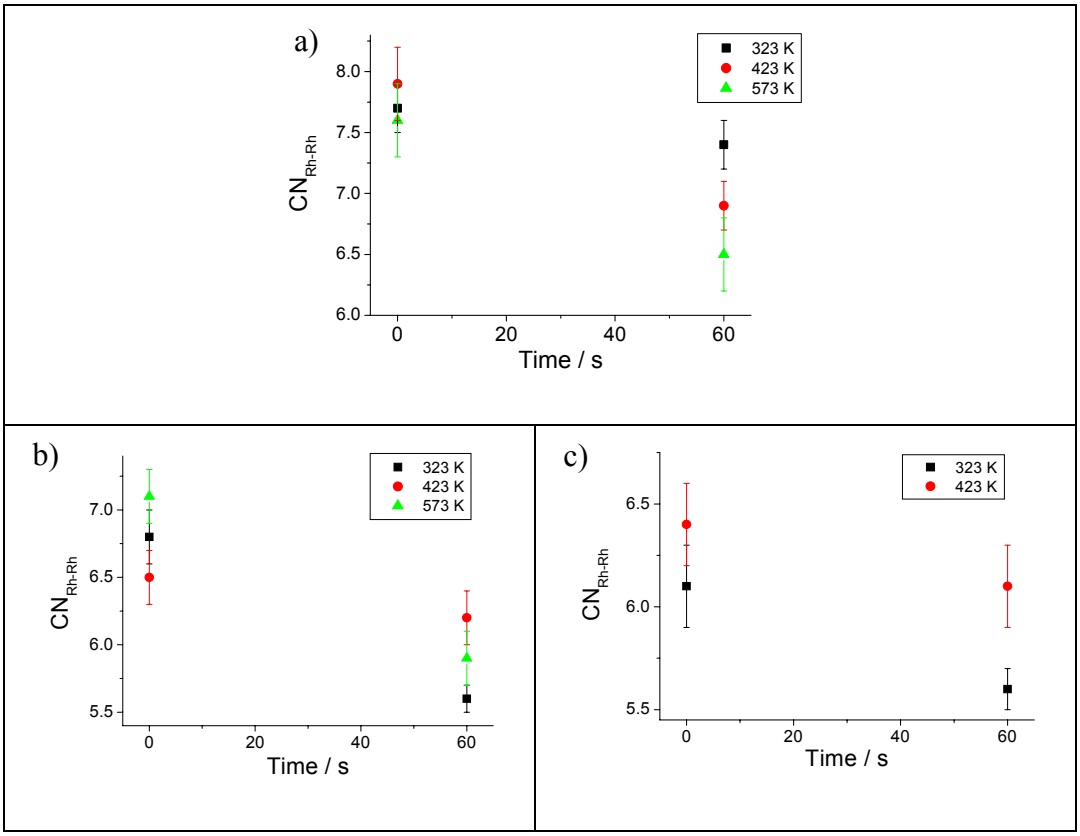

Figure 4.22 Variation of RhRh coordination number of 4 wt% $Rh/ZrO_2/Al_2O_3$ (a), 4 wt% $Rh/CeO_x/ZrO_2/Al_2O_3$, (Ce:Zr;1:1) (b); (Ce:Zr;2:1) (c) before and after CO exposure at the temperature indicated.

Figures 4.23a and 4.23b present the RhRh bond lengths and coordination number variations of 4 wt% Rh/Al_2O_3 along with Zr and Ce/Zr modified Rh catalysts under different conditions. The reported parameters (CN_{RhRh}) for all Rh catalysts derived from scanning EXAFS experiment correlate well with the EDE data, presented above. Similar trends in structural changes can be identified for each Rh catalyst as described in details above. The largest Rh particles are observed for zirconiated Rh catalysts throughout CO exposure at the temperatures studied, which was also reported by the EDE data.

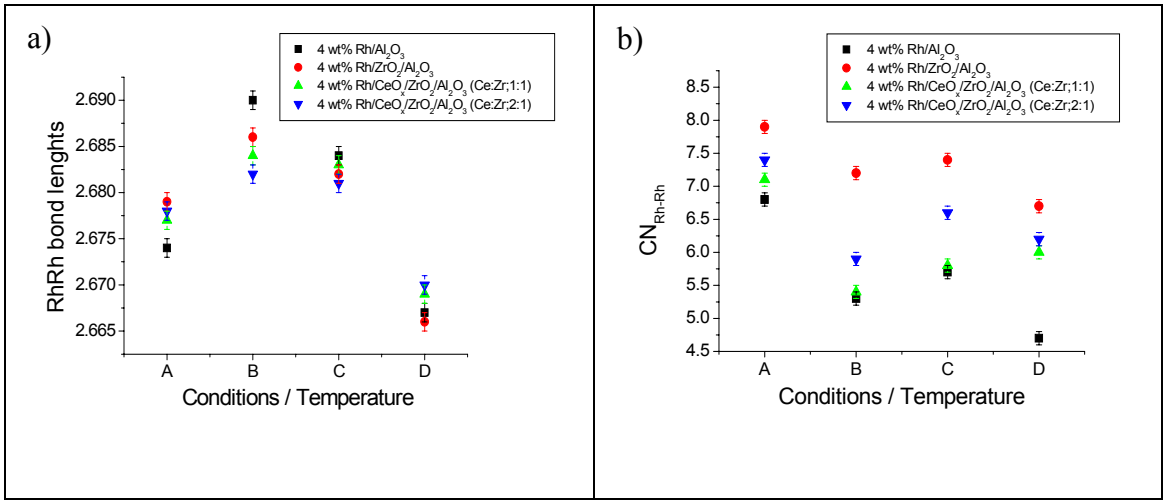

Figure 4.23 Variation of RhRh bond lengths (a) and RhRh coordination number (b) of 4 w% Rh/Al_2O_3 and Ce/Zr modified Rh catalysts under different conditions; A – 5 % H_2/He, 323 K, B – 5 % CO/He, 323 K, C – 5 % CO/He, 423 K, D – 5 % CO/He, 573 K.

Figure 4.24 show that the CO uptake of zirconia and ceria-zirconia doped Rh catalysts which hardly changes with increasing temperature, within experimental error. This phenomenon can be attributed to the possibility of CO adsorption on Ce and Zr sites for different types of catalysts. However, the poor quality of IR spectra does not allow distinguishing any isolated "Ce-CO", and "Zr-CO" frequencies. The lowest value of CO uptake for at all temperatures (~1.3 CO molecules per 1 Rh atom) is observed for the 4 wt% $Rh/ZrO_2/Al_2O_3$, which can be explained by the limited adsorption of CO molecules to the extended Rh surface, as the EDE data indicates the largest Rh particles of this system under the conditions investigated.

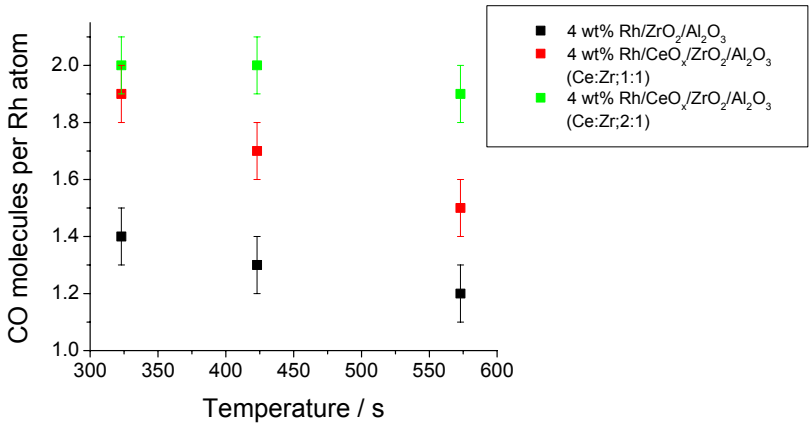

Figure 4.24. CO coverage for 4 wt% Rh systems in the function of temperature

4.3.3.2 1.6 wt% Rh systems

Figures 4.25 show the DRIFTS spectra of 1.6 wt% Rh/Al_2O_3 promoted by zirconia and ceria-zirconia with different Ce loading (Ce:Zr; 1:1, 2:1). Identical CO species are observed on the Rh surface as for the 1.6 wt% Rh on alumina i.e. linear, bridged and geminal dicarbonyl species. The presence of other species such as CO species bridged between Rh and Ce atoms which peak would exist around 1700 cm^{-1} cannot be excluded due to the low data quality. Therefore, caution needs to be applied while analysing and interpreting these data, particular at higher temperatures.

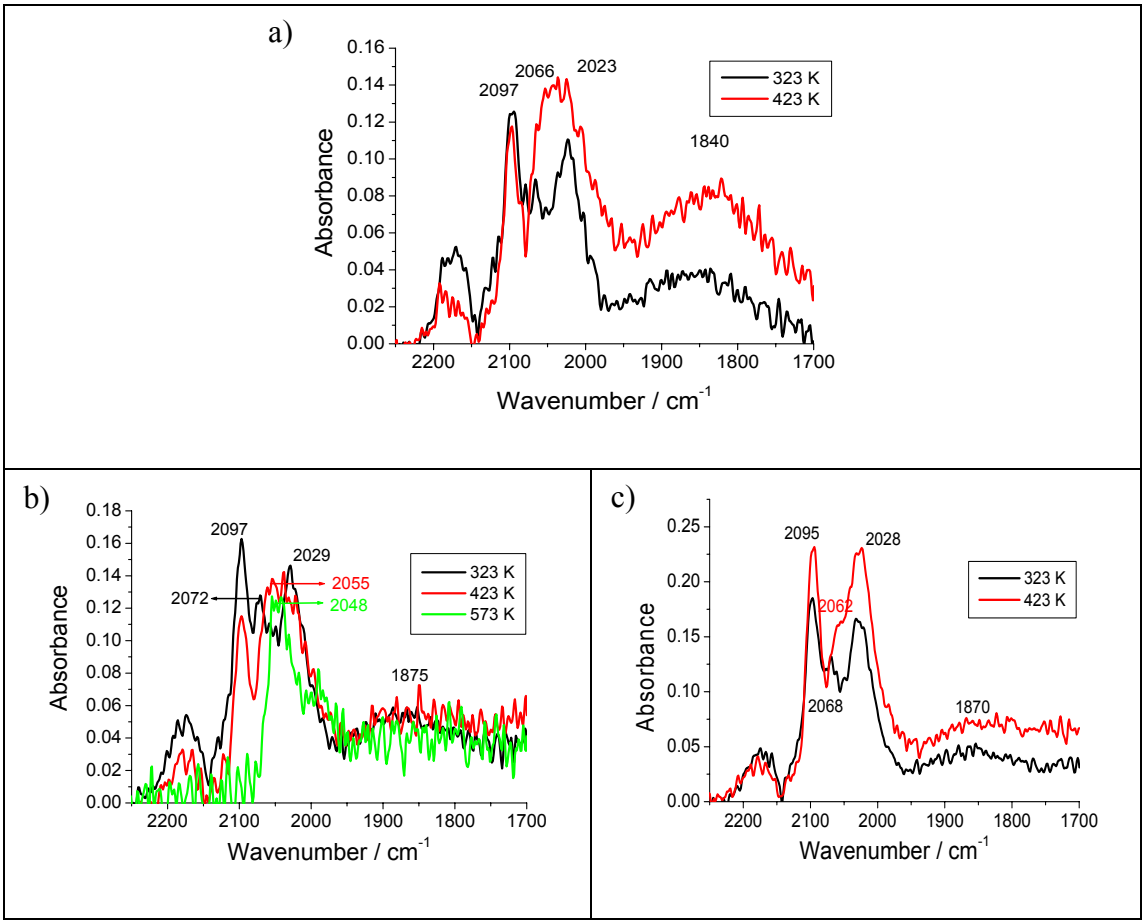

Figure 4.25 DRIFTS spectra of 4 wt% $Rh/ZrO_2/Al_2O_3$ (a) and 4 wt% $Rh/CeO_x/ZrO_2/Al_2O_3$ b) (Ce:Zr;1:1); c) (Ce:Zr;2:1) after CO exposure at varies temperature: 323 K, 423K, 573 K

The EXAFS analysis highlights the structural changes of Rh particles throughout the extensive CO exposure at different temperatures (Figure 4.26). As was described for higher Rh loadings, a similar tendency of RhRh bond lengths and RhRh coordination number variations is established. The increase in Rh-Rh distance as well as the reduction of RhRh CN after CO exposure at 323 K indicates the break up of Rh particles. Further heating of the system to 573 K decreases the RhRh bond lengths and the RhRh coordination numbers are slightly increased, which can

suggest some Rh particle agglomeration. Moreover, the zirconia and ceria-zirconia doping increase the size of Rh particles, the size becoming comparable to 4 wt% Rh supported on alumina.

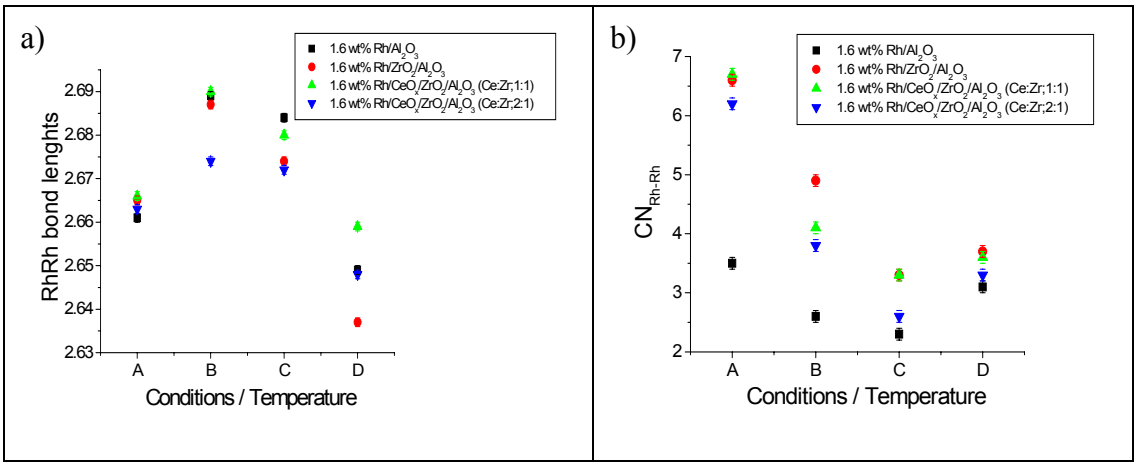

Figure 4.26 Variation of RhRh bond lengths (a) and RhRh coordination number (b) of 1.6 w% Rh/Al_2O_3 and Ce/Zr modified Rh catalysts under different conditions; A – 5 % H_2/He, 323 K, B – 5 % CO/He, 323 K, C – 5 % CO/He, 423 K, D – 5 % CO/He, 573 K.

4.4 Discussion

4.4.1 Rh/Al_2O_3 catalysts

Exposing 4 wt% Rh/Al_2O_3 catalysts to 5 % CO/He induced the structural change of the Rh particles. The EDE and IR data obtained both report that subsequent disruption of the Rh nanoparticles take place on the alumina. The process of the oxidative disruption of Rh particles by CO is well known and has been studied in the past [7]. However, clear correlations exist between temperature and the extensive disruption of Rh nanoparticles.

In the case of CO interaction with the 4 wt% Rh/Al_2O_3 catalyst at 323 K, the nearest neighbour Rh-Rh coordination has decreased from 7.2 to 5.4, corresponding to average particles with ca. 32-46 Rh atoms to ca. 12-17 Rh atoms. No distances other than Rh-Rh are statistically significant for 4 wt% Rh catalysts. As noted by scanning EXAFS, particles adopt the bulk, face centred cubic structure, as evidence by the presence of the appropriate further neighbour coordination distances. The FT spectrum clearly shows that the CO has interacted with the Rh atoms and disrupted their particles and the formation of isolated Rh^+ sites is indicated by DRIFTS study. The study by Johnston *et al.* also supported the obtained results [40]. In the EXAFS study Van't Blik *et al*. observed also that small Rh crystallites initially present in Rh/Al_2O_3 catalysts broke up into isolated Rh complexes upon CO exposure, forming

$Rh(CO)_2$ species [6]. This was confirmed by Solymosi and Pasztor in their IR investigations [4]. The EDE/IR/MS results indicate that the level of Rh disruption is slightly increased when increasing the temperature up to 423 K. However, the long CO exposure through the Rh catalyst at 423 K affects the agglomeration of the small Rh particles as the RhRh occupation increased whilst Rh-Rh distance decreased. Focusing on the ν_{CO} region associated with Rh bound CO, a number of prominent changes are apparent in the spectra as the temperature is increased.

The formation of $Rh^I(CO)_2$ species can therefore be directly correlated to the disruption of Rh particles. This result correlates well with the previous findings of the disruptive capacity on similar Rh systems, where the corrosion of Rh nanoparticles has been associated with the adsorption of geminal dicarbonyl species [5, 7, 41].

Analysis of the DRIFTS data shows within the first ca. 4 seconds of CO exposure, there is a rapid formation of $Rh^I(CO)_2$ species. It appears that the evolution of carbonyl containing surface species is, within 323 – 423 K, independent of the temperature used. They stabilise by ca. 20 seconds. Simultaneously the Rh-Rh coordination number derived from the EDE data is seen to decrease over this time. As the $CN_{Rh\text{-}Rh}$ value of the $Rh^I(CO)_2$ species is formally 0, the obtained RhRh coordination number after CO exposure indicates the amount of larger Rh particles present in the system, wherein the linear and bridged species adsorbed. The formation of these CO species is due to both steric and electronic limitations of extended Rh surfaces under these conditions [16]. It has been proposed that the adsorption of CO on Rh crystallites supported on Al_2O_3 generates a geminal dicarbonyl, linear and bridged Rh species as it is shown on Scheme 4.1 adapted from Basu *et al.* [2]. At the beginning CO molecules are adsorbed on the Rh surface. Step 2 involves the weakening of Rh-Rh bonds by the adsorption of CO on Rh^0 surface sites, which spread out the smaller Rh particles across the whole support. Such disruption in favourable sites leads to the liberation of atomically dispersed Rh species which can migrate across the oxide surface to isolated OH, creating geminal dicarbonyl species. The adsorbed linear and bridged species adsorbed on the extended surface area seem to be stable.

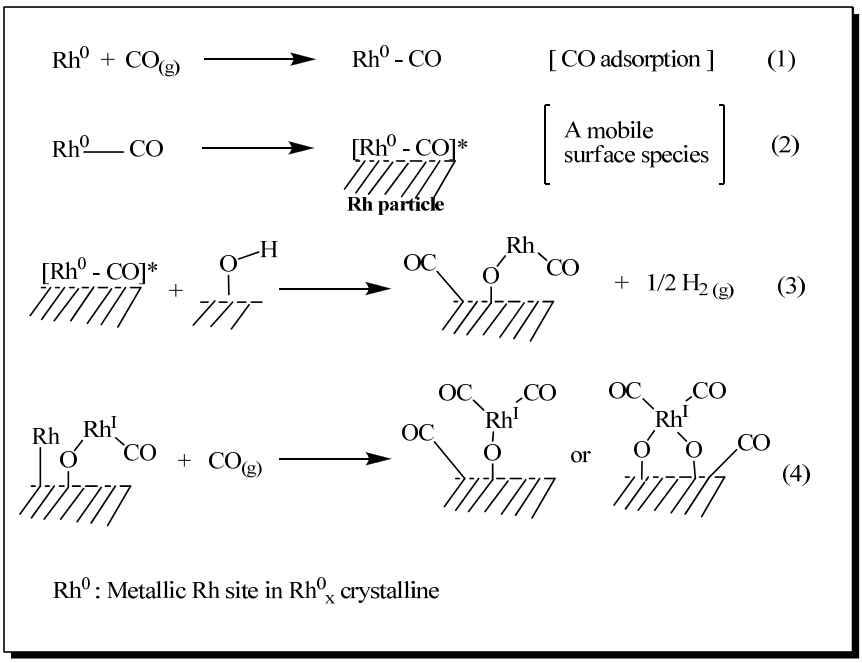

Scheme 4.1. A illustrative mechanism for formation of Rh $^{I}(CO)_2$, linear and bridged species on γ-Al_2O_3.

Whereas at higher temperatures, 473-573 K, another effect of adsorbed CO comes into prominence, which leads to the formation of the metallic Rh fraction at the expense of isolated Rh sites. The CO dissociation, which depends on the metal particle size and temperature, could block the sites for the $Rh(CO)_2$ adsorption. Moreover, the geminal dicarbonyl species become thermally unstable at higher temperatures and even if transiently formed decomposed quickly. The intensity of geminal dicarbonyl species is greatly diminished at 473 K and they are essentially gone at 573 K. This result shows that Rh particles are quickly reduced under CO exposure at 573 K diminishing the interaction of Rh with γ-Al_2O_3 as a result of CO molecules adsorbing on the reduced Rh surface in the form of linear and bridging species. These results indicate that although Rh particles are corroded at higher temperature, larger particles remaining on the surface at the end of the experiment. Such particle sintering also explains the overall decrease in the number of Rh particles present after CO exposure at higher temperature. Ballinger *et al*. [21] suggests that the heating of similar Rh systems from 400 K, initiates the removal of 'isolated' Al-OH groups that decrease the $Rh^{I}(CO)_2$ adsorption. The removal of OH groups at higher temperatures could therefore inhibit the disruption process and larger, metallic Rh particles would present on the surface.

Analogous experiments performed upon lower metal loading, 1.6 wt% Rh/γ-Al_2O_3, show that the adsorption characteristics and overall processes involved to be similar. The EDE and IR data obtained reveal the oxidative disruption of the Rh nanoparticles on the alumina support. As indicated by DRIFTS data all three IR active CO species are formed during CO exposure as in the case of 4 wt% Rh sample. However, relatively large amounts of the Rh geminal dicarbonyl entities than the other CO species are formed on the Rh surface when compared to 4 wt% Rh system. At 323 K, the drop of the Rh-Rh coordination number of 1.6 wt% Rh/Al_2O_3 reflects a decrease in the number of atoms in the average particle from ca. 13 to 7 and the additional RhO shell has been detected. Since RhRh occupation is still present even after 60 seconds of CO exposure and CO species adsorbed also on the metallic Rh the obtained results suggests that merely the partial disruption of Rh particles to atomically dispersed Rh entities occur in this system. The calculation of CO uptake indicates that an average of two CO molecules correspond to one Rh atom. Considering the fact, that the initial Rh particle size of 1.6 wt% Rh sample are much smaller than 4 wt% Rh loading case, the complete disruption Rh particles to atomic level has not occurred as it was the case in the previous studies [5, 33].

Increasing temperature to 423 K, the EDE and IR data highlight larger Rh disruption as well as greater quantity of $Rh^I(CO)_2$ adsorption. On the other hand, as TEM analysis indicates, rhodium particles of fresh 1.6 wt% and 4 wt% Rh catalysts calculated from particle size distribution, are very similar in size ~2 nm (chapter 3, section 3.2.2). However, the coordination number derived from EDE data is an average of all the particles present in the system, which the diverse range of sizes can be distinguish from the particle size distribution of TEM image.

At 573 K, geminal dicarbonyl species are not present while only linear and bridged bound CO on rhodium have been observed, which are increased in intensity and shifted to lower frequency with increasing temperature. The formation of this species at the expense of the geminal dicarbonyl species after heating of rhodium in CO flow has been previously reported by others and is indicative of the agglomeration of isolated rhodium ions and formation of metal crystallites [4, 42, 43].

4.4.2 $Rh/CeO_x/Al_2O_3$ catalysts

The significant difference of catalytic behaviour has been observed between the two ceriated 4 wt% Rh catalysts depending on the synthesis procedure.

First of all, it is worth mention that the initial Rh particles size is much smaller for 4 wt% $Rh/CeO_x/Al_2O_3$ (method I) than for ceriated Rh catalysts produced by method II, although the Rh loading is the same. At 323 K, particles of the former catalysts contains an average of 17 Rh atoms, however the latter Rh sample includes greater particles with an average of 68 Rh atoms. The observed outcome is supported with TEM analysis, highlighting the mean particle size of fresh 4 wt% $Rh/CeO_x/Al_2O_3$ (method I) estimated to 1.9 nm and 4 wt% $Rh/CeO_x/Al_2O_3$ (method II) containing the Rh particles of ca. 2.6 nm. Thus, the distinct structural-functional variations of these systems could be expected throughout CO exposure.

During the exposure of the ceriated Rh catalysts to 5 % CO/He, the EDE data indicates that the similar level of the Rh disruption occurs on the Rh surface at varies temperatures. Focusing on $Rh/CeO_x/Al_2O_3$ (I), smaller Rh particles exist while CO exposure at varies temperatures when compared with the undoped Rh on alumina. On the other hand, the IR and MS results highlight very similar adsorption characteristics and overall processes to be involved.

However, the larger Rh particles of 4 wt% $Rh/CeO_x/Al_2O_3$ (method II) have been observed throughout the entire CO exposure at various temperatures when compared with the ceria-doped Rh catalysts (method I). This phenomenon suggests that ceria is in very intimate contact with the rhodium in this system. Therefore, Rh particles are isolated from easy oxidation, containing mostly metallic fraction. The XPS study of Suopanki et al. indicated that the part of reducible Rh is found to have the best catalytic activity. They have explained the existence of metallic Rh in the system by burying of the active material into the bulk of the washcoat [44]. The absence of geminal dicarbonyl species on isolated Rh sites evidence by IR spectroscopy also points to the vicinity of Rh and ceria. Thus, the adsorption of linear and bridged CO species on metallic Rh surface mostly has been reported. These CO species are in relatively good agreement with those reported for CO adsorbed on Rh/reduced CeO_2 (111) monitored by HREELS [45]. The additional bridged CO species adsorbed between Rh and Ce atoms for both ceriated Rh catalysts clearly highlights the presence of Rh and Ce next to each other as it was already indicated by the STEM EDX HAADF line profile analysis, described in the previous chapter.

As it was already observed in the previous studies [35, 46-49], ceria is also able to adsorb carbon monoxide forming the bridged, bidentate and polydentate carbonate entities. The IR technique detects these CO species in the 1700 cm^{-1} – 1200 cm^{-1} range showing the complex spectrum of adsorbed CO. Additionally, two bands at 2166 cm^{-1} and 2150 cm^{-1} are ascribed to CO-Ce^{4+} species [47]. However, our IR study of ceriated Rh catalysts does not detect any other CO species adsorbed on Ce sites such as carbonates and carboxylate species, which could be due to low Ce loading in the overall Rh catalysts.

The infrared spectrum of CO absorbed on both ceriated Rh samples displays a blue shift of linear CO frequency, with larger variation of ν(CO) for ceria promoted Rh catalysts (method II). This phenomenon is associated with larger Rh particles and the Ce and Rh particles interactions. The electron density, which could be used to back bond to the CO, is removed and consequently weakens the Rh-CO bond (Scheme 4.2) [39]. This is consistent with XAFS results, where the coordination number of Rh-Rh shell is higher for the ceriated sample produced by method II than for ceriated Rh catalyst (method I) and undoped Rh catalyst. Larger Rh particles observed for ceriated Rh catalyst (method II) can be also a result of extended reduction step within this synthesis procedure (Chapter 3, section 3.2.1). The Raman investigation of similar systems by Murrell et al. has proved the interaction between the precious metal and the ceria existed on the surface [50].

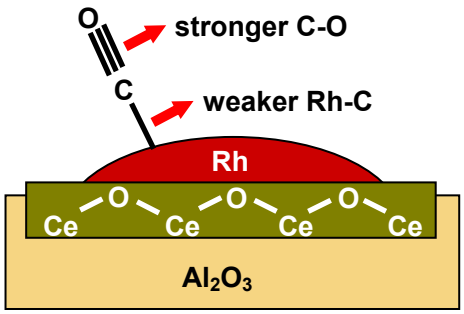

Scheme 4.2 Structural rearrangement of the Rh sites due to Rh – Ce interaction

The postulated explanation has been supported by MS results indicating the lowest CO coverage of 4 wt% $Rh/CeO_x/Al_2O_3$ (II) among three catalysts investigated (4 wt% Rh/Al_2O_3, 4 wt% $Rh/CeO_x/Al_2O_3$ (I), 4 wt% $Rh/CeO_x/Al_2O_3$ (II)). This phenomenon can be assigned to the steric and electronic limitation of CO adsorption to greater Rh particles or to Ce coverage on Rh particles.

Analogous results have been obtained over 1.6 wt% Rh catalysts promoted by ceria. The substantial oxidative disruption of Rh particles occurs over both Rh samples, highlighted by the drop of RhRh coordination number throughout CO exposure. Furthermore, DRIFTS data show all three IR active CO species formed during CO exposure as in the case of undoped 1.6 wt% Rh sample. However, a relatively larger amount of the linear CO entities than the other CO species are formed on the Rh surface at 323 K when compared to Rh on alumina system. The blue shift of linear CO band has also been reported over both ceriated Rh catalysts when compared to undoped Rh sample. Moreover, the presence of the additional band in the region of 1700 cm^{-1} for both samples indicates the close contact of Rh and Ce atoms. On the other hand, the STEM EDX study carried out over a fresh form of these catalysts show that Rh particles exist together with the Ce atoms of $Rh/CeO_x/Al_2O_3$ (II) as it is not the case for ceriated Rh catalysts prepared by method I. Furthermore, the XPS/XANES study over fresh Rh catalysts indicates that ceria located on the rhodium surface of $Rh/CeO_x/Al_2O_3$ (method II) only provides partial protection of rhodium for oxidation. However, it can be suggested that the pre-treatment procedure modifies the Rh/Ce particles morphology.

The overview of all results has proved that structural performance of the catalysts cannot be modified by simply adding ceria to the catalytic system.

4.4.3 $Rh/ZrO_2/Al_2O_3$ – $Rh/CeO_x/ZrO_2/Al_2O_3$

At the start of the experiment, 4 wt% $Rh/ZrO_2/Al_2O_3$ exhibits the largest Rh particles containing an average of ca. 53 Rh atoms at 323 K. Thus, the greatest RhRh occupation throughout CO exposure at various temperatures has been detected by EDE data. The MS results show the lowest CO uptake that is due to steric and electronic limitation of extended Rh surface, previously observed in ceriated Rh catalysts (method II) case. However, the absorption of geminal dicarbonyl, linear and bridged CO species has been reported in the DRIFTS spectra highlighting that Zr dopant only does not isolate the Rh particles from easy oxidation as it has been observed in ceria doping of Rh catalyst behaviour prepared by the same synthesis method. No signal was detected in the 1700 cm^{-1} – 1200 cm^{-1} ascribed to carbonates linked to zirconia [48] that can be attributed to low ZrO_2 loading in the systems investigated.

Incorporation of CeO_x in the zirconiated Rh catalysts diminished the RhRh occupation under conditions investigated. Larger CeO_x loading in the Rh system increases relatively amount of linear CO species adsorbed on the Rh surface as well as the presence of bridged Rh-(CO)-Ce species suggesting the presence of the Ce-Rh interaction. Furthermore, the blue shift of linear CO species rises up with the CeO_x doping. It has been already investigated that introduction ZrO_2 into the CeO_x lattice generates a structural modification of Rh catalysts enhancing the redox properties of Ce^{3+}/Ce^{4+} during the catalytic process [51-53]. However, in our XAFS/DRIFTS/MS studies over ceria-zirconia promoted Rh catalysts the particular ZrO_2 effect on CeO_x behaviour could not be detected. In fact, the additional *in situ* Ce K edge XANES or *in situ* XPS study would be necessary in order to follow the ZrO_2 impact in behaviour of the investigated Rh catalysts.

In the view of 1.6 wt% Rh catalysts doped with zirconia and ceria-zirconia, the DRIFTS spectra detects three main peaks assigned to geminal dicarbonyl, linear and bridged CO species. However, the poor quality of IR data excludes the possibility of detection of the other CO species such as bridged Rh-(CO)-Ce species displayed previously on ceriated Rh catalysts. The EXAFS studies of zirconia and ceria-zirconia doped 1.6 wt% Rh catalysts demonstrate large Rh particles comparable to the size of 4 wt% Rh/Al_2O_3 sample.

4.5 Conclusion

In this work the CO interaction with the wide range of Rh catalysts has been investigated using the array of XAFS/DRIFTS/MS techniques in the time-resolved, *in situ* manner. This experimental method, which allows obtaining interesting information about the catalysts structure, performance and reactivity, proved the compatibility of these techniques.

Analysis of the CO exposure over Rh catalysts at various temperatures effectively illustrates the processes that occur over these systems. Generally, in the range of the temperatures 323-423 K, the IR results indicated that after CO exposure mostly geminal dicarbonyl species adsorbed on the Rh surface while the EXAFS analysis suggests the reduction of Rh particles size with the elongation of RhRh bonds which is due to the oxidative disruption of Rh particles. This phenomenon is supported by increased amount of CO uptake calculated from MS gas evolution. However, an altered structural response has been mainly observed for Rh catalysts doped by ceria (method II). The ceria deposited on pre-supported Rh catalysts minimise the Rh-γ-Al_2O_3 interaction and have some impact on the formation of larger Rh particles, wherein the linear and bridged species are mainly adsorbed on the Rh surface. However, Rh catalysts with Zr doping containing the largest Rh particles still adsorb geminal dicarbonyl, linear and bridged CO species. Additionally, the lowest CO uptake has been observed by MS. The addition of CeO_x in the zirconiated Rh catalysts decrease the RhRh occupation and relatively larger amount of linear and bridged CO species was adsorbed on the Rh surface, which is assigned to ceria protection from facile Rh oxidation.

In the case of 473 K and above, predominantly linear and bridged species adsorbed on the Rh surface of all Rh catalysts, the RhRh occupation increased with the shortening of Rh-Rh distance. At the same time a reduced amount of CO molecules adsorbed on the Rh surface has been observed. This has been assigned to the agglomeration of Rh particles, which exist in the system in the reduced form and no strong interaction with the alumina support is present. However, a closer analysis of the disruption and agglomeration of Rh particles using the battery of EDE/DRIFTS/MS techniques is very complicated with factors such as particle morphology, temperature and promoters playing key roles in the behaviour of this system.

4. 6 References

1. Antoniewicz, P.R., Cavanagh, R. R., Yates, J. T., J. Chem. Phys., 1980. **73**: p. 3456-3459.
2. Basu, P., Panayotov, D., Yates, J. T., J. Am. Chem. Soc., 1988. **110**: p. 2074-2081.
3. Diaz, A.L., Quigley, W. W. C., Yamamoto, H. D., Bussell, M. E., Langmuir, 1994. **10**: p. 1461-1471.
4. Solymosi, F., Pasztor, M., J. Phys. Chem., 1985. **89**: p. 4789-4793.
5. Suzuki, A., Inada, Y., Yamaguchi, A., Chihara, T., Yuasa, M., Nomura, M., Iwasawa, Y., Angew. Chem. Intl. Ed., 2003. **42**: p. 4795-4799.
6. Van't Blik, H.F.J., Van Zon, J. B. A. D., Huizinga, T., Vis, J. C., Koningsberger, D. C., Prins, R., J. Chem. Phys., 1983. **87**: p. 2264-2267.
7. Yang, A.C., Garland, C. W., J. Phys. Chem., 1957. **61**: p. 1504-1512.
8. Newton, M.A., Dent, A. J., Fiddy, S. G., Jyoti, B., Evans, J., Phys. Chem. Chem. Phys., 2007. **9**: p. 246-249.
9. Evans, J., Hayden, B. E., Newton, M. A., Surf. Sci., 2000. **462**: p. 169-180.
10. Taylor, K.C., Catal. Rev. - Sci. Eng., 1993. **35**: p. 457-481.
11. Trovarelli, A., Catal. Rev. - Sci. Eng., 1996. **1996**: p. 439-520.
12. Balducci, G., Kaspar, J., Fornasiero, P., Graziani, M., Islam, M. S., Gale, J. D., J. Phys. Chem., 1997. **101**: p. 1750-1753.
13. Fornasiero, P., Di Monte, R., Ranga Rao, G., Kaspar, J., Meriani, S., Trovarelli, A., Graziani, M., J. Catal., 1995. **151**: p. 168-177.
14. Suhonen, S., Valden, M., Hietikko, M., Laitinen, R., Savimaki, A., Harkonen, M., Appl. Catal., A, 2001. **218**: p. 151-160.
15. Cavers, M., Davidson, J. M., Harkness, I. R., Rees, L. V. C., McDougall, G. S., J. Catal., 1999. **188**: p. 426-430.
16. Rice, C.A., Worley, S. D., Curtis, C W., Guin, J. A., Tarrer, A. R., J. Chem. Phys., 1981. **74**: p. 6487-6497.
17. Yates, J.T.J., Duncan, T. M., Worley, S. D., Vaughan, R. W., J. Chem. Phys., 1979. **70**: p. 1219-1224.
18. Hyde, E.A., Rudham, R., Rochester, C. H., J. Chem. Soc. Faraday Trans. 1, 1983. **79**: p. 2405-2423.
19. Worley, S.D., Rice, C. A., Mattson, G. A., Curtis, C. W., Guin, J. A., Tarrer, A. R., J. Chem. Phys., 1982. **86**: p. 2714-2717.

20. Newton, M.A., Dent, J. A., Diaz-Moreno, S., Fiddy, S. G., Jyoti, B., J., Evans, J., Chem. Eur. J., 2006. **12**: p. 1975-1985.
21. Ballinger, T.H., Yates, J. T., J. Phys. Chem., 1991. **95**: p. 1694-1698.
22. Paul, D.K., Yates, J. T., J. Phys. Chem., 1991. **95**: p. 1699-1703.
23. Zaki, M.I., Ballinger, T. H., Yates, J. T., J. Phys. Chem., 1991. **95**: p. 4028-4033.
24. Hayden, B.E., King, A., Newton, M. A., Yoshikawa, N., J. Mol. Catal., 2001. **167**: p. 33-46.
25. Johnston, P., Joyner, R. W., J. Chem. Soc. Faraday Trans., 1993. **89**: p. 863-864.
26. Newton, M.A., Jyoti, B., Dent, A. J., Fiddy, S. G., Evans, J., Chem. Commun., 2004: p. 2382-2383.
27. Koningsberger, D.C., van Zon, J. B. A. D., van't Blik, H. F. J., Visser, G. J., Prins, R., Mansour, A. N., Sayers, D. E., Short, D. R., Katzer, J. R., J. Phys. Chem., 1985. **89**: p. 4075-4081.
28. Jentys, A., Phys. Chem. Chem. Phys., 1999. **1**: p. 4059-4065.
29. Sinfelt, J.H., Via, G. H., Lytle, F. W., J. Chem. Phys., 1977. **67**: p. 3831-3837.
30. van Zon, J.B.A.D., Koningsberger, D. C., van't Blik, H. F. J., Sayers, D. E., J. Chem. Phys., 1985. **12**: p. 5742-5749.
31. Van't Blik, H.F.J., Van Zon, J. B. A. D., Huizinga, T., Vis, J. C., Koningsberger, D. C., Prins, R., J. Am. Chem. Soc., 1985. **107**: p. 3139-3147.
32. Yates, J.T.J., Duncan, T. M., Vaughan, R. W., J. Chem. Phys., 1979. **71**: p. 3908-3915.
33. Jyoti, B., *PhD Thesis*, in *Chemistry*. 2006, University of Southampton: Southampton.
34. Newton, M.A., Dent, A. J., Fiddy, S. G., Jyoti, B., Evans, J., J. Mater. Sci., 2007. **42**: p. 3288-3298.
35. Lavalley, J.C., Saussey, J., Lamotte, J., Breault, R., Hindermann, J. P., Kiennemann, A., J. Phys. Chem., 1990. **94**: p. 5941-5947.
36. Ulmer, S.W., Skarstad, P. M., Burlitch, J. M., Hughes, R. E., J. Am. Chem. Soc., 1973. **92**: p. 4469-4471.

37. Kiennemann, A., Breault, R., Hindermann, J. P., J. Chem. Soc. Faraday Trans., 1987. **83**: p. 2119-2128.
38. Loof, P., Kasemo, B., Andersson, S., Frestad, A., J. Catal., 1991. **130**: p. 181-191.
39. Blyholder, G., J. Phys. Chem., 1964. **68**: p. 2772-2777.
40. Johnston, P., Joyner, R. W., Pudney, P. D. A., J. Phys. Condensed Matter, 1989. **1**: p. SB171-SB176.
41. Anderson, J.A., J. Chem. Soc. Faraday Trans., 1991. **87**: p. 3907-3911.
42. Anderson, J.A., Rochester, C. H., J. Chem. Soc. Faraday Trans., 1991. **87**: p. 1479-1483.
43. Dictor, R., Roberts, S., J. Phys. Chem., 1989. **93**: p. 2526-2532.
44. Suopanki, A., Polvinen, R., Valden, M., Harkonen, M., Catal. Today, 2005. **100**: p. 327-330.
45. Stubenrauch, J., Vohs, J. M., Catal. Lett., 1997. **47**: p. 21-25.
46. Bensalem, A., Muller, J. C., Tessier, D., Bozon-Verduraz, F., J. Chem. Soc. Faraday Trans., 1996. **92**: p. 3233-3237.
47. Bozon-Verduraz, F., Bensalem, A., J. Chem. Soc. Faraday Trans., 1994. **90**: p. 653-657.
48. Daturi, M., Binet, C., Lavalley, J. C., Blanchard, G., Surf. Interface Anal., 2000. **30**: p. 273-277.
49. Li, C., Sakata, Y., Arai, T., Domen, K., Maruya, K., Onishi, T., J. Chem. Soc. Faraday Trans., 1989. **85**: p. 929-943.
50. Murrell, L.L., Tauster, S. J., Anderson, D. R., Stud. Surf. Sci. Catal., 1991. **71**: p. 275-285.
51. He, H., Dai, H. X., Ng, L. H., Wong, K. W., Au, C. T., J. Catal., 2002. **206**: p. 1-13.
52. Sun, H.P., Pan, X. P., Graham, G. W., Jen, H. W., McCabe, R. W., Thevuthasan, S., Peden, C. H. F., App. Phys. Lett., 2005. **87**: p. 201915-1-3.
53. Vlaic, G., Fornasiero, P., Geremia, S., Kaspar, J., Graziani, M., J. Catal., 1997. **168**: p. 386-392.

Chapter 5

5. The study of CO oxidation over supported Rh catalysts

5.1 Introduction

The previous chapter investigated the interaction of CO with Rh nanoparticles using the complimentary data afforded by the XAFS/DRIFTS/MS experiment. The results obtained over the series of Rh catalysts across various temperatures successfully delivered an understanding of the disruptive processes occurring over the Rh. To this effect this chapter will aim at understanding the catalytic behaviour of Rh samples within the CO oxidation process. The dynamic nature of the catalytic system upon interaction with reactants such as: CO and O_2 requires monitoring the formation of the potential active phases during the course of the reaction. For this reason, the array of XAFS/DRIFTS/MS techniques in the *in situ*, time-resolved manner was used to follow the CO oxidation process over a series of Rh catalysts.

CO catalytic oxidation has been extensively studied over Rh catalysts in the last couple of decades [1-6]. A high scientific interest of this process is due to the importance of removing toxic CO from industrial and automotive exhausts [7-9] and traces of CO from H_2 feed gas for fuel cells [10, 11]. Therefore, the main aim of that research is developing the novel catalysts that can work under extreme process conditions, increasing its efficiency and working time.

It has been widely reported that the CO oxidation reaction is greatly promoted by the incorporation of CeO_x oxides with the Rh nanoparticles supported on alumina [12, 13]. It was highlighted that the intimate contact between the CeO_2 based oxides and the Rh metal may alter the oxidation state of the supported Rh particles. Yu Yao concluded that two types of surface sites (zero-valent and oxidised) may be considered to explain the striking differences observed in CO-O_2 kinetics on CeO_2-promoted Rh catalysts compared with undoped Rh catalysts [14]. Oxidations and reductions of ceria are fast and it is thus capable of storing oxygen during lean periods and releasing it during rich periods [13]. The induction of zirconium to the cubic structure of ceria prevents the grain growth of ceria crystallites at high temperatures and thus increases the thermal stability of the catalysts [15]. Moreover, the dissolution of zirconia into ceria enhances the oxygen mobility which improves its ability to store oxygen [16]. Therefore, the constant improvement of three-way catalyst's efficiency revealed the need of study the Ce-Rh and Zr-Ce-Rh interactions through the CO oxidation.

The scope of experiments will then be focused to study both the ceria and zirconia effect on the activity of Rh catalysts and the influence of nature of Rh metal on the CO oxidation catalytic reaction. In the experiment, each reactive gas in feedstock will be periodically alternated at various temperatures to monitor the structural response of the system to such changes in the reactive environment. In the next experiment the effectiveness of the Rh catalysts was studied by determining the temperature light-off of CO conversion.

5.2 Experimental section

5.2.1 O_2/CO switching experiment

The O_2/CO switching experiment over the series of Rh catalysts has been studied throughout two allocated beamtimes (CH2194, CH2335) on ID24 at ESRF in Grenoble, France using the combined EDE/DRIFTS/MS apparatus. The detailed description of these techniques is given in chapter 2. First, samples has been reduced *in situ* before reaction by heating up to 573 K under the flow of 5 % H_2/He, then oxidised by 5 % O_2/He until the H_2O and carbonaceous deposition disappear from the system, and subsequently was switched back to 5 % H_2/He. After full pre-treatment, the system was cooled down in H_2 to the determined temperature and purged by He. The O_2–CO switching experiment was investigated over the analysed rhodium catalysts at different temperatures: 323, 373, 423, 473, 573 K. The representative reactive gases of O_2 and CO have been used in this project as a mixture of 5 % O_2/He and 5 % CO/He, respectively. The order of gases was as follow: He–O_2>CO>O_2>CO>O_2>CO–He with a flow of 25 cm^3 min^{-1}. During first beamtime time of exposure for each gas in one switch was 45 s at 323, 373, 423 K and 20 s at 473, 573 K. The longer period of time for one switch is needed at lower temperatures, because the reaction rate is much slower than at higher temperatures. In the second beamtime the gas exposure for one switch was increased to 60 s, in order to ensure that the step of the oxidation and CO adsorption took place completely. The total catalyst load used was about 0.025 g. All experiments lasted 360 s and EDE/DRIFTS/ME data were collected simultaneously. EXAFS detection was carried out via the FReLoN CCD camera with a total acquisition time with 10 spectra of ca. 10 ms. The DRIFTS and mass spectrometric data obtained matched the repetition rate of the EDE.

5.2.2 CO oxidation reaction in temperature ramp mode

The reactivity of Rh catalysts throughout CO oxidation has been monitored by using a Pfeiffer mass spectrometer in Southampton University. In a typical experiment, the catalyst sample (ca. 0.025 g) has been loaded into a quartz tube (ca. 4 mm internal diameter, wall thickness ca. 0.2 mm) and secured in place using quartz wool plugs, yielding a sample bed of around 5 mm in length. The tube has been placed into a microreactor and a 0.5 mm mineral insulated thermocouple was inserted directly into the catalyst bed. Each catalyst was pre-treated *in situ* prior to the experiment according to the same procedure using the DRIFTS cell. The pre-treatment includes the reduction at 573 K under the flow of 5 % H_2/He, oxidation under 5 % O_2/He and again reduction under 5 % H_2/He at 573 K. After full pre-treatment, the system was cooled down to room temperature in H_2 and purged by He. The CO oxidation reaction has been tested by exposing the Rh catalysts to a reactive gas mixture (derived from flows of 5 % CO/He and 5 % O_2/He mixed in predetermined proportions) with a total flow of 25 ml min^{-1}. Samples were then heated up to 573 K whilst the post sample composition of the feedstock was continuously monitored by using a quadrupole Pfeiffer mass spectrometer interfaced to the gas flow through a fused silica capillary.

5.3 Results

The quality of the EDE spectra obtained for 1.6 wt% Rh systems was not sufficient to permit the structural analysis of EXAFS region, therefore only the XANES parameters of these systems will be reported upon to indicate the structural behaviour of these Rh catalysts.

5.3.1 Rh/γ-Al_2O_3

5.3.1.1 4 wt% Rh systems

At the start of EDE/DRIFTS/MS data analysis of the O_2/CO switching experiment the variation of XANES region during the catalytic process was studied in order to understand and quantify the redox processes that occur over supported Rh catalysts.

Figure 5.1 shows raw Rh K edge EDE data taken at 573 K for both a fully reduced and oxidised 4 wt% Rh/Al_2O_3 with an acquisition time of 100 ms. The characteristic XANES features of Rh at different oxidation states can be observed by a simple

survey of the spectra. The energy of 23250 eV was used to indicate the point where major changes in the XANES pattern occur between the diverse phases of Rh under the oxidised and reduced conditions.

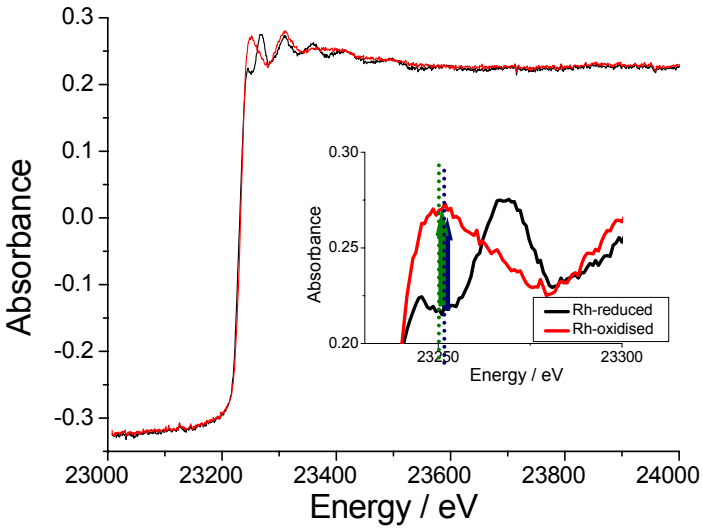

Figure 5.1 Raw EDE adsorption data derived from fully reduced (black line) and oxidised (red line) Rh nanoparticles at 573 K. The green arrow highlights the region in XANES that is used to follow the redox cycles.

Figures 5.2a and 5.2b show the dynamic response of 4 wt% Rh/Al_2O_3 to the oxidation and the reduction by CO as a function of time at the temperature indicated as measured by changes in Rh K edge XANES observed at 23250 eV. Each trace has been set to 0 at the start of the experiment, where Rh is fully reduced. The time-resolved XAFS data revealed the system to be far from static. The variations presented are due to the interaction of the O_2 and CO with the Rh particles. During oxygen exposure the XANES difference increased (rhodium remains oxidised) and while CO exposure the XANES variation decreased (rhodium becomes more reduced). The oxidation degree of Rh particles at the particular reaction step correlated well with increasing temperature. The level of Rh oxidation at 323 K and 373 K after the first switch was equivalent; however only in the former case during second cycle rhodium was getting more oxidised drastically with the delay of 30s. Subsequently rhodium becomes more reduced when the gas is switched back to CO. It can be observed that the last cycle (O_2/CO) does not modify the Rh oxidation state; it seems to be constant until the end of this experiment. In the range of temperatures, 373 – 423 K, the following cycles (O_2/CO) indicate a progressive

decrease in the degree of oxidation of the Rh phase during O_2 exposure. The shapes of the XANES variations at higher temperature 473-573 K show constant oscillations for each cycle. Therefore, for our purpose the further DRIFTS/EXAFS analysis will consider mainly the extreme points of this process observed by XANES variations.

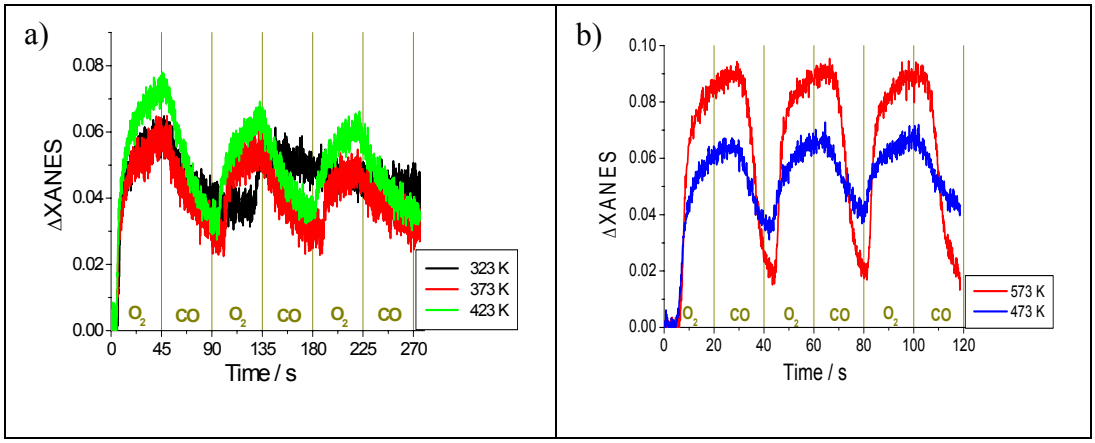

Figure 5.2. Changes in Rh K edge XANES during CO oxidation of 4 wt% Rh/Al_2O_3 at a) 323 K, 373 K, 423 K, b) 473 K, 573 K.

The O_2/CO switching experiment has been studied over the Rh catalysts comparing two different times of gas exposure: 20s and 60s (Figure 5.3). After 20 s of oxidation the Rh component reached the same level of oxidation at each O_2 step (ΔXANES ~ 0.09). The following CO exposure for 20 s reduced the Rh particles partially. When the gas exposure was increased to 60 s slightly larger Rh oxidation (ΔXANES ~ 0.1) was observed although still the complete plane response of Rh oxidation was not obtained. However the Rh particles are completely reduced under CO exposure. In order to follow in detail the structural response of the Rh catalysts upon O_2 and CO environment, the time exposure for one gas was increased for zirconia, ceria-zirconia doped Rh catalysts as is indicated in section 5.2.1.

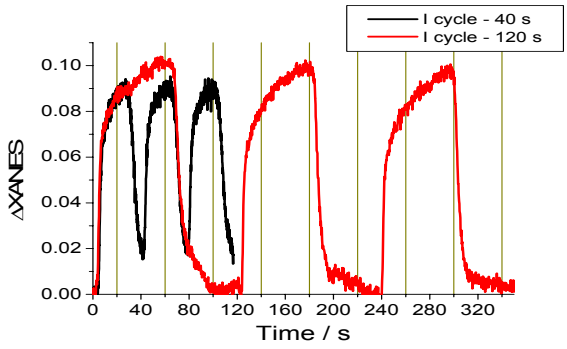

Figure 5.3 Variation of XANES during CO oxidation of 4 wt% Rh/Al_2O_3 at 573 K with two different switching time periods.

Figures 5.4a – 5.4e show the overview of IR active species observed on the Rh surface of 4 wt% Rh/Al_2O_3 during CO exposure of the first, second and third cycles at the range of temperature of 323 – 573 K. Apart of the highest temperature investigated the same series of carbonyl species adsorbed on the Rh surface are detected. Following the experiment at 323 K, the spectrum displayed the two sharp peaks at 2101 cm^{-1} and 2029 cm^{-1} assigned to rhodium geminal dicarbonyl species ($Rh^{+}(CO)_2$). These bands are overlapped with the signal of the linear species (Rh-CO) at 2071 cm^{-1}. A broad band present around 1880 cm^{-1} is ascribed to the bridged CO species. Additionally, a new band appeared at ca. 2126 cm^{-1} which is assigned to the RhO(CO) species [17]. The high frequency of this species indicates a weakly adsorbed CO species. Other workers have also observed the presence of CO adsorbed on oxidised Rh following oxidation of Rh on alumina [18, 19]. The following (O_2/CO) cycles highlight the adsorption of the same CO species and shows that their intensities gradually increase. However, at higher temperatures, 423 – 473 K, the next (O_2/CO) switches slowly diminished the amount of linear and bridged CO species, keeping the evolution of geminal dicarbonyl species constant. Considering the fact that adsorption of linear and bridged CO species occurs on the metallic Rh form, it indicates that the following O_2 exposures cause further Rh oxidation.

At 573 K, the present IR bands of CO species are typical of sites on metallic rhodium. The DRIFTS spectra displayed one sharp peak at 2043 cm^{-1} ascribed to the rhodium linear species. The bridged CO species gave a broad signal around 1880 cm^{-1}. The intensities of all signals were similar at each cycle. There was no adsorption due to the geminal dicarbonyl species on the oxidised Rh surface, even though before CO exposure the catalyst was exposed to O_2, which largely oxidised the Rh particles. These results indicate that Rh particles are quickly reduced under the flow of CO, and in the next step, CO molecules are adsorbed on the reduced Rh surface as a form of linear and bridged CO species.

Furthermore, a red shift is observed for the linear CO species when increasing the temperature, from ν ~2071 cm^{-1} at 323 K to ν ~2062 cm^{-1} at 473 K, and to ν ~2043 cm^{-1} at 573 K. The red shift of the linear CO species observed is consistent with the lower CO coverage due to the change in electron density on the particle and the reduction in the inter-CO vibrational coupling. Due to the fact that the Rh catalysts

exhibits similar behaviour detected by IR upon (O_2/CO) switches at the range of temperatures, 323 K – 473 K, only the analysis of the experiments done at 323 K, 423 K and 573 K will be included in this chapter.

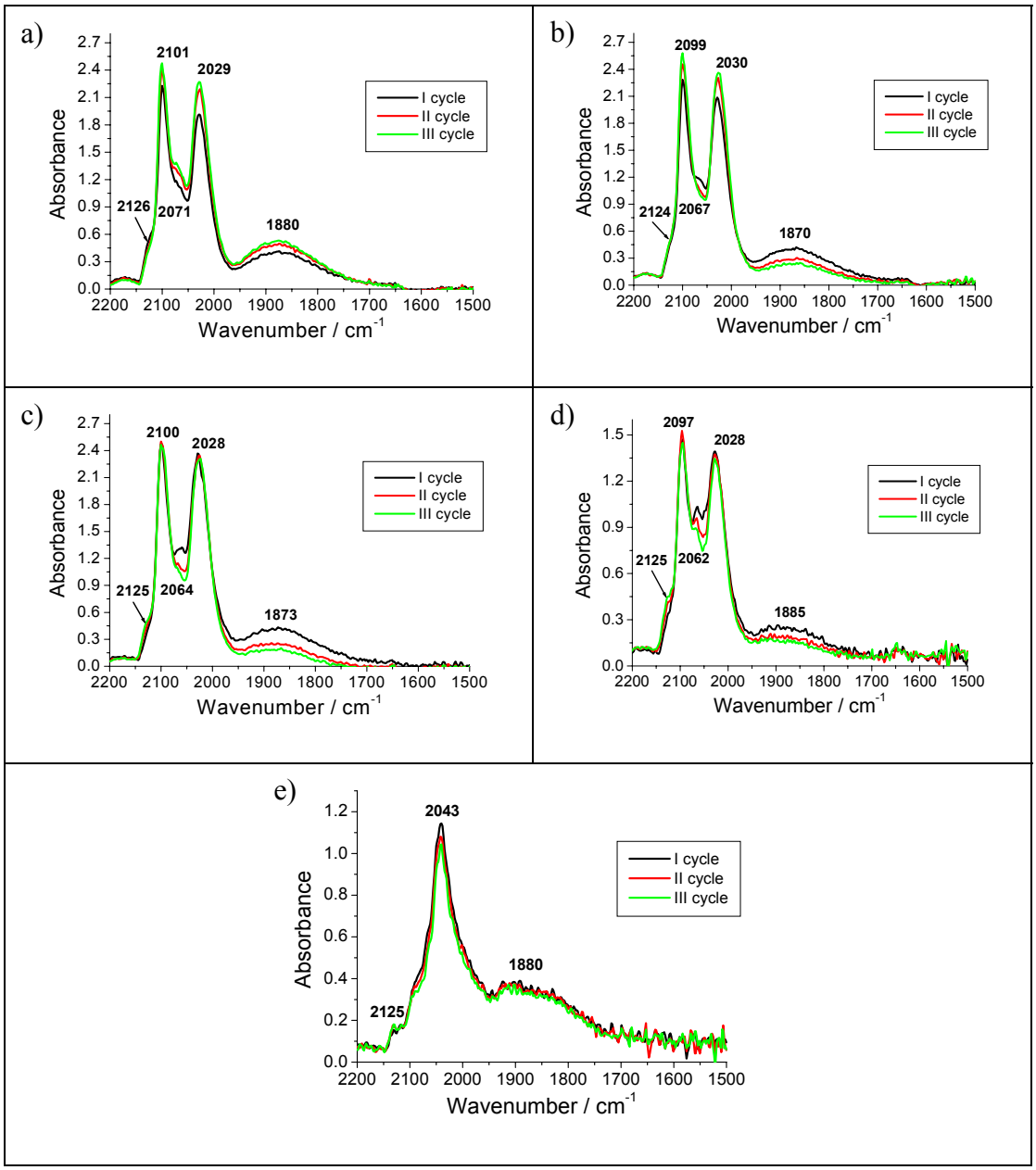

Figure 5.4. DRIFTS spectra of 4 wt% Rh/Al_2O_3 during I, II, III cycle of CO exposure at a) 323 K, b) 373 K, c) 423 K, d) 473 K, e) 573 K

Figures 5.5a, 5.5b and 5.5c show the evolution of the linear, geminal dicarbonyl and bridged CO species and CO_2 produced on the Rh surface of 4 wt% Rh/Al_2O_3 between the reduced and oxidised steps of the CO oxidation reaction at the temperatures investigated: 323 K, 423 K, 573 K. In the view of 323 K experiment (Figure 5.5a), originally the pre-reduced Rh catalyst was oxidised under the flow of 5 % O_2/He for 45 s, subsequently the flowing gas was switched to 5 % CO/He.

Simultaneously the evolution of linear, geminal dicarbonyl and bridged CO species adsorbed on the Rh surface as well as the pulse of CO_2 production were observed by DRIFTS. However, the integral intensity of symmetric vibrations of $Rh(CO)_2$ (green line) includes also the evolution of CO gas, which is not converted during the catalysis. The comparatively similar position of these two bands does not allow separation of them in the CO exposure step. Following the second cycle, after 30 s of O_2 exposure, the direct and incomplete desorption of geminal dicarbonyl species (asymmetrical mode), linear and bridged CO species occurred in the expense of some CO_2 production. In the next CO/O_2 switches the analogous trend of Rh catalysts behaviour was present; however the amount of geminal dicarbonyl species gradually increased indicating that the next O_2 exposures provided further oxidation of Rh particles. At higher temperature, 423 K, the same types of CO species adsorbed on the Rh surface, highlighting similar evolution throughout the whole experiment. Nonetheless, a large amount of CO species was removed from the Rh surface immediately and converted to CO_2 after switching to O_2 gas. It can be seen that the increase of the temperature to 573 K significantly modifies the Rh structure. The evolution of linear and bridged CO species highlighted clear oscillations of their adsorption while CO exposure and complete CO entities desorption of the surface throughout the oxidising step producing large amount of CO_2 gas. The integration of the CO species present diminished gradually within the succeeding cycles.

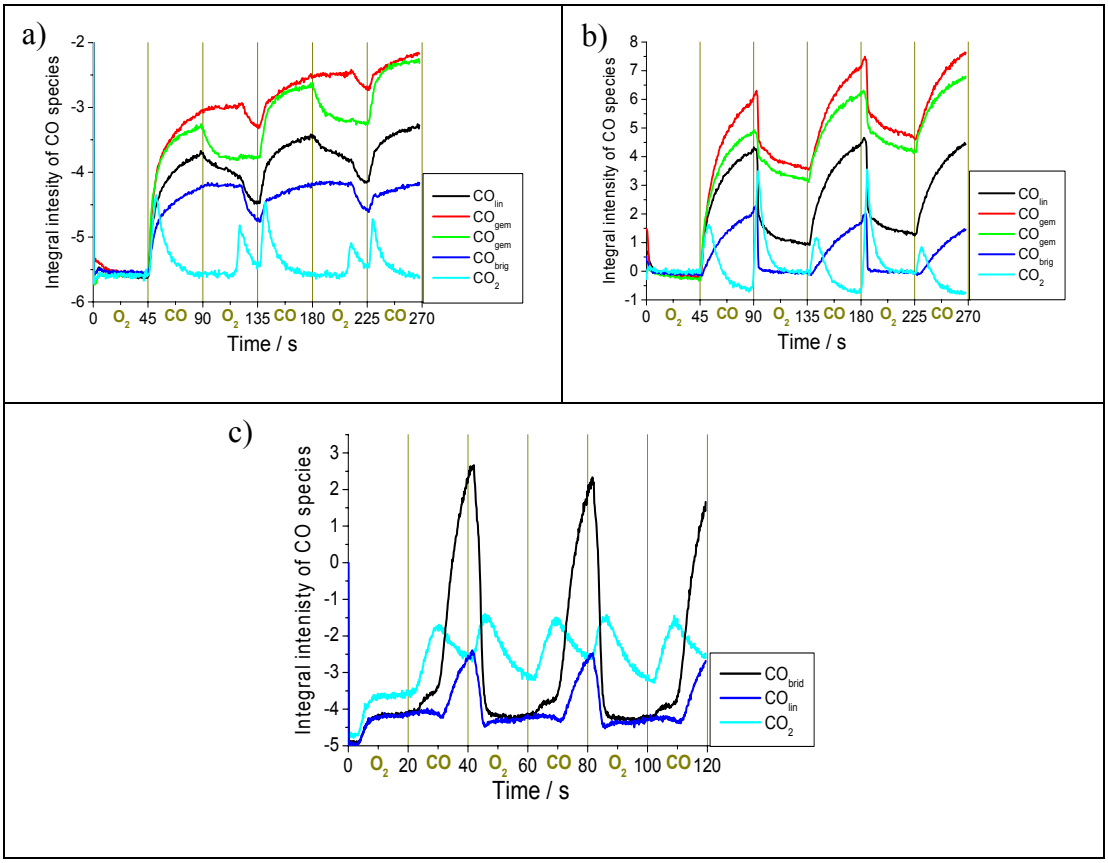

Figure 5.5 Variation of integral intensity of CO species adsorbed on the Rh surface during the O_2/CO switching experiment over 4 wt% Rh/Al_2O_3 at a) 323 K, b) 423 K, c) 573 K

Figure 5.6 combines the two experimental techniques by indexing the ΔXANES at 23250 eV and the DRIFTS integrals of the two dominant surface CO species (linear, bridged) throughout CO/O_2 switching experiment over 4 wt % Rh/Al_2O_3 at 573 K. The two techniques used for this experiment correlate well during the entire process. At the start of the experiment the sample was oxidised under the flow of 5 % O_2/He; the trend shown in red (right) indicates the maximum Rh oxidation value (~ 0.087), which was stabilised after 15 s of O_2 purging. Subsequently, the flowing gas was switched to 5 % CO/He producing a large amount of CO_2 gas converted from the interaction of CO with the O adsorbed on the Rh surface. After 10 s of CO exposure the Rh oxidation state significantly decreased and simultaneously the linear and bridged CO species adsorbed on the Rh surface. Following O_2 exposure at the second cycle, the CO species desorbed were rapidly converting to CO_2. After the full desorption of CO entities from the metallic surface the Rh particles were oxidised with the same degree of oxidation as for the first cycle. During the third (O_2/CO) cycle the analogous behaviour of Rh particles was observed. The clear oscillations of the CO species evolution and level of Rh

oxidation highlight that the surface species and Rh particles respond effectively to the gaseous environment.

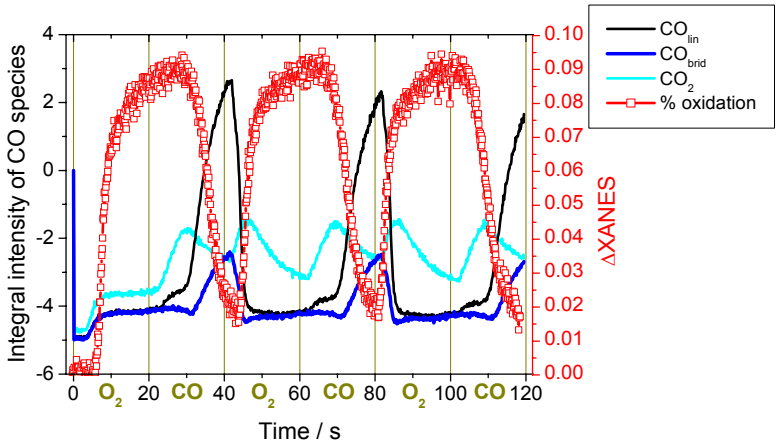

Figure 5.6 Variation of integral intensity of CO species and ΔXANES at 23250 eV during the O_2/CO switching experiment over 4 wt% Rh/Al_2O_3 at 573 K.

Figure 5.7a and 5.7b show mass spectrometric responses for the gases analysed: O_2, CO, CO_2 obtained for 4 wt% Rh/Al_2O_3 during O_2/CO switches at 573 K for switch time t = 20 s and 60 s, respectively. The presented gas evolution is compatible with the DRIFTS and XANES results described above. In all Rh systems, the formation of CO_2 gas occurs after every gas change, which is consistent with the earlier research [20, 21]. The catalytic activity of this catalyst observed by MS roughly correlates with the evolution of CO_2 detected by IR. First CO_2 formation appears going from O_2 to CO and the Rh surface is partially oxidised before induction of CO. The amount of CO_2 produced includes CO_2 coming from both the catalytic oxidation of CO in the presence of gaseous oxygen and the oxygen stored on the Rh surface. The next CO_2 production appears when the catalyst is partially reduced during the reverse switch from CO to O_2. Therefore, the CO_2 formed derived from only the catalytic oxidation of CO. It is also considered that CO_2 is a result of reaction between adsorbed O_2 and preadsorbed CO via the Langmuir-Hinshelwood (L-H) reaction mechanism. Concentrating on the experiment with the switch time of 20 s, the CO_2 formations after each switch are not easily resolved. For comparison, the gas evolutions are presented as a function of switch time.

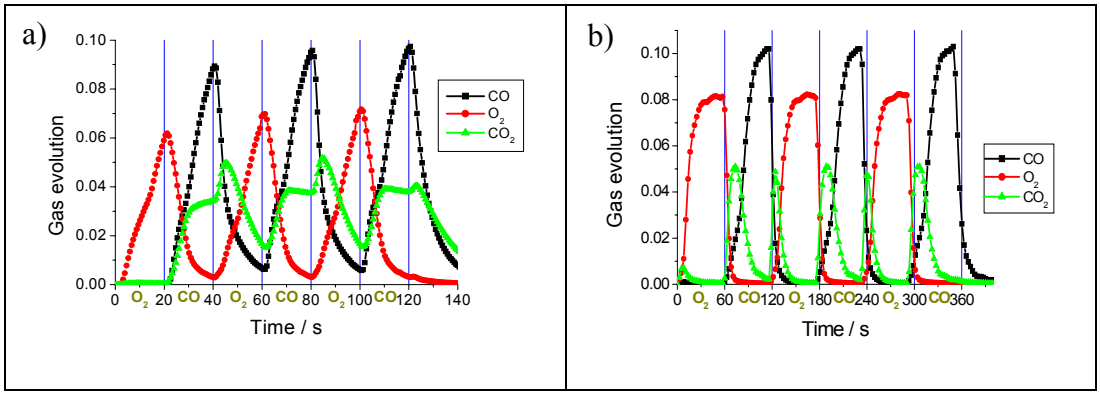

Figure 5.7 Evolution of reactants (CO and O_2) and product (CO_2) over 4 wt% Rh/Al_2O_3 upon reaction at 573 K during O_2/CO switching experiment for two different time length of one switch: a) 20 s, b) 60 s.

The DRIFTS data shows that various surface processes occur in the system, which suggests that some structural changes should occur over the 4 wt% Rh catalysts, which can be verified by synchronously obtained EXAFS data.

By analysing the EXAFS data at the beginning and at each O_2/CO step of the time-resolved experiment, an idea of the structural variances occurring can be obtained. Figure 5.8 shows k^3 weighted Rh K-edge EDE spectra for 4 wt% Rh/Al_2O_3 before and after exposure to 5 % O_2/He at 573 K, along with the corresponding Fourier transforms. The structural and statistical information derived from these spectra are given in Table 5.1. For each of the spectral analyses, ten experimental spectra are averaged. The static EDE data in Figure 5.8a shows the pre-treated, reduced 4 wt% Rh/Al_2O_3 with an expected $CN_{Rh\text{-}Rh}$ of ca. 5.7. Upon exposing the system to a flow of 5 % O_2/He for 20 s, the EXAFS signal reports significant structural changes to have occurred, with the coordination number of RhRh shell falling to a value of ca. 1.3. The Rh-Rh bond length changes throughout the oxidising step from 2.64 to ca. 2.66 Å. The presence of the additional RhO shell at 2.04 Å with the coordination of the RhO shell of ca. 2.6 clearly show the predominantly oxidic state of the Rh. The obtained results are consistent with the scanning EXAFS results reported by Martens *et al.* [22, 23]. The structure of the Rh catalysts present upon O_2 exposure at 573 K has been compared with the crystal structure of Rh oxides and the Rh surface oxide based on the FT calculations. All structural information about the compounds applied is included in Chapter 3, section 3.3.5. The whole series of FT simulations done for the particular Rh oxides and the Rh surface oxide has confirmed that the oxidised Rh nanoparticles supported on alumina represent a complex structure, which is very difficult to identify. The Rh

particles can enclose the Rh oxides, the oxidic Rh layers and some metallic form of Rh.

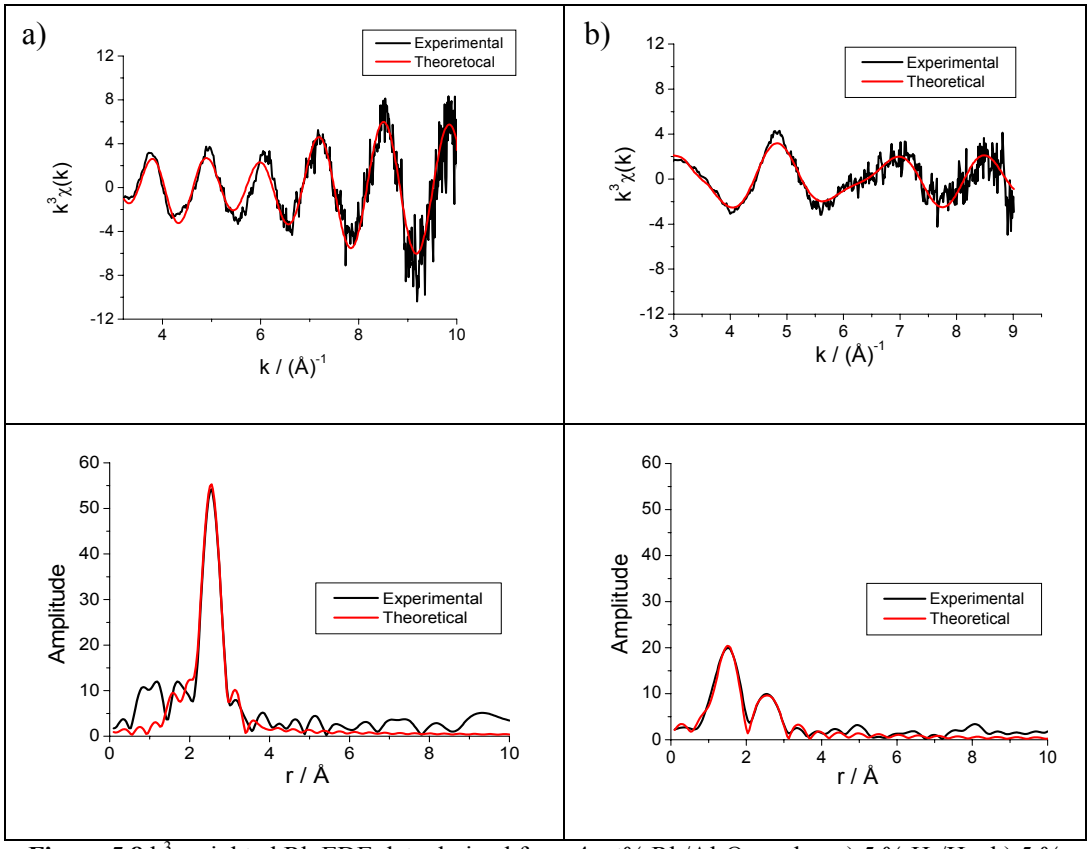

Figure 5.8 k^3 weighted Rh EDE data derived from 4 wt% Rh/Al_2O_3 under: a) 5 % H_2/He, b) 5 % O_2/He at 573 K. The corresponding Fourier Transform (not phase corrected) is given underneath each spectrum.

Conditions	Scatterer	CN	r (Å)	$2\sigma^2$/Å^2	E_F (eV)	R (%)
He at 573 K	Rh	5.7 (3)	2.64 (1)	0.0175	-1.3	39
5 % O_2/He at 573 K	Rh O	1.3 (2) 2.6 (2)	2.66 (1) 2.04 (1)	0.0175 0.018	-5.9	47

Table 5.1 Structural and statistical data for 4 wt% Rh/Al_2O_3 derived from the analysis of spectra given in Figure 5.8. Other parameters: a) k = 3 – 10 Å^{-1}, b) 3 – 9 Å^{-1}.

In order to analyse the third step of the O_2/CO switching experiment (CO exposure), various models were used to try and delineate the structure of the catalyst after being exposed to 5 % CO/He, derived from previous studies of CO exposure on similar Rh systems. According to the DRIFTS results reported above, at the temperature below 473 K, the complex Rh systems includes three different types of Rh sites on the alumina support; with CO bound on terminal sites, bridged and a geminal dicarbonyl entities. However, at 573 K, only the linear and bridged CO

species, which are known to be associated with metallic Rh surface, were observed throughout CO exposure. These structures were all taken into consideration on analysing the EDE data.

Due to the low quality of EDE data and short k-range, the 'best fit' or lowest R factor obtained in EXAFS analysis was achieved by using the model of four shells. In general, the RhRh and RhO shells were refined as the single scatterers, and multiple scattering included one unit of the RhC and Rh…O shells.

Refinement constraints of CN_{RhC} and CN_{RhO} were employed for the analysis; refinement of the two carbonyl ligands was done simultaneously by fixing their Debye-Waller and bond lengths together. Figure 5.9 presents k^3 weighted EDE spectra of 4 wt% Rh/Al_2O_3 under 5 % CO/He in the $(O_2/CO)_3$ switching experiment at 573 K, along with the corresponding Fourier transforms. The theory fits the $k^3\chi(k)$ and Fourier transform to the proposed models. The structural and statistical information derived from these spectra are given in Table 5.2. The static EDE spectra reveal significant structural changes to have occurred to the catalysts upon switching the flowing gas from O_2 to CO at 573 K. An increase of RhRh occupation from ca. 1.3 under O_2 to ca. 4.3 and the drop of CN_{RhO} from ca. 2.6 to ca. 1 were observed upon CO exposure. The EXAFS shows the evidence of Rh-CO bonding with the angle of the Rh-C-O unit being around 179 ^{o}. The bond lengths of RhRh, RhO, and Rh-C-O shells are consistent with the crystallographic database. Farrugia has reported the crystal structure of $Rh_4(CO)_{12}$ with the Rh-Rh bond lengths of 2.672 Å, the average Rh-C distance of 1.951 Å for terminal CO species and Rh-C bond length of 2.05 Å for bridged CO species , and the Rh-C-O distance of 3.069 Å [24].

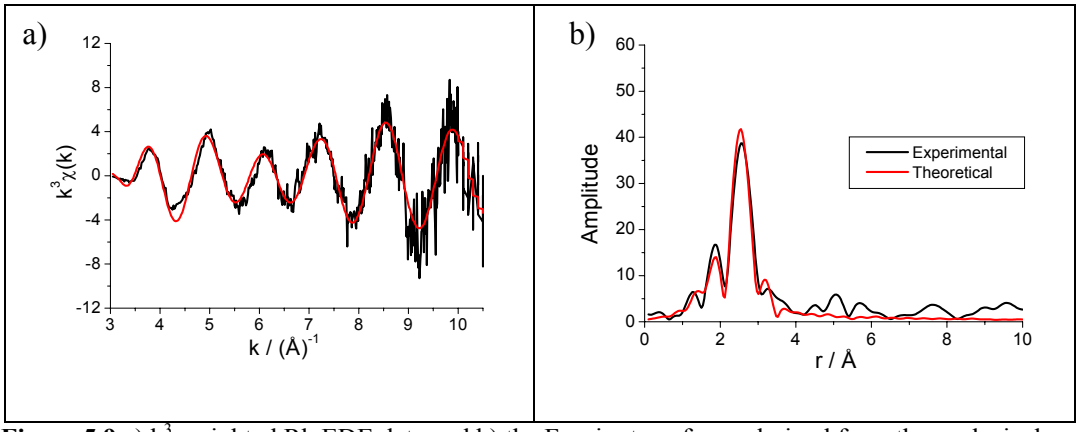

Figure 5.9 a) k^3 weighted Rh EDE data and b) the Fourier transforms derived from the analysis done over 4 wt% Rh/Al_2O_3 under 5 % CO/He at 573 K.

Scatterer	CN	r (Å)	$2\sigma^2/Å^2$	Angle Rh-C-O unit	E_F (eV)	R (%)
Rh	4.3 (2)	2.64 (1)	0.0175	179 °(5)	1.7	45
O	1.0 (3)	2.09 (3)	0.018			
C	1.0 (1)	1.92 (2)	0.022			
O	1.0 (1)	2.93 (2)	0.023			

Table 5.2 Structural and statistical data for 4 wt% Rh/Al_2O_3 derived from the analysis of spectra given in Figure 5.9. Data taken with the k range 3 – 10.5 $Å^{-1}$.

Significantly smaller disruption of Rh particles occurred over Rh system by $(O_2/CO)_3$ switches at 373 K. Figure 5.10 shows k^3 weighted Rh K-edge EDE spectra for 4 wt% Rh/Al_2O_3 before and after exposure to 5 % O_2/He and to 5 % CO/He at 373 K, along with the corresponding Fourier transforms. The structural and statistical information derived from these spectra are given in Table 5.3. Upon exposing the system to a flow of 5 % O_2/He for 45 s a major oxidation of Rh particles was observed by the drop of the RhRh occupation from ca. 5.7 to ca. 2.8 and the presence of further Rh-O shell at 2.01 Å with the coordination number CN_{RhO} of ca. 1.1. Upon switching the flowing gas to CO small variations of RhRh and RhO coordination numbers were detected. However, EXAFS analysis detected the contribution of the CO species formed on the Rh particles, with the overall coordination number Rh-CO of ca. 1.2 and the Rh-CO bond length of ca. 1.94 Å and Rh-C-O to be around 2.96 Å.

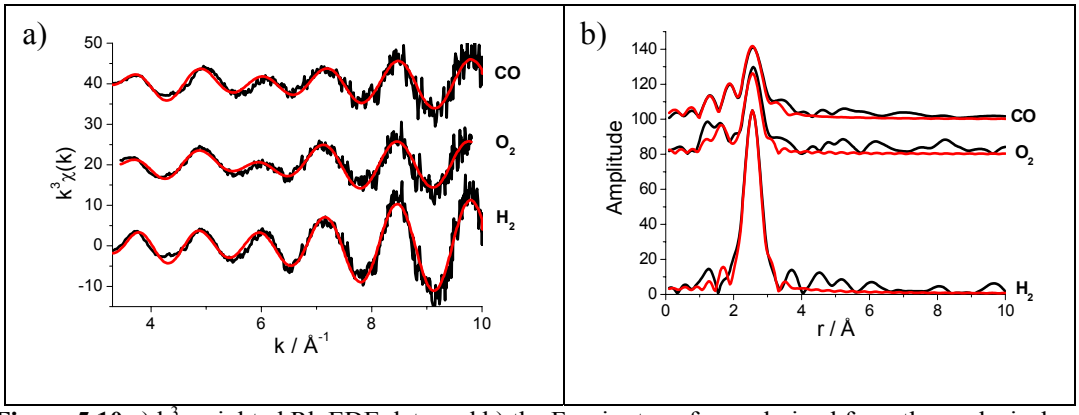

Figure 5.10 a) k^3 weighted Rh EDE data and b) the Fourier transforms derived from the analysis done over 4 wt% Rh/Al_2O_3 under 5 % H_2/He, 5 % O_2/He and 5 % CO/He at 373 K.

Conditions	Scatterer	CN	r (Å)	$2\sigma^2/Å^2$	E_F (eV)	R (%)
5 % H_2/He	Rh	5.7 (2)	2.65 (1)	0.0115	-3.8	38
5 % O_2/He	Rh	2.8 (2)	2.65 (1)	0.0115	-2.6	39
	O	1.1 (2)	2.01 (2)	0.012		
5 % CO/He	Rh	3.3 (2)	2.66 (1)	0.0115	1.1	45
	O	0.8 (2)	2.07 (2)	0.012		
	C	1.2 (3)	1.94 (2)	0.012		
	O	1.2 (3)	2.96 (1)	0.012		

Table 5.3 Structural and statistical data for 4 wt% Rh/Al_2O_3 derived from the analysis of spectra given in Figure 5.10. Data taken with the k range 3 – 10.5 $Å^{-1}$.

Figure 5.11a shows the representative Fourier transforms derived from Rh K edge EDE of 4 wt% Rh/Al_2O_3 during $(O_2/CO)_3$ switching experiment at 573 K. The relative intensities of the Rh-Rh and Rh-O contribution presented in the radial distribution functions show the gradual drop of the Rh-Rh coordination number and the evolution of the Rh-O occupation as O_2 is introduced to the catalyst. Subsequently, the gradual increase of the Rh-Rh occupation and the decrease of Rh-O contribution were observed as the CO was switched into the feedstock. The similar changes were reported in the following (O_2/CO) cycles. Clearly, the Rh-Rh contribution increased upon the next CO exposure; however it is still smaller than the Rh-Rh occupation at the beginning of the experiment. Figure 5.11b presents the top view of the Fourier transforms shown in Figure 5.11a, indicating the distributions of the intensities of the Rh-Rh and the Rh-O shells at each step of $(O_2/CO)_3$ cycles. A clear synchrony between the structural response of the nanoparticulate Rh and the gas switching was observed at 573 K.

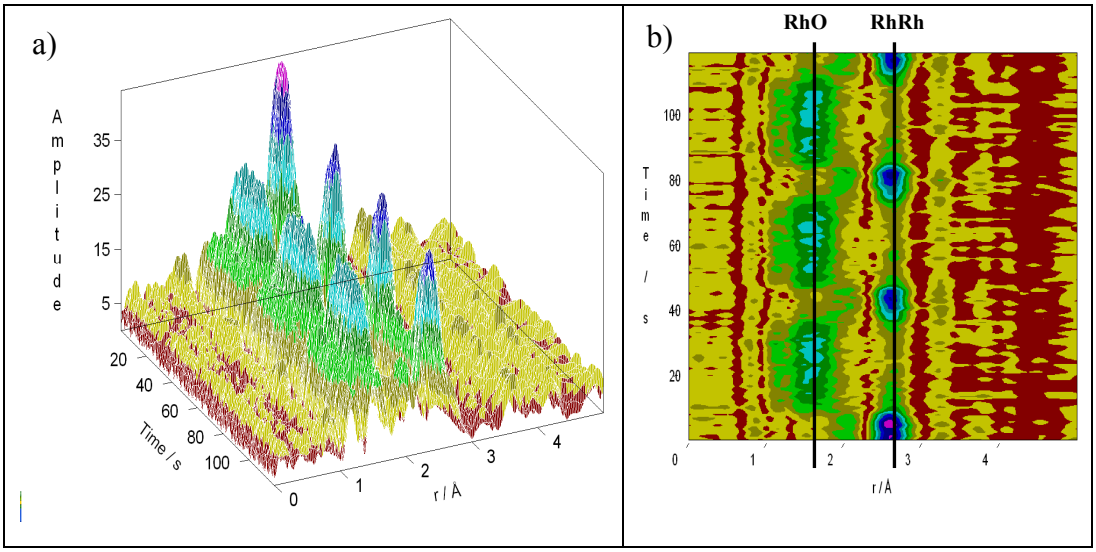

Figure 5.11 a) Radial distribution functions (not phase corrected) derived from Rh K edge during $(O_2/CO)_3$ switching experiment at 573 K. Spectra recorded every 100 ms. b) Corresponding top view of the presented Fourier transforms.

Figure 5.12 displays the variation in the Rh-Rh coordination number during the O_2/CO switching experiment over 4 wt% Rh/Al_2O_3 at four different temperatures investigated: 373 K, 423 K, 473 K, and 573 K. There are substantial changes in the RhRh occupation with gas switching, apart of the experiment done at 373 K. Firstly, the plot highlights that the initial switch from He to O_2 induced the rapid oxidation. At the start of the process the metallic rhodium particles are larger ($CN_{RhRh} \sim 6$) and while O_2 exposure the CN_{RhRh} drops to ca. 2. The RhRh occupation subsequently increases during CO exposure. The aforementioned 'cycles' can be viewed to proceed with the following (O_2/CO) gas switching. The behaviour of the rhodium systems strongly depends on the temperature. The CN_{RhRh} variations between oxidised and metallic form of the catalyst during (O_2/CO) switches appears to be larger and more constant at higher temperature.

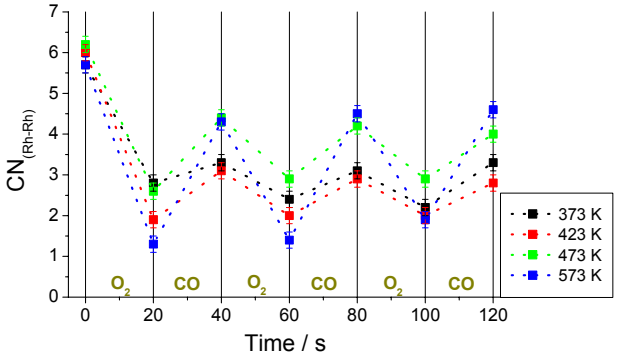

Figure 5.12 Variations of RhRh coordination number during the O_2/CO switching experiment over 4 wt% Rh/Al_2O_3 at the temperature indicated.

5.3.1.2 1.6 wt% Rh systems

Figure 5.13a and 5.13b display the dynamic response of 1.6 wt% Rh/Al_2O_3 to the flow of reactive gases such as to O_2 and CO at the temperatures investigated as measured by changes in Rh K edge XANES observed at 23250 eV. During oxygen exposure the XANES difference increases (rhodium remains oxidised) and while CO exposure the XANES variation decreases (rhodium becomes more reduced). The oxidation degree of Rh particles at the particular reaction step is dependent on temperature; which indexes a larger Rh oxidation as the temperature is increased. Within the analysis the dead time of a gas switch of ca. 4 s needs to be taken in consideration. At 323 K, the Rh component is easily oxidised; within 8 s of O_2 exposure reaches the value of ΔXANES ~ 0.04, the next CO flow reduced the Rh particles slightly. However, the further (O_2/CO) switches do not indicate any significant modification of the Rh particles. At higher temperature, 423 K the larger Rh oxidation (ca. 0.08) and the periodic behaviour of Rh component dependent on the reactive feedstock gas can be observed. Moreover, the following cycles (O_2/CO) indicates a progressive decrease in the degree of oxidation of the Rh phase while O_2 exposure as it was observed for 4 wt% Rh system. In the temperature range 473 – 573 K, the periodic changes of the Rh oxidation are observed for each cycle. Generally, the level of Rh oxidation is larger for 1.6 wt% Rh/Al_2O_3 when compared with the 4 wt% Rh system. This phenomenon can be explained by the fact that the disruption of smaller Rh nanoparticles is more facile than the larger Rh particles. Due to the poor quality of EDE data which does not permit any structural analysis by EXAFS it cannot be establish if there is still some metallic Rh component existed under O_2 flow at 573 K.

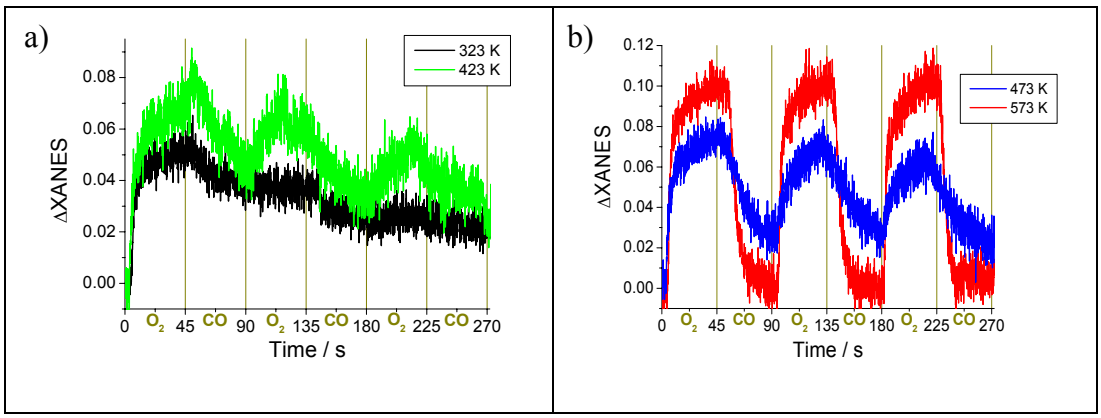

Figure 5.13 Changes in Rh K edge XANES during CO oxidation of 1.6 wt% Rh/Al_2O_3 at a) 323 K, 423 K, b) 473 K, 573 K.

The IR spectra at 323 K and 423 K shown in Figure 5.14a and 5.14b are dominated by the signal from the $Rh(CO)_2$ species (ν_{sym} ~ 2098 cm^{-1}, ν_{asym} ~ 2028 cm^{-1}). Additionally, there is also contribution from species associated with extended Rh surface as such linear at ca. 2070 cm^{-1} at 323 K, ca. 2064 cm^{-1} at 423 K and bridged CO species at ca. 1860 cm^{-1}. The additional small peak at ca. 2127 cm^{-1} can be resolved and attributed to RhO(CO) species. The band contours and positions are identical at each CO cycle. The geminal dicarbonyl species clearly become more pronounced relative to those for larger Rh loading. Furthermore, Figure 5.13c shows that only the linear species at ca. 2049 cm^{-1} and bridged CO species around 1851 cm^{-1} appear at 573 K as noted previously for 4 wt% Rh catalysts.

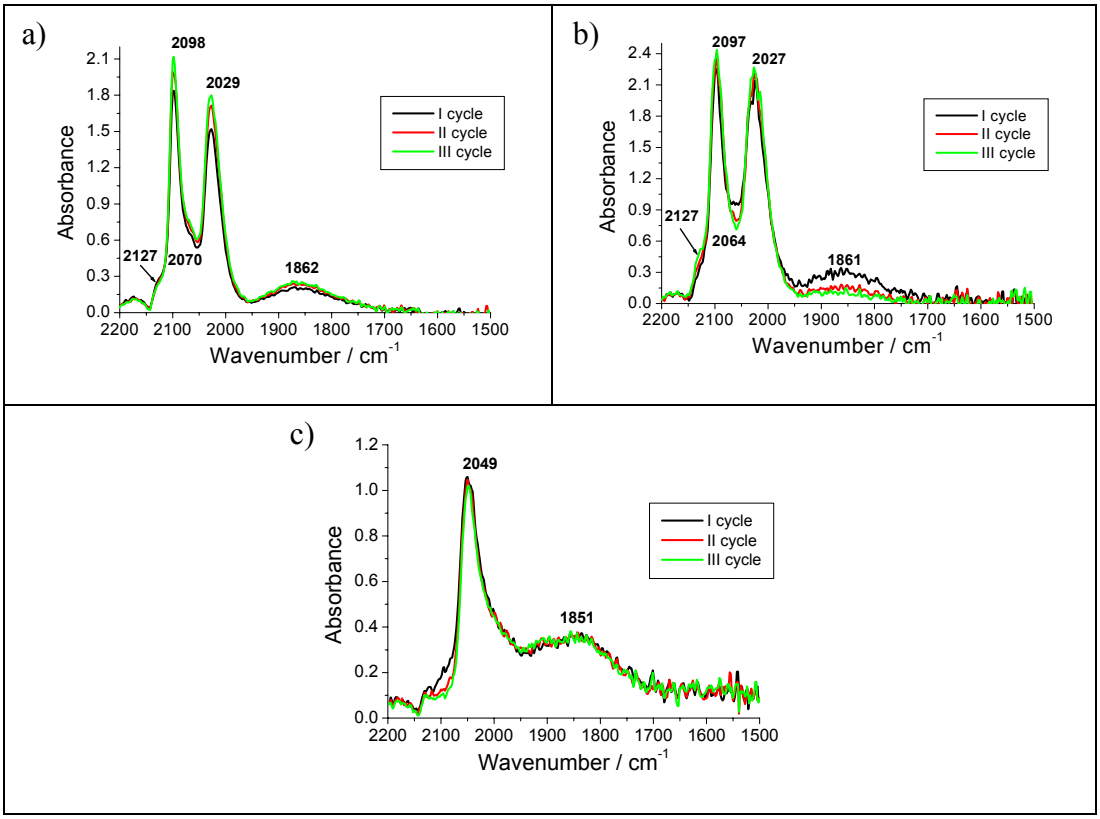

Figure 5.14 DRIFTS spectra of 1.6 wt% Rh/Al_2O_3 during I, II, III cycle of CO exposure at a) 323 K, b) 423 K, c) 573 K

5.3.2 $Rh/CeO_x/\gamma\text{-}Al_2O_3$

5.3.2.1 4 wt% Rh systems

The effect of ceria on the catalytic performance of rhodium catalysts has been studied considering two samples derived from two different preparation methods as described in Chapter 3, section 3.2. In the first method, the ceria is deposited on the

alumina support and subsequently Rh metal; however in the second one ceria is placed on the pre-supported Rh metal.

Figures 5.15a – 5.15d display the dynamic response of ΔXANES for 4 wt% $Rh/CeO_x/Al_2O_3$ (method I and II) to the flow of reactive gases such as to O_2 and CO at the temperatures investigated. The XANES variations indicate a relatively simple and progressive increase in the degree of Rh oxidation as a function of temperature. Above 323 K the XANES pattern of response to the gaseous environment by the facile oxidation and reduction of the Rh component is repeated throughout the (O_2/CO) switches in consistent 'cycles'. The overall temporal dependences of the changes in XANES observed for both ceriated catalysts are similar to that observed in the non-ceriated Rh sample. Howover, clearly within all range of temperatures the magnitude of the changes in XANES structure for 4 wt% $Rh/CeO_x/Al_2O_3$ (II) is smaller when compared to the XANES response of ceriated Rh catalysts (method I). These patterns indicate a particular limitation of the Rh particles oxidation promoted by ceria (method II) keeping still some metallic Rh phase. Similar behaviour of this Rh catalyst was observed in the previous experiment investigated the CO interaction with the Rh catalysts.

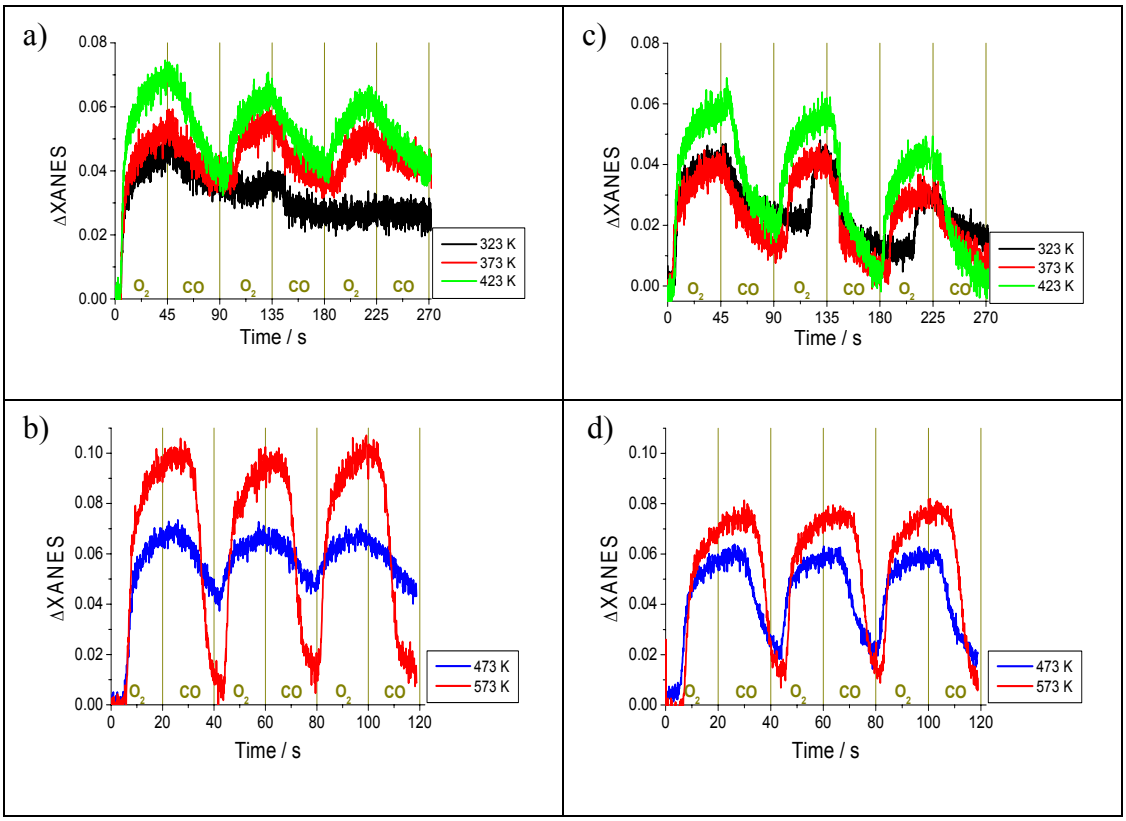

Figure 5.15 Changes in Rh K edge XANES during CO oxidation of 4 wt% $Rh/CeO_x/Al_2O_3$ (I) at a) 323, 373, 423 K, b) 473 K, 573 K and 4 wt% $Rh/CeO_x/Al_2O_3$ (II) at c) 323, 373, 423 K, d) 473 K, 573 K.

The DRIFTS spectra shown in Figure 5.16a – 5.16b illustrate that mainly three adsorbed CO species: geminal dicarbonyl species (ν_{sym} ~ 2100 cm^{-1}, ν_{asym} ~ 2030 cm^{-1}), linear (ν_{lin} ~ 2074 cm^{-1}) and bridged CO species (ν_{brid} ~ 1867 and 1895 cm^{-1}) are present on the Rh surface of both ceriated Rh catalysts at 323 K. The additional broad signal around 1720 cm^{-1} observed only for 4 wt% $Rh/CeO_x/Al_2O_3$ (I) is characteristic for bridged CO species positioned between Rh and Ce atoms. Figure 5.15c – 5.15d show the all range of IR active species observed on the surface of the ceriated Rh catalysts at 423 K. The presence of the same carbonyl species is observed as it is the case at 323 K. However, the intensity of bridged CO species is clearly diminished for both catalysts at higher temperature. Furthermore, a new band appeared at 2134 cm^{-1} for 4 wt% $Rh/CeO_x/Al_2O_3$ (I) and at 2139 cm^{-1} for 4 wt% $Rh/CeO_x/Al_2O_3$ (II). In the light of the previous findings the peak position of these species ~ 2139 cm^{-1} is rather controversial. Others have observed the band at 2177 cm^{-1} assigned to CO linearly adsorbed on Ce^{4+} and the signal at 2156 cm^{-1} to Ce^{4+} in a more unsaturated coordination state [25]. On other hand, a band in the 2118 – 2127 cm^{-1} range is ascribed to CO-Ce^{3+} species [26]. After the detailed analysis it can be observed that the evolution of this species increases in the following (O_2/CO) cycle in the expense of linear CO species. This fact could attribute the detected peak to RhO(CO) species, blue shifted from 2125 cm^{-1} for undoped Rh catalysts to 2134 cm^{-1} for ceriated Rh catalysts. The blue shift observed is consistent with the previous results included in Chapter 4, within the presence of the blue shift for the linear CO species was attributed to the strong Ce-Rh interaction which removes the electron density used for back bonding and consequently weakens the Rh-CO bond. The integrated intensities of the adsorption bands for linear CO species are relatively higher for ceriated Rh catalyst (method II) when compared with Rh supported on ceria-alumina (method I). The DRIFTS spectra at 573 K shown in Figure 5.15e – 5.15f display the predominance of the linear (ν_{lin} ~ 2045 and 2049 cm^{-1}) and bridged CO species (ν_{brid} ~ 1908 and 1916 cm^{-1}) adsorbed on the Rh surface for both ceriated Rh catalysts, respectively. On increasing the temperature from 323 K to 573 K a red shift for the linear species from 2074 to 2045 cm^{-1} can be observed as well as a blue shift for the bridged species from 1867 to 1908 cm^{-1} for $Rh/CeO_x/Al_2O_3$ (I). Similar trend of the band shifts is observed for ceriated Rh catalysts (II): the frequencies of

the linear, bridged CO species, RhO(CO) species are blue shifted at each temperature when referred to ceriated Rh catalysts (I).

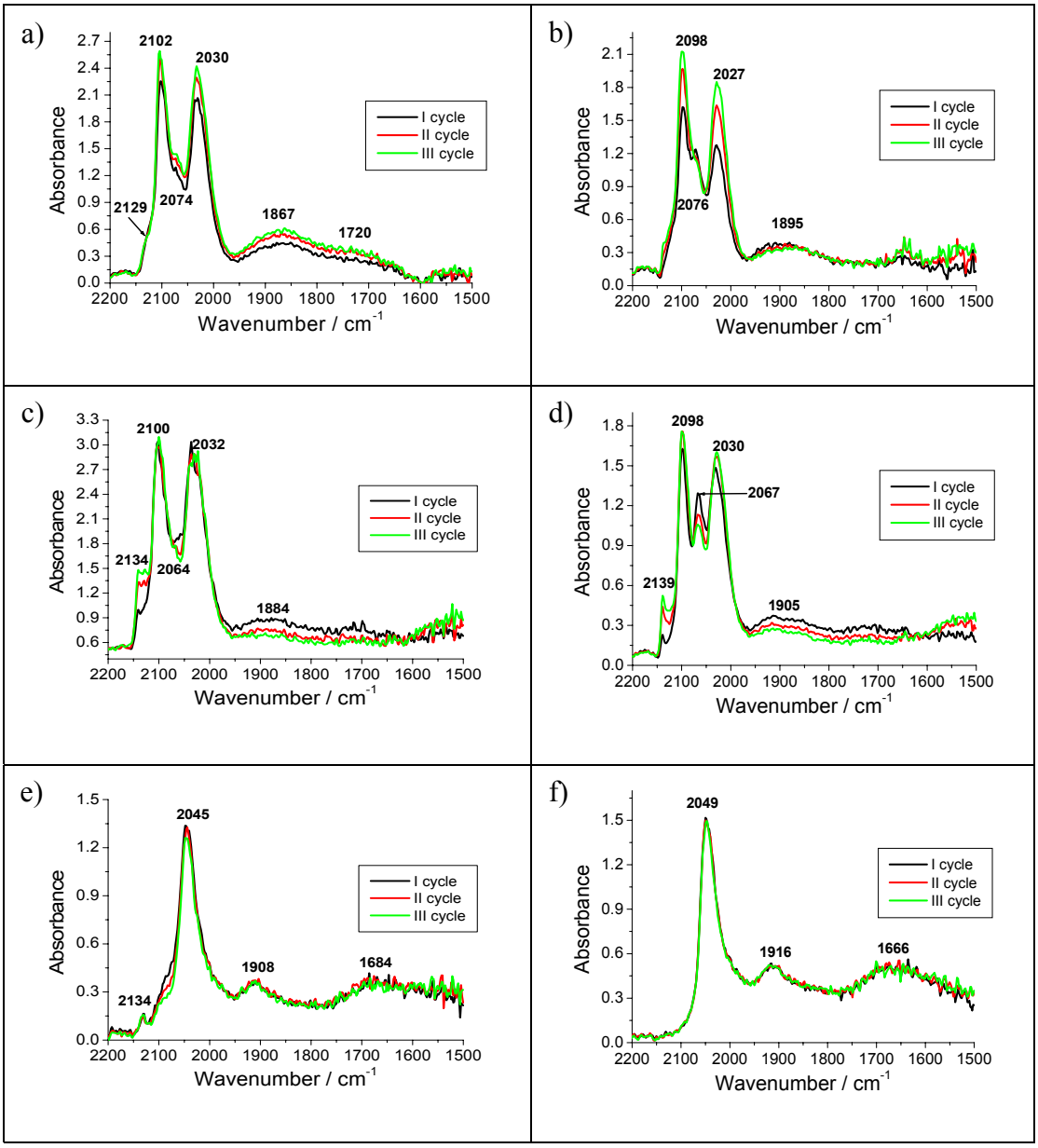

Figure 5.16 DRIFTS spectra of 4 wt% $Rh/CeO_x/Al_2O_3$ (I) at a) 323 K, c) 423 K, e) 573 K and 4 wt% $Rh/CeO_x/Al_2O_3$ (II) at b) 323 K, d) 423 K, f) 573 K during I, II, III cycle of CO exposure step.

Figure 5.17 combines the two experimental techniques by indexing the ΔXANES at 23250 eV and the DRIFTS integrals of the two dominant surface CO species (linear, bridged) throughout CO/O_2 switching experiment over 4 wt % $Rh/CeO_x/Al_2O_3$ (II) at 573 K. Firstly, the figure shows that the initial switch from He to O_2 induces the rapid oxidation, however switching the flowing gas to CO produced CO_2 gas and decreased the Rh oxidation. These changes are mirrored in the DRIFTS signal with a sharp increase in internal intensity for both IR active species:

linear and bridged. The constant 'cycles' can be viewed to proceed with the gas switching: the evolution/depopulation of CO species with the oscillation of the Rh oxidation. Moreover, the doping of ceria to Rh catalysts induces the evolution of CO species to be more constant throughout the entire experiment when compared with the undoped Rh sample.

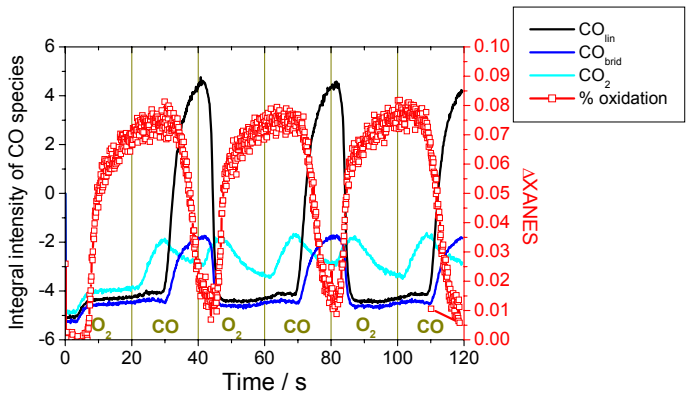

Figure 5.17 Variation of integral intensity of CO species and ΔXANES at 23250 eV during the O_2/CO switching experiment over 4 wt% Rh/CeO_x/Al_2O_3 (II) at 573 K.

Figures 5.18a and 5.18b display the temporal variation of Rh-Rh coordination number of two ceriated Rh catalysts (method I and II) during O_2/CO cycling. Below 473 K there is no significant change in the Rh-Rh coordination following the initial, extensive oxidation (large drop of CN_{Rh-Rh}) for both Rh catalysts. However, apart of the experiment done at 373 K the slight variations in coordination that do occur appear to follow the gas switching such as a decrease of CN_{Rh-Rh} during O_2 exposure and an increase of Rh occupation while CO exposure. At 573 K the Rh systems structurally follows the pattern of gas switching indicating clear oscillations of Rh occupation. There is a significant increase in the mean RhRh shell coordination number of ceriated Rh catalyst (method II) (CN_{Rh-Rh} ~ 6.6 upon H_2 at 573 K) than for the Rh/CeO_x/Al_2O_3 (I) (CN_{Rh-Rh} ~ 4.5 upon H_2 at 573 K), implying a greater mean particle size throughout the entire experiment.

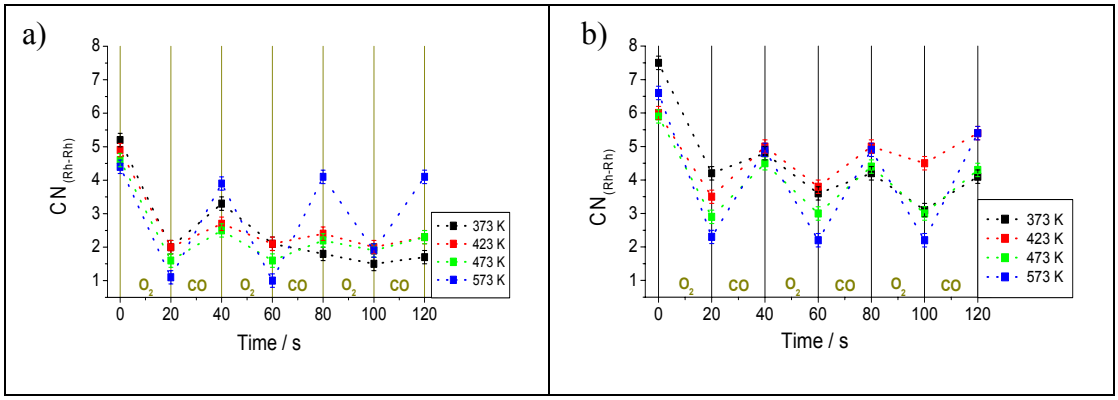

Figure 5.18 Variations of RhRh coordination number during the O_2/CO switching experiment over a) 4 wt% $Rh/CeO_x/Al_2O_3$ (I) and b) 4 wt% $Rh/CeO_x/Al_2O_3$ (II) at the temperatures investigated.

5.3.2.2 1.6 wt% Rh systems

The ceria effect has been additionally studied over rhodium catalysts, taking in consideration lower Rh concentration in the system. Figures 5.19a – 5.19d show the XANES features (E = 23250 eV) for 1.6 wt% $Rh/CeO_x/Al_2O_3$ (method I and II) at the temperatures investigated. The XANES variations indicate a relatively simple and progressive increase in the degree of Rh oxidation as a function of temperature. In the whole range of temperatures the XANES pattern of response to the gaseous environment by the facile oxidation and reduction of the Rh component is repeated throughout the (O_2/CO) switches in closely consistent 'cycles' for both Rh systems. The changes in XANES observed for both ceriated catalysts are larger to that observed in the 4 wt% Rh case. Nonetheless, the XANES variations of 1.6 wt% $Rh/CeO_x/Al_2O_3$ (II) seems to be similar at each temperature investigated (ΔXANES ~ 0.06). The significance of this effect would have to be probed further, as the observations may be due to experimental error. As it was previously observed for 4 wt% Rh systems, clearly within all range of temperatures the magnitude of the changes in XANES structure for 1.6 wt% $Rh/CeO_x/Al_2O_3$ (II) is smaller than the XANES response of ceriated Rh catalysts (method I). These patterns indicate that structural behaviour of ceriated Rh catalysts strongly depends on the synthesis method. Clearly, following method II, ceria protects the Rh particles against an extensive oxidation. Similar behaviour of this Rh catalyst was also observed in the previous experiment investigated the CO interaction with the Rh catalysts (Chapter 4, section 4.3.2).

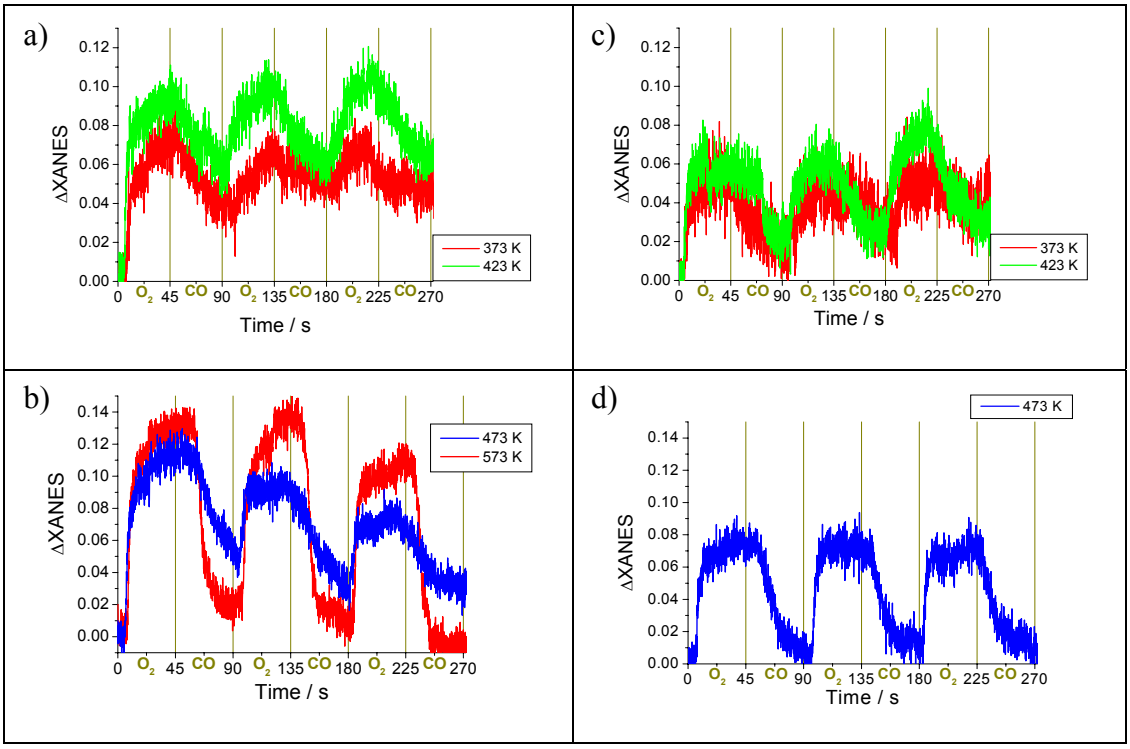

Figure 5.19 Changes in Rh K edge XANES during CO oxidation of 1.6 wt% $Rh/CeO_x/Al_2O_3$ (I) at a) 373, 423 K, b) 473 K, 573 K and 1.6 wt% $Rh/CeO_x/Al_2O_3$ (II) at c) 373, 423 K, d) 473 K.

Figure 5.20a – 5.20f present the DRIFTS spectra of 1.6 wt% Rh catalysts derived from method I and method II collected upon the CO exposure step of the I, II and III cycle at 323, 423, 573 K. The same dominant types of CO species adsorbed on the Rh surface are observed for both catalysts as in the 4 wt% Rh catalysts case. In the range of 323 – 423 K the geminal dicarbonyl, linear and bridged CO species are formed for both ceriated Rh catalysts (Figure 5.20a – 5.20d). Furthermore, at 423 K a sharp peak around 2135 cm^{-1} for $Rh/CeO_x/Al_2O_3$ (I) and 2141 cm^{-1} for $Rh/CeO_x/Al_2O_3$ (II) ascribed to blue shifted peak of RhO(CO) species is observed. The intensity of that signal is increased and the amount of linear and bridged CO species is decreased with the following (O_2/CO) switches. However, no CO adsorption at 1720 cm^{-1} (the bridged CO species between Rh and Ce atoms) was detected. The DRIFTS spectra at 573 K shown in Figure 5.20e – 5.20f display the predominance of the linear (ν_{lin} ~ 2050 and 2045 cm^{-1}) and bridged CO species (ν_{brid} ~ 1907 and 1845 cm^{-1}) adsorbed on the Rh surface for both ceriated Rh catalysts, respectively. As an example of 1.6 wt% $Rh/CeO_x/Al_2O_3$ (I) by increasing the temperature to 573 K the red shift of linear CO species from 2071 cm^{-1} to 2050 cm^{-1} can be reported as well as the blue shift of the bridged CO species from 1862 cm^{-1} to 1907 cm^{-1}.

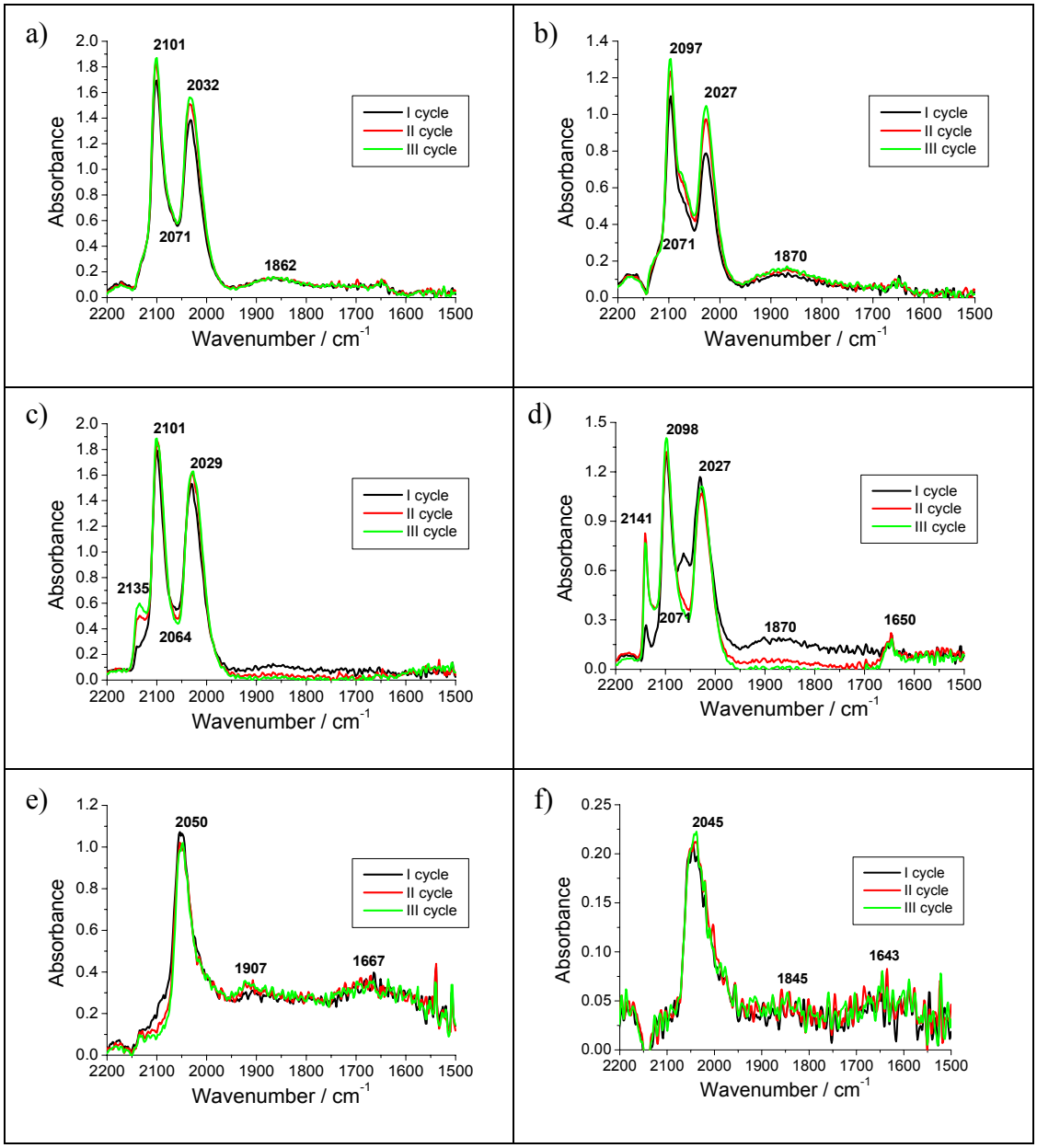

Figure 5.20 DRIFTS spectra of 1.6 wt% $Rh/CeO_x/Al_2O_3$ (I) at a) 323 K, c) 423 K, e) 573 K and 1.6 wt% $Rh/CeO_x/Al_2O_3$ (II) at b) 323 K, d) 423 K, f) 573 K during I, II, III cycle of CO exposure step.

5.3.3 $Rh/ZrO_2/\gamma\text{-}Al_2O_3$

The effect of zirconia and ceria/zirconia on the structural behaviour of rhodium catalysts has been studied, in view of three samples with different Ce:Zr ratio as 0:1, 1:1, and 2:1.

5.3.3.1 4 wt% Rh systems

Figure 5.21 shows the XANES structures (E = 23250 eV) during CO oxidation of 4 wt% $Rh/ZrO_2/Al_2O_3$ at 323 K, 423 K, 573 K. The XANES variations indicate a relatively progressive increase in the degree of Rh oxidation as a function

of temperature. At 323 K there were slight variations in the oxidation state of the Rh component that follow the gas switching. At 423 – 573 K the Rh phase of the zirconated Rh catalysts altered consistently with the oxidised and reduced gas feedstock. The XAFS data of the (O_2/CO) switching experiment over 4 wt% $Rh/ZrO_2/Al_2O_3$ at 573 K were analysed merely up to the second cycle as the last O_2 switch failed. Clearly within all range of temperatures the magnitude of the changes in XANES structure for 4 wt% $Rh/ZrO_2/Al_2O_3$ was smaller when compared to the XANES response of 4 wt% Rh catalyst (Figure 5.2). The level of Rh oxidation seemed to be limited for the zirconated Rh catalyst, even though it was exposed to O_2 and CO for longer period of time than undoped Rh catalyst.

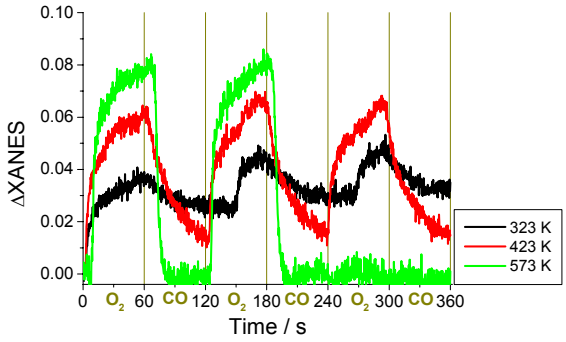

Figure 5.21 Changes in Rh K edge XANES during CO oxidation of 4 wt% $Rh/ZrO_2/Al_2O_3$ at 323, 423 K and 573 K.

Figure 5.22a – 5.22c display the DRIFTS spectra of 4 wt% $Rh/ZrO_2/Al_2O_3$ obtained upon the CO exposure step of the cycles I, II and III at 323, 423, 573 K. The same dominant types of CO species adsorbed on the Rh surface were observed such as the geminal dicarbonyl, linear and bridged CO species in the range of 323 – 423 K and the linear and bridged carbonyl entities at 573 K. The intensities of the geminal dicarbonyl species, observed at 323 – 423 K, were increased with the following (O_2/CO) switches. Relatively larger proportions of the linear and bridged species were observed at higher temperature. Furthermore, the red shift of linear CO species from 2065 cm^{-1} at 323 K to 2049 cm^{-1} at 573 K was displayed.

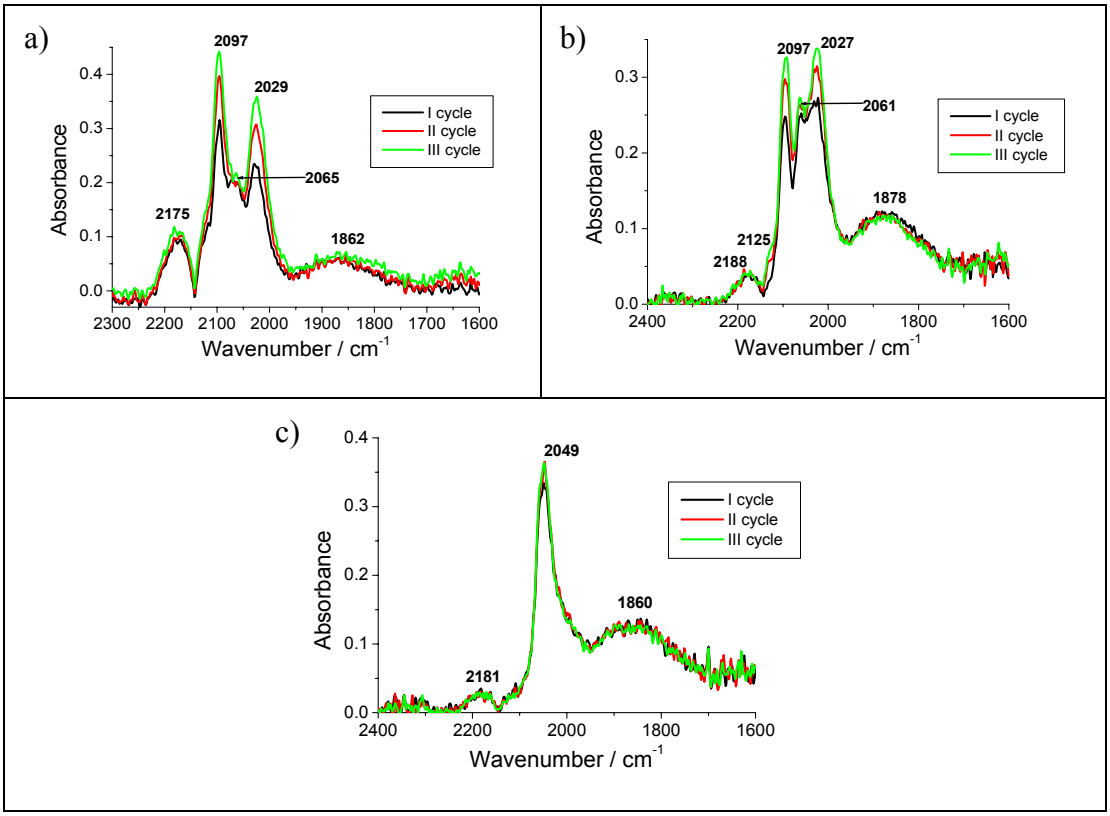

Figure 5.22 DRIFTS spectra of 4 wt% $Rh/ZrO_2/Al_2O_3$ during I, II, III cycle of CO exposure at a) 323 K, b) 423 K, c) 573 K.

Figure 5.23 displays the temporal variation of Rh-Rh coordination number of 4 wt% $Rh/ZrO_2/Al_2O_3$ during O_2/CO cycling at 423 K and 573 K. At lower temperature, 423 K, significant change in the Rh-Rh coordination was observed after the initial, extensive oxidation (drop of RhRh occupation). However, at 573 K the zirconated Rh system structurally followed the pattern of gas switching clearly indicating 'cycles' of Rh occupation. There was a significant increase in the mean RhRh shell coordination number of zirconiated Rh catalyst ($CN_{Rh\text{-}Rh}$ ~ 7.2 upon H_2/He at 473 K) than for the Rh/Al_2O_3 ($CN_{Rh\text{-}Rh}$ ~ 6.4 upon H_2/He at 473 K), implying a greater mean particle size throughout the entire experiment.

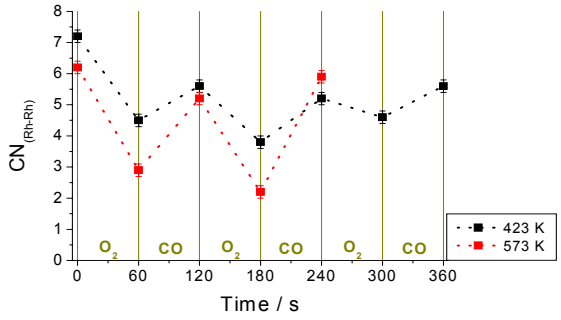

Figure 5.23 Variations of RhRh coordination number during the O_2/CO switching experiment over 4 wt% $Rh/ZrO_2/Al_2O_3$ at the temperatures investigated.

5.3.3.2 1.6 wt% Rh systems

The DRIFTS spectra shown in Figure 5.24a – 5.24c demonstrate that identical CO entities are adsorbed on the Rh surface of 1.6 wt% $Rh/ZrO_2/Al_2O_3$ as in the 4 wt% Rh case upon the CO exposure step of the cycles I, II and III at 323, 423, 573 K. The dominant CO species adsorbed on the Rh surface were typically the geminal dicarbonyl, linear and bridged CO species in the range of 323 – 423 K and the linear and bridged carbonyl entities at 573 K. Again, the intensities of the geminal dicarbonyl species, observed at 323 – 423 K, were increased with the following (O_2/CO) switches. The red shift of linear CO species from 2063 cm^{-1} at 323 K to 2048 cm^{-1} at 573 K was detected. However, some caution needs to be applied to analysis of IR data due to its poor quality. The gas-phase CO appeared at near 2180 cm^{-1} and 2107 cm^{-1} that was overlapped with the symmetrical stretching of $Rh(CO)_2$.

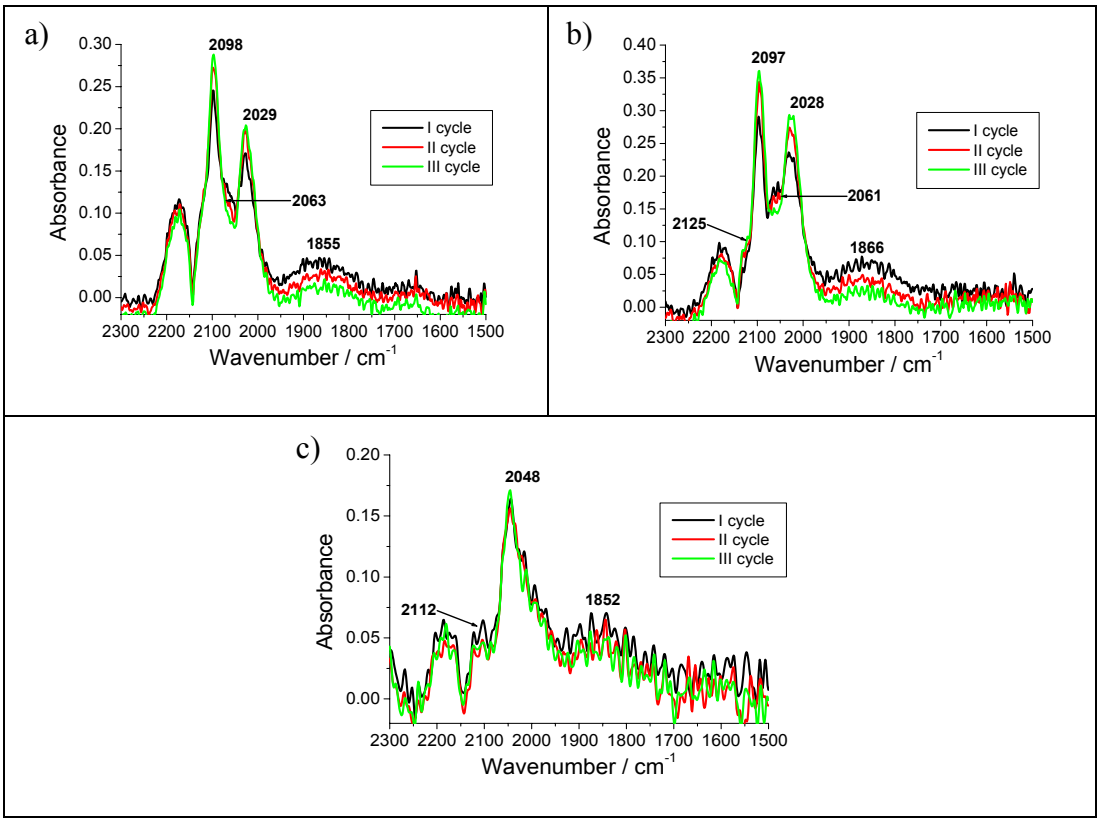

Figure 5.24 DRIFTS spectra of 1.6 wt% $Rh/ZrO_2/Al_2O_3$ during I, II, III cycle of CO exposure at a) 323 K, b) 423 K, c) 573 K.

5.3.4 $Rh/CeO_x/ZrO_2/Al_2O_3$

5.3.4.1 4 wt% Rh systems

Figures 5.25a and 5.25b display the XANES variations (E = 23250 eV) of 4 wt% Rh/ Al_2O_3 promoted by ceria-zirconia with different Ce:Zr ratio as 1:1 and 2:1, respectively. As was previously observed for all series of Rh catalysts, the XANES changes indicated a relatively simple and progressive increase in the degree of Rh oxidation as a function of temperature. Above 323 K the XANES pattern of response to the gaseous environment by the facile oxidation and reduction of the Rh component was repeated throughout the (O_2/CO) switches in consistent 'cycles'. Similar levels of the Rh component oxidation for both Rh catalysts were observed throughout the (O_2/CO) switches. Moreover, clearly above 323 K the magnitude of the changes in XANES structure for both Rh catalysts doped by ceria/zirconia were larger when compared to the XANES response of zirconiated Rh catalysts. These patterns indicate that Rh particles undergo more facile oxidation in the system of Ce/Zr mixture than in the only zirconated Rh catalysts.

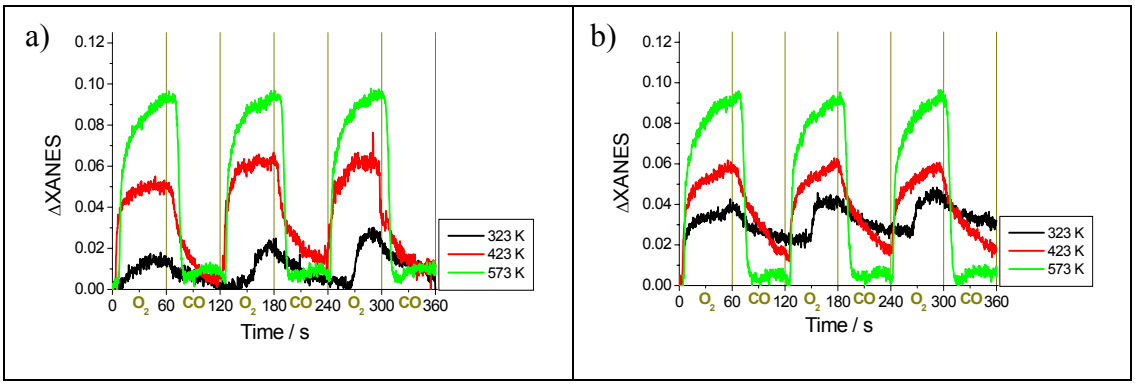

Figure 5.25 Changes in Rh K edge XANES during CO oxidation of a) 4 wt% $Rh/CeO_x/ZrO_2/Al_2O_3$ (Ce:Zr;1:1) at 373, 423 K, 573 K and b) 4 wt% $Rh/CeO_x/ZrO_2/Al_2O_3$ (Ce:Zr;2:1) at 323, 423 K, 573 K.

The DRIFTS spectra of the series of catalysts indicated were plotted in Figure 5.26a – 5.26f displaying at 323 – 423 K the same three dominant CO entities (Rh-CO, $Rh(CO)_2$ and bridged) formed on the Rh surface of ceria-zirconia doped catalysts as in the 4 wt% Rh/Al_2O_3 case. Furthermore, below 573 K a sharp peak around 2125 cm^{-1} assigned to the RhO(CO) species was observed for both Rh catalysts. The Rh particles of both catalysts became more oxidised after the following (O_2/CO) switches as the intensities of geminal dicarbonyl species increased slightly. Additionally, the amount of linear and bridged CO species relatively increased with increasing the temperature to 573 K which indicates an

enrichment of reduced Rh particles. Again, the red shift of linear CO species from 2069 cm^{-1} at 323 K to 2047 cm^{-1} at 573 K was observed for both Ce, Zr-doped Rh catalysts.

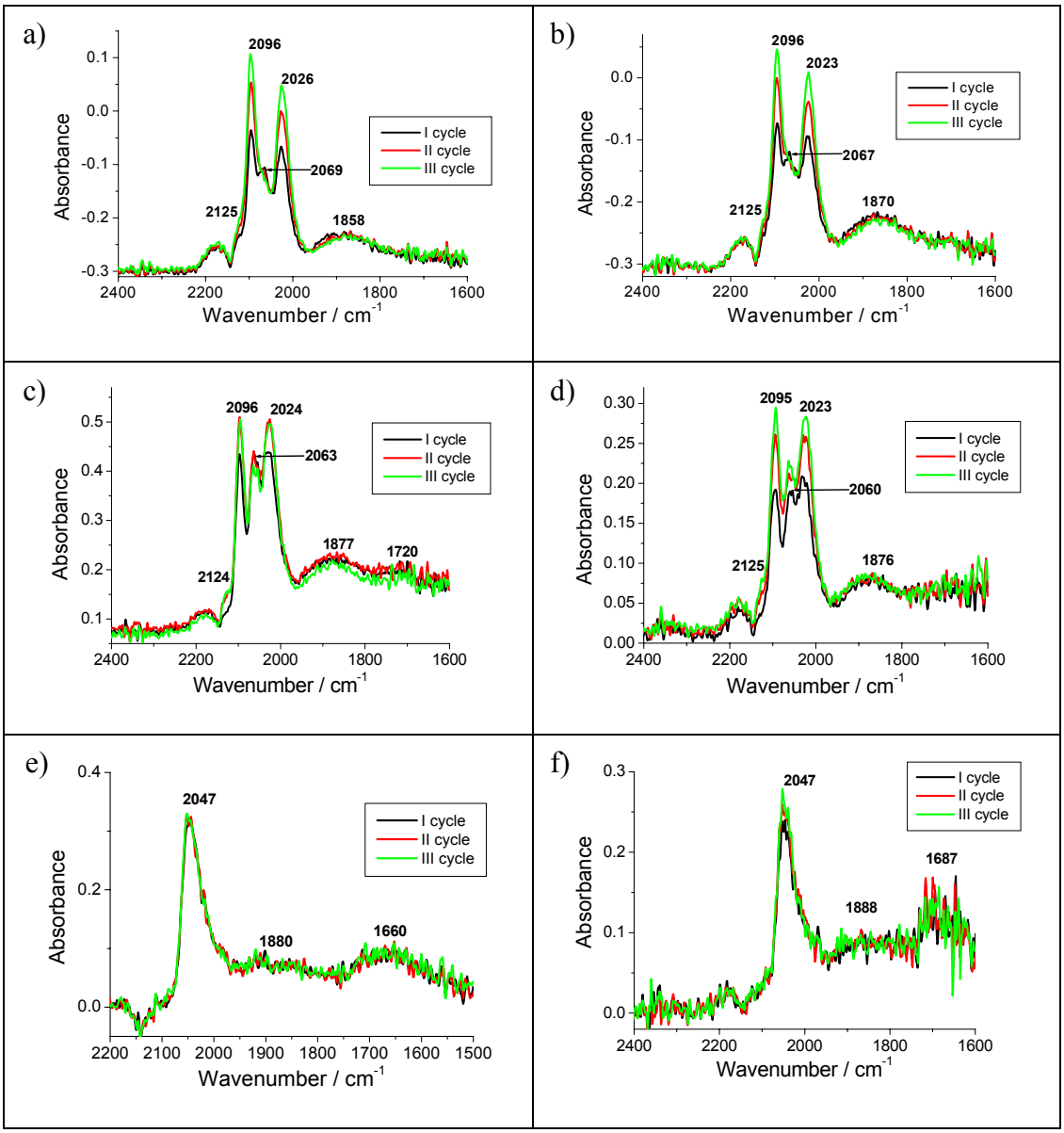

Figure 5.26 DRIFTS spectra of 4 wt% $Rh/CeO_x/ZrO_2/Al_2O_3$ (Ce:Zr;1:1) at a) 323 K, c) 423 K, e) 573 K and 4 wt% $Rh/CeO_x/ZrO_2/Al_2O_3$ (Ce:Zr;2:1) at b) 323 K, d) 423 K, f) 573 K during I, II, III cycle of CO exposure step.

The EDE data, obtained simultaneously with the DRIFTS data presented above, display the structural changes for the Rh particles of two ceria-zirconia doped Rh catalysts during O_2/CO cycling at 423 K and 573 K (Figure 5.27a – 5.27b). The structural response of both Rh catalysts for (O_2/CO) at 423 K was markedly different. The CN_{RhRh} variation of 4 wt% $Rh/CeO_x/ZrO_2/Al_2O_3$ (Ce:Zr;1:1) followed the pattern of gas switching such as a decrease of Rh occupation during O_2 exposure

and an increase of Rh particle size during CO exposure. In the case of 4 wt% $Rh/CeO_x/ZrO_2/Al_2O_3$ (Ce:Zr;2:1) there was a smaller change in the Rh-Rh coordination following the initial oxidation. At 573 K both Rh systems structurally followed the pattern of gas switching indicating clear oscillations of Rh occupation. There was an increase in the mean RhRh shell coordination number of ceriated-zirconiated Rh catalyst (Ce:Zr;1:1) (CN_{Rh-Rh} ~ 7.6 upon H_2 at 473 K) than for 4 wt% Rh/Al_2O_3 (CN_{Rh-Rh} ~ 6.4 upon H_2 at 473 K), implying a greater mean particle size throughout the entire experiment.

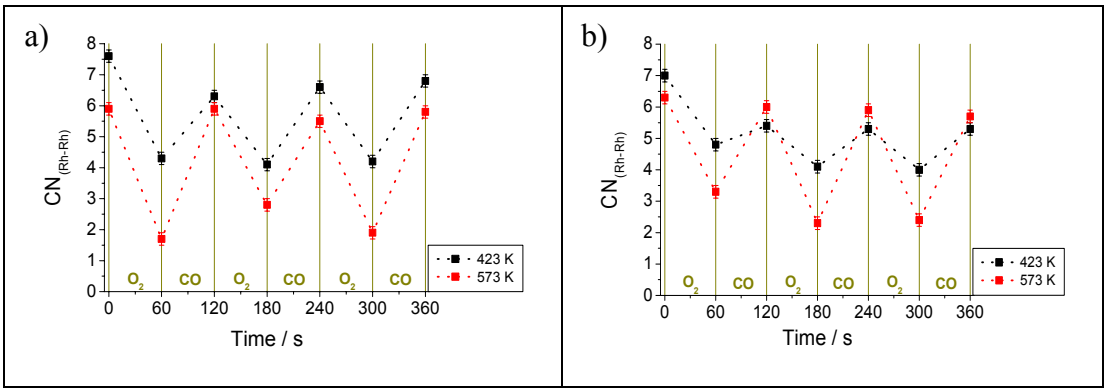

Figure 5.27 Variations of RhRh coordination number during the O_2/CO switching experiment over a) 4 wt% $Rh/CeO_x/ZrO_2/Al_2O_3$ (Ce:Zr;1:1) and b) 4 wt% $Rh/CeO_x/ZrO_2/Al_2O_3$ (Ce:Zr;2:1) at 423K and 573 K

5.3.4.2 1.6 wt% Rh systems

Figure 5.28a – 5.28f show the DRIFTS spectra of 1.6 wt% Rh/Al_2O_3 promoted by ceria-zirconia with different Ce loading (Ce:Zr;1:1;2:1). The identical carbonyl species were observed on the Rh surface as for the 1.6 wt% Rh on alumina case, i.e. linear, bridged, geminal dicarbonyl and RhO(CO) species. In the range of temperatures, 373 – 423 K, the following cycles (O_2/CO) indicated a progressive increase in the degree of oxidation of the Rh phase as the intensities of geminal dicarbonyl species increased. However, the caution needs to be applied analysis IR data due to the poor quality of the data.

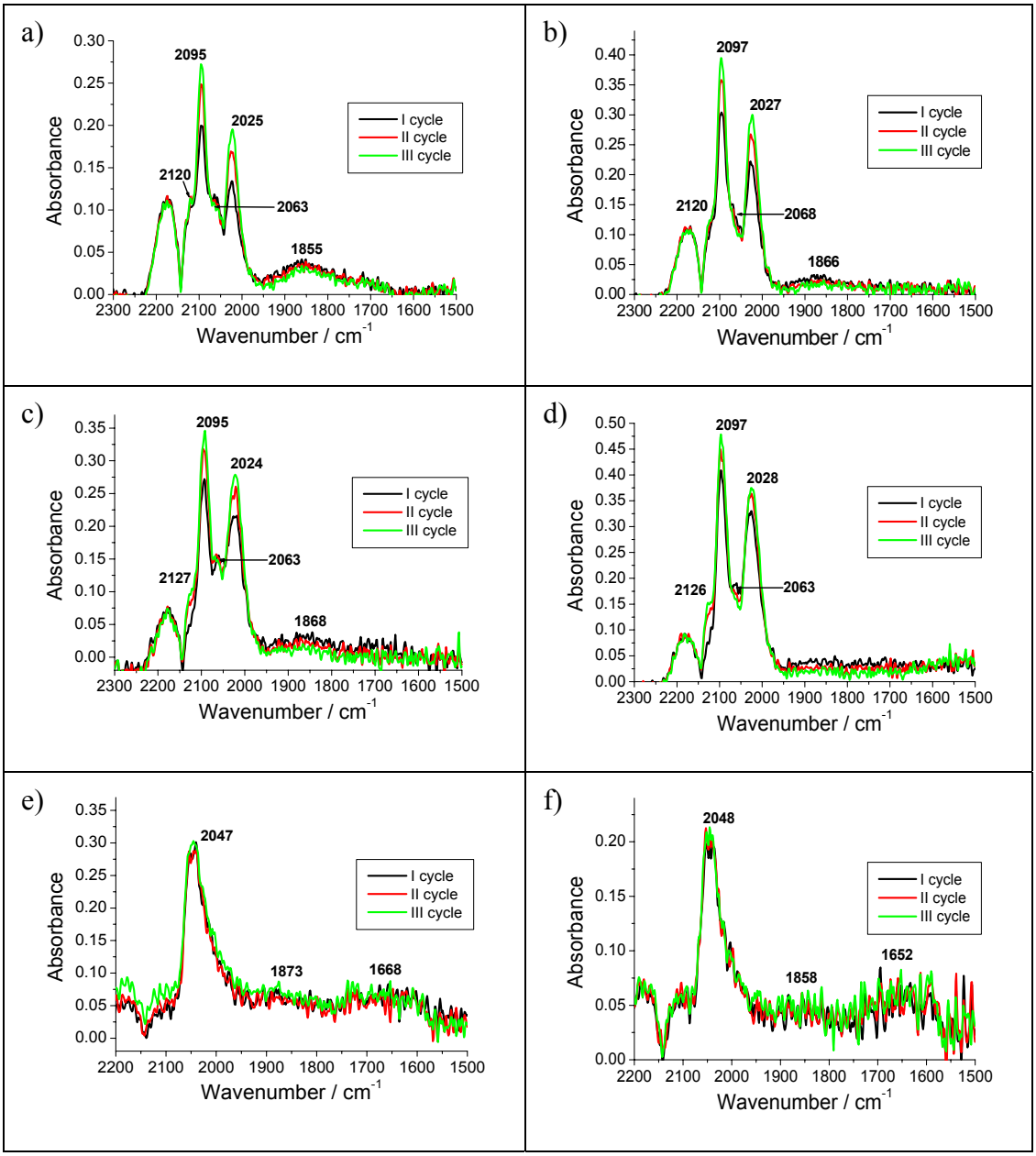

Figure 5.28 DRIFTS spectra of 1.6 wt% $Rh/CeO_x/ZrO_2/Al_2O_3$ (Ce:Zr;1:1) at a) 323 K, c) 423 K, e) 573 K and 1.6 wt% $Rh/CeO_x/ZrO_2/Al_2O_3$ (Ce:Zr;2:1) at b) 323 K, d) 423 K, f) 573 K during I, II, III cycle of CO exposure step.

The reactivity of the Rh catalysts throughout CO oxidation process was additionally studied by monitoring the CO conversion as the temperature was increasing and varies feedstock composition was exposed. The microreactor set up used for this experiment is described in chapter 2, section 2.9.2. Figures 5.29a – 5.29c show the net level of CO conversion obtained for 4 wt% Rh/Al_2O_3 and 4 wt% $Rh/CeO_x/Al_2O_3$ (method II), 4 wt% $Rh/CeO_x/ZrO_2/Al_2O_3$ (Ce:Zr;1:1) catalysts exposed to a feedstock of varying O_2/CO ratios, 1:2, 1:1, 2:1, respectively, at room temperature and then heated at 10 $Kmin^{-1}$ to 573 K. Under all feedstock

compositions, a high level of CO conversion (~100 %) was achieved. The temperature at which catalysis was initiated varies considerably, the reaction light off occurred at lower temperature for more oxidising conditions than in the reducing feedstock. The temperature light off for 4 wt% Rh/Al_2O_3 catalysts was observed in the temperature range of 411 K – 437 K depending on the gas composition. Among all Rh samples investigated, ceria-promoted Rh catalyst was assumed to be a highly effective catalyst due to the lowest light off temperature (386 K – 423 K) observed under all feedstock composition investigated. It can be observed that the zirconia doping to the ceriated Rh catalysts did not improve the efficiency of Rh catalysts throughout the CO oxidation indicating slightly higher temperature light off than 4 wt% $Rh/CeO_x/Al_2O_3$. However, the light off point for 4 wt% $Rh/CeO_x/ZrO_2/Al_2O_3$ was observed between undoped and ceriated Rh catalysts, which can be due to the lower Ce content present in this system. In between the two extremes of feedstock composition a particularly interesting situation was displayed above temperature light off over all Rh catalysts under the most oxidising gas composition. Clearly, the most significant oscillatory behaviour of CO conversion was observed for 4 wt% Rh/Al_2O_3 only by exposing the most oxidising feedstock in the temperature range of 420 – 460 K. These oscillations were generated by a shift in the O_2 and CO adsorption/desorption kinetics. The onset of oscillations has been attributed to periodic oxidation/reduction of the Rh surface. The kinetics of this reaction over Rh systems has been analysed by Ioannides *et al.* [3]. Another group has observed the oscillation reaction during CO oxidation on Rh by field-controlled selective Li coadsorption on a selected area of Rh field emitter tip [27]. The oscillatory response of CO conversion was also observed for ceriated Rh catalysts under CO lean conditions.

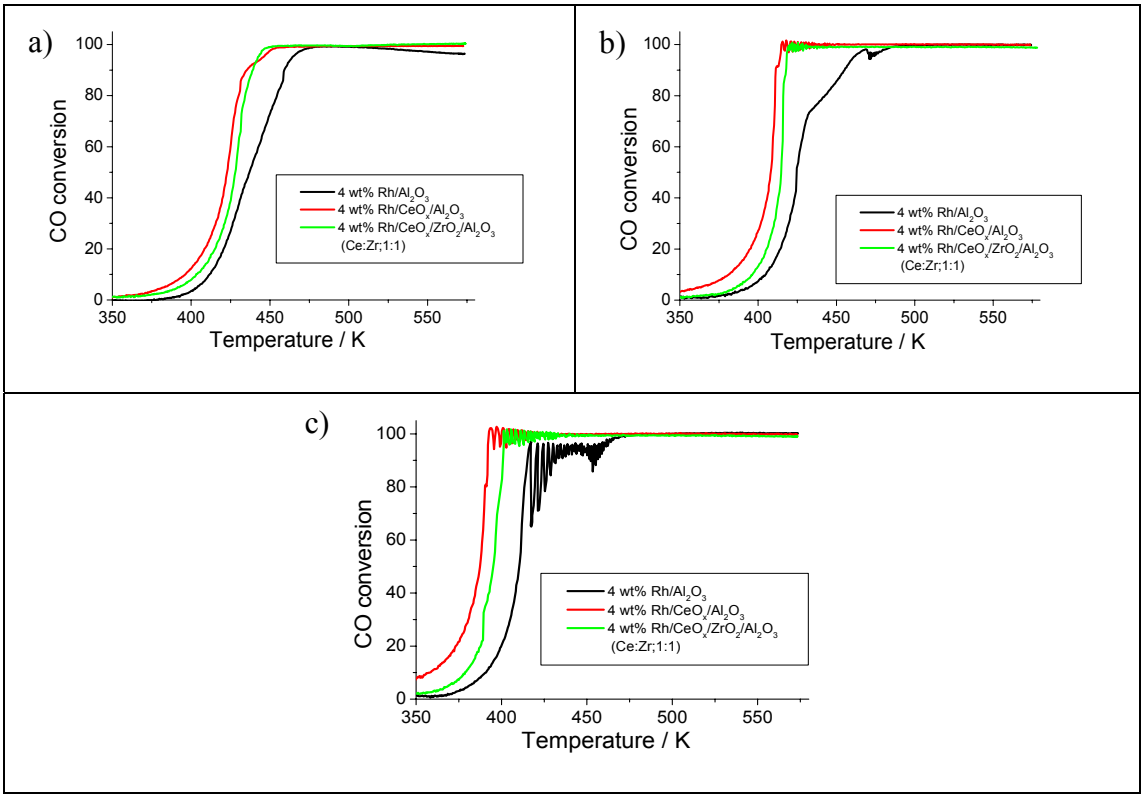

Figure 5.29 Variation in the observed CO conversion attained over 4 wt% Rh/Al_2O_3, 4 wt% $Rh/CeO_x/Al_2O_3$ (II), 4 wt% $Rh/CeO_x/ZrO_2/Al_2O_3$ as a function of temperature under different feedstock composition a) (O_2:CO;1:2), b) (O_2:CO;1:1), c) (O_2:CO;2:1) during CO oxidation reaction (after subtracting contributions to the mass 28 signal due to formation of CO_2.

The oscillatory behaviour of the CO oxidation reaction over 4 wt% Rh/Al_2O_3 ($CO:O_2$;1:2) in temperature range of 410 – 460 K was investigated in detail by following the effluent of CO, O_2 and CO_2 in Figure 5.30. The O_2, CO, CO_2 oscillations appeared to have quite a regular periodic pattern, however the amplitude became smaller when increasing the temperature. It was observed that the CO_2 concentration at the peak maximum exceeded the feed concentration of CO. This implied that CO accumulated on the catalyst surface prior to the occurrence of the maximum in the CO_2 production. Oscillations over Rh/Al_2O_3 catalysts have been studied using transmission infrared spectroscopy [28]. It was found that oscillations in the CO_2 production rate were accompanied by adsorption of linear CO species, while the coverage of the Rh dicarbonyl species did not exhibit any oscillatory pattern. Thus, it has been proved that the geminal dicarbonyl species plays a role of the spectators in the CO oxidation. The oscillatory kinetics in catalytic CO oxidation over Pt(110) has been also studied by Gerard Ertl and this work was considered to be the basis for the awarding of the Nobel Prise in 2007 [29, 30].

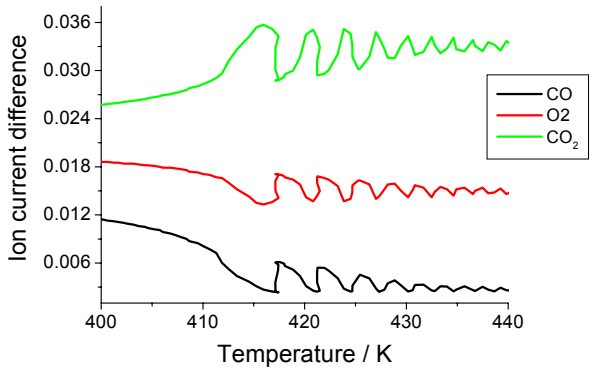

Figure 5.30 Oscillatory behaviour of the CO/O_2 reaction over 4 wt% Rh/Al_2O_3 catalysts. Gas composition ($CO:O_2$;1:2). T = 410 K – 440 K.

The CO oxidation experiment over two Rh catalysts (4 wt% Rh/Al_2O_3, 4 wt% $Rh/CeO_x/Al_2O_3$) ($CO:O_2$;1:1) was repeated in the DRIFTS cell connected with the mass spectrometer in order to follow the CO adsorption while CO conversion increased very rapidly including the temperature light off point. The CO conversion level and temperature light off appeared to be very similar when using the microreactor set up. Therefore, the evolution of CO species formed on the Rh surface was followed in the temperature range of 390 K – 450 K and 375 K – 415 K for 4 wt% Rh/Al_2O_3 and 4 wt% $Rh/CeO_x/Al_2O_3$ (II), respectively as indicated by Figures 5.31a and 5.31b. As an example of 4 wt% Rh/Al_2O_3 at 390 K mainly the Rh geminal dicarbonyl species were formed on the Rh surface (2029 cm^{-1}, 2097 cm^{-1}), additionally there was a significant amount of linear CO species adsorbed on the metallic Rh (2072 cm^{-1}) and on the oxidised Rh (2130 cm^{-1}). As established from the previous results (Figure 5.28) when increasing temperature the CO conversion raised up, in addition the DRIFTS data indicated a decrease of $Rh(CO)_2$ and Rh-CO species formation and constant adsorption of RhO(CO) species on the Rh surface. However, figure 5.31b displays significant adsorptions of geminal dicarbonyl species as well as RhO(CO) species on the Rh surface of 4 wt% $Rh/CeO_x/Al_2O_3$ (II), which desorbed from the Rh surface forming CO_2 gas when increasing temperature. The obtained results indicated that at low temperature the surface of the Rh catalysts was mostly covered by adsorbed CO molecules. The rate of reaction was relatively low at this condition as the O_2 adsorption was strongly inhibited by the formation of CO species. When the temperature of the catalyst was raised, the CO coverage of the Rh surface decreased and opened up the space on the Rh metal for O_2 to dissociatively

adsorb. As the CO coverage droped the rate of reaction between adsorbed CO molecules and oxygen atoms became significant forming CO_2.

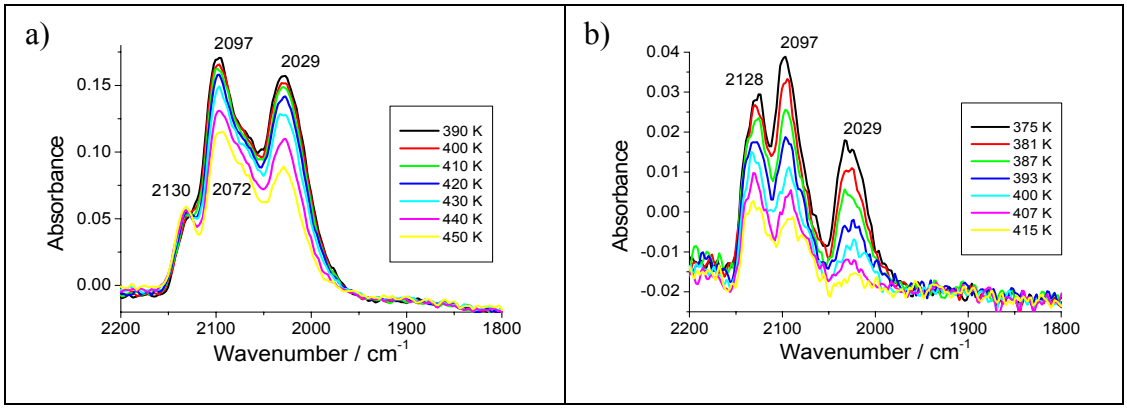

Figure 5.31 DRIFTS spectra of a) 4 wt% Rh/Al_2O_3 and b) 4 wt% $Rh/CeO_x/Al_2O_3$ (II) in a flow of CO/O_2 mixed in the ratio 1:1 as a function of temperature.

5.4 Discussion

Two experiments of CO oxidation have been utilised within this chapter: the (O_2/CO) switching experiment monitored by the EDE/DRIFTS/MS techniques and CO oxidation in the temperature ramp mode. Both of them were used in the *in situ*, time-resolved manner which allow expanding of the understanding of the complex nature of Rh catalysts, additionally promoted by ceria or/and zirconia under catalytic conditions.

5.4.1 $Rh/\gamma\text{-}Al_2O_3$

The exposure of 4 wt% Rh catalysts to 5 % O_2/He results in the extensive oxidation of the Rh particles. Oxygen reacts exothermically at room temperature causing substantial changes in the Rh K-edge XAFS [4]. Simple inspection of the XANES region of the EDE data indicates that the Rh component becomes more oxidised when increasing the temperature. Moreover, the XANES measurement suggests that most of the reactive chemistry in this case is occurring within the first few seconds. The structural analysis of the EXAFS data indicates the drop of Rh-Rh coordination number from ca. 5.7 under 5 % H_2/He to ca. 1.3 with the presence of a new component attributable to Rh-O evident upon 5 % O_2/He exposure at 573 K. Assuming a constant spherical morphology and fcc structure [31], the obtained CN_{RhRh} correspond to an average particles with ca. 13 – 21 Rh atoms to ca. 2 – 4 Rh atoms, respectively. Consequently, larger Rh-Rh occupation after the oxidising step is observed for Rh catalyst when lower temperature is employed. The detailed

EXAFS study excluded the presence of nanoparticulate Rh_2O_3. The controlled oxidation carried out over a thin surface of Rh(111) [32] and Rh(110) [33] has shown the formation of a hexagonal trilayer of O-Rh-O on the surface of the metal. The initial oxidation of Rh nanoparticles which forms a thin layer of oxide surrounding the metallic core can be viewed as a facile process as it was already observed for 5 wt% Rh catalysts [4]. However, any subsequent oxidation becomes rate limited by diffusion of atomic oxygen into the remaining metallic core. The logarithmic dependence of the Rh oxidation rate upon time has been postulated previously by B. Jyoti [34]: the rapid formation of an oxide layer decreases the amount of O_2 dissociation.

Exposing 4 wt% Rh/Al_2O_3 to 5 % CO/He induced the structural changes of the Rh particles observed by the XANES variations. The level of Rh reduction appears to be closely correlated to the temperature employed: with an increased reduction being indicated at increasing temperature. There is a diversity of adsorption pathway which can be identified both by EXAFS and IR spectroscopy. In the temperature range of 323 K – 373 K, after the extensive oxidation of Rh particles in the first step, the subsequent CO exposure does not alter the RhRh occupation of the Rh catalyst. However, the presence of RhO shell and the contribution of CO species adsorbed on the Rh surface can be detected in the EXAFS study. The DRIFTS study indicates that the Rh geminal dicarbonyl species, linear and bridged CO species are dominant, with little CO_2 being formed. Furthermore, the following O_2 flows oxidise the Rh surface more effectively which promotes the evolution of geminal dicarbonyl species during CO exposures. The IR study over Rh catalysts done by Solymosi *et al.* suggests that the presence of NO (a stronger oxidant than O_2) can assist in the formation of the geminal dicarbonyl species [35]. It has been postulated that NO forming strong bonds with Rh crystallites causes the oxidative disruption of Rh-Rh bonds and forms the Rh^+ sites. The easily dissociable oxidant O_2 is well documented to oxidise metallic centres more readily than CO. As the temperature is raised to 473 K, the same CO species adsorbed on the Rh surface, however the relative increase of linear CO species can be observed. At the same time, the EXAFS study indicates an enlargement of Rh particles. In the case of CO interaction with the 4 wt% Rh/Al_2O_3 catalyst at 573 K, the nearest neighbour Rh-Rh coordination has increased from 1.3 to 4.2, corresponding to average particles with ca. 2 – 4 Rh atoms to ca. 7 – 10 Rh atoms. Additionally, the presence of RhO shell is

still observed as well as the contribution of CO species adsorbed can be detected by EXAFS study. At higher temperature, 473 – 573 K, there is a clear synchrony between the following (O_2/CO) switches and the structural response of the nanoparticulate Rh; with essentially linear CO species forming on wholly metallic fcc Rh under gaseous CO and partially oxidised Rh under flow of O_2, with large amount of CO_2 produced between each switch. However, the MS observations does not show any differences in the CO oxidation kinetics of the reaction being between CO and Rh-bound O and the reverse reaction as it was observed by Descorme *et al.*, showing that the CO_2 formation strongly relates to the oxygen storage process occurring on the oxidised catalyst surface when O_2 is replaced by CO [36]. The recent study of CO oxidation reactivity over Rh(111) and Rh(100) by Gustafson *et al.* has shown that the Rh surface is much more active in the surface oxide phase than in the metallic form [37]. However, it was reported that the formation of rhodium oxide led to catalyst deactivation under extremely oxidising conditions ($CO:O_2$;1:30) [38].

The second experiment of CO oxidation applied over 4 wt% Rh/Al_2O_3 catalysts shows the dynamic behaviour of Rh catalysts in the presence of O_2 and CO. In terms of temperature light off, CO removal is considerably more efficient in the oxidising conditions than in reducing environment. At high CO fraction the effectiveness of the CO conversion is determined by the CO desorption from the Rh surface to leave free Rh active sites for the dissociative adsorption of O_2. The same trend of Rh catalytic behaviour has been previously demonstrated by Newton *et al.* for similar samples under O_2/CO feedstock [4]. The EDE studies over these catalysts has shown that below the light off temperature the Rh exist in the oxidised states irrespective of gas composition and the predominant formation of metallic Rh is detected during attainment of maximum CO conversion. The DRIFTS data displays the desorption of geminal dicarbonyl and linear CO species and the slight evolution of RhO(CO) entities over the CO conversion range (390 K – 450 K) for the gas feedstock containing an equal amount of O_2 and CO. The formation of CO species adsorbed on oxidised rhodium sites over all Rh catalysts under the oxidising conditions could indicate the improvement of CO oxidation activity. This could be attributed to the fact that more facile CO dissociation occurs under oxidising conditions than under reducing conditions [39]. This is due to the fact that the activation barrier is proportional to binding energy of carbon and oxygen adsorbed, which is stronger on

the metallic particles. Moreover, the CO species adsorbed at oxidised Rh centres (2125 cm^{-1}) could be assigned as an active species for CO oxidation. The high reactivity in the presence of such an oxidised Rh phase during CO oxidation catalysis has been previously postulated by others [1-3]. The IR measurements made over similar supported Rh catalysts have shown that the active CO species are the CO entities formed on oxidised Rh sites rather than geminal dicarbonyl or linear CO on Rh metal. This fact would suggest that the geminal dicarbonyl and linear CO species can be replaced by the active RhO(CO) species effectively forming the CO_2 gas.

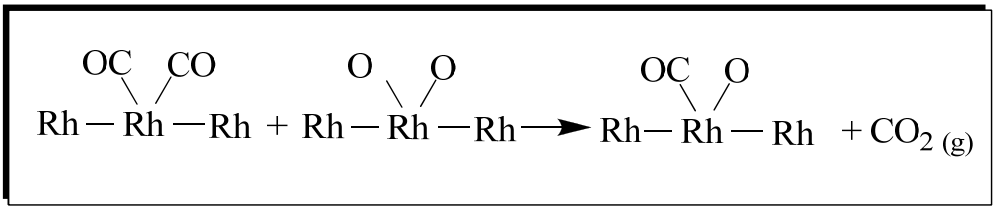

Scheme 5.1 Postulated transformation of geminal dicarbonyl, linear species for an active RhO(CO) species forming CO_2

The results obtained indicate that the catalytic activity of the RhO(CO) species is derived from a Mars Van Krevelen redox mechanism, where O_2 is consumed from the catalyst surface by reaction with adsorbed CO to form CO_2 and then the active site is replenished by oxygen from the gas phase.

A schematic representation of the structural changes under O_2/CO gases is represented in Figure 5.32. Upon O_2 exposure the Rh particles are partially oxidised and the oxidation degree strongly depends on the temperature used. After switching the exposing gas to CO a different structural behaviour of the metal particles is observed at lower (< 473 K) and higher temperature (> 473 K). The obtained results derived from DRIFTS/XAFS/MS measurements suggest that upon O_2/CO exposure below 473 K occurs the fragmentation of Rh nanoparticles into a mixture of discrete $Rh(CO)_2$ units and partially oxidised small Rh clusters. Although above 473 K, the Rh system is observed to remain structurally stable as the metallic Rh phase is reformed upon exposure to CO in a consistent, cyclic manner.

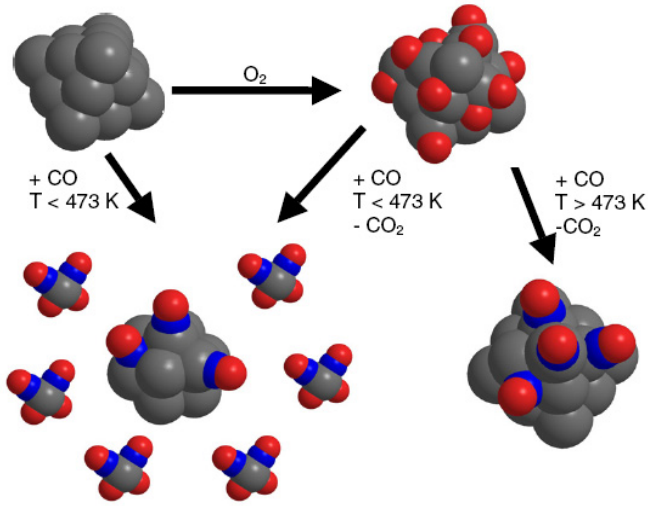

Figure 5.32 Representation of the structural changes of 4 wt% Rh/Al_2O_3 under O_2/CO exposure [40].

Analogous experiments performed upon lower metal loading, 1.6 wt% Rh/γ-Al_2O_3 reveal the adsorption characteristics and overall processes involved to be similar as the 4 wt% Rh sample case described above. However, the EDE data displays the slightly larger oxidation of the Rh nanoparticles during O_2 exposure. Furthermore, throughout CO exposures at 323 K – 423 K relatively larger amount of the Rh geminal dicarbonyl entities than the other CO species are formed on the Rh surface when compared to 4 wt% Rh system. The direct comparison of the XANES variation throughout the O_2/CO switches at 473 – 573 K cannot be undertaken as different exposure time was used for both catalytic systems.

5.4.2 $Rh/CeO_x/\gamma\text{-}Al_2O_3$

The DRIFTS, XAFS and mass spectrometric results obtained for 4 wt% $Rh/CeO_x/Al_2O_3$ (I) and elemental 4 wt% Rh/Al_2O_3 system show the catalysts display similar behaviour in terms of selectivity, metal phase changes and activity during CO oxidation. At lower temperature, 323 K – 423 K, the Rh component was oxidised with the same level as an undoped sample. However, at 473 K – 573 K, the Rh phase of the ceriated Rh catalysts is even oxidised more efficiently than the 4 wt% Rh/Al_2O_3 case. The EXAFS study indicates similar level of the Rh disruption occurred on the Rh surface of the ceriated Rh catalysts as the undoped Rh catalysts upon different O_2/CO feedstock as a function of the temperature. Furthermore, the DRIFTS results indicate that the same type of CO species was formed on the ceriated Rh surface as on the 4 wt% Rh/Al_2O_3 catalyst. On the other hand, the ceria effect

was only observed by the small blue shift of the RhO(CO) frequencies (from 2125 cm^{-1} to 2129 cm^{-1}), the minor blue shift of the linear CO species and the bridged CO species (e.g. from 1880 cm^{-1} to 1908 cm^{-1} at 573 K). It is a typical fingerprint of the Rh particles behaviour being in close vicinity with the cerium components. The proportion of RhO(CO) species, potentially an active species for CO oxidation, increases after the following O_2/CO switches.

Clearly, the significant difference of catalytic behaviour was observed between the two catalysts: 4 wt% Rh/Al_2O_3 and 4 wt% $Rh/CeO_x/Al_2O_3$ (II), produced by induction of ceria to pre-supported Rh on alumina. Firstly, at the start of the experiment the larger Rh particles are present in the ceriated Rh catalysts, e.g. at 573 K contain ca. 24 – 33 Rh atoms at the same time as the undoped Rh catalysts have ca. 13 – 19 in an average Rh particle. Ceria protects the Rh particles against an extensive oxidation as the smaller oxidation degree was displayed by XANES variations. Moreover, larger oscillations of Rh oxidation as well as the Rh occupation was observed throughout the different O_2/CO gas feedstock in particular at 473 K. The fact that the same carbonyl species adsorbed on the Rh surface, the DRIFTS spectra highlights the blue shift of the RhO(CO) frequency from 2125 cm^{-1} to 2139 cm^{-1}. The intensity of that species relatively increases after the following (O_2/CO) switches. The relatively larger amount of linear CO species was formed on the ceriated Rh surface than in the non-ceriated Rh catalysts case. The blue shifts of the peak assigned to the CO species for both ceriated Rh catalysts were previously observed in the CO interaction with the Rh systems (chapter 4, section 4.3.2). A commonly proposed mechanism for this phenomenon was explained by the Blyholder model [41]. The π component of Rh-CO bonding is formed throughout the empty antibonding π^* orbital of CO molecule as the acceptor for the electron density from the occupied metal d orbital. Due to the Rh-Ce interaction, a weakening of the Rh-CO bond occurs by transfer of the electrons from Rh to Ce, consequently the CO bond strength is increased. This spectroscopic feature correlates well to the earlier kinetic data [42], which showed a significant decrease in the adsorption enthalpy of CO on $Pt/Rh/Al_2O_3/CeO_2$ when compared to the non-ceriated Rh catalysts.

Furthermore, the improvement in activity for ceria promoted Rh samples was observed by testing the Rh catalysts throughout the CO oxidation in the temperature ramp mode under different (O_2/CO) gas compositions. The onset of CO_2 formation

occurred at the same temperature in both cases; however, the ceriated Rh catalyst exhibited sharper light-off achieving 100% CO conversion at the lower temperature than the undoped Rh catalyst, suggesting the cerium has played an important role during CO oxidation. As reported widely, CeO_2 as a oxygen storage can provide oxygen species to the close active phase, generating corresponding vacancies, which are eliminated by adsorption of oxygen from gas phase [20, 21, 43]. The oxygen vacancies can also comprise part of the active site for CO dissociation as the adsorbed oxygen atoms on the Rh particles produced by dissociation of CO at step sites may diffuse onto the CeO_2 [44]. In addition, the cerium oxide interacts with the Rh metal dislocating its electron density towards CO molecules adsorbed. The temperature at which catalysis is initiated varies considerably, the reaction light off occurs at lower temperature for more oxidising conditions than in the reducing feedstock. It has been postulated that the active CO species in the CO oxidation are associated with the Rh on +1 oxidation state [2]. The presence of partially oxidised Rh for the ceria doped catalyst determined by XPS can be associated with the Ce^{3+}/Ce^{4+} redox properties of ceria that facilitates electron transfer from Rh to CeO_2 [45]. The CO oxidation reaction over an oxidized rhodium on ceria was suggested by Descorme *et al.* [36]. The catalytic system was investigated under dynamic conditions with alternative CO and O_2 pulses. The presence of ceria induced a new reaction pathway through the reaction mechanism. This study has shown that the CO_2 formation occurred after modification in the gas phase composition. CO_2 could form on a pre-oxidised catalyst when O_2 was replaced by CO. Additionally; carbon dioxide was produced on a pre-reduced catalyst when O_2 replaced CO. Scheme 5.2 shows the schematic mechanism of the CO-O_2 switching experiment. CO could be activated on the metal surface and reacted with oxygen atoms coming from the oxide support (CeO_2) **(1)**. Oxygen transferred from the support to the metal surface depending on oxygen mobility at the surface **(2)** and on the metal/support interface **(3)**. The partially oxidized state of Rh promotes CO oxidation, which is related to its high ability to accept σ electrons of CO [46]. The direct CO oxidation on the support was assumed to be very low **(4)**.

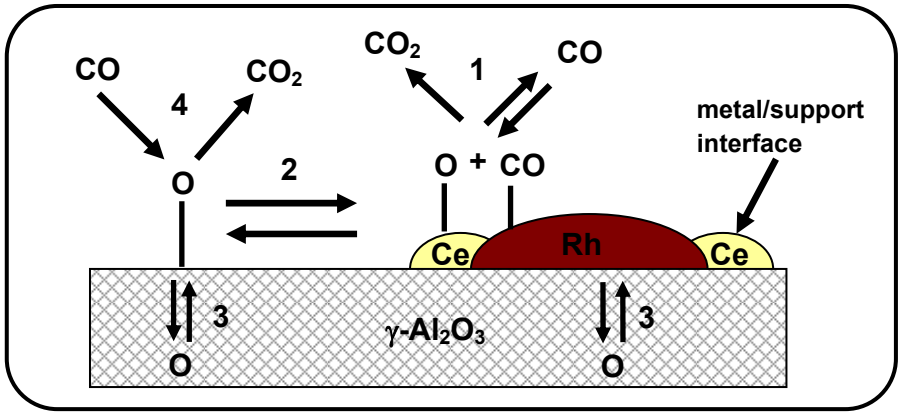

Scheme 5.2 Schematic representation of all processes over Rh catalyst supported on alumina and promoted by CeO_x [36].

Similar trends of the catalytic behaviour have been obtained over 1.6 wt% Rh catalysts promoted by ceria. The substantial oxidative disruption of Rh particles occurred over both Rh samples, however, the Rh particles of ceriated Rh catalysts (I) become significantly larger oxidised that the Rh component of $Rh/CeO_x/Al_2O_3$ (II). The infrared spectra of CO adsorbed on both ceriated Rh samples display a blue shift of RhO(CO) species, with larger variation of ν(CO) for ceria promoted Rh catalysts (II) (from 2127 cm^{-1} to 2141 cm^{-1}). Moreover, an increase of RhO(CO) species formed on the Rh surface at the expense of linear and bridged CO species desorption was observed in the following (O_2/CO) cycles.

5.4.3 $Rh/ZrO_2/\gamma\text{-}Al_2O_3$ – $Rh/CeO_x/ZrO_2/\gamma\text{-}Al_2O_3$

As it had been already observed in the CO interaction study with the Rh systems, the zirconated Rh catalysts exhibit the largest Rh particles e.g. under H_2 at 423 K, an average Rh particle contains ca. 40 Rh atoms. Therefore, less significant Rh oxidation throughout the O_2/CO switches at varies temperatures was detected by XANES variations and EDE data. The DRIFTS study presents the same carbonyl species formed on the Rh surface as in the undoped Rh catalysts case. However, the intensity of linear and bridged CO species is relatively higher, indicating larger metallic fraction of zirconated Rh catalysts than in the Rh/Al_2O_3 system. This phenomenon is consistent with the EDE analysis highlighting the largest RhRh occupation during O_2/CO switches. Moreover, no blue shift of the RhO(CO) frequency was detected by IR study as it was the case of the ceriated Rh catalysts. The earlier study over Rh/ZrO_2 indicates that the Rh particles in the close contact with Zr are completely reduced [45].

Addition of CeO_x to the zirconated Rh catalysts increased the level of Rh oxidation under conditions investigated, in particular at 573 K. However, the oscillations of the RhRh occupation seem to respond to the O_2/CO feedstock in a similar manner for both systems, displaying the largest CN_{RhRh} variations at highest temperatures. The same CO entities were formed on the Rh surface of these catalysts such as linear, bridged and geminal dicarbonyl species, nonetheless, the intensities of linear and bridged CO species are relatively higher when Ce doping is increased in the Rh system.

The catalytic activities of the ceriated Rh catalysts were not enhanced by the zirconia doping as the higher temperature light off was observed for $Rh/CeO_x/ZrO_2/Al_2O_3$ than for only CeO_x doped Rh catalysts. However, it was shown previously by Vlaic *et. al.* [47] that the oxygen storage capacity was increased by addition of the other oxides e.g. ZrO_2 to ceria. Moreover, the DFT calculations carried out by Yang [48] has shown that the Zr doping to ceria perturbs the structure of CeO_2 which enhances its reducibility and the oxygen mobility.

In the view of 1.6 wt% Rh catalysts doped with zirconia, ceria-zirconia, the DRIFTS spectra detects the same three main signals attributed to geminal dicarbonyl, linear and bridged CO species.

5.5 Conclusion

The relationship between the catalyst structure and the CO oxidation reactivity over the series of the Rh catalysts was studied within this chapter. To conclude, using an *in situ* time-resolved EDE/DRIFTS/MS array over Rh/Al_2O_3 and Rh/Al_2O_3 doped by ceria or/and zirconia during the (O_2/CO) switching experiment, very rapid and reversible structural changes of the catalyst and its reactivity have been revealed. All Rh systems show practically similar behaviour. Introducing O_2 the previously reduced Rh particles undergo rapid and extensive oxidation, subsequent flowing CO reduces the oxide and leaves the system in a more metallic phase. While the IR results indicate that mostly geminal dicarbonyl species, linear and bridged CO species adsorbed on the Rh surface after CO exposure below 473 K, however at 573 K mainly the linear CO species are formed on the Rh surface, suggesting the formation of only the metallic Rh phase in the system by CO exposure at 573 K even though the Rh catalysts was previously oxidised. The degree of Rh oxidation as well as the oscillations of the Rh-Rh coordination number throughout (O_2/CO) cycles increases when increasing the temperature.

In general, similar structure-function behaviour was observed for both ceriated Rh catalysts, produced from two different methods, however, larger Rh particles and consequently lower degree of Rh oxidation throughout the entire process at all temperatures can be observed for $Rh/CeO_x/Al_2O_3$ (II). Furthermore, the differences in the strength of the CO-Rh bond can be observed by the DRIFTS indicating that CO is more weakly adsorbed over ceriated Rh catalysts than the undoped Rh supported on alumina.

The Rh catalysts with zirconia doping contain the largest Rh particles among all Rh catalysts under investigation. As a result, the oxidation of the Rh component is limited at the conditions used as smaller variation of XANES features can be observed.

In the study of CO oxidation process, when the O_2/CO ratio is larger the CO conversion rate for both Rh systems (4 wt% Rh/Al_2O_3, 4 wt% $Rh/CeO_x/Al_2O_3$ (II), 4 wt% $Rh/CeO_x/ZrO_2/Al_2O_3$) clearly increases. Furthermore, ceriated Rh catalyst indicates lower temperature light off of CO conversion than the undoped Rh catalysts. This clearly shows that the ceria doping plays a crucial part in the high activity of a Rh model catalyst.

5.6 Reference

1. Anderson, J.A., J. Chem. Soc. Faraday Trans., 1991. **87**: p. 3907-3911.
2. Cavers, M., Davidson, J. M., Harkness, I. R., Rees, L. V. C., McDougall, G. S., J. Catal., 1999. **188**: p. 426-430.
3. Ioannides, T., Efstathiou, A. M., Zhang, Z. L., Verykios, X. E., J. Catal., 1995. **156**: p. 265-272.
4. Newton, M.A., Dent, J. A., Diaz-Moreno, S., Fiddy, S. G., Jyoti, B., J., Evans, J., Chem. Eur. J., 2006. **12**: p. 1975-1985.
5. Oh, S.H., Fisher, G. B., Carpenter, J. E., Goodman, D. W., J. Catal., 1986. **100**: p. 360-376.
6. Oh, S.H., Eickel, C. C., J. Catal., 1991. **128**: p. 526-536.
7. Gandhi, H.S., Graham, G. W., McCabe, R. W., J. Catal., 2003. **216**: p. 433-442.
8. Kummer, J.T., J. Phys. Chem., 1986. **90**: p. 4747-4752.
9. Twigg, M.V., Catal. Today, 2006. **117**: p. 407-418.
10. Armor, J.N., App. Catal. A, 1999. **176**: p. 159-176.
11. Rostrup-Nielsen, J.R., Anderson, J. R., Boudart, M., *Catalysis: Science & Technology*, ed. Springer. Vol. 5. 1884, Berlin.
12. Oh, S.H., Eickel, C. C., J. Catal., 1988. **112**: p. 543-555.
13. Polvinen, R., Vippola, M., Valden, M., Lepisto, T., Suopanki, A., Harkonen, M., J. Catal., 2004. **226**: p. 372-381.
14. Yu Yao, Y.F., J. Catal., 1984. **87**: p. 152-162.
15. Duran, F., Gonzalez, M., Moure, C., Pasucual, C., J. Mater. Sci., 1990. **25**: p. 5001-5006.
16. Gonzalez-Velasco, J.R., Gutierrez-Ortiz, M. A., Marc, J. L., Botas, J. A., Gonzales-Marcos, M. P., Blanchard, G., App. Catal. B, 2000. **25**: p. 19-29.
17. Rice, C.A., Worley, S. D., Curtis, C W., Guin, J. A., Tarrer, A. R., J. Chem. Phys., 1981. **74**: p. 6487-6497.
18. Primet, M., J. Chem. Soc. Faraday Trans., 1978. **74**: p. 2570-2575.
19. Yang, A.C., Garland, C. W., J. Phys. Chem., 1957. **61**: p. 1504-1512.
20. Laachir, A., Perrichon, V., Badri, A., Lamotte, J., Catherine, E., Lavalley, J. C., Fallah, J. El., Hilaire, L., Normand, F. L., Quemere, E., Sanvion, G. N., Touret, O., J. Chem. Soc. Faraday Trans., 1991. **87**: p. 1601-1609.
21. Sugiura, M., Catal. Surv. Asia, 2003. **7**: p. 77-87.

22. Martens, J.H.A., Prins, R., Zandbergen, H., Koningsberger, D. C., J. Phys. Chem., 1988. **92**: p. 1903-1916.
23. Martens, J.H.A., Prins, R., Koningsberger, D. C., J. Phys. Chem., 1989. **93**: p. 3179-3185.
24. Farrugia, L.J., J. Cluster Sci., 2000. **11**: p. 39-53.
25. Li, C., Sakata, Y., Arai, T., Domen, K., Maruya, K., Onishi, T., J. Chem. Soc. Faraday Trans., 1989. **85**: p. 929-943.
26. Bozon-Verduraz, F., Bensalem, A., J. Chem. Soc. Faraday Trans., 1994. **90**: p. 653-657.
27. Medvedev, V.K., Suchorski, Y., Block, J. H., Surf. Sci., 1995. **343**: p. 169-179.
28. Shanks, B.H., Bailey, J. E., J. Catal., 1988. **110**: p. 197-205.
29. Ertl, G., Angew. Chem. Intl. Ed., 2008. **47**: p. 3524-3535.
30. Sander, M., Imbihl, R., Ertl, G., J. Chem. Phys., 1991. **97**: p. 5193-5204.
31. Jentys, A., Phys. Chem. Chem. Phys., 1999. **1**: p. 4059-4065.
32. Gustafson, J., Mikkelsen, A., Borg, M., Lundgren, E., Kohler, L., Kresse, G., Schmid, M., Varga, P., Yuhara, J., Torrelles, X., Quiros, C., Andersen, J. N., Phys. Rev. Lett., 2004. **92**: p. 126102,1-4.
33. Gustafson, J., Mikkelsen, A., Borg, M., Andersen, J. N., Lundgren, E., Klein, C., Hofer, W., Schmid, M., Varga, P., Kohler, L., Kresse, G., Kasper, N., Stierle, A., Dosch, H., Phys. Rev. Lett., 2005. **71**: p. 115442,1-9.
34. Jyoti, B., *PhD Thesis*, in *Chemistry*. 2006, University of Southampton: Southampton.
35. Solymosi, F., Bansagi, T., Novak, E., J. Catal., 1988. **112**: p. 183-193.
36. Descorme, C., Taha, R., Mouaddib-Moral, N., Duprez, D., App. Catal. A, 2002. **223**: p. 287-299.
37. Gustafson. J., W., R., Mikkelsen, A., Torrelles, X., Balmes, O., Bovet, N., Andersen, J. N., Baddeley, C. J., Lundgren, E., Phys. Rev. B., 2008. **78**: p. 045423-1-6.
38. Kellogg, G.L., J. Catal., 1985. **92**: p. 167-177.
39. Cho, B.K., Stock, C. J., J. Catal., 1989. **117**: p. 202-217.
40. Tromp, M., Evans, J., J. Phys.: Condens. Matter, 2008. **20**: p. 184020-1-10.
41. Blyholder, G., J. Phys. Chem., 1964. **68**: p. 2772-2777.

42. Granger, P., Delannoy, L., Lecomte, J. J., Dathy, C., Praliaud, H., Leclercq, L., Leclercq, G., J. Catal., 2002. **207**: p. 202-212.
43. Si, R., Zhang, Y. W., Li, S. J., Lin, B. X., Yan, C. H., J. Phys. Chem. B, 2004. **108**: p. 12481-12488.
44. Stubenrauch, J., Vohs, J. M., Catal. Lett., 1997. **47**: p. 21-25.
45. Eriksson, S., Rojas, S., Boutonnet, M., Fierro, J. L. G., App. Catal. A, 2007. **326**: p. 8-16.
46. Wang, R., Xu, H., Li, X., Ge, Q., Li, W., Appl. Catal., A, 2006. **305**: p. 204-210.
47. Vlaic, G., Fornasiero, P., Geremia, S., Kaspar, J., Graziani, M., J. Catal., 1997. **168**: p. 386-392.
48. Yang, Z., Woo, T. K., Hermansson, K., J. Chem. Phys., 2006. **124**: p. 224704-224711.

Chapter 6

The study of the NO reduction by CO over supported Rh catalysts

6.1 Introduction

The previous chapter has been focused towards investigating the response of the Rh catalysts' structure and their reactivity upon the (O_2/CO) switching experiment. The CO oxidation study has demonstrated varies array of performances and behaviours of Rh systems in the function of temperature and the promoter used. This chapter will aim to understand the effect of ceria and zirconia on the structural and functional variations of Rh particles upon the CO/NO reaction.

Rh was found to be essential for the reduction of NO by CO. Comparative surface science studies under UHV conditions, over single crystals, have shown that Rh exhibits the most interesting properties towards the dissociation of NO into chemisorbed N and O atoms with the subsequent desorption of N_2 [1-3]. Therefore, the Rh catalysts are mostly used in an automotive exhaust environment to reduce NO efficiently. However, the previous study has also observed incomplete reduction of NO into N_2O [4]. Others have found that Rh supported on ceria exhibited a high activity in the decomposition of N_2O [5]. Its high activity was ascribed to the inherent function of Rh coupled with the oxygen deficient sites in ceria which also decompose N_2O. On other hand, ceria itself has poor thermal stability and at high temperatures it loses its ability to disperse Rh; Rh aggregates on the surface of ceria. The insertion of ZrO_2 into CeO_x lattice, leading to the formation of Ce-Zr mixed oxides has been found to be effective in preventing the ceria from sintering and promoting the oxygen mobility in the bulk [6-8].

The reactions of NO and CO over heterogeneous catalysts have been extensively studied, mainly by using the infrared spectroscopy for the identification of adsorbed intermediates on Rh/Al_2O_3 catalysts [9-13]. Nitric oxide has the tendency to undergo both molecular and dissociative reactions on Rh forming various coordination species such as $Rh(NO)_2$, $Rh(N_2O)$, $RhNO^+$ and $RhNO^-$, which are readily distinguishable spectroscopically.

Although the role of CO and NO in modifying the Rh surface state and morphology has been clearly elucidated, little is known about the effect of ceria and zirconia on the Rh surface sites and their adsorbates/activities during the CO/NO reaction. Moreover, as the NO molecule is also strong oxidant than previously studied O_2 this could provide additional information about the reduction-oxidation state of catalyst surfaces. Energy dispersive EXAFS (EDE) and DRIFTS techniques coupled with mass spectrometry in a time-resolved, *in situ* manner was used to determine the

structural variation of Rh particles, the adsorbate structure and product formation during the NO-CO reaction.

6.2 Experimental section

6.2.1 CO/NO switching experiment

The CO/NO switching experiment over the series of Rh catalysts has been studied throughout one allocated beamtime (CH2335) on ID24 at ESRF in Grenoble, France using the combined EDE/DRIFTS/MS apparatus. The detailed description of these techniques is given in chapter 2. First, samples has been reduced *in situ* before reaction by heating up to 573 K under the flow of 5 % H_2/He, then oxidised by 5 % O_2/He until the H_2O and carbonaceous deposition disappear from the system, and subsequently was switched back to 5 % H_2/He. After full pre-treatment, the system was cooled down in H_2 to the determined temperature and purged by He. The CO-NO switching experiment was investigated over the analysed rhodium catalysts at different temperatures: 423, 573 K. The representative reactive gases of CO and NO have been used in this project as a mixture of 5 % CO/He and 5 % NO/He, respectively. The order of gases was as follow: He–CO>NO>CO>NO>CO>NO–He with a flow of 25 cm^3 min^{-1}. The gas exposure for one switch was set up to 60 s, in order to ensure that the step of the oxidation by NO and the reduction by CO took place completely. The total catalyst load used was about 0.025 g. All experiments last 360 s and EDE/DRIFTS/ME data were collected simultaneously. EXAFS detection was done via the FReLoN CCD camera [14] with a total acquisition time with 10 spectra of ca. 10 ms. The DRIFTS data obtained matched the repetition rate of the EDE and the mass spectrometric data were collected simultaneously.

6.3 Results

6.3.1 Rh/Al_2O_3

Figure 6.1 shows the dynamic response of 4 wt% Rh/Al_2O_3 to the adsorption of CO and NO as a function of temperature measured by changes in Rh K edge XANES observed at 23250 eV. Each trace has been set up to 0 at the beginning of the experiment as the Rh sample is fully reduced. The oxidation degree of Rh particles at the particular reaction step correlates well with increasing temperature.

The variations of XANES indicate that Rh particles remained metallic after the first cycle of CO exposure at 573 K. The subsequent NO exposure affected firstly a little drop of Rh oxidation and within 10 s of NO flow Rh particles were oxidised. This phenomenon suggests that CO desorption occurred before the NO species formed on the Rh surface significantly oxidising the Rh particles (ΔXANES ~ 0.07). The XANES trend clearly highlights two distinct regimes; the second oxidation process is much slower than the first. A complete oxidation does not occur within this time frame as a slow, progressive Rh oxidation is observed until the following switch to CO. The switch back to a flow of CO fully re-reduces the particles within a few seconds of the exposure. During the following (CO/NO) cycles a similar pattern of oscillatory Rh behaviour is observed.

However, at 423 K, the minor oxidation of Rh component can be observed while initial CO exposure. The following NO exposure partially oxidised the Rh particles and again the Rh phase is partially reduced upon the next CO exposure.

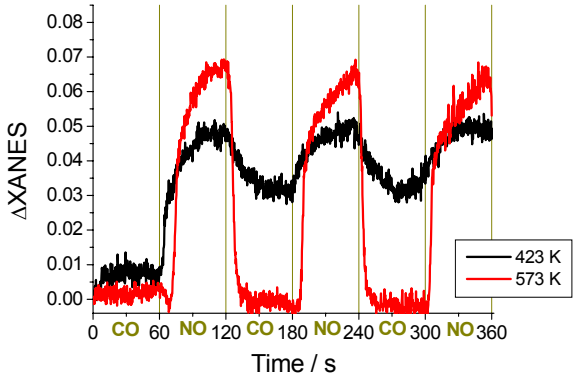

Figure 6.1 Changes in Rh K edge XANES during CO/NO switches of 4 wt% Rh/Al_2O_3 at 423 K and 573 K.

Figures 6.2a and 6.2b present the DRIFTS spectra of 4 wt% Rh/Al_2O_3 under exposures of CO and NO during the experiment performed at 573 K. The sharp peak at 2038 cm^{-1}, assigned to the linear CO species, and the broad signal centred on ca. 1869 cm^{-1}, of bridged CO species, were detected upon CO exposure (figure 6.2a). This is consistent with the results obtained in the studies of CO exposure over Rh systems (chapter 4) were the same carbonyl species were detected at 573 K. Upon the following CO exposures the formation of the same CO species with the equivalent intensities were observed. Figure 6.2b highlights the range of NO species that are observed over Rh on alumina surface during NO exposures. By induction of NO to the gas feedstock, the bands of linear and bridged CO species disappeared and

the peak at ca. 1896 cm^{-1} appeared which is attributed to the linear $Rh(NO)^+$ species [10, 15, 16] with the residual broad signal at ca. 1639 cm^{-1}. Based on the previous studies, the band at lower wavenumber could be assigned to the number of species. These include nitrates adsorbed on the alumina support [10, 15, 16], a 'low wavenumber' $Rh(NO)^-$ species [12, 17, 18] and molecular NO adsorbed in two or threefold sites on metallic Rh clusters [1, 19].

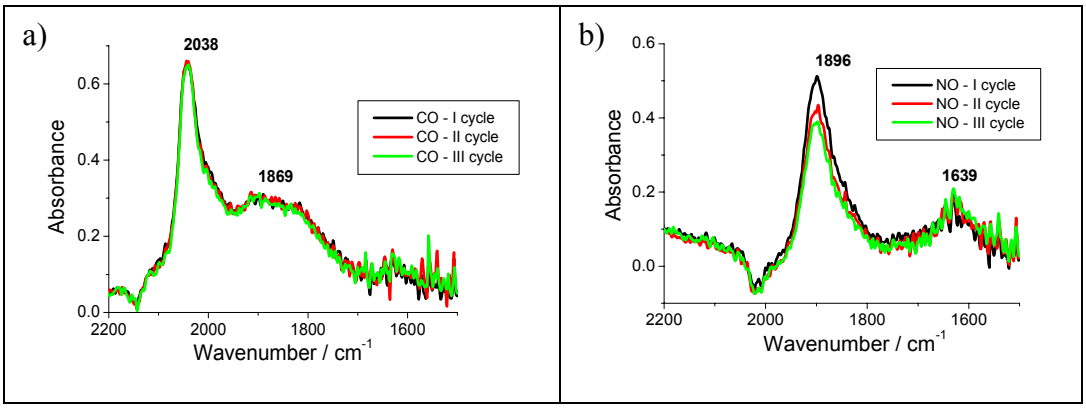

Figure 6.2 DRIFTS spectra of 4 wt% Rh/Al_2O_3 during I, II, III cycle of a) CO exposure and b) NO exposure at 573 K.

Figure 6.3 presents the temporal adsorption characteristics of the 4 wt% Rh/Al_2O_3 as it is exposed to a flow of CO and NO at 573 K. The time-resolved DRIFTS data reveal the Rh system to be far from static. The evolution of the bridged CO species and linear $RhNO^+$ species cannot be clearly separated as the band frequencies are very similar (green line). However, according to Figure 6.2 it can be distinguished that upon CO exposure, the progression of the bridged CO species was observed as under NO flow, the rapid development of linear $RhNO^+$ species was detected. The time frame of 60 s for one switch was chosen as it effectively portrays a typical 'cycle' of switching and the associated response of the key surface species, i. e. switching from $CO_{(g)} \rightarrow NO_{(g)} \rightarrow CO_{(g)}$. The linear and bridged CO species are seen to evolve within 3 s of CO flow showing their gradual formations throughout the entire CO exposure. The subsequent depopulation of these species as $NO_{(g)}$ is introduced to the Rh system is accompanied firstly by the rapid production of N_2O and CO_2 gases and in the second step by the formation of the linear nitrosyl species. This pattern of response to the gaseous environment by the dominant linear CO species and linear NO^+ species is repeated throughout the experiment in consistent 'cycles'.

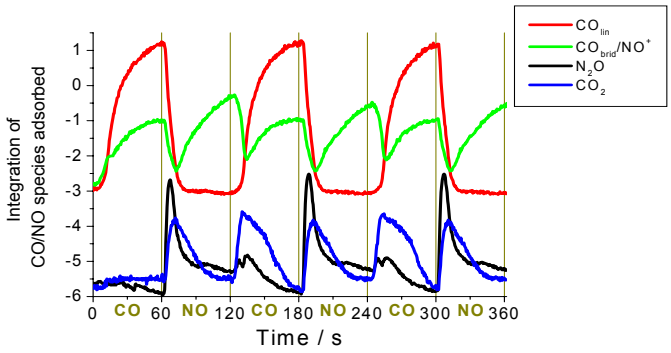

Figure 6.3 Variation of integral intensity of CO species adsorbed on the Rh surface during CO/NO switching experiment over 4 wt% Rh/Al_2O_3 at 573 K.

Figure 6.4 shows mass spectrometric response of the gases analysed: CO, NO and the produced gases: N_2, N_2O, CO_2 obtained for 4 wt% Rh/Al_2O_3 during $(CO/NO)_3$ switches at 573 K for switch time of 60 s. The presented gas evolution is compatible with the DRIFTS results described above. As the gas switch occurred (CO → NO), the two monoxides react to form N_2 (mass 28), N_2O and CO_2 (mass 44). However, the same mass of these gases does not allow distinguishing the gas production between N_2O and CO_2. At the same time the formation of N_2 gas is overlapped with the CO evolution while switching the flowing gas from CO to NO and in the reverse order.

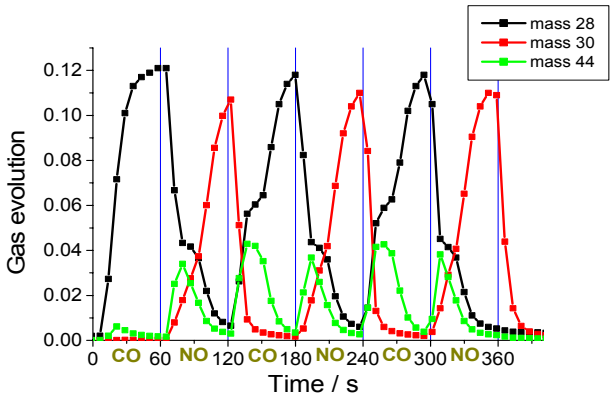

Figure 6.4 Evolution of reactants CO and NO (mass 28, 30) and products: N_2, N_2O, CO_2 (mass 28, 44) over 4 wt% Rh/Al_2O_3 upon reaction at 573 K during CO/NO switching experiment for 60 s of one switch.

Figure 6.5 shows k^3 weighted Rh K-edge EDE spectra derived from 4 wt% Rh/Al_2O_3 maintained under flowing H_2/He and after exposure to 5 % CO/He and subsequently to 5 % NO/He at 573 K, along with the corresponding Fourier transforms. The structural and statistical information derived from these spectra are

given in Table 6.1. Upon exposing the system to a flow of 5 % CO/He for 60 s a minor structural perturbation of Rh particles was observed by the drop of the RhRh occupation from ca. 6.1 to ca. 5.7. Upon switching the flowing gas to NO for 60 s, the EXAFS signal reports significant structural changes to have occurred, with the coordination number falling to a value of ca. 2.6. The amplitude and the phase of the Rh EXAFS are different to those obtained under 5 % CO/He exposure. The data was not of sufficient quality to permit the modelling of any adsorbed nitrosyl species but the RhO shell was detected at 2.07 Å with the CN_{RhO} of ca. 2, which indicated the formation of an oxidic form of Rh phase. This perturbation can be interpreted as a reduction in the average particle size of the Rh component in the response to NO adsorption. However, the EDE results reports that the Rh system still retained some metallic character throughout the NO exposure.

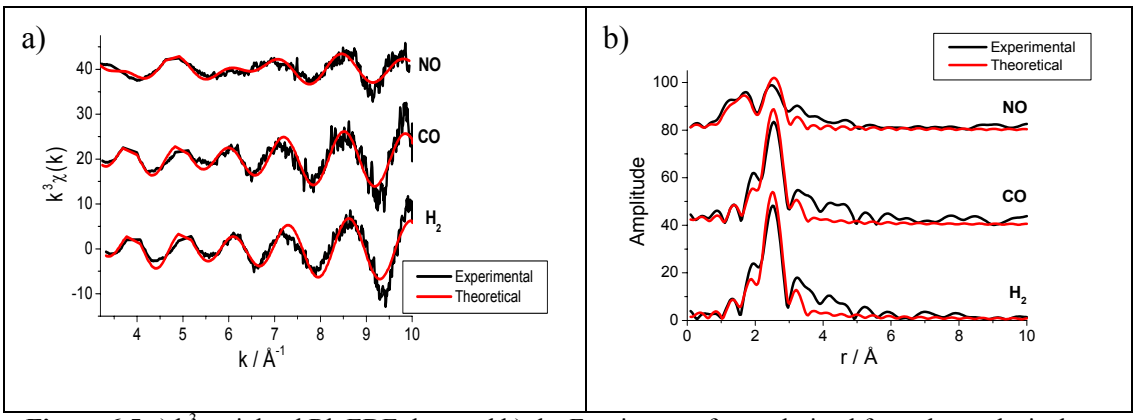

Figure 6.5 a) k^3 weighted Rh EDE data and b) the Fourier transforms derived from the analysis done over 4 wt% Rh/Al_2O_3 under 5 % H_2/He, 5 % CO/He and 5 % NO/He at 573 K.

Conditions	Scatterer	CN	r (Å)	$2\sigma^2/Å^2$	E_F (eV)	R (%)
5 % H_2/He	Rh	6.1 (2)	2.64 (1)	0.0175	7.7	44
5 % CO/He	Rh	5.7 (2)	2.64 (1)	0.0175	5.1	48
5 % NO/He	Rh	2.6 (2)	2.66 (1)	0.0175	-4.6	50
	O	1.9 (2)	2.07 (2)	0.018		

Table 6.1 Structural and statistical data for 4 wt% Rh/Al_2O_3 derived from the analysis of spectra given in Figure 6.5. Data taken with the k range 3 – 10$Å^{-1}$.

Figure 6.6a shows a representative Fourier transforms derived from Rh K edge of 4 wt% Rh/Al_2O_3 during $(CO/NO)_3$ switching experiment at 573 K taken from the analysis performed in Xmult [20]. The quality of the EDE data allowed mainly the Rh-Rh contribution upon the CO/NO cycles to be distinguished, however, the Rh-O shell was also detected. At the start of the experiment, the Rh nanoparticles were

fully reduced, indicating only the contribution of Rh-Rh shell. The slight drop of the RhRh occupation was observed upon the initial CO exposure, the following switch from CO to NO induced the rapid drop of RhRh coordination and the presence of Rh-O shell. The evolution/depopulation of the RhRh shells intensity can be viewed to proceed with the gas switching, highlighting the similar RhRh occupation at the start of the experiment and upon the following CO exposures. Figure 6.6b presents the top view of the Fourier transforms (Figure 6.6a). Clearly, the dark blue and pink areas indicated the distributions of the strongest intensities of the RhRh shell at the beginning of the experiment as well as the Rh nanoparticles were exposed to CO.

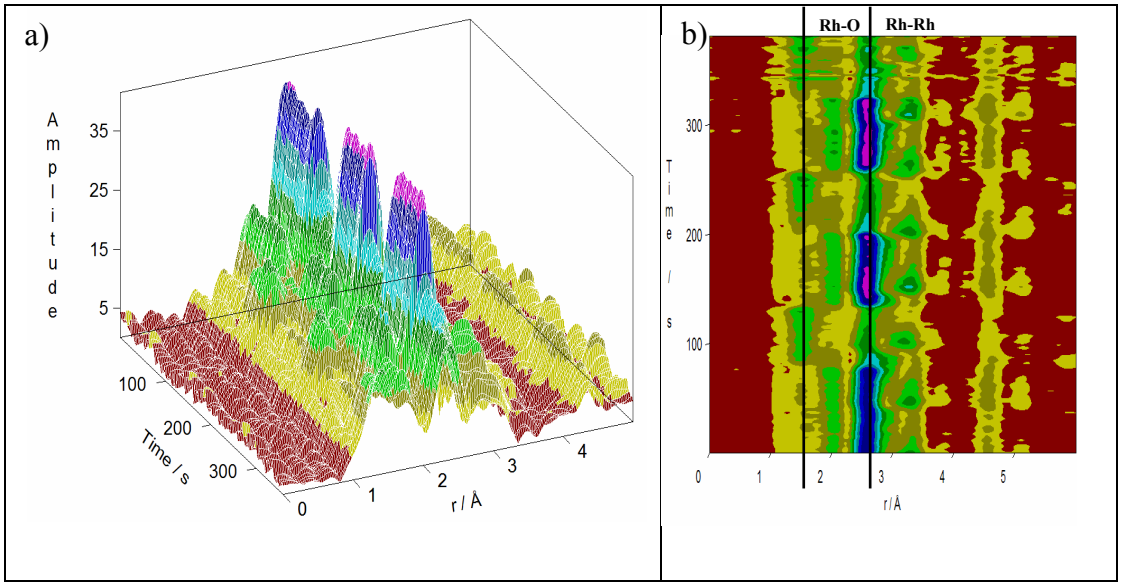

Figure 6.6 a) Radial distribution functions (not phase corrected) derived from Rh K edge during $(O_2/CO)_3$ switching experiment at 573 K. Spectra recorded every 100 ms, b) Corresponding top view of the presented Fourier transforms.

The XAFS spectra of 4 wt% Rh/Al_2O_3 upon the flow of O_2 and NO were compared in Figure 6.7. It can be observed that the Rh phase upon NO exposure is distinct from that formed through exposure to O_2. This is most clearly evidence in the XANES where the intensity of the white line is significantly diminished and has different shape relative to the obtained on the latter case [21, 22].

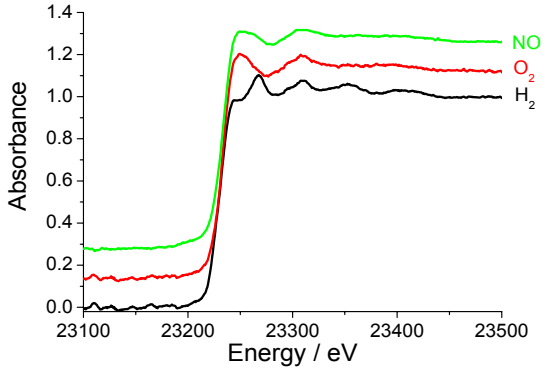

Figure 6.7 Normalised Rh K edge EDE spectra after H_2, O_2, NO exposures to 4 wt% Rh/Al_2O_3 at 573 K.

Figure 6.8a and 6.8b reveal the range of IR active species present on the Rh surface after 5 % CO/He and 5 % NO/He exposures at each cycle of the experiment done at 423 K.

After CO exposure to the Rh sample in the first cycle, the spectrum (figure 6.8a, black line) displays the two sharp peaks at 2098 cm^{-1} and 2025 cm^{-1} assigned to rhodium geminal dicarbonyl species (Rh^{+}-$(CO)_2$). These bands are overlapped with the signal of the linear species (Rh-CO) at 2056 cm^{-1}. A broad band present around 1865 cm^{-1} is ascribed to the bridged CO species. The following (CO/NO) cycles highlight the adsorption of the same CO species while CO exposure, however the intensities of the bands associated with the metallic Rh surface (linear, bridged) are largely decreased. Moreover, the succeeding (NO/CO) switches resulted in the emergence of the NO species adsorbed on the Rh surface. The broad band centred at ca. 1644 cm^{-1} can be attributed to varies species as outlined in the $(CO/NO)_3$ switches at 573 K. The peak at 1910 cm^{-1} is due to the $Rh(NO)^{+}$ species. The broad peak centred at ca. 1833 cm^{-1} can be assigned to a monodispersed $Rh(NO)^{-}$ species and/or to the $Rh(NO)_2$ site [23-25]. In the light of the previous findings the peak position at ca. 2252 cm^{-1} is assigned to an Al-NCO species [9, 13, 24]. Formation of this species indicates the occurrence of N-O dissociation and combination of adsorbed N and CO species.

The DRIFTS spectrum in figure 6.8b shows the range of nitrosyl species formed and residual carbonyl species present on the Rh surface after ca. 60 s of 5 % NO/He exposure at each cycle. The intense band at 1654 cm^{-1} could be assigned to 'low-wavenumber' $Rh(NO)^{-}$ species, molecular NO adsorbed upon Rh surfaces and

nitrates adsorbed upon the alumina surface. The intense peak centred at 1733 cm^{-1} seems to be problematic to assign as a band in this region has been previously associated to the bent, 'high-wavenumber' $Rh(NO)^{-}$ species [17, 23, 26] and to the asymmetric N-O stretch of the geminal dinitrosyl species $Rh(NO)_2$ [12]. The presence of the corresponding band of the symmetric N-O frequency at 1828 cm^{-1} confirms that the dinitrosyl species does form on the Rh surface. The weak signal at 1913 cm^{-1} is attributed to the linear $Rh(NO)^{+}$ species. Apart from the nitrosyl species adsorbed on the Rh surface throughout NO exposure steps, there is also a small contribution of the geminal dicarbonyl species (ν_{sym}~ 2096 cm^{-1}, ν_{asym}~ 2023 cm^{-1}) and the Al-NCO species adsorbed (ν~2252 cm^{-1}).

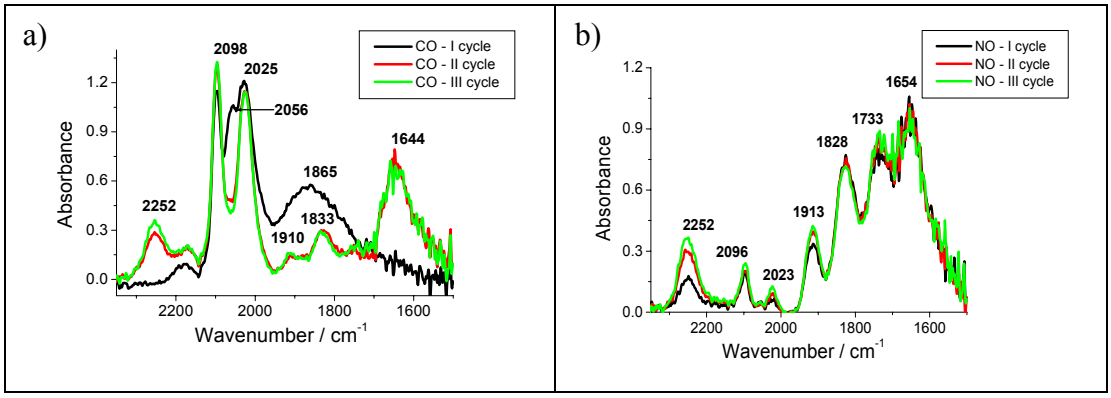

Figure 6.8 DRIFTS spectra of 4 wt% Rh/Al_2O_3 during I, II, III cycle of a) CO exposure and b) NO exposure at 423 K.

Figure 6.9 shows k^3 weighted EDE spectra for 4 wt% Rh/Al_2O_3 before and after exposure to 5 % CO/He and subsequently to 5 % NO/He at 423 K, along with the corresponding Fourier transforms. The structural and statistical information derived from the analyses is given in Table 6.2. A nanoparticulate structure of Rh phase was observed upon 5 % H_2/He. The EXAFS and FT features reveal structural changes to have occurred to the catalyst upon exposure to a flow of 5 % CO/He at 423 K. The coordination number of the RhRh shell decreased from ca. 7.5 under H_2 to ca. 5.1 indicating partial disruption of Rh particles. Upon exposing the system to a flow of 5 % NO/He for 60 s, EXAFS reports significant disruption of Rh particles as the drop of the RhRh coordination number to ca. 3 and the presence of an additional RhO shell with the coordination number of ca. 1 were observed.

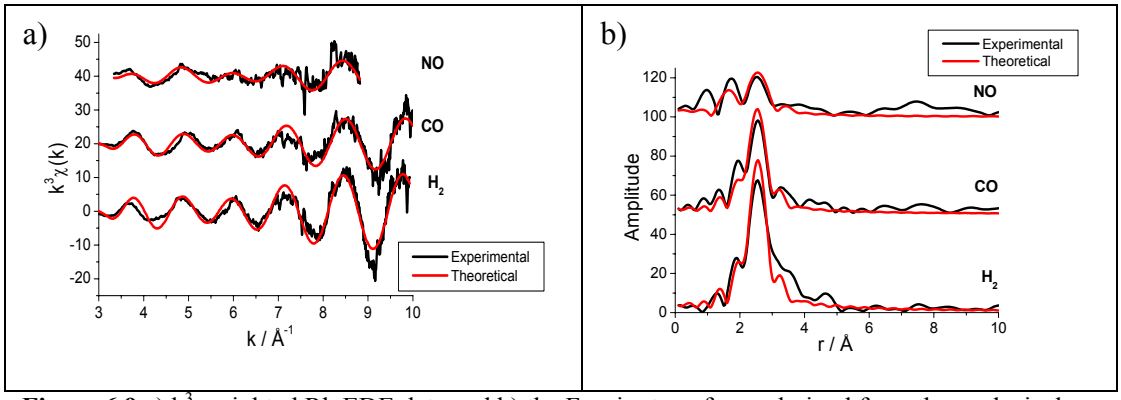

Figure 6.9 a) k^3 weighted Rh EDE data and b) the Fourier transforms derived from the analysis done over 4 wt% Rh/Al_2O_3 under 5 % H_2/He, 5 % CO/He and 5 % NO/He at 423 K.

Conditions	Scatterer	CN	r (Å)	$2\sigma^2/Å^2$	E_F (eV)	R (%)
5 % H_2/He	Rh	7.5 (2)	2.66 (1)	0.0135	-5.7	39
5 % CO/He	Rh	5.1 (2)	2.64 (1)	0.0135	-0.4	45
5 % NO/He	Rh	3.0 (2)	2.66 (2)	0.0135	2.1	58
	O	0.8 (2)	2.07 (3)	0.014		

Table 6.2 Structural and statistical data for 4 wt% Rh/Al_2O_3 derived from the analysis of spectra given in Figure 6.9. Other parameters: H_2, CO step: k = 3 – 10 $Å^{-1}$, NO: 3 – 9 $Å^{-1}$.

Figure 6.10 displays the variation in the Rh-Rh coordination number during the CO/NO switching experiment over 4 wt% Rh/Al_2O_3 at 423 K and 573 K. The EXAFS parameters show the 4 wt% Rh system to exhibit a significantly different structural response to 5 % CO/He and 5 % NO/He at two different temperatures. At 573 K (red line), substantial changes in the RhRh occupation took place with gas switching. Firstly, very little structural change occurred over Rh particles after the initial switch from He to CO. The subsequent NO exposure induced an extensive oxidation of Rh component. Afterwards the RhRh occupation increased during CO exposure. The variations of RhRh occupation effectively show that structurally the system closely follows the pattern of gas switching, and such changes are significant when compared to the case at 423 K. Relatively larger disruption of Rh particles upon initial CO exposure was observed at lower temperature (black line) and an extensive oxidation of Rh particles occurred after first NO exposure. However, upon the following (CO/NO) the RhRh occupation seems to be similar. The average CN_{RhRh} observed in this system under the initial NO exposure and upon the following (CO/NO) cycle was around 3 indicating particles of an average atomicity of ca. 7 – 4 Rh atoms [27].

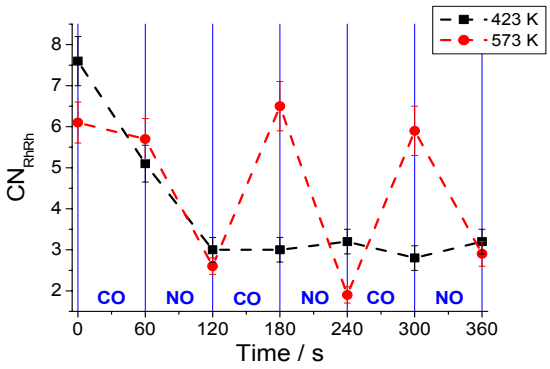

Figure 6.10 Variations of RhRh coordination number during the CO/NO switching experiment over 4 wt% Rh/Al_2O_3 at the temperature indicated.

Figure 6.11a and 6.11b reveal the temporal IR adsorption characteristics of the 4 wt% Rh catalyst as it is exposed to a flow of 5 % CO/He and 5 % NO/He at 323 K, respectively. The DRIFTS spectra display the same carbonyl and nitrosyl species present on the Rh surface as is the case of CO and NO adsorption over Rh catalyst at 423 K (Figure 6.8). However, significantly more $Rh(NO)^+$ and $Rh(CO)_2$ species were formed and no detection of isocyanate species at ca. 2252 cm^{-1} were observed throughout the NO exposure steps. Caution needs to be applied when analysing the DRIFTS spectra collected at 323 K due to the poor quality of data.

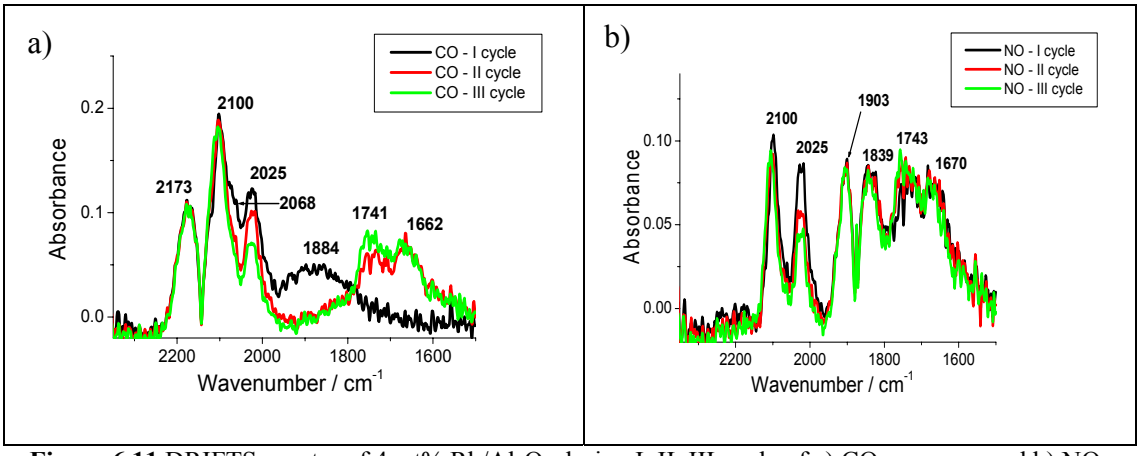

Figure 6.11 DRIFTS spectra of 4 wt% Rh/Al_2O_3 during I, II, III cycle of a) CO exposure and b) NO exposure at 323 K.

6.3.2 $Rh/CeO_x/\gamma\text{-}Al_2O_3$

The effect of ceria on the catalytic performance of rhodium catalysts has been studied considering the sample derived from the second preparation method as described in chapter 3, section 3.2. In this method, the ceria is deposited on the pre-supported Rh metal on $\gamma\text{-}Al_2O_3$.

Figure 6.12 displays the dynamic response of ΔXANES for 4 wt% $Rh/CeO_x/Al_2O_3$ (II) to the flow of reactive gases such as to CO and NO at the temperatures employed (423 K, 573 K). The XANES variations indicate a relatively simple and progressive increase in the degree of Rh oxidation upon NO exposure as a function of temperature. The XANES pattern of response to the gaseous environment by the facile oxidation and reduction of the Rh component is repeated throughout the (CO/NO) switches in consistent 'cycles'. The overall temporal dependence of the changes in XANES observed for ceriated Rh catalyst are similar to that observed in the non-ceriated Rh sample. However, clearly at 573 K the magnitude of the changes in XANES structure for 4 wt% $Rh/CeO_x/Al_2O_3$ (II) upon the oxidising steps are slightly larger (ΔXANES ~ 0.08) when compared to the XANES response of undoped Rh catalysts.

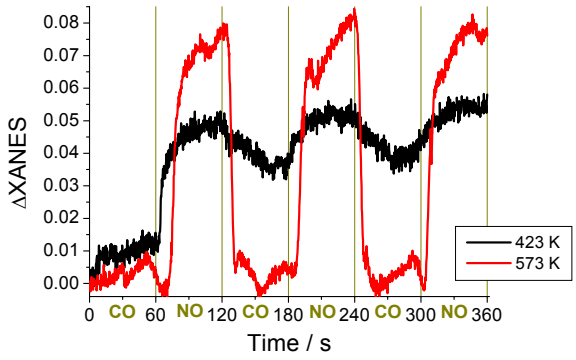

Figure 6.12 Changes in Rh K edge XANES during CO/NO switches of 4 wt% $Rh/CeO_x/Al_2O_3$ (II) at 423 K and 573 K.

The DRIFTS spectra of 4 wt% $Rh/CeO_x/Al_2O_3$ upon 5 % CO/He exposure at 573 K shown in Figure 6.13a display the predominance of the linear (ν_{lin} ~ 2041 cm^{-1}) and bridged CO species (ν_{brid} ~ 1845 cm^{-1}) as was the case of 4 wt% Rh on alumina. The formation of the linear $Rh(NO)^+$ species ($\nu_{Rh(NO)+}$ ~ 1892 cm^{-1}) and the species around 1640 cm^{-1} (outlined above) were observed throughout exposing 5 % NO/He to ceriated Rh catalysts (Figure 6.13b). The DRIFTS spectra show all the carbonyl and nitrosyl species to display very similar adsorption behaviour in the

following (CO/NO) cycles. However, caution needs to be applied analysis IR data due to the poor quality of data.

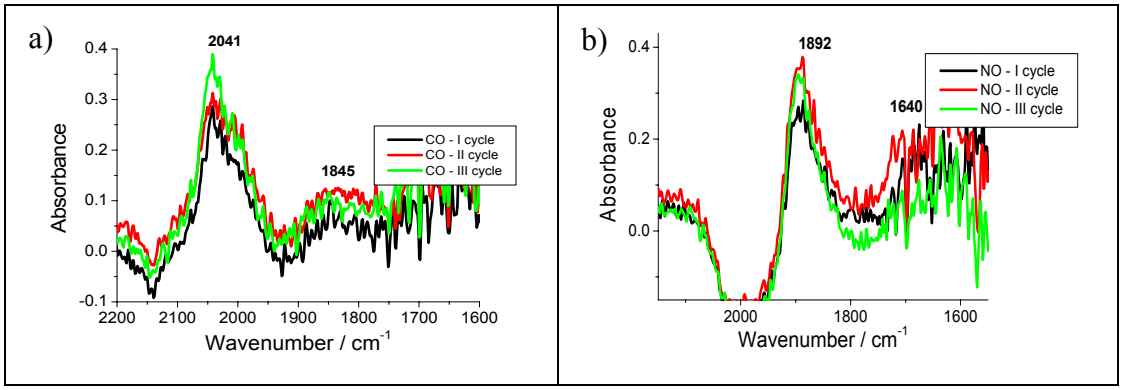

Figure 6.13 DRIFTS spectra of 4 wt% $Rh/CeO_x/Al_2O_3$ during I, II, III cycle of a) CO exposure and b) NO exposure at 573 K.

Figures 6.14a and 6.14b show the DRIFTS spectra of 4 wt% $Rh/CeO_x/Al_2O_3$ (method II) under exposures of CO and NO during the switching experiment at 423 K. During the initial CO exposure the spectra (figure 6.13a, black line) show mainly a sharp peak appearing around 2062 cm^{-1} assigned to the linear CO species which intensity is relatively higher than the residual CO peaks present as it was previously observed in the study of Rh-CO interaction (chapter 4). There are two shoulders associated with the rhodium geminal dicarbonyl species at 2100 and 2029 cm^{-1}. Furthermore, the presence of the additional peak around ~1710 cm^{-1} assigned to bridged CO species between Rh and Ce atoms also confirms the strong interaction between ceria and rhodium. The bridged CO species give a broad signal around 1870 cm^{-1}. The drop of the linear and bridged CO species and the absence of the Rh(CO)Ce species was observed during the following CO exposures. At the same time the DRIFTS spectra display the evolution of the other carbonyl and nitrosyl species such as the Al-NCO species (ν~2245 cm^{-1}), $Rh^+(CO)_2$ (ν_{sym}~ 2100 cm^{-1}, ν_{asym}~ 2029 cm^{-1}), $Rh^+(NO)$ (ν~1905 cm^{-1}), $Rh(NO)_2$ (ν_{sym}~ 1830 cm^{-1}) and varies species assigned to 1640 cm^{-1}.

Upon 5 % NO/He exposure the identical nitrosyl species are observed on the Rh surface of the ceriated Rh catalysts as for the 4 wt% Rh on alumina case, i.e. the Al-NCO species (ν~2249 cm^{-1}), $Rh^+(CO)_2$ (ν_{sym}~ 2095 cm^{-1}, ν_{asym}~ 2024 cm^{-1}), $Rh^+(NO)$ (ν~1909 cm^{-1}), $Rh(NO)_2$ (ν_{sym}~ 1829 cm^{-1}, ν_{asym}~ 1731 cm^{-1}) and varies species assigned to 1656 cm^{-1}. However, the gradual increase of the Al-NCO and $Rh^+(NO)$ species was detected throughout the following NO switches. Moreover, the

residual amount of geminal dicarbonyl species stayed on the Rh surface upon the NO flow.

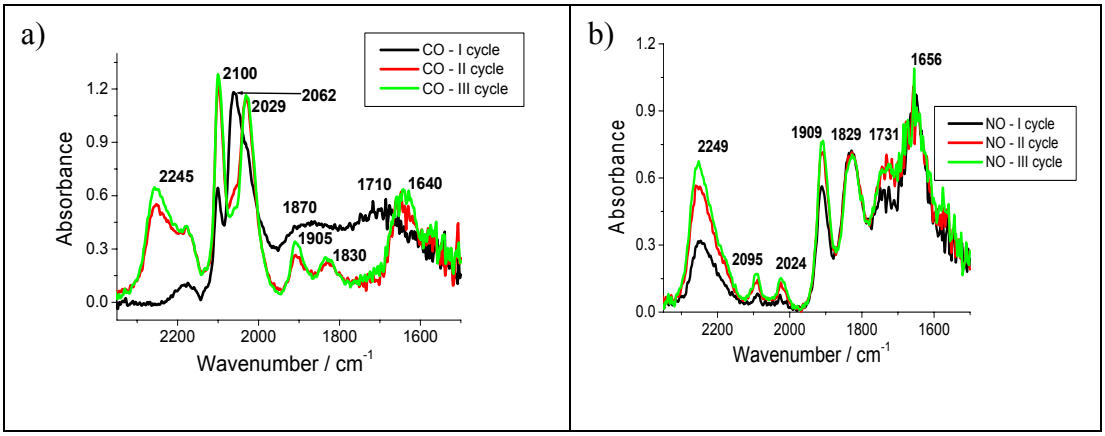

Figure 6.14 DRIFTS spectra of 4 wt% $Rh/CeO_x/Al_2O_3$ during I, II, III cycle of a) CO exposure and b) NO exposure at 423 K.

The apparent variations in the first shell Rh-Rh coordination number as a function of temperature for 4 wt% $Rh/CeO_x/Al_2O_3$ is shown in Figure 6.15. At 423 K there is no significant change in the Rh-Rh coordination following the initial, structural disruption of Rh particles upon 5 % CO/He and then extensive oxidation (large drop of CN_{Rh-Rh}) upon 5 % NO/He exposure. Nonetheless, at 573 K the Rh systems structurally follows the pattern of gas switching indicating clear oscillations of Rh occupation between the metallic or oxidised Rh phase.

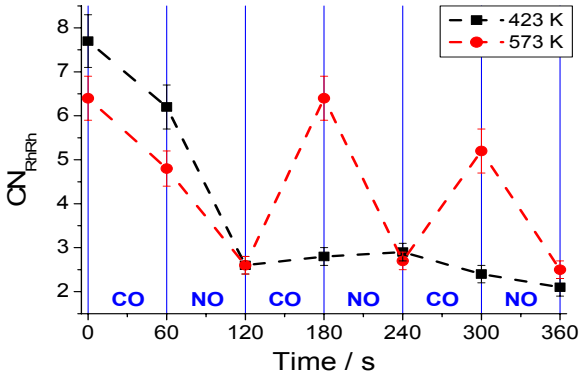

Figure 6.15 Variations of RhRh coordination number during the CO/NO switching experiment over 4 wt% $Rh/CeO_x/Al_2O_3$ at the temperature indicated.

6.3.3 $Rh/ZrO_2/\gamma\text{-}Al_2O_3$ – $Rh/CeO_x/ZrO_2/\gamma\text{-}Al_2O_3$

The effect of zirconia and ceria/zirconia on the structural behaviour of rhodium catalysts has been studied, in view of three samples with different Ce:Zr ratio as 0:1, 1:1, and 2:1.

6.3.3.1 $Rh/ZrO_2/Al_2O_3$

Figure 6.16 shows the XANES structures (E = 23250 eV) during (CO/NO) switches over 4 wt% $Rh/ZrO_2/Al_2O_3$ at 423 K, 573 K. The XANES variations indicate a relatively progressive increase in the degree of Rh oxidation as a function of temperature. At 423 K after an extensive oxidation of the Rh component under 5 % NO/He flow, slight variations in the oxidation state of the Rh component are observed throughout the following (CO/NO) switching. At 573 K the Rh phase of the zirconated Rh catalysts alters consistently with the oxidised and reduced gas feedstock. Clearly within two temperatures employed the magnitude of the changes in XANES structure for 4 wt% $Rh/ZrO_2/Al_2O_3$ indicated the similar level of Rh oxidation as the Rh particles derived from ceriated Rh catalysts (Figure 6.12).

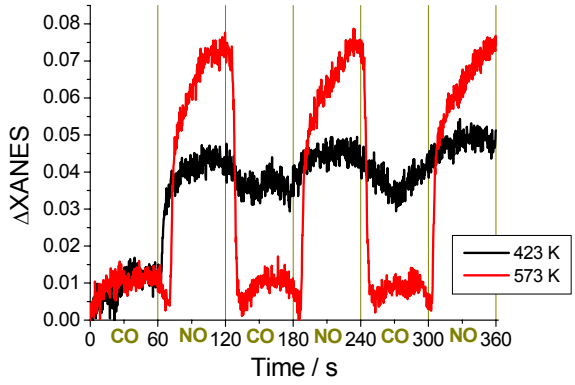

Figure 6.16 Changes in Rh K edge XANES during CO/NO switches of 4 wt% Rh/ ZrO_2/Al_2O_3 at 423 K and 573 K.

The DRIFTS spectra of 4 wt% $Rh/ZrO_2/Al_2O_3$ upon 5 % CO/He exposure at 573 K shown in Figure 6.17a display the linear (ν_{lin} ~ 2048 cm^{-1}) and bridged CO species (ν_{brid} ~ 1868 cm^{-1}) being the predominant forms on the Rh surface. The formation of the linear $Rh(NO)^+$ species ($\nu_{Rh(NO)+}$ ~ 1890 cm^{-1}) and the species around 1625 cm^{-1} (outlined above) were observed throughout exposing 5 % NO/He to zirconated Rh catalysts (Figure 6.17b). The DRIFTS spectra show very similar

adsorption behaviour of all the carbonyl and nitrosyl species in the following (CO/NO) cycles.

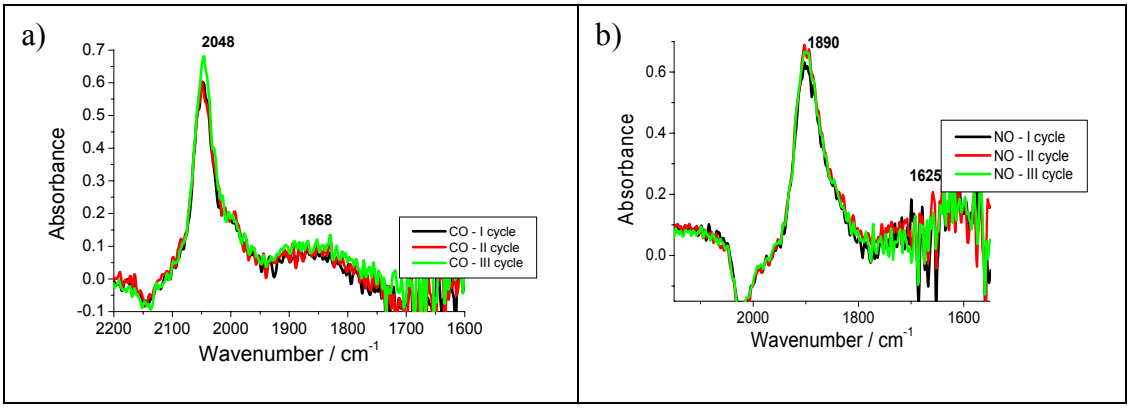

Figure 6.17 DRIFTS spectra of 4 wt% $Rh/ZrO_2/Al_2O_3$ during I, II, III cycle of a) CO exposure and b) NO exposure at 573 K.

Figures 6.18a and 6.18b display the DRIFTS spectra of 4 wt% $Rh/ZrO_2/Al_2O_3$ obtained upon the CO exposure and NO exposure steps, respectively, of I, II and III cycle at 423K. Upon the initial CO exposure the same dominant types of CO species adsorbed on the Rh surface are observed as for ceriated Rh catalysts such as linear (ν_{lin} ~ 2062 cm^{-1}) and bridged CO species (ν_{brid} ~ 1868 cm^{-1}) with a minor quantity of geminal dicarbonyl species (ν_{sym} ~ 2098 cm^{-1}, ν_{asym} ~ 2027 cm^{-1}). Throughout the following (CO/NO) switches the intensity of the geminal dicarbonyl species increased in the expense of the linear and bridged CO species. At the same time the DRIFTS spectra display the evolution of the other carbonyl and nitrosyl species such as the Al-NCO species (ν~2251 cm^{-1}), $Rh^+(NO)$ (ν~1908 cm^{-1}), $Rh(NO)_2$ (ν_{sym}~ 1834 cm^{-1}) and varies species assigned to 1643 cm^{-1}.

Upon the oxidising step of this process (NO exposure) the identical nitrosyl species are observed on the Rh surface of the zirconiated Rh catalysts as for the 4 wt% Rh on alumina case, i.e. the Al-NCO species (ν~2249 cm^{-1}), $Rh^+(CO)_2$ (ν_{sym}~ 2094 cm^{-1}, ν_{asym}~ 2024 cm^{-1}), $Rh^+(NO)$ (ν~1912 cm^{-1}), $Rh(NO)_2$ (ν_{sym}~ 1830 cm^{-1}, ν_{asym}~ 1736 cm^{-1}) and various species assigned to 1659 cm^{-1}. The evolutions of the Al-NCO, $Rh^+(CO)_2$ and $Rh^+(NO)$ species are slightly increased upon the following NO switches.

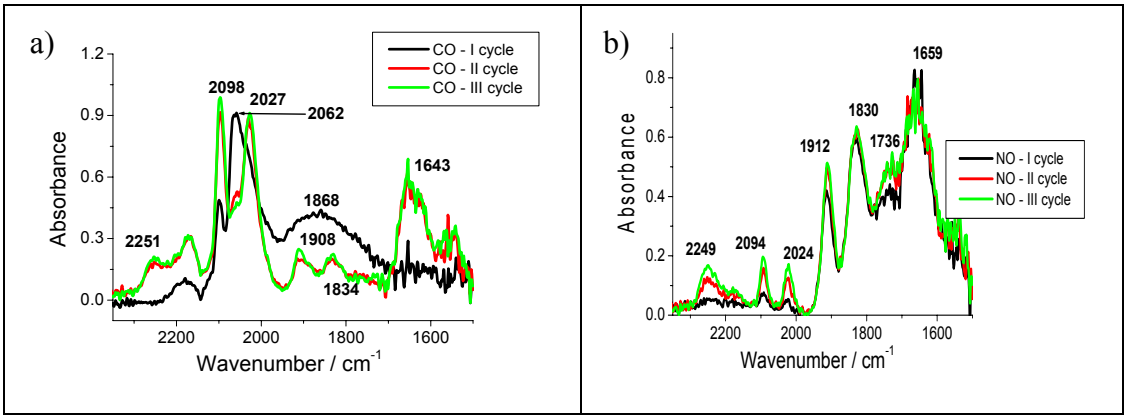

Figure 6.18 DRIFTS spectra of 4 wt% $Rh/ZrO_2/Al_2O_3$ during I, II, III cycle of a) CO exposure and b) NO exposure at 423 K.

6.3.3.2 $Rh/CeO_x/ZrO_2/Al_2O_3$

Figures 6.19a and 6.19b display the XANES variations (E = 23250 eV) of 4 wt% Rh/ Al_2O_3 promoted by ceria-zirconia with different Ce:Zr ratio as 1:1 and 2:1, respectively throughout the (CO/NO) switching experiment at 423 K – 573 K. As was previously observed for all series of Rh catalysts, the XANES changes indicate a relatively simple and progressive increase in the degree of Rh oxidation as a function of temperature. At 573 K the XANES pattern of response to the gaseous environment by the facile oxidation and reduction of the Rh component is repeated throughout the (CO/NO) switches in consistent 'cycles'. A slightly smaller level of the Rh component oxidation is observed for 4 wt% $Rh/CeO_x/ZrO_2/Al_2O_3$ (Ce:Zr;1:1) than for 4 wt% $Rh/CeO_x/ZrO_2/Al_2O_3$ (Ce:Zr;2:1) at 573 K throughout the (CO/NO) switches.

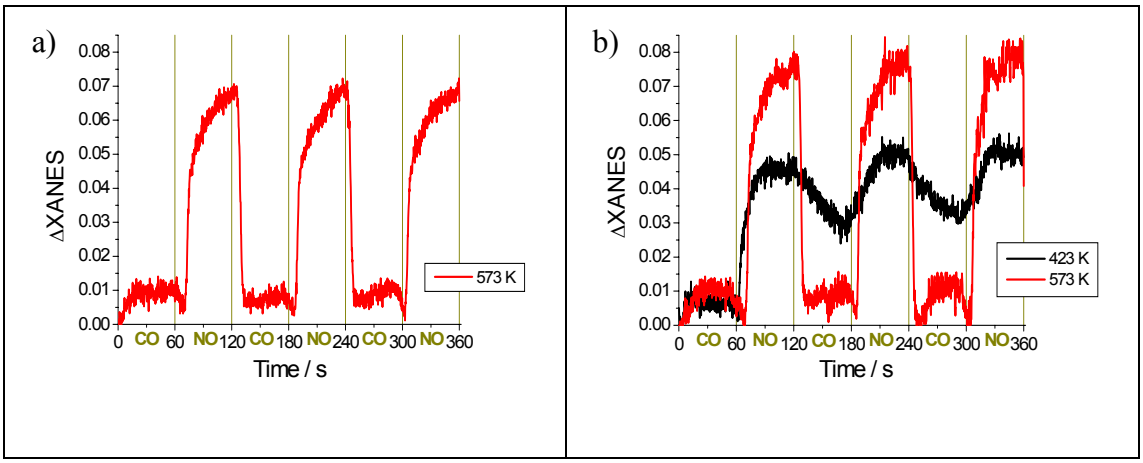

Figure 6.19 Changes in Rh K edge XANES during CO/NO switches of a) 4 wt% $Rh/CeO_x/ZrO_2/Al_2O_3$ (Ce:Zr:;1:1) and b) 4 wt% $Rh/CeO_x/ZrO_2/Al_2O_3$ (Ce:Zr:;2:1) at the temperatures indicated.

The DRIFTS data shown in Figure 6.20a and 6.20b for 4 wt% Rh/Al_2O_3 doped by ceria-zirconia with the ratios of (Ce:Zr;1:1) and (Ce:Zr:2:1), respectively, show the evidence of the metallic environment during the following CO flows at 573 K with the linear (ν_{lin} ~ 2047 cm^{-1}) and bridged CO species (ν_{brid} ~ 1870 cm^{-1}) formation. The formation of the linear $Rh(NO)^+$ species ($\nu_{Rh(NO)+}$ ~ 1896 cm^{-1}) and the species with the frequency of ca. 1630 cm^{-1} (outlined above) were reported throughout exposing 5 % NO/He to both Rh catalysts doped by ceria-zirconia (Figure 6.20c, 6.20d). The DRIFTS spectra show all the carbonyl and nitrosyl species to display very similar adsorption behaviour in the following (CO/NO) cycles.

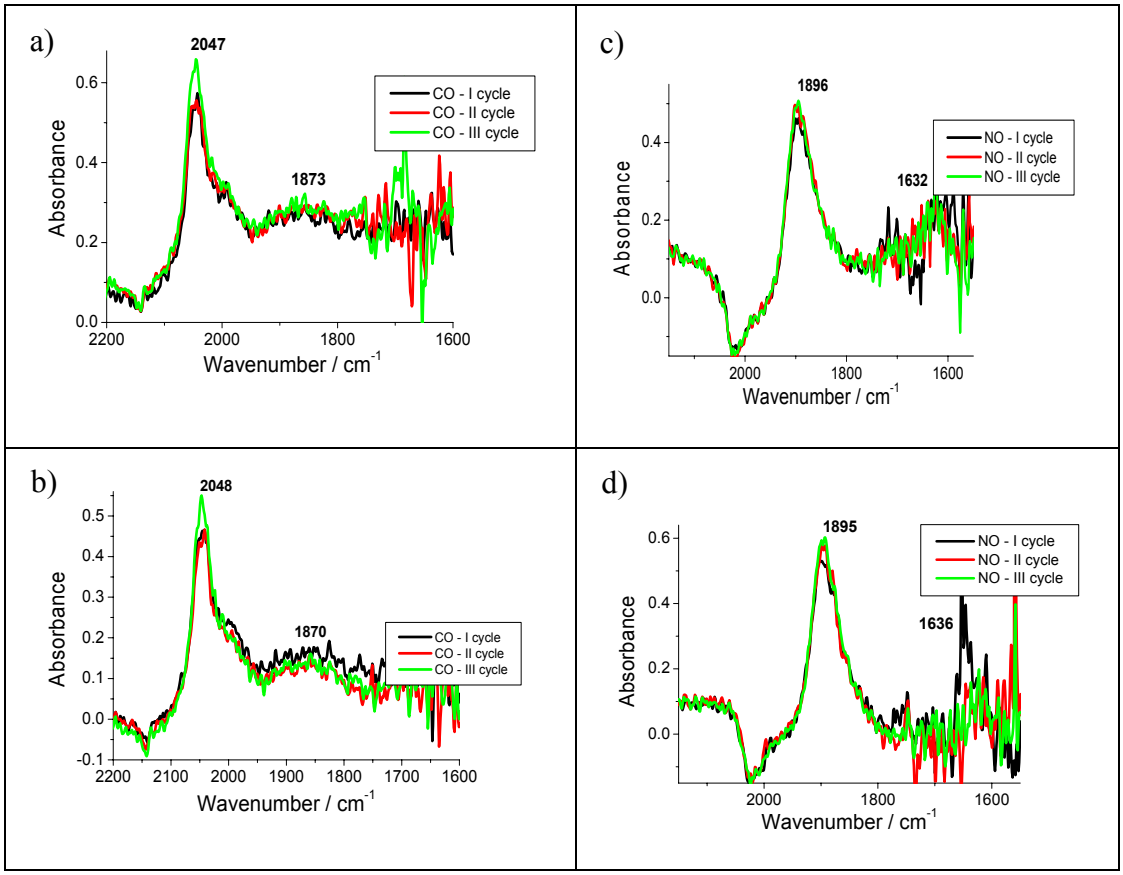

Figure 6.20 DRIFTS spectra of 4 wt% $Rh/CeO_x/ZrO_2/Al_2O_3$ (Ce:Zr;1:1) under a) CO exposure and c) NO exposure and 4 wt% $Rh/CeO_x/ZrO_2/Al_2O_3$ (Ce:Zr;2:1) under b) CO exposure d) NO exposure during I, II, III cycle at 573 K.

The EDE data, obtained simultaneously with the DRIFTS data presented above, display the structural changes for the Rh particles of two ceria-zirconia and only zirconia doped Rh catalysts during CO/NO cycling at 573 K (Figure 6.21). In general, after the initial disruption of Rh particles upon CO and NO exposures the structural response of the investigated Rh catalysts throughout $(CO/NO)_3$ switches

follows similar oscillatory pattern of Rh occupation such as a decrease of Rh occupation during NO exposure and an increase of Rh particle size while CO exposure. However, in the case of zirconated Rh catalyst, the relatively smaller disruption of Rh particles is observed upon the initial (CO/NO) exposure.

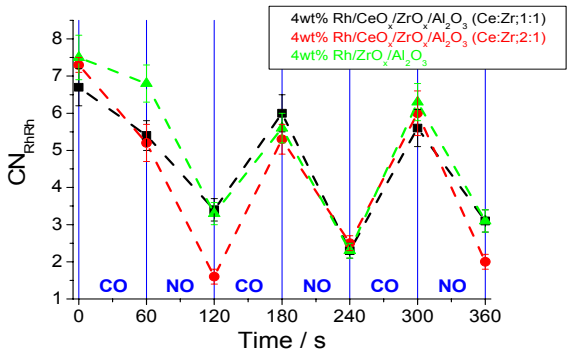

Figure 6.21 Variations of RhRh coordination number during the CO/NO switching experiment over 4 wt% $Rh/ZrO_2/Al_2O_3$, 4 wt% $Rh/CeO_x/ZrO_2/Al_2O_3$ (Ce:Zr; 1:1, 2:1) at 573 K.

The DRIFTS spectra of the series of catalysts (4 wt% $Rh/CeO_x/ZrO_2/Al_2O_3$ (Ce:Zr;1:1;2:1) indicated upon initial 5 % CO/He exposure at 423 K were plotted in Figure 6.22a and 6.22b displaying the same two dominant CO entities (Rh-CO, bridged) with minor quantity of $Rh(CO)_2$ species formed on the Rh surface of ceria-zirconia doped catalysts as in the ceriated Rh/Al_2O_3 catalyst. Moreover, the formation of the bridged CO species between Rh and Ce atoms was detected at ca. 1691 cm^{-1} and 1705 cm^{-1}. The following (CO/NO) switches decreased the amount of CO species adsorbed on the metallic surface increasing the $Rh(CO)_2$ formation. At the same time the DRIFTS spectra display the evolution of the other nitrosyl species such as the Al-NCO species, $Rh^+(NO)$, and varies species assigned to 1642 cm^{-1}.

Figures 6.22c and 6.22d show that upon 5 % NO/He exposure the identical nitrosyl species were formed on the Rh surface of the ceria-zirconia doped Rh catalysts as for the 4 wt% Rh on alumina case, i.e. the Al-NCO species ($\nu \sim 2249$ cm^{-1}), $Rh^+(NO)$ ($\nu \sim 1908$ cm^{-1}), $Rh(NO)_2$ ($\nu \sim 1830$ cm^{-1}, 1737 cm^{-1}) and varies species assigned to ca. 1660 cm^{-1} with the residual quantity of $Rh^+(CO)_2$ formed. However, the gradual increase of the Al-NCO and $Rh^+(NO)$ species as well as geminal dicarbonyl species were detected throughout the following NO switches as it was reported for only ceriated Rh catalysts.

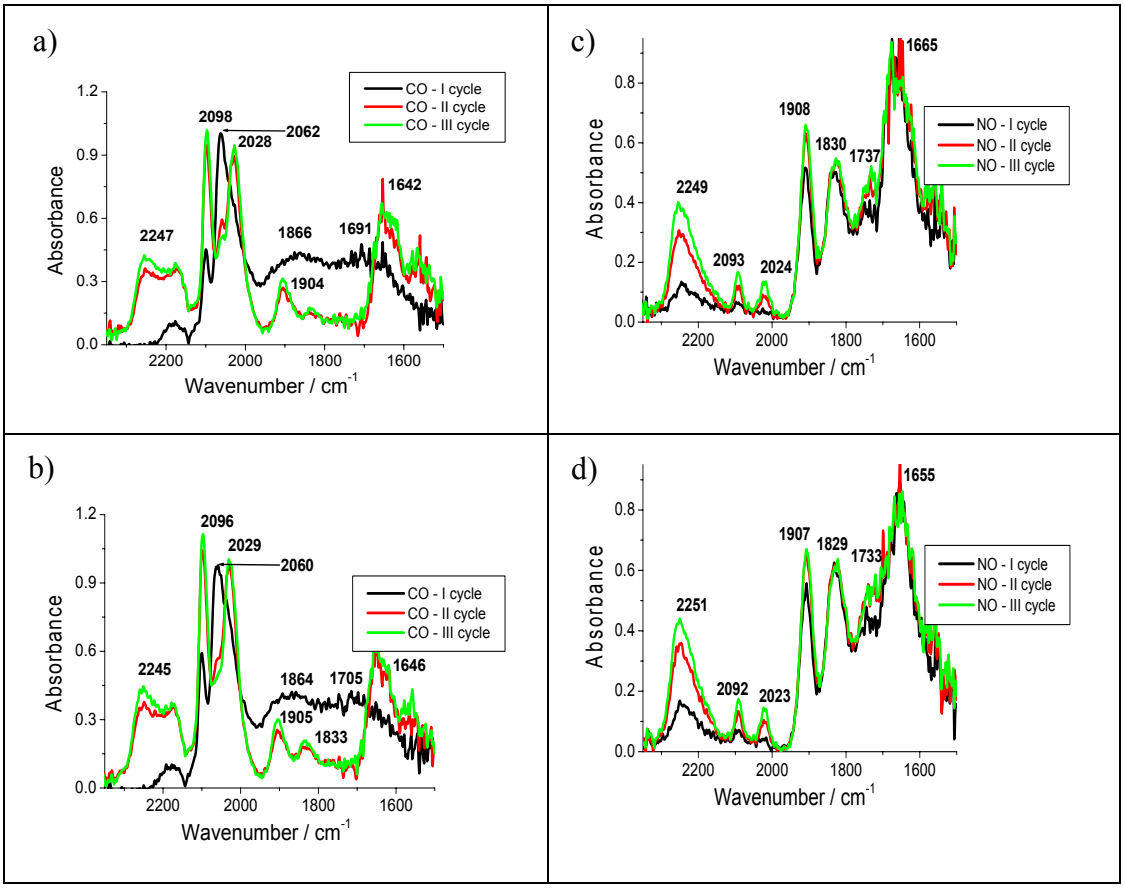

Figure 6.22 DRIFTS spectra of 4 wt% $Rh/CeO_x/ZrO_2/Al_2O_3$ (Ce:Zr;1:1) under a) CO exposure and c) NO exposure and 4 wt% $Rh/CeO_x/ZrO_2/Al_2O_3$ (Ce:Zr;2:1) under b) CO exposure d) NO exposure during I, II, III cycle at 423 K.

Figure 6.23 displays the variation in the Rh-Rh coordination number during the CO/NO switching experiment over Rh catalysts doped by ceria-zirconia and only zirconia at 423 K. The same structural behaviour of Rh particles can be observed upon (CO/NO) cycles for all Rh catalysts investigated. The initial CO exposure induced the partial disruption of Rh particles (reducing CN_{RhRh} from ca. 8 to ca. 6.5) and first switch from CO to NO extensively oxidised the Rh component. However, throughout the following (CO/NO) cycles there is no significant change in the Rh-Rh coordination number.

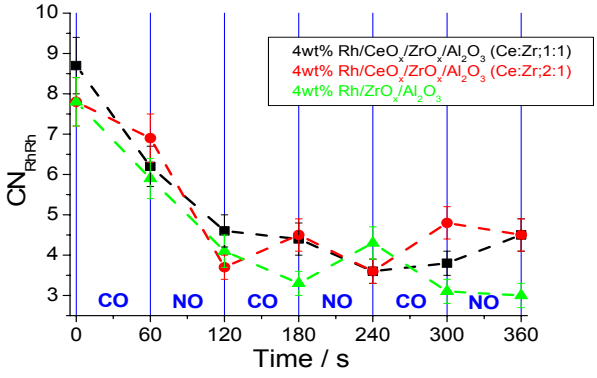

Figure 6.23 Variations of RhRh coordination number during the CO/NO switching experiment over 4 wt% $Rh/ZrO_2/Al_2O_3$, 4 wt% $Rh/CeO_x/ZrO_2/Al_2O_3$ (Ce:Zr; 1:1, 2:1) at 423 K.

6.4 Discussion

The time resolved and synchronous XAFS/DRIFTS/MS experiment, described within this chapter, reveals the complex response to the adsorption of CO and NO over the Rh catalysts investigated. Indeed, the structural behaviour of the Rh catalysts altered significantly when compared the results from two different temperatures employed.

For the high temperature, simple inspection of XANES region indicates that Rh particles were retained as metallic upon 5 % CO/He exposure at 573 K. Subsequently, the Rh component was rapidly dominated by the oxidised form under 5 % NO/He flow. The XANES features highlighted a rapid, initial oxidation of the Rh particles, with a slower, deeper oxidation followed within time of NO exposure. The detailed EXAFS analysis demonstrated very little changes of RhRh occupation of 4 wt% Rh/Al_2O_3 (from 6.1 to 5.7) after CO exposure and upon NO flow a significant drop of the average Rh particle size (CN_{RhRh} ~ 2.6) and the emergence of the additional Rh-O shell (CN_{RhO} ~ 2) was detected. It is well known that CO can disperse very small Rh particles over longer timescales [28]. However, over Rh catalysts used in this project, the initial CO flow fails to introduce large changes in the observed Rh EXAFS, when compared with the extensive disruption of Rh particles by NO exposure. The NO interaction with Rh particles was an expected result based upon previous findings [29, 30] where NO exposure induced rapid and extensive oxidation of the Rh component. The highly exothermic dissociative chemisorption of NO was found to be the initial step for the phase changes.

Furthermore, the EDE data were in good agreement with the corresponding DRIFTS spectra, confirming that the linear and bridged CO species (entities associated with extended Rh surfaces) were predominant upon CO exposure, however under NO exposure, mostly the formation of the $Rh(NO)^+$ species was detected. The positive charge of NO in the $Rh\text{-}NO^+$ species is induced by an oxygen atom or a nitrate anion adsorbed at the same time or an adjacent Rh site. The easily dissociable oxidant NO is well documented to oxidise metallic centres more readily than CO. This is due to lower dissociation energy of NO (630 kJ/mol) compared to CO (1076 kJ/mol) [31]. The rapid oxidation of the Rh phase at higher temperature results in preference for the electron donation and the formation of the thermally stable, linear Rh nitrosyl species. When compared with the experiment performed at lower T, an enhancement of the peak attributed to $RhNO^+$ species and the red shift from 1913 cm^{-1} at 423 K to 1896 cm^{-1} at 573 K was observed. The previous study has also concluded that this species can be a highly transient form of $Rh(NO)_2$ [32]. Throughout the following (CO/NO) cycles, no apparent evidence for particle fragmentation was observed as the system was effectively re-reduced to its original RhRh occupation upon CO exposure. Clearly, the RhRh occupation was modified under reaction conditions indicating the oxidative disruption and reductive agglomeration processes to have occurred over Rh catalysts. The combined MS/DRIFTS results indicate that CO_2, N_2 and N_2O gases were generated upon every switch $CO_{(g)} \rightarrow NO_{(g)}$ and $NO_{(g)} \rightarrow CO_{(g)}$. The formation of N_2O required the presence of CO which enhanced the NO dissociation. Scheme 6.1 highlights a mechanism of the reaction between NO and CO over Rh catalysts deposited on γ-alumina proposed by Hecker and Bell [24]. Firstly the CO and NO molecules adsorbed on the Rh surface (1, 2) and then NO directly decomposed via an activated process to form atomic nitrogen and oxygen (3). The N_2 formation from two adsorbed nitrogen atoms (5) appears to be rate limiting step of the reaction. The oxygen is removed from the catalyst surface via an interaction with CO (6) playing a role of reducing agent. The proposed mechanism is involved in the formation of the intermediate species of N_2O (7) and under TWC these species are rapidly converted to N_2 (8).

$$CO \rightarrow CO_a \quad (1)$$

$$NO \rightarrow NO_a \quad (2)$$

$NO_a \rightarrow N_a + O_a$ * (3)

$NO_a + N_a \rightarrow N_2 + O_a$ * (4)

$2N_a \rightarrow N_2$ * (5)

$CO_a + O_a \rightarrow CO_2$ * (6)

$NO_a + N_a \rightarrow N_2O$ * (7)

$N_2O \rightarrow O_a + N_2$ * (8)

* indicates a vacant adsorption site

Scheme 6.1. Mechanism of the NO/CO reactions over Rh.

In the low temperature, the levels of Rh oxidation and the particle disruption of 4 wt% Rh/Al_2O_3 were reported to be smaller upon NO exposures when compared to the $(CO/NO)_3$ experiment performed at 573 K. The EXAFS results show that after the oxidative disruption of Rh particles upon the first NO exposure, the mean Rh-Rh coordination number is near a value of 3 and no additional variation of CN_{RhRh} was detected upon the following (CO/NO) cycles. However, it needs to be noted that decreasing the temperature appears to increase the average coordination number of RhRh first shell of Rh catalysts under H_2. This effect can be partially attributed to asymmetric pair distribution functions [33]. Furthermore, a more diverse array of nitrosyl functionality was observed over the investigated Rh catalysts, which included mostly the formation of molecular NO adsorbed such as $Rh(NO)_2$ at the edges sites, the "high-wavenumber" $Rh(NO)^-$ species with the minority of $Rh(NO)^+$ entities. The previous studies established the linear correlation between the increased level of Rh oxidation and the higher intensity of $RhNO^+$ signal [34]. Based on the previous observations $Rh(NO)^-$ entities were suggested to be the precursor for NO dissociation and Rh oxidation as to form this species, the electron transfers from the reduced Rh surface to the antibonding orbital of adsorbed NO and results in the Rh-N=O bond formation [12, 26, 35]. It is clear that the particles react structurally to the adsorption of NO, still resisting the large oxidative disruption to have occurred over Rh particles and the Rh component retain their fcc structure, which has been assigned by comparing the obtained EDE data with the scanning EXAFS analyses. It can be a result of the sizeable average Rh particles within the limited oxidative disruption has occurred by molecularly adsorbed NO or it can be due to large oxidation of mostly the smaller particles of the particle size distribution presented by TEM and leaving the largest intact. The interactions postulated cannot be

distinguished only on the base of EXAFS analysis. Moreover, there is an apparent relationship between the $Rh(NO)^+$ adsorption and the level of Rh oxidation – higher temperature allows more extensive Rh oxidation and larger $Rh(NO)^+$ production. On the other hand, a larger Rh perturbation was observed as the CO gas was introduced to the gas feedstock than in the 573 K case, indicating that Rh nanoparticles disrupted onto a mixture of discrete $Rh(CO)_2$ units and small Rh clusters. After the NO exposure following, the DRIFTS spectra exhibited mainly $Rh(CO)_2$ centres being the predominant carbonyl species upon CO flow. Considering the fact that Rh structure was not modified significantly upon flowing CO alone, it is evident that the addition NO to the gas feedstock results in the promotion of $Rh(CO)_2$ formation. The previous studies have also shown that high NO/CO ratio and low temperature favour the $Rh^+(CO)_2$ formation which is indicative of the occurrence of oxidative disruption of the metallic Rh particles [13, 36]. Moreover, subsequent addition of CO led to an increase of isocyanate formation possibly via a Langmuir-Hinshelwood mechanism, involving CO adsorption on vacant sites and reaction between N adatoms and adsorbed CO molecules. Therefore, the appearance of this species may be attributed to the existence of a high population of adjacent N atoms and vacant active sites before the CO exposure [11].

The EXAFS/DRIFTS/MS results indicate that all Rh systems investigated display essentially similar structure-function characteristics. The Ce and/or Zr doping to the Rh catalysts do not introduce any significant differences in the structure-function behaviour when compared to the undoped Rh sample, described in detail above. However, it was expected that the facile disruption of the Rh component could be eliminated by the introduction of Ce to the catalyst composition as it was the case throughout (O_2/CO) switching experiment included in chapter 5. As mentioned previously in chapter 1, rhodium supported on γ-Al_2O_3 was found to sinter easily and react irreversibly with the support forming irreducible Rh oxide phase. It has been postulated by others [37, 38] that Al_2O_3 modified by Ce-Zr exhibited better oxygen storage capacity and high thermal stability, keeping the metal dispersion intact. Due to the fact that the range of temperature employed within this project was limited (up to 573 K) it is unclear if the metal dispersion at high temperature and thermal stability of ceria and/or zirconia doped Rh catalysyts were enhanced. In this case, further investigation would be required to answer for this question. Moreover, the

lack of the MS calculation prevented to establish if the Ce doping to Rh catalysts improved the selectivity of the NO reduction by CO towards the N_2 formation.

6.5 Conclusion

The development of operando studies, coupling simultaneous *in situ* spectroscopic and catalytic measurements under working conditions provides detailed information relating to the catalyst nature, generation of intermediates involved in the catalytic reactions. In general, the structure-function response of Rh catalyst is strongly correlated to the temperature employed.

The catalysts appear to be extensively oxidised at each NO step and fully reduced upon CO exposures throughout $(CO/NO)_3$ cycles at 573 K when compared to the experiments performed at lower temperature (423 K). The structural variations correlates well to the gas flows they are introduced to: the local coordination values falls as NO oxidised the system and the re-reduction of the Rh particles was detected when the gas was switched back to CO gas. This pattern of the structural responses of Rh particles was accompanied with the presence of the linear CO species on the metallic surface and linear $Rh(NO)^+$ entities on the partially oxidised Rh phase.

By carrying out the switching experiment over Rh catalysts at 423 K, different structural changes of Rh nanoparticles and an array of adsorbed intermediates was detected. In the presence of strongly coordinating reagents such as CO and NO, oxidised centres can be stabilised as mononuclear sites which play a role of spectators in the catalytic process. After the initial oxidation of Rh particles by NO exposure, the gas switch introduced an exchange between the two oxidic sites: $Rh(CO)_2$ and O_x-Rh-NO.

The results obtained indicate that NO like O_2 plays similar role in the redox cycle of the Rh catalyst surface, oxidising the Rh surface.

6.6 References

1. Root, T.W., Fisher, G. B., Schmidt, L. D., J. Chem. Phys., 1986. **85**: p. 4679-4686.
2. Schmatloch, V., Jirka, I., Kruse, N., J. Chem. Phys., 1994. **100**: p. 8471-8482.
3. Sellmer, C., Schmatloch, V., Kruse, N., Catal. Lett., 1995. **35**: p. 165-174.
4. Castner, D.G., Somorjai, G. A., Surf. Sci., 1979. **83**: p. 60-82.
5. Imamura, S., Hamada, R., Saito, Y., Hashimoto, K., Jindai, H., J. Mol. Catal. A, 1999. **139**: p. 55-62.
6. Martinez-Arias, A., Fernandez-Garcia, M., Hungria, A. B., Inglesias-Juez, A., Duncan, K., Smith, R., Anderson, J. A., Conesa, J. C., J. Catal., 2001. **204**: p. 238-248.
7. Vlaic, G., Fornasiero, P., Martra, G., Fonda, E., Kaspar, J., Marchese, L., Tomat, E., Coluccia, S., Graziani, M., J. Catal., 2000. **190**: p. 182-190.
8. Wu, X., Xu, L., Weng, D., App. Surf. Sci., 2004. **221**: p. 375-383.
9. Almusaiteer, K.A., Chuang, S. S. C., J. Phys. Chem. B, 2000. **104**: p. 2265-2272.
10. Arai, H., Tominaga, H., J. Catal., 1976. **43**: p. 131-142.
11. Hyde, E.A., Rudham, R., Rochester, C. H., J. Chem. Soc. Faraday Trans., 1984. **80**: p. 531-547.
12. Liang, J., Wang, H. P., Spicer, L. D., J. Phys. Chem., 1985. **89**: p. 5840-5845.
13. Solymosi, F., Bansagi, T., Novak, E., J. Catal., 1988. **112**: p. 183-193.
14. Bravin, A., Fiedler, S., Coan, P., Labiche, J.-C., Ponchut, C., Peterzol, A., Thomlinson, W., Nucl. Instrum. Methods Phys. Res., Sect. A, 2003. **510**: p. 35-40.
15. Anderson, J.A., Millar, G. J., Rochester, C. H., J. Chem. Soc. Faraday. Trans., 1990. **86**: p. 571-576.
16. Srinivas, G., Chuang, S. S. C., Debnath, S., J. Catal., 1994. **148**: p. 748-758.
17. Dictor, R., J. Catal., 1988. **109**: p. 89-99.
18. Hyde, E.A., Rudham, R., Rochester, C. H., J. Chem. Soc. Faraday. Trans., 1984. **80**: p. 531-547.
19. Loffreda, D., Simon, D., Sautet, P., Chem. Phys. Lett., 1998. **291**: p. 15-23.
20. Binsted, N., *X-Mult*, in *University of Southampton*. 2006: Southampton.

21. Martens, J.H.A., Prins, R., Koningsberger, D. C., J. Phys. Chem., 1989. **93**: p. 3179-3185.
22. Newton, M.A., Dent, J. A., Diaz-Moreno, S., Fiddy, S. G., Jyoti, B., J., Evans, J., Chem. Eur. J., 2006. **12**: p. 1975-1985.
23. Granger, P., Dujardin, C., Paul, J. -F., Leclercq, G., J. Mol. Catal. A, 2005. **228**: p. 241-253.
24. Hecker, W.C., Bell, A. T., J. Catal., 1983. **84**: p. 200-215.
25. Dujardin, C., Mamede, A. S., Payen, E., Sombret, B., Huvenne, J. P., Granger, P., Top. Catal., 2004. **30-31**: p. 347-357.
26. Nieuwenhuys, B.E., Adv. Catal., 2000. **44**: p. 259-266.
27. Jentys, A., Phys. Chem. Chem. Phys., 1999. **1**: p. 4059-4065.
28. Van't Blik, H.F.J., Van Zon, J. B. A. D., Huizinga, T., Vis, J. C., Koningsberger, D. C., Prins, R., J. Chem. Phys., 1983. **87**: p. 2264-2267.
29. Campbell, T., Dent, A. J., Diaz-Moreno, S., Evans, J., Fiddy, S. G., Newton, M. A., Turin, S., Chem. Commun., 2002: p. 304-305.
30. Newton, M.A., Dent, A. J., Diaz-Moreno, S., Fiddy, S. G., Evans, J., Angew. Chem. Intl. Ed., 2002. **41**: p. 2587-2589.
31. Raval, R., Harrison, M. A., Haq, S., King, D. A., Surf. Sci, 1993. **294**: p. 10-20.
32. Newton, M.A., Dent, A. J., Fiddy, S. G., Jyoti, B., Evans, J., J. Mater. Sci., 2007. **42**: p. 3288-3298.
33. Koningsberger, D.C., Prins, R., *X-ray Absorption Spectroscopy*. 1988, New York: Wiley, John.
34. Newton, M.A., Dent, A. J., Fiddy, S. G., Jyoti, B., Evans, J., Phys. Chem. Chem. Phys., 2007. **9**: p. 246-249.
35. Anderson, J.A., Millar, G. J., Rochester, C. H., J. Chem. Soc. Faraday Trans., 1990. **86**: p. 571-576.
36. Almusaiteer, K.A., Chuang, S. S. C., Tan, C. D., J. Catal., 2000. **189**: p. 247-252.
37. Kaspar, J., Fornasiero, P., Hickey, N., Catal. Today, 2003. **77**: p. 419-425.
38. Ozawa, M., J. Alloys. Comp., 1998. **886**: p. 275-277.

Chapter 7

Conclusions and future work

7.1 Conclusion

In this thesis on Rh catalysts on supported γ-Al_2O_3, the effects of ceria and zirconia on their performance are explored under various conditions. Initially, the prepared Rh samples have been investigated in the atmosphere of air using TEM, STEM EDX HAADF, EDX, XPS and XAFS. In the next step of this project the catalytic performance, structural response and reactivity of nanoparticulate Rh catalysts were studied using the array of EDE/DRIFTS/MS techniques.

The TEM measurement reveals that the produced Rh samples consist of well-dispersed Rh nanoparticles supported on γ-Al_2O_3. The Rh particle size distributions demonstrate a similar pattern of Rh particles size in the range of 0.7 nm to 4 nm for all Rh catalysts investigated. Slightly larger PSDs are observed for ceriated and/or zirconated Rh catalysts (method II) when compared with undoped Rh/Al_2O_3 or ceriated Rh sample (method I), in particular for 4 wt% of Rh loading. Moreover, the STEM EDX HAADF analyses indicate that following the surface controlled modification procedure (method II) the Ce is successfully deposited in the close vicinity to Rh particles. The detailed analysis of Rh and Ce/Zr interactions are further investigated by the spectroscopic techniques. XPS, XAFS in the *ex situ* mode results over a series of Rh catalysts highlight the considerable effect the nature of the promoter (Ce,Zr) can have on the size and phase of the Rh supported on γ-Al_2O_3. The following observations can be highlighted:

- Rh/Al_2O_3 – Rh nanoparticles are mostly oxidised (~90 %). However, slightly more reduced component is observed for larger Rh loading. The Rh particles of 4 wt% Rh sample are sufficiently large to retain an metallic core beneath the oxide shell.
- Rh/CeO_x/Al_2O_3 (I) – Rh particles are extensively oxidised for both Rh loadings. The curve fitting analysis of Ce 3d XPS spectra reveal that CeO_x/Al_2O_3 support contains a significant amount of Ce^{4+} (ca. 70 %). Subsequent Rh deposition results in the equivalent level of Ce^{3+} and Ce^{4+} present in the system;
- Rh/CeO_x/Al_2O_3 (II) – a larger proportion of the metallic Rh component (~ 40 %) present in this sample indicates that pre-supported Rh particles are active for the Ce deposition. The CeO_x phase partially keeps the Rh metallic thereby protecting them from

oxidation while it was not the case for ceriated Rh catalysts (method I). Similar amounts of Ce^{3+} and Ce^{4+} are also displayed by the Ce 3d XPS studies over this catalytic system.

- $Rh/CeO_x/ZrO_2/Al_2O_3$ (Ce:Zr;1:1) – the level of Rh oxidation, for both Rh loadings, is similar as for ceriated Rh catalysts (II). Zirconia doping promotes the reducibility of ceria and the dominant form in the system becomes Ce^{3+} (~ 70 %).
- $Rh/CeO_x/ZrO_2/Al_2O_3$ (Ce:Zr;2:1) – surprisingly, the level of Rh oxidation is high (~ 80 %) for 1.6 wt% Rh loading. In the case of 4 wt% Rh sample, the proportion of the oxidised Rh phase is similar to that for Ce and Ce/Zr (1:1) doped Rh catalysts. Clearly, the Zr doping supports the reduction of ceria to the Ce^{3+} form (~ 60 %). It can be observed that the larger amounts of Zr employed increase relatively the reducibility of ceria in the system.
- $Rh/ZrO_2/Al_2O_3$ – both Rh 3d XPS and Rh K edge XAFS analysis indicate that the largest proportion of the reduced fraction of Rh particles (~ 50 %) and the largest Rh particles are observed for this system among all the Rh catalysts investigated.

The application of EDE/DRIFTS/MS in the time-resolved, *in situ* manner to study of gas-solid processes over supported Rh catalysts within this project has revealed new insights into the details of physical character, the nature of the Rh components and the reactivity of the Rh catalysts under varied conditions (different temperature and gas feedstock). This approach has been used to investigate the interaction of H_2, O_2, CO and NO gases with the series of supported Rh on γ-Al_2O_3 additionally doped by ceria/zirconia. The formation of the potential active phases (metallic and oxidic) has a significant influence on the performance of the catalytic Rh systems altering the selectivity and rates of the reaction. Rhodium metal as an active metal of TWC changes its oxidation state rapidly upon the different gas compositions and temperatures employed. Moreover, the structural response of Rh component upon the atmosphere of air, H_2 and CO was investigated using scanning EXAFS in order to verify the reliability of EDE data and the presence of other neighbours around the Rh metal.

The XAFS studies reveal that after reduction of all Rh systems under 5 % H_2/He, the metallic Rh core is regenerated which shows the characteristics of a fcc structure. However, each catalyst material has substantially different average particle size. Upon CO exposure to the Rh systems, structural disruption of Rh particles is observed, the levels of which decreases relatively with increasing temperature. The larger disruption of Rh particles is associated mainly with the adsorption of geminal dicarbonyl species. At higher T (>400 ^oC), the $Rh(CO)_2$ species are intrinsically not stable and decompose, which inhibits the disruption process, consequently larger, metallic Rh particles are present on the surface. Moreover, the CO dissociation on Rh is particle size and temperature dependent and may simply block sites for geminal dicarbonyl formation. Among all the Rh catalysts investigated significant differences of structure-function Rh behaviour upon CO flow are observed for the ceriated Rh catalyst (II). The deposition of Ce on the pre-supported Rh catalysts appears to minimise the Rh and Al_2O_3 support interaction, which leads to the enlargement of Rh particles before CO exposure and to the formation of mainly linear and bridged CO species even at 323 – 423 K. Moreover, a series of ceriated Rh catalysts exhibit the additional IR signal at ca. 1700 cm^{-1} assigned to the bridged CO species between Rh and Ce metals. A main conclusion is that CeO_x strongly influences the oxidation behaviour of the Rh nanoparticles by increasing the amount of Rh metal at the surface of the catalysts. This effect is ascribed to the occurrence of strong metal support effects which protects the Rh phase against oxidation. However, the reduction treatment within method II can also have an influence on the presence of larger metallic Rh fraction. Furthermore, the presence of ZrO_2 in the catalysts is shown to influence the Rh oxidation state, leading to an even more metallic behaviour of the Rh particles.

In view of $(O_2/CO)_3$ switching experiment, a similar trend of structural Rh response is observed for all catalysts investigated. Exposing 5 % O_2/He to the pre-reduced Rh catalysts, the supported Rh nanoparticles undergo rapid and extensive oxidation. This results in the formation of a thin layer oxide surrounding the metallic core. This layer is a barrier for the subsequent oxidation, which can only proceed through migration of dissociated oxygen, thus, relatively slow oxidation occurs over the metallic core. The subsequent flowing 5 % CO/He to Rh systems reduces the level of Rh oxidation. In the range of 473 K – 573 K, a clear synchrony between the

following (O_2/CO) switches and the structural response of the nanoparticulate Rh is present: partial oxidation of Rh under flow of O_2 and formation of linear CO species on a wholly metallic Rh surface upon CO exposure, with significant amount of CO_2 produced between each switch. Noticeably, larger Rh particles and larger oscillations of Rh oxidation were observed for ceriated Rh catalysts (II). Moreover, the catalytic activity of Ce-doped Rh catalyst (II) over CO oxidation tends to be slightly better when compared with the undoped and Ce/Zr promoted Rh systems. Introduction of ZrO_2 to γ-Al_2O_3 supported Rh catalysts results in the presence of the largest Rh particle size and limitation of Rh oxidation throughout the entire $(O_2/CO)_3$ switching experiment.

Summarising the $(CO/NO)_3$ switching experiment over a series of Rh systems, the Rh nanoparticles are disrupted under CO in a similar manner as seen throughout the CO interaction with Rh particles. Upon 5 % NO/He exposure at lower temperature (423 K), rapid, oxidative disruption of Rh particles was observed. The Rh components reside as smaller oxidic particles which promotes the formation of the $Rh(CO)_2$ species under the following CO switch. Thus, the system remains predominantly oxidised throughout the entire process with no evidence of the Rh agglomerating back to its original form. At highest temperature employed (573 K), the Rh phase is extensively oxidised under 5 % NO/He flow. The structure of Rh particles respond in the consistent, cyclic manner upon the succeeding (CO/NO) cycles, highlighting the synchrony between CO bound on metallic Rh on reduced and formation of linear nitrosyl species on partially oxidised Rh particles.

The results of this thesis show that there is a clear need for a further development of new TWC which are based on significantly smaller Rh loading (0.5 wt% Rh in the system). This is due to high cost of this rare transition metal and also enhanced activity and selectivity of the catalyst can be obtained by well dispersed metal particles [1]. Apart from CeO_x and ZrO_2 promoters utilised in this project, other dopants such as La_2O_3 and BaO could be incorporated to the catalytic system, as they increase the catalytic activity and stabilise the metal dispersion at high temperature [2]. As such, this complex system would correspond more closely to real working catalysts in the automobile industry [3, 4]. Furthermore, XAFS studies over

highly dispersed metal catalysts could detect the presence of other metal neighbours around the active metal [5].

However, the quality of spectroscopic techniques such as EDE and DRIFTS, used to provide direct structural and functional information about the metal in a relevant environment, are sensitive to the metal particle size and the presence of other adsorbents (CeO_x, ZrO_2, La_2O_3 etc.), that may scatter X-rays. Thus, in the current setting of this approach, by investigating the smaller metal particles only the small range of XAFS energy at Rh K edge (XANES region) and poorer quality of DRIFTS spectra would be expected to collected. Therefore, the other challenge of this project would be the improvement of the instrumentation including the optical components and detector, which could enhance the beam stability and its homogeneity.

7.2 References

1. Van't Blik, H.F.J., Van Zon, J. B. A. D., Huizinga, T., Vis, J. C., Koningsberger, D. C., Prins, R., J. Am. Chem. Soc., 1985. **107**: p. 3139-3147.
2. Heck, R.M., Farrauto, R. J., App. Catal. A, 2001. **221**: p. 443-457.
3. Farrauto, R.J., Heck, R. M., Catal. Today, 1999. **51**: p. 351-360.
4. Webster, D.E., Top. Catal., 2001. **16/17**: p. 33-37.
5. van Zon, J.B.A.D., Koningsberger, D. C., van't Blik, H. F. J., Sayers, D. E., J. Chem. Phys., 1985. **12**: p. 5742-5749.